

**ANALYSIS OF MULTIPLE
TRANSITIONAL
STRIPPED-ENVELOPE
CORE-COLLAPSE SUPERNOVAE**

by

Kyle Medler

A thesis submitted in partial fulfillment for the
degree of Doctor of Philosophy

November 20, 2023

Declaration

The work presented in this thesis was carried out at the Astrophysics Research Institute, Liverpool John Moores University. Unless otherwise stated, it is the original work of the author.

While registered as a candidate for the degree of Doctor of Philosophy, for which submission is now made, the author has not been registered as a candidate for any other award. This thesis has not been submitted in whole, or in part, for any other degree.

Kyle Medler
Astrophysics Research Institute
Liverpool John Moores University
IC2, Liverpool Science Park
146 Brownlow Hill
Liverpool
L3 5RF
UK

NOVEMBER 20, 2023

Abstract

Massive stars, with $M_{\text{ZAMS}} > 8 M_{\odot}$, end their lives as explosive events known as core-collapse supernovae (CC-SNe). A sub-class of these CC-SNe have had some or part of their outer hydrogen/helium envelope removed prior to the collapse of the iron core and explosion of the progenitor, known commonly as a stripped envelope SNe (SE-SNe). Depending on the degree of stripping the progenitor undergoes several different classifications of SE-SNe can occur. If a significant mass of hydrogen, $\sim 0.01 M_{\odot}$, remains within the outer envelope a Type IIb SN occurs (SN IIb), however if the majority of the hydrogen is removed from the outer envelope and only helium remains a Type Ib SN (SN Ib) occurs. Finally if both the hydrogen and a large majority of the helium is stripped from the progenitor prior to core-collapse a Type Ic SN (SN Ic) is observed. It is thought that the transition between the hydrogen-rich and hydrogen/helium-poor SNe may be a smooth continuum dependent primarily on the stripping mechanism. Observations of events that display features that transition between classifications are needed to determine the boundaries between different types of SE-SNe. In this work I present the study of three such SE-SNe that exploded within the last 5 years. The first two of these events have been identified to display features not typically associated with their initial classification.

In the first case, I present the study of SN 2020cpg a SN Ib that exhibits fast hydrogen lines within its early phase spectra which grew in strength until it rivalled the strength seen in SNe IIb. The presence of the hydrogen feature lead to a reclassification of SN 2020cpg as a SN Ib(II). In addition to the fast hydrogen features a light curve comparison between SN 2020cpg and other modelled SE-SNe show SN 2020cpg ejected $\sim 5.5 \pm 2.0 M_{\odot}$ of material with a kinetic energy of $\sim 9.0 \pm 3.0 \times 10^{51}$ erg. This light curve comparison

method can account for the mass of helium that is usually not taken into account due to the high excitation energy required for helium emission.

Then I discuss the work on SN 2020acat, a SN IIb that displayed a fast rise to bolometric peak. Analysis of the light curve of SN 2020acat shows the lack of a shock cooling phase, a rise time at the lower limit of SN IIb and ejecta mass/kinetic energy indicative of an intermediate mass progenitor. Analysis of the [O I] $\lambda\lambda 3600, 3636$ feature and comparisons with other SNe IIb during the nebular phase suggests that SN 2020acat originated from a reasonably high mass progenitor star. From the analysis of the optical observations of SN 2020acat I then move on to the near infrared (NIR) spectroscopic evolution and the development of a flat-top shape that emerges within the helium 1.0830 and 2.0581 μm lines. The shape of the NIR helium features indicate a central region within SN 2020acat that lacked mixing of the helium shell with the inner oxygen-rich shell. Evidence of similar features are present within the literature, which alongside to optical observations of SN 2020acat, suggest the flat-top shape is related to the structure of the progenitor.

Finally I use the examination of a GRB-SN, SN 2019oyw, to study the energy mass relation between different types of helium-poor SE-SNe. Initially I present the data and analysis of the photometry and spectra of SN 2019oyw, using a light curve comparison method to obtain an expected ejecta mass of $10.0 \pm 3.0 M_{\odot}$ and a kinetic energy of $\sim 19.5 \pm 8.0 \times 10^{51}$ erg for SN 2019oyw. The validity of the light curve comparison method is tested by comparing the results obtained using a semi-analytic and the light curve comparison for SN 2019oyw. From the spectroscopy of SN 2019oyw a new classification as a SNIc-3/4 is suggested, which is further confirmed by the energy-mass ratio. Lastly I analyse the energy-mass relation of hydrodynamically modelled SNe Ic-BL and GRB-SNe to determine if there is a smooth function that can capture the evolution of both types of helium-poor SNe.

Publications

During the course of the preparation of this thesis, the work within Chapters 2, 3 and 4 have been presented in the following jointly authored publications:

1 “*SN 2020cpg: an energetic link between type IIb and Ib supernovae*”

K. Medler, P. A. Mazzali, J. Teffs, S. J. Prentice, C. Ashall, M. Amenouche, J. P. Anderson, J. Burke, T. W. Chen, L. Galbany, M. Gromadzki, C. P. Gutiérrez, D. Hiramatsu, D. A. Howell, C. Inserra, E. Kankare, C. McCully, T. E. Müller-Bravo, M. Nicholl, C. Pellegrino, J. Sollerman, 2021, MNRAS, Volume 506, Issue 2, P 1832.

2 “*SN 2020acat: an energetic fast rising Type IIb supernova*”

K. Medler, P. A. Mazzali, J. Teffs, C. Ashall, J. P. Anderson, I. Arcavi, S. Benetti, K. A. Bostroem, J. Burke, Y-Z. Cai, P. Charalampopoulos, N. Elias-Rosa, M. Ergon, L. Galbany, M. Gromadzki, D. Hiramatsu, D. A. Howell, C. Inserra, P. Lundqvist, C. McCully, T. Müller-Bravo, M. Newsome, M. Nicholl, E. Padilla Gonzalez, E. Paraskeva, A. Pastorello, C. Pellegrino, P. J. Pessi, A. Reguitti, T. M. Reynolds, R. Roy, G. Terreran, L. Tomasella, D. R. Young, 2022, MNRAS, Volume 513, Issue 4, P 5540.

3 “*A massive, energetic model for the luminous transitional Type Ib/IIb SN 2020cpg*”

J. Teffs, P. A. Mazzali, **K. Medler**, S. Hachinger, 2022, MNRAS, Volume 517, Issue 4, P 5678.

4 “*Flat-topped NIR profiles originating from an unmixed helium shell in the Type IIb SN 2020acat*”

K. Medler, P. A. Mazzali, C. Ashall, J. Teffs, M. Shahbandeh, B. Shappee, 2023, MNRAS:Letters, Volume 518, Issue 1, L40.

5 “*The study of SN 2019oyw and an initial inspection of the M_{ej}/E_k relation in helium-poor stripped-envelope supernovae*”

K. Medler,, 2023(In Prep), MNRAS

Publication 1 forms the basis for Chapter 2, and discusses the photometric and spectroscopic evolution of the Type IIb SN 2020cpg and the emergence of a high velocity hydrogen feature. The original manuscript was prepared by K.Medler, with an important contribution from P.A.Mazzali, and minor comments from co-authors, colleagues and an anonymous referee were incorporated later.

Publication 2 forms the basis of Chapter 3, and is based on the study of a fast rising Type IIb SN 2020acat and the follow-up campaign that observed SN 2020acat well into the nebular phase. The original manuscript was prepared by K.Medler, with an important contribution from P.A.Mazzali and J.Teffs, and minor comments from co-authors, colleagues and an anonymous referee were incorporated later.

Publication 4 forms the basis of Chapter 4, and covers the analysis of the near infrared observations of the Type IIb supernovae SN 2020acat. The original manuscript was prepared by K.Medler, with an important contribution from P.A.Mazzali, and minor comments from co-authors, colleagues and an anonymous referee were incorporated later.

Publication 5 forms the basis of Chapter 5, and examines the optical photometric and spectroscopic observations of a recent GRB-SN SN 2019oyw, comparing it to other SNe Ic-BL. The original manuscript was prepared by K.Medler, with an important

contribution from P.A.Mazzali and E.Pian, and minor comments from co-authors, colleagues and an anonymous referee were incorporated later.

Acknowledgements

I would like to thank my supervisor Paolo Mazzali who has guided me through my PhD. I would also like to thank my friends at the ARI, especially those in room 3.18, who have helped keep my sanity during the difficult times during my PhD. I thank my parents, both old and new, for giving me the drive and support to persist in my work and for continuing to push me forward onto greater heights. I also thank all my family for strengthening me as a person. Finally, a big thanks is given to my friends scattered around the UK for the support and encouragement that have provided.

“In all things of nature there is something of the marvellous.”

– Aristotle

“It’s not worth doing something unless someone, somewhere, would much rather you weren’t doing it.”

– Terry Pratchett

“It is sometimes an appropriate response to reality to go insane.”

– Philip K. Dick

“This is how you do it: you sit down at the keyboard and you put one word after another until its done. It’s that easy, and that hard.”

– Neil Gaiman

Contents

Declaration	ii
Abstract	iii
Publications	v
Acknowledgements	viii
List of Figures	xiii
List of Tables	xvii
1 Introduction	1
1.1 Core-Collapse Supernovae explosion mechanism	1
1.1.1 SE-SNe explosion mechanism	1
1.1.2 GRB-SNe explosion mechanisms	7
1.2 CC-SNe classification	8
1.2.1 Spectroscopic evolution	8
1.2.1.1 SNe IIb	10
1.2.1.2 SNe Ib	11
1.2.1.3 SNe Ic and GRB-SNe	13
1.2.2 New classification and transitional events	13
1.2.3 Photometric evolution	15
1.2.3.1 SNe IIb, Ib and Ic	15
1.2.3.2 SNe Ic-BL and GRB-SNe	16
1.2.4 Kinetic energy distribution across SE-SNe	19
1.3 SE-SNe formation channels	20
1.3.1 Single Star Model	20
1.3.2 Binary Star Model	22
1.3.3 Single Star vs Binary Progenitor Models	23
1.3.4 Observational Evidence of SE-SNe Progenitors	25
1.4 Thesis statement	26
2 The intermediate H-rich SN 2020cpg	27

2.1	Introduction	27
2.2	Observations and Data Reduction	29
2.2.1	Explosion date and Host Galaxy	29
2.2.2	Photometry	30
2.2.3	Spectroscopy	31
2.3	Method	33
2.3.1	Pseudo-bolometric Light curve	33
2.3.2	Physical parameters	35
2.4	Results	37
2.4.1	Multi-colour light curves	37
2.4.2	pseudo-bolometric Light Curves	39
2.4.3	Spectral Evolution and Comparison	41
2.5	Discussion	46
2.5.1	Hydrogen Envelope	47
2.5.2	Model Comparisons	48
2.5.3	Re-scaled Light curves	53
2.6	Summary and Conclusions	57
3	The fast rising Type IIb SN 2020acat	60
3.1	Introduction	60
3.2	Host Galaxy and Explosion Date	61
3.3	Data Acquisition	63
3.3.1	Photometry	63
3.3.2	Spectroscopy	65
3.4	Photometry Analysis	69
3.4.1	UV to NIR Light Curves	69
3.4.2	Colour Evolution	71
3.4.3	Bolometric light curve	75
3.5	Spectroscopic Analysis	83
3.5.1	Early Phase	84
3.5.1.1	Pre-maximum light	84
3.5.1.2	Post-maximum light	87
3.5.2	Line Velocity Evolution	88
3.5.3	Transition into the Nebular phase	90
3.5.4	Nebular Phase	92
3.5.5	Oxygen mass and $[\text{Ca II}]/[\text{O I}]$ ratio	93
3.6	Conclusions	98
4	The flat-top shape of the NIR He profile of SN 2020acat	100
4.1	Introduction	100
4.2	SN 2020acat optical analysis	101
4.3	NIR Spectra	101
4.4	Flat-topped P-Cygni profiles	104
4.5	Helium 1.0830 & 2.0581μm Features	105

4.6	SNe I Ib Helium Structure	108
4.7	Conclusions	110
5	The study of SN 2019oyw and an initial inspection of the $M_{\text{ejc}}/E_{\text{k}}$ relation in He-poor stripped-envelope supernovae.	113
5.1	Introduction	113
5.2	The GRB associated with SN 2019oyw	115
5.3	Photometry	116
5.3.1	GRB afterglow	116
5.3.2	Photometry of SN 2019oyw	118
5.4	Pseudo-Bolometric light curve	118
5.5	Spectroscopy	120
5.5.1	Spectral Evolution and line velocities	122
5.5.2	Spectral Comparison	125
5.5.3	Re-classification	127
5.6	Explosion Parameters	128
5.6.1	Light curve comparison	128
5.6.2	Semi-Analytical light curve model	131
5.6.3	Model comparisons	133
5.7	Mass and Energy relation	135
5.8	Conclusion	138
6	Conclusions and Future Work	141
6.1	Conclusions	141
6.2	Future work	148
	Bibliography	149
	Appendix	167

List of Figures

1.1	Artistic impression of the Type IIb supernova, SN 1993J that exploded in the galaxy M81 in early 1993.	2
1.2	Core evolution of a high mass star as it undergoes core-collapse.	4
1.3	Standard view of CC-SNe classification, from the hydrogen rich to the helium poor.	9
1.4	Spectroscopic evolution of the SN IIb SN 1993J and the SN Ib SN 2008D.	11
1.5	Spectroscopic evolution of the SN Ic SN 1994I and the SN Ic-BL SN 1998bw.	12
1.6	V-band photometric observations of SN 1993J, 2008D, 1994I and 1998bw, showing the photometric diversity of the different types of SE-SNe.	15
1.7	The VRI-band afterglow of GRB 990510 fit with a broken power law.	18
1.8	Cumulative distribution of the kinetic energies found across the different types of SE-SNe.	19
1.9	Evolution of the hydrogen envelope in single star and binary star models prior to core-collapse.	21
1.10	HST images of the site of SN 2011dh, a Type IIb SN, taken prior and post explosion to determine the progenitor of the SN.	24
2.1	Localisation image of SN 2020cpg and its host galaxy from stacked BgVri-band images.	28
2.2	[Absolute magnitude photometry of SN 2020cpg obtained over the ~ 130 day follow-up campaign.]The absolute magnitude photometry of SN 2020cpg in the BgVri-bands along with the ATLAS c and o-band covering ~ 130 days from the explosion date. The individual band light curves have been corrected for extinction, shifted by a constant magnitude and are shown in rest frame. The red dashed lines denote the epochs at which spectra were taken.	30
2.3	Optical spectra of SN 2020cpg obtained during the follow-up campaign and the main spectral features.	32
2.4	The pseudo-bolometric light curve of SN 2020cpg constructed from the BgVri-band photometry.	34
2.5	Multi-band photometric comparison of SN 2020cpg with several other well observed SNe Ib and SNe IIb.	38
2.6	Comparison of the pseudo-bolometric light curves for several helium rich SE-SNe with SN 2020cpg. In addition fitting of an Arnett-like model is shown for each SN.	40

2.7	Evolution of the position of the absorption minima for the hydrogen, helium and iron lines. The hydrogen line has been split into a high and low velocity component and followed throughout its evolution.	42
2.8	Line velocity of the H α , He I and Fe II lines obtained from the spectra of SN 2020cpg. The low velocity component of the H α line lies on top of the velocity of the fastest helium line.	45
2.9	Comparison of the H α regions between SN 2020cpg, a characteristic SN Ib, SN 2015ap, and SN IIb, SN 2011dh, to determine the similarities in the evolution of the hydrogen feature. The feature seen in SN 2020cpg shows a similarity with both types of SE-SNe at different epochs.	46
2.10	Spectroscopic modelling of SN 2020cpg using different energies with the assumption that SN 2020cpg was either a SN IIb, with the inclusion of a thin hydrogen envelope (Top), or a SN Ib, which lacked any hydrogen envelope (Bottom).	50
3.1	<i>ugriz</i> stacked image of SN 2020acat, its host galaxy and standard stars taken on 22/12/2020.	62
3.2	UV, optical and NIR photometry of SN 2020acat in rest frame absolute and apparent magnitudes.	64
3.3	Optical spectroscopic evolution of SN 2020acat, normalised to peak of the H α or O I $\lambda\lambda$ 6300, 6363 feature.	66
3.4	<i>B</i> -band rise time of SN 2020acat compared to the <i>B</i> -band rise times of a sample of both SNe II and other SNe IIb, showing SN 2020acat rose faster than the majority of SNe IIb.	71
3.5	Comparison of the several different colour evolutions of SN 2020acat with several other well observed SNe IIb. SN 2020acat was fit with a decay function to follow the evolution of colour at late times.	73
3.6	Pseudo-bolometric light curve of SN 2020acat, alongside UV+optical, optical and optical+NIR pseudo-bolometric light curves (Top). Contribution of the different regions of the electromagnetic spectrum to the total pseudo-bolometric light curve (Bottom).	76
3.7	The pseudo-bolometric light curves of SN 2020acat and several other well observed SNe IIb, in addition SN 2020acat was fit with an Arnett-like model to determine the physical parameters of the explosion.	79
3.8	Pre-peak, day \sim 9, spectroscopic comparison of SN 2020acat with several other SNe IIb.	81
3.9	Spectroscopic comparison between SN 2020acat and other SNe IIb taken around peak time, day \sim 20.	84
3.10	H α , H β , He I λ 5876 and Fe II λ 5018 line velocity evolution obtained from the spectra of SN 2020acat over the first 100 days after explosion. Additional line velocities are shown for other SNe IIb.	87
3.11	Spectral comparison of SN 2020acat with several well observed SNe IIb roughly 60 days after explosion.	88
3.12	Comparison of nebular phase spectra, taken around day 170, between SN 2020acat and other SNe IIb, ordered with respect to the [O I]/[Ca II] ratio.	91

3.13	Evolution of the nebular phase [O I] $\lambda\lambda 6300, 6363$ (left) and the [Ca II] $\lambda\lambda 7292, 7324$ (right) emission profiles.	94
3.14	Nebular phase one-zone spectral modelling of SN 2020acat compared to the observed spectra taken at ~ 171 (top) and ~ 233 (bottom) days.	96
4.1	NIR rest frame spectroscopic evolution of SN 2020acat, the final spectrum has a smoothed spectrum overlaid to provide clarity to the spectral features.	103
4.2	Evolution of the He I $1.0830 \mu\text{m}$ and $2.0581 \mu\text{m}$ in velocity space displaying the emergence of the flat-topped feature as the photosphere recedes through the ejecta of SN 2020acat.	104
4.3	Comparison between the model spectrum, fit to the day ~ 75 spectrum of SN 2020acat without the presence of helium below $\sim 5000 \text{ km s}^{-1}$, and the observed He I $0.5876, 1.0830, \text{ and } 2.0581 \mu\text{m}$ features.	106
4.4	Comparison of the late time [O I] $6300, 6363$ peak and the smoothed NIR He I features (Top). Structure of the He/O-rich shells in the progenitor of SN 2020acat corresponding to the velocities derived from the spectra (Bottom).	109
4.5	The late time He I $1.0830 \mu\text{m}$ and $2.0581 \mu\text{m}$ features of SN 2020acat compared to those observed SN 2008ax and SN 2011dh at similar epochs.	111
5.1	Photometric observations of GRB 190829A/SN 2019oyw, corrected for extinction and redshift. Photometry prior to 3 days post detection was fit with single power laws to determine the GRB afterglow contribution to the SN photometry.	114
5.2	Comparison between the r -band of SN 2019oyw, the R -band of SN 1998bw and the re-scaled R -band light curve of SN 1998bw.	120
5.3	Pseudo-bolometric light curve of SN 2019oyw and several other SNe Ic-BL, covering the first 90 days since their explosion, showing a clear similarity between SN 2019oyw and SN 1998bw.	121
5.4	Spectral evolution of SN 2019oyw, with all spectra having been corrected for extinction and redshift. In addition a smoothed spectrum is given at each epoch to reduce to amount of noise in each spectrum.	123
5.5	Evolution of the photospheric velocity, v_{ph} , of SN 2019oyw and several other H/He-poor SNe, showing the transition of SN 2019oyw between a velocity similar to SN 1998bw and SN 2006aj.	125
5.6	Photospheric spectral comparison of SN 2019oyw and other SNe Ic-BL around 10 days post explosion.	126
5.7	Peak-time spectral comparison of SN 2019oyw with multiple SN Ic-BL obtained around 20 post explosion.	130
5.8	Evolution of the Fe II peak as it shifts to longer wavelengths seen in SN 1998bw (left), SN 2019oyw (middle) and SN 2006aj (right).	133
5.9	Ejecta mass vs kinetic energy relation obtained through hydrodynamical modelling for SNe Ic, SNe Ic-BL and GRB/SNe. SN 2019oyw has been placed based on the M_{ejc} and E_{k} derived in Section 5.6.1. A continuous power law function, fit to the SNe Ic-BL and GRB/SNe, is also shown.	136

5.10	Progenitor mass vs kinetic energy for the He-poor SE-SNe, with SN 2019oyw included in the GRB/SNe region.	139
6.1	M_{H} distribution of several SNe IIb and SN Ib showing SN 2020cpg lies on the upper limit of SNe Ib.	143
6.2	B -band rise time distribution for SN II and SNe IIb showing SN 2020acat possessed a faster rise time than the majority of SNe IIb.	145
6.3	Power-law fit to the M_{ejc} vs E_{k} of He-poor SE-SNe.	146

List of Tables

2.1	Details on the spectroscopic observations obtained throughout the follow-up campaign of SN 2020cpg.	33
2.2	Photometric properties of the $BgVcroi$ -bands which includes epoch of maximum, rise time and maximum apparent and absolute magnitude . . .	37
2.3	Details on several historical Type Ib and IIb SNe that are used to compare with the light curve properties of SN 2020cpg	40
2.4	Physical properties of several SE-SNe, including SN 2020cpg, derived from the fitting of the Arnett-like model to their pseudo-bolometric light curves.	43
2.5	Details on the observation date and instrument for the SNe using in the spectral comparison of the $H\alpha$ region in SN 2020cpg that is shown in Figure 2.9.	48
2.6	Kinetic energies and ejecta masses derived for SN 2020cpg obtained through the comparison of its light curve with several SE-SNe that have undergone hydrodynamic modelling.	52
2.7	Opacities derived for several SE-SNe from the opacity of SN 2020cpg using the average kinetic energy and ejecta mass found in Section 2.5.3.	57
3.1	Information on spectroscopic follow-up campaign for SN 2020acat, including phase, observation date, telescope and instrument used and wavelength range covered by the observation.	67
3.2	Continuation of spectral information from Table 3.1.	68
3.3	Photometric details on the $UVW2, UVM2, UVW1, u, U, D, gV, r, i, z$ -bands, includes date of peak magnitude, rise time and both apparent and absolute peak magnitudes.	70
3.4	Information on the SNe IIb that are used as comparisons to SN 2020acat.	75
3.5	Light curve details and physical parameters derived from fitting the pseudo-bolometric light curves for SN 2020acat and the other SNe IIb with the Arnett-like fit.	78
3.6	Mass of oxygen obtained from the late time spectra of SN 2020acat using equation. 3.4.	96
4.1	Observational details for the NIR spectra of SN 2020acat, including phase from explosion, instrument used, telluric STD, air mass and exposure time used for the observation.	102
4.2	Line velocity of the He τ 1.0830 μm and 2.0581 μm lines derived from fitting the absorption minimum with a Gaussian fit.	105

4.3	Velocity of the helium shell at the edges of the flat-topped region found from the He I 1.0830 μm and 2.0581 μm features.	107
5.1	Optical band temporal flux decay indices, α_{opt} , of GRB 190829A	117
5.2	Rise time and peak magnitudes of $rRiIz$ -bands of SN 2019oyw obtained from the fitting of a low order polynomial to the peak time observations.	118
5.3	Information on the spectral observations of SN 2019oyw.	121
5.4	Explosion properties of SN 2019oyw derived from equations 5.1 and 5.2, Comp, and the parameters obtained from the best-fit light curve model fit to the pseudo-bolometric light curve, Best-fit.	135
A1	Apparent $BgVri$ LCO Photometry of SN 2020cpg, no k-correction or extinction correction applied.	168
B1	Apparent ri LCO Photometry of SN 2020cpg, no k-correction or extinction correction applied.	169
C1	Apparent c+o band ATLAS photometry for SN 2020cpg. Photometry has not been corrected for either extinction or k-correction.	170
D1	UV Swift	171
E1	LCO $BgVri$	172
F1	Table above cont	173
G1	ZTF	174
H1	LT	175
I1	UBVRI ALFOSC AFOSC Morivan	176
J1	ugvriz ALFOSC AFOSC Morivan	177
K1	NIR data	178
L1	$grRiIz$ photometry for GRB 190829A/SN 2019oyw. Photometry has not been corrected for host or galactic extinction as well as k-correction and GRB afterglow. Phase is given relative to initial detection and is in rest-frame.	178

...

Chapter 1

Introduction

1.1 Core-Collapse Supernovae explosion mechanism

1.1.1 SE-SNe explosion mechanism

Core-collapse supernovae (CC-SNe), initially described in the 1930's by [Baade & Zwicky \(1934\)](#), are the disruptive end of stars with a Zero Age Main Sequence (ZAMS) mass, $M_{\text{ZAMS}} > 8 M_{\odot}$ ([Woosley et al., 1995](#); [Smartt, 2009](#)). There are several mechanisms that can explosively disrupt a high mass star resulting in a SN. Firstly, the electron capture SNe that explode low mass ($M_{\text{ZAMS}} = 8 - 10 M_{\odot}$) oxygen-Neon-magnesium core stars ([Miyaji et al., 1980](#); [Nomoto, 1984](#)), also the pair-instability SNe where temperatures within the core of massive stars ($M_{\text{ZAMS}} = 100 - 140 M_{\odot}$ ([Chen et al., 2014](#))) enable electron-positron pair formation destabilising the star ([Fowler & Hoyle, 1964](#); [Barkat et al., 1967](#); [Fraley, 1968](#); [Rakavy & Shaviv, 1967](#)) and finally, the iron core-collapse SNe where nuclear fusion is halted within the core of a high mass star ($M_{\text{ZAMS}} = 8 - 40 M_{\odot}$) and the star collapses inwards under gravitational forces ([Colgate & White, 1964](#); [Arnett, 1980b](#); [Wilson, 1980](#); [Bowers & Wilson, 1982](#); [Wilson et al., 1986](#)). Out of the three types of SNe mentioned the iron CC-SNe (hereafter CC-SNe) has been most prominent in both the literature and is considered the main formation channel of high mass supernovae ([Takahashi, 2018](#)).

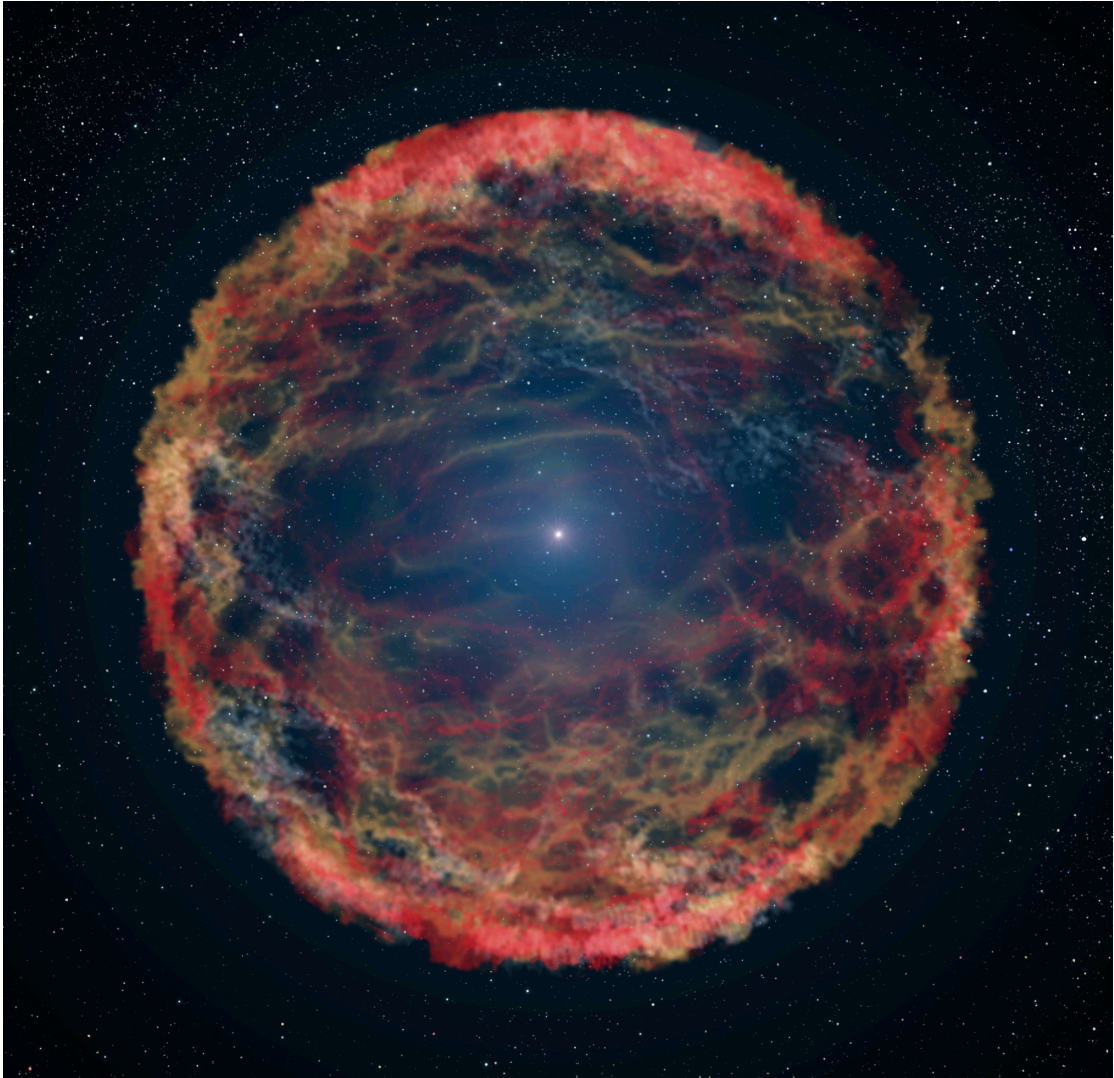


FIGURE 1.1: Artistic impression of SN 1993J, a SN IIb that exploded in the galaxy M81 in early 1993. Credit: NASA¹, ESA², and G. Bacon (STScI) STSci-PRC14-38a.

The process of CC-SNe formation starts once a star has reached the silicon burning phase at which point an iron ash is synthesised and begins to build up within the inner core (Arnett, 1977). At the point of silicon burning, the temperature and pressure within the core is insufficient to fuse the iron. The iron ash continues to accumulate within the core as it grows in size (Woosley & Janka, 2005). At earlier stages of stellar evolution, the development of a higher mass core from the ashes of the previous burning stage would initially result in the contraction of the core, leading to an increase in temperature and pressure and ultimately culminating in the burning of the current core element and synthesis of heavier elements. See Hansen et al. (2012) for an overview of stellar

¹<http://www.nasa.gov/>

²<http://spacetelescope.org/>

evolution prior to core-collapse. However, this process of ignition does not occur for the newly formed core as iron possesses one of the highest binding energies per nucleon which, coupled with the lack of alpha particles, is unable to be burned within the stellar core. At this point core burning halts and the iron core is held up by electron degeneracy pressure alone. The lack of nuclear fusion reactions occurring within the core leads to a decrease in the total radiation pressure that is crucial to uphold massive stars (Brunish et al., 1984). As a result, the star is no longer in equilibrium, leading to the gravitational collapse of the star, driving up core temperature and pressure (Bethe et al., 1979). The collapse of the star further speeds up the rate of silicon burning and build up of the iron core. Once the core has grown to an effective Chandrasekhar mass, around $\sim 1.4M_{\odot}$, electron degeneracy pressure breaks and the core enters a phase of rapid gravitational collapse (Chandrasekhar, 1931). The collapse of the core is further enhanced up by the photodisintegration of core material and the capture of core electrons. This leads to a large flux of neutrinos released by the core, removing a significant fraction of the energy required to combat gravitational collapse and a reduction in the electron density additionally weakening the effect of electron degeneracy pressure in the outer core. This process continues over the course of a few fractions of a second as the core falls inward at free-fall velocity (Bethe, 1990). As the inner core collapses, a large flux of neutrinos formed in the electron capture process occurring within the inner core that transforms the core-material into neutron-rich matter, escape the core. While the protoneutron star is forming the inner region of the iron core continues to collapse homogeneously inwards until it reaches a central density of $\rho_c > 2.8 \times 10^{14} \text{gcm}^{-3}$, at which point the collapse is halted by neutron degeneracy pressure as the equation of state for the inner core stiffens, forming a neutron star (Colgate, 1971). At the nuclear densities within the collapsing core the neutrinos are held below the density where the diffusion timescale for the neutrinos become equivalent to the collapse timescale of the protoneutron star, a location known as the neutrinosphere. This sudden change in the equation of state for the inner core generates a shock or ‘bounce’ that propagates out from the inner core. The outer core continues to fall inwards at supersonic speeds and collides with the outgoing shock front.

At this point it is thought that one of two processes can occur; the stalling of the

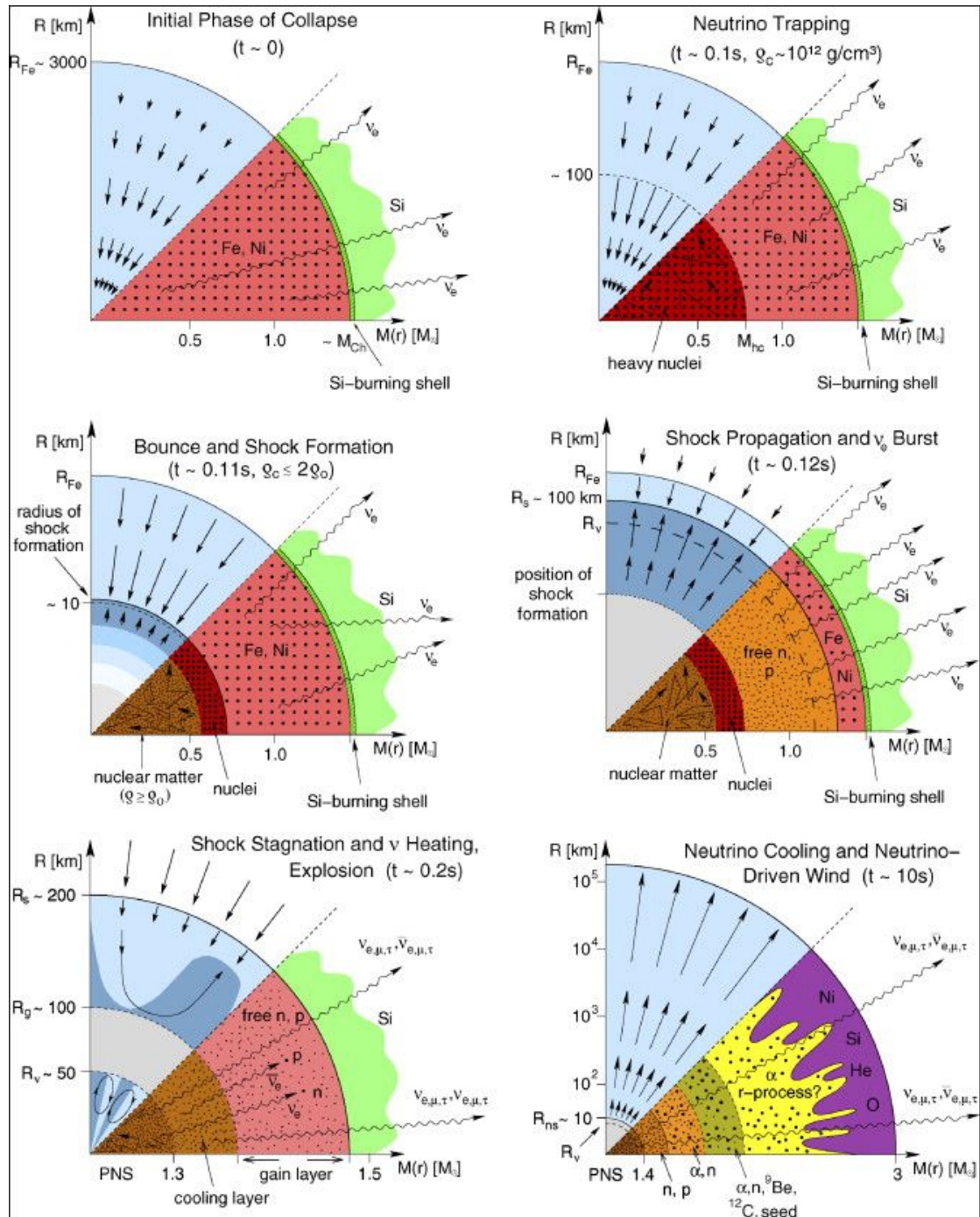


FIGURE 1.2: Representation of the core-collapse process occurring within an iron core of a high mass star. The initial three stages illustrates the start of the collapse; the trapping of neutrinos within the proto-neutron star, the bounce when the inner core reaches nuclear densities and the formation of the shock. The remaining stages depict the stalling of the shock and subsequent heating via neutrino interaction leading to the ejection of the outer layers of the star as a CC-SNe. This image was taken from [Janka et al. \(2007\)](#)

outward shock or the propagation of the shock front to the stellar surface. In the failed shock process, the shock front loses energy via interaction with the collapsing outer core through the dissociation of the infalling iron into helium and cannot overcome the ram pressure (Bethe, 1990) resulting in the shock stalling below the neutrinosphere. Continued accretion onto the stalled shock eventually leads to fallback and the core collapsing directly into a black hole with no observed SN (O'Connor & Ott, 2011). However, if the shock gains additional energy, it can propagate through the outer core to the stellar surface where a SN occurs, leaving behind a compact remnant, commonly a neutron star (Burrows & Lattimer, 1986). In order for the shock to fully propagate through the remaining stellar envelope it must gain additional energy from an external power source. A shock powered solely by the bounce energy is insufficient to overcome energy losses to the infalling iron (Wilson et al., 1986; Janka et al., 2005). It is believed that the revival of the shock is brought about by the delayed interaction between the shock and the large flux of neutrinos. The neutrino flux extracts the majority of the gravitational energy of the collapse out of the star, reaching a peak luminosity of $\sim 10^{53}$ erg s⁻¹ (Müller, 2019), while depositing a small but significant fraction into the stalled shock (Colgate & White, 1966; Bethe & Wilson, 1985; Rampp & Janka, 2000). These neutrinos, initially trapped within the core, escape and travel outwards to the neutrinosphere, depositing energy into the stalling shock (Bethe, 1990). Additional neutrinos are released over a period of several seconds from the protoneutron star as it cools via Kelvin-Helmholtz contraction. The energy deposited by the continuous flux of neutrinos is sufficient to power the shock as it propagates through the outer envelope to the stellar surface resulting in a SNe (Burrows & Lattimer, 1986). Also see Janka (2001) for a detailed description of the shock revival process. As the shock propagates through the remaining layers of the star, the synthesis of elements all the way up to $Z = 50$ occurs through the r -process (Timmes et al., 1995; Wanajo et al., 2001; Pruet et al., 2005) with additional nucleosynthesis occurring as neutrinos escape the core (Woosley et al., 1990). The evolution of the inner core, core bounce, shock propagation and revival, and formation of the protoneutron star are shown in Figure 1.2.

Of the elements synthesised during the explosion of a CC-SNe, ⁵⁶Ni is of vital importance as the power source of the SN light curve. The light curve is powered by the radioactive

decay of ^{56}Ni to more stable iron group elements;



As the main power source of the light curve of CC-SNe, the mass of ^{56}Ni (M_{Ni}) synthesised during the explosion is directly linked to the peak luminosity of the event. This was first formalised by [Arnett \(1980a, 1982\)](#) which, while initially created to model the light curve properties of Type Ia SNe the thermonuclear destruction of a white dwarf, has since been used prolifically to model CC-SNe. The total luminosity at peak of the SN event is related to the mass of ^{56}Ni by;

$$L_p = M_{\text{Ni}}((\epsilon_{\text{Ni}} - \epsilon_{\text{Co}})e^{-t_r/t_{\text{Ni}}} + \epsilon_{\text{Co}}e^{-t_r/t_{\text{Co}}}), \quad (1.2)$$

where t_r is the rise time of the SN, ϵ_{Ni} and ϵ_{Co} are the specific heating rates ^{56}Ni and ^{56}Co , which have values of $3.90 \times 10^{10} \text{ergs}^{-1} \text{g}^{-1}$ and $6.78 \times 10^9 \text{ergs}^{-1} \text{g}^{-1}$ respectively, and finally $t_{\text{Ni}} = 8.8$ days and $t_{\text{Co}} = 111.3$ days are the decay times of ^{56}Ni and ^{56}Co respectively ([Sutherland & Wheeler, 1984](#)). The photons released by the radioactive decay of ^{56}Ni are then absorbed and re-emitted throughout the outer layers of the SN ejecta, eventually escaping at the photosphere. While the connection between the peak bolometric light and the mass of synthesised ^{56}Ni , along with its daughter products, has been believed for a long time ([Arnett, 1980a](#); [Clocchiatti & Wheeler, 1997](#)) and has been used prominently in the literature to compare the properties of different types of SNe ([Valenti et al., 2008](#); [Drout et al., 2011](#); [Lyman et al., 2016](#); [Prentice et al., 2016](#); [Taddia et al., 2018](#)). However, in recent years the use of the analytical method detailed by [Arnett \(1982\)](#) and the assumptions used in determining the explosion parameters of SE-SNe, especially with determining the value of M_{Ni} , have been called into question. This discrepancy is especially apparent when comparing the parameters to the derived values determined using more detailed radiation transfer codes ([Dessart et al., 2016](#); [Khatami & Kasen, 2019](#); [Meza & Anderson, 2020](#)). Through the use of several different methods, including radiation transfer codes ([Dessart et al., 2016](#)) and late-time photometric modelling ([Sharon & Kushnir, 2020](#)) it has been found that

the Arnett-like model typically overestimates the nickel mass of SE-SNe by anywhere between $\sim 10\%$ – $\sim 50\%$ (Dessart et al., 2016; Meza & Anderson, 2020; Sharon & Kushnir, 2020) and in some cases as much as twice the Arnett-like derived values (Afsariardchi et al., 2021).

1.1.2 GRB-SNe explosion mechanisms

Unlike the explosions seen with typical SE-SNe, which are expected to undergo a similar formation independent of their composition and how they were stripped of their outer envelope. There exists a subgroup of SE-SNe that are associated with the bright directional events known as Gamma Ray Bursts (GRBs), known as GRB-SNe. These energetic events do not undergo the standard expulsion of their outer envelope and formation of a compact remnant within their cores. GRB-SNe are observed to emit a strongly collimated beam of ejecta travelling at relativistic velocities, powered by a central engine, within the first seconds to minutes of their explosion (Kouveliotou et al., 1993). There are several proposed mechanisms in which the relativistic jet associated with GRBs can form from a central engine, either through the collapsar mechanism (Woosley, 1993; MacFadyen & Woosley, 1999) or by the formation of a magnetar (Usov, 1992; Zhang & Mészáros, 2001).

In the collapsar mechanism the heating of the neutrino heated shock is insufficient to eject the stellar envelope causing fall back onto the core, this results in the formation of a central black hole within the progenitor. As more of the progenitor falls inwards an accretion disk around the black hole forms, which acts as the central engine in this mechanism. This material is accreted onto the black hole and a portion is funnelled towards and along the axis of the black holes rotation (Woosley, 1993), forming the jet which becomes collimated as it propagates through the outer envelope (Zhang et al., 2003). The jet in the collapsar model is powered by the combination of energy deposited to the ejecta through the conservation of momentum as material is accreted onto the black hole, the magnetic interaction between the black hole and the accretion disk (Blandford & Znajek, 1977) and the annihilation of neutrinos (Popham et al., 1999).

These mechanisms deposit enough energy for the jet to breakthrough the stellar envelope and form a GRB-SNe.

The other commonly suggested formation channel for GRB-SNe places a highly magnetized, rapidly rotating neutron star as the central engine (Usov, 1992), known as a magnetar. This newly formed magnetar possesses a very high rotational velocity, with a period on the order of a few milli-seconds, as the momentum of the in falling progenitor core is conserved. In addition magnetars carry an incredibly strong magnetic field on the order of 10^{15} Gauss (Duncan & Thompson, 1992), a property that has been confirmed through the observations of soft gamma repeaters (Kouveliotou et al., 1998; Tiengo et al., 2013). Initially the proto-neutron star lacks a magnetic field strength high enough to contribute to the powering of the neutrino-driven wind seen in all CC-SNe. However, if the intensity of the magnetic field grows to sufficient levels the magnetic influence dominates over the thermal contribution of the energy transference to the neutrino wind (Metzger et al., 2007). The magnetically dominated wind generated by the proto-magnetar form a bipolar jet that starts to clear out a channel through the progenitor to the stellar surface. The wind then becomes relativistic leading to a concentration of the power of the jet at lower depths, due to the collapse of collimation within ultrarelativistic outflows (Bucciantini et al., 2006), forming a region of dense material surrounding the magnetar. The magnetic forces of then direct this material towards the poles, (Begelman & Li, 1992; Uzdensky & MacFadyen, 2007) providing more material for the jet which continues to propagate through the stellar envelope at a significant fraction of the speed of light (MacFadyen & Woosley, 1999; Zhang et al., 2003) until it breaks out at the stellar surface and a GRB is formed.

1.2 CC-SNe classification

1.2.1 Spectroscopic evolution

While the explosion mechanism that underpins CC-SNe are expected to be largely consistent across the majority of events, CC-SNe are observed to display a wide range

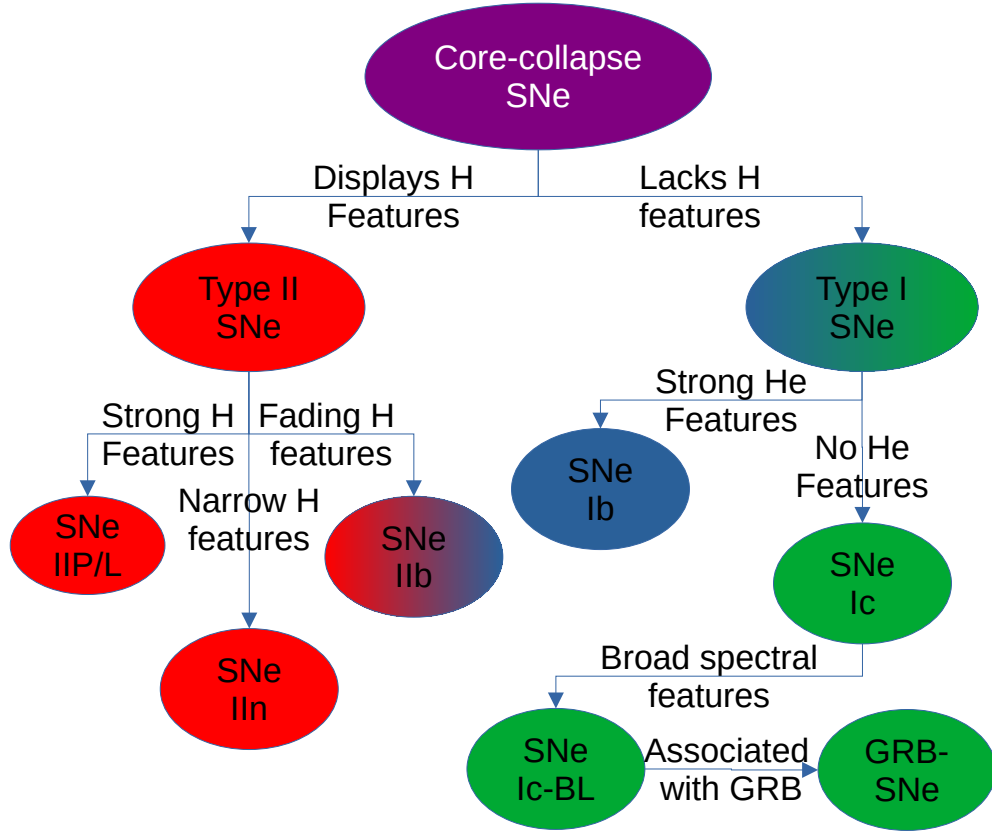


FIGURE 1.3: Standard view of CC-SNe classification, with the colour denoting the presence of hydrogen/helium (red), only helium (blue) and no hydrogen/helium (green).

of photometric and spectroscopic properties. This has led to CC-SNe being classified into two main groups, those CC-SNe that display strong hydrogen features in their spectra throughout its evolution known as the Type II SNe (SN II [Filippenko, 2000](#)) and those that display weak hydrogen features or completely lack any traces of hydrogen altogether known as the stripped envelope SNe (SE-SNe [Minkowski, 1941](#); [Filippenko, 1997](#)), which account for $\sim 63 - 78\%$ and $\sim 22 - 37\%$ of all CC-SNe respectively ([Smartt, 2009](#); [Arcavi et al., 2010](#); [Smith et al., 2011](#); [Shivvers et al., 2017](#)). Of the events that are classified as a SE-SNe, they can be further divided into one of three major groups. First there are the H/He-rich Type IIb SNe (SNe IIb), then the H-poor/He-rich Type Ib SNe (SNe Ib) and finally the H/He-poor Type Ic SNe (SNe Ic). There have been several population studies to determine the relative fraction of each type of the SE-SNe group, with SNe IIb, SNe Ib and SNe Ic having a relative fraction of between $15 - 34\%$, $16 - 38\%$ and $25 - 59\%$ respectively ([Smartt, 2009](#); [Arcavi et al., 2010](#); [Smith et al.,](#)

2011; Shivvers et al., 2017). Finally the relative fraction of the energetic SNe Ic-BL are on the order of $\sim 4\%$ (Shivvers et al., 2017), which is similar to the upper limit placed on the fraction of GRB-SNe which ranges from $\sim 0.6 - 3\%$ of all SE-SNe (Madau et al., 1998; Gal-Yam et al., 2006). While there are similarities between the rates of SNe Ic-BL and GRB-SNe there are a number of well studied SNe Ic-BL that lack any association with a GRB event, such as SN 2002ap (Hurley et al., 2002; Mazzali et al., 2002). Studies have suggested that the number of SNe Ic-BL associated with a GRB account for up to $\leq 41\%$ of SNe Ic-BL (Corsi et al., 2016), although more recent work has the number of GRB-SNe to $\leq 19\%$ of SNe Ic-BL (Corsi et al., 2023).

1.2.1.1 SNe IIb

SNe IIb are characterised by the initial appearance of strong hydrogen P-Cygni profiles within their spectra, which over the course of a few months, fade as the SN transitions from the photospheric phase, dominated by black body emission and spectral lines originating from the outer layers of the progenitor star, into the nebular phase where spectra are dominated by emission lines from deeper within the progenitor such as O I $\lambda 6300, 6363$ and Ca II $\lambda 8498, 8542, 8662$. The slow decline of the hydrogen features seen within the spectra of SNe IIb was originally found in the archetypal SNe IIb SN 1993J and explained as the progenitor possessing a thin layer of hydrogen prior to core-collapse (Woosley et al., 1994). The evolution of SN 1993J is shown in the left-hand panel of Figure 1.4. It is typically assumed that a maximum mass of around $M_{\text{H}} < 1 M_{\odot}$ of hydrogen is required to give rise to a SNe IIb as opposed to a Type II SN (Nomoto et al., 1993; Woosley et al., 1994). Spectroscopic modelling of SNe IIb done by several different groups suggest that an outer envelope containing as little as $M_{\text{H}} \sim 0.001 - 0.03 M_{\odot}$ of hydrogen is required to form the spectral features seen in SNe IIb (Dessart et al., 2011; Hachinger et al., 2012; Gilkis & Arcavi, 2022), suggesting that some SNe IIb may not have been fully stripped of their hydrogen envelope prior to core collapse (Hachinger et al., 2012).

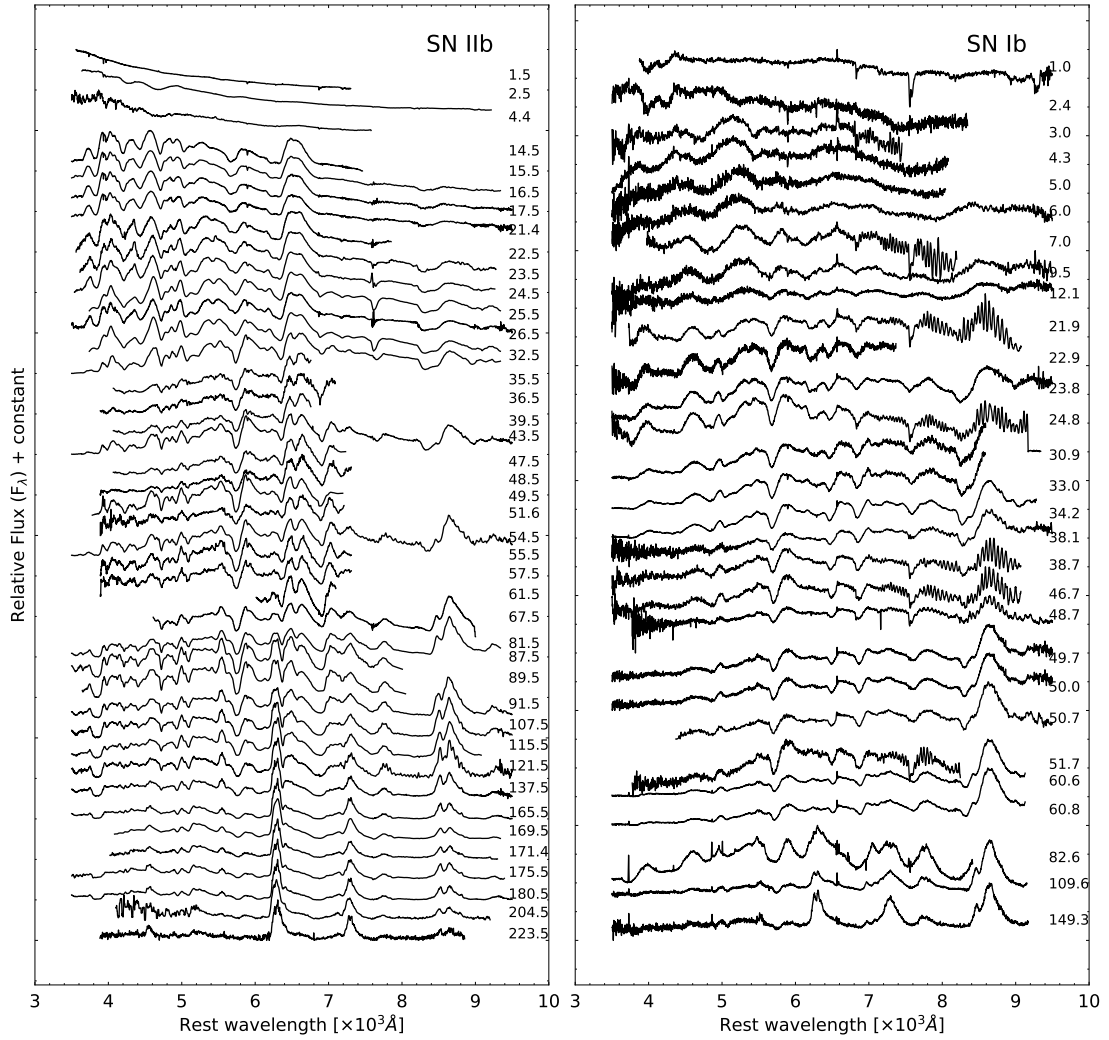


FIGURE 1.4: Spectroscopic evolution of the SN IIB SN 1993J (left) and the SN Ib SN 2008D. All spectra are corrected for redshift with the phase relative to explosion are given on the left. The spectroscopic evolution of SN 1993J displays clear hydrogen and helium features during its photospheric phase which faded as it evolved. On the other hand, SN 2008D showed prominent helium lines during this time. At late times both SNe exhibited strong oxygen and calcium lines.

1.2.1.2 SNe Ib

SNe Ib originate from progenitors that have been fully stripped of their hydrogen envelope leaving a bare helium star to undergo core-collapse. As such, the optical spectra of SNe Ib are dominated by the helium $\lambda\lambda 4471, 5876, 6678, 7065$ lines during their photospheric phase before transitioning to the nebular phase dominated by the presence of oxygen and calcium features similar to those of SNe IIB. This type of spectral evolution was originally discussed by Bertola (1964), but were not fully identified as a different

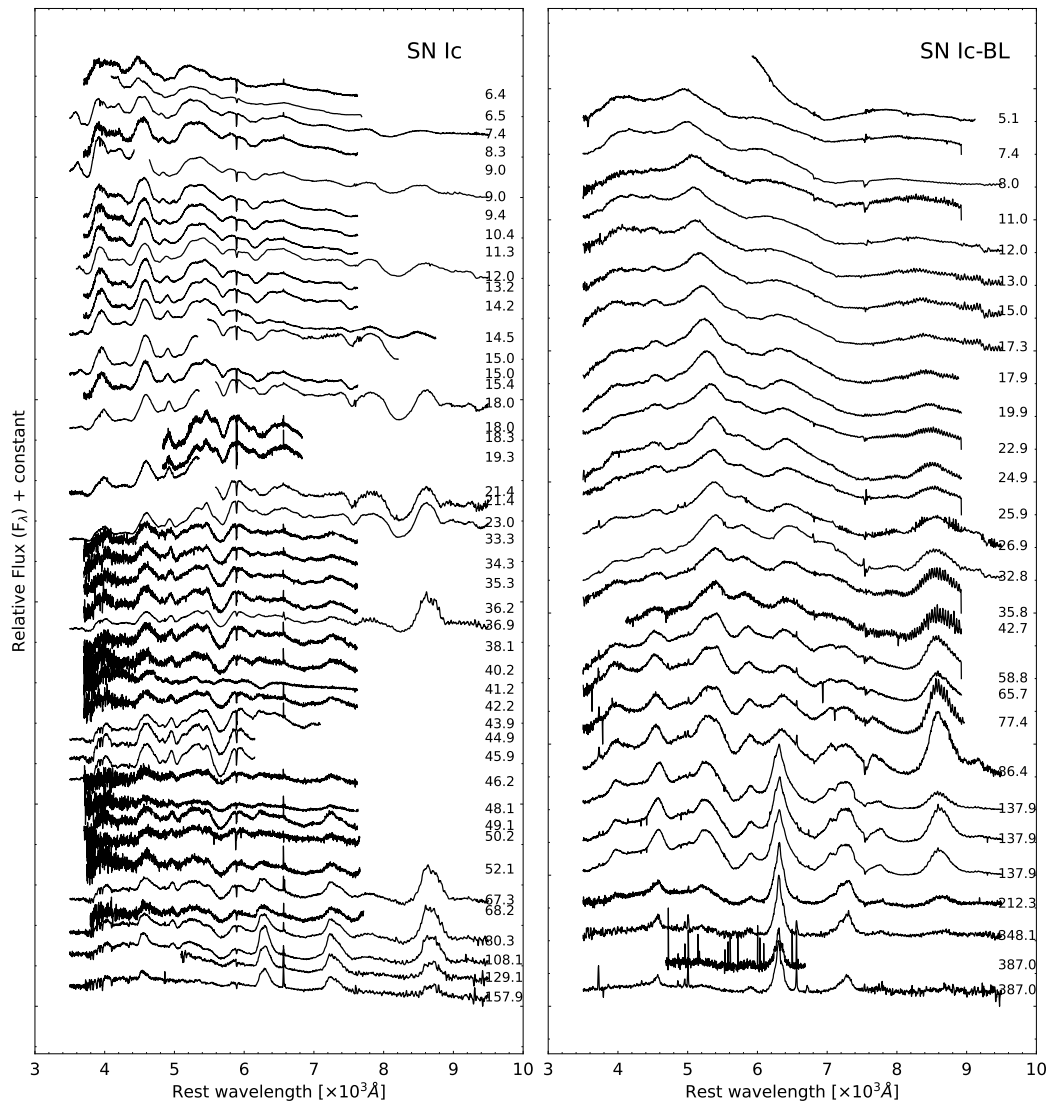


FIGURE 1.5: The spectroscopic evolution of the SN Ic SN 1994I (left) and the SN Ic-BL SN 1998bw (right). All spectra are corrected for redshift with the phase relative to explosion given on the left. Both SNe display similar chemical evolutions, being dominated by oxygen, calcium and iron throughout. The main difference between these SNe is the width of the absorption features indicating the high velocities of the ejecta material.

classification of Type I SNe until several decades later [Elias et al. \(1985\)](#); [Porter & Filippenko \(1987\)](#). The spectroscopic evolution of SN 2008D is shown in the right-hand panel of Figure 1.4.

1.2.1.3 SNe Ic and GRB-SNe

Finally, there are the hydrogen/helium deficient SE-SNe the SNe Ic. These SNe display strong lines of intermediate mass elements synthesised within the cores of high mass stars. Their spectra is dominated by the presence of both oxygen and calcium lines, along with iron, silicon and magnesium lines (Filippenko, 1997). In addition to the lack of low mass elements within their ejecta, SNe Ic have been shown to exhibit a much wider range in explosion properties compared to other SE-SNe. SNe Ic can be typically split into two groups. The first of these groups display spectral features with velocities corresponding to several $\times 10^3$ km s⁻¹ and kinetic energies on the order of a few $\times 10^{51}$ erg, comparable to the parameters found associated with other types of SE-SNe, and these events are classified as standard SNe Ic such as SN 1994I (Puckett et al., 1994; Filippenko et al., 1995). The second of these groups exhibit broad spectral features resulting in a large degree of blending between different lines. These SNe Ic have much higher velocities than standard SNe Ic reaching values of a few $\times 10^4$ km s⁻¹ and possess kinetic energies on the order of $\times 10^{52}$ erg. Due to the prevalence of the broad and highly blended spectral features seen in these highly energetic SNe they are labelled broad line SNe Ic (SNe Ic-BL). In addition to their broad spectral features several SNe Ic-BL have been linked to the directional highly energetic events known as GRBs, first seen with GRB 980425/SN 1998bw (Galama et al., 1999). Due to their high energy and strong beaming effect GRB's have been detected at redshifts as high as $z = 8.1^{+0.1}_{-0.3}$ (Palmer et al., 2009; Salvaterra et al., 2009). A comparison of the spectroscopic evolution of both the standard SN Ic SN 1994I and the typical SN Ic-BL SN 1998bw are shown in the left and right-hand panels of Figure 1.5.

1.2.2 New classification and transitional events

While the classifications discussed above for SE-SNe have been used throughout the literature for several decades, in the last decade the analysis of several of well classified SE-SNe that all possess comprehensive spectroscopic observations has shown many SE-SNe that do not cleanly fit into the classical, more rigid, classification system. It has

been shown that some SNe Ib progenitors have not been fully stripped of their hydrogen envelope (Spencer & Baron, 2010; Gilkis & Arcavi, 2022) and that SNe Ic progenitors can possess a non-negligible amount of helium in their outer envelope while lacking any prominent optical helium lines (Hachinger et al., 2012; Teffs et al., 2020). In addition to the work on individual transitional types of SE-SNe, Prentice & Mazzali (2017) have shown that within the SE-SNe group SNe Iib and SNe Ib can be grouped together to form a continual progression composed of four different groups SNe Iib SNe Iib(I), SNe Ib(II) and SNe Ib, based on the relative strength of the absorption and emission components of the H_α feature where in the classical SNe Iib, H_α emission dominates over absorption and the classical SNe Ib is dominated by Si II. From the study of 27 helium-rich SE-SNe, Prentice & Mazzali (2017) found that the population was made up of $\sim 30\%$ SNe Iib, $\sim 15\%$ SNe Iib(I), $\sim 30\%$ SNe Ib(II) and $\sim 26\%$ SNe Ib, suggesting that a significant portion of helium-rich SE-SNe progenitors can not be fully stripped of their hydrogen envelope. The study of these transitional events to determine their explosion parameters, such as amount of ^{56}Ni synthesised, mass of ejected material, kinetic energy of the explosion and the mass of hydrogen required to form their spectral features, is vital to determining the true distribution of different helium-rich SE-SNe and how much hydrogen can remain in the outer envelope before spectral features are observed. The continued study of these events will allow the dominant formation channels of different types of SE-SNe to be determined, as well as whether the formation channel is consistent across all types of SE-SNe or if there exists a hard boundary within the parameter space that a specific formation channel can not cross, such as a limit to the mass of hydrogen that can be removed via binary interaction.

In addition, Prentice & Mazzali (2017) found that SNe Ic can be split into several groups based on the average number of blended line features found between 4000 – 8000 Å, $\langle N \rangle$, within the pre-peak spectra, with lower average numbers associated with higher velocity events that possess a greater energy to mass ratio, thus allowing for a more precise classification over the vague umbrella-term of 'broad-line'. From the analysis of 21 different helium-poor SE-SNe Prentice & Mazzali (2017) found that SNe Ic tended to fit into one of two categories, the low $\langle N \rangle$ possessing between 3 – 4 blended features and the high $\langle N \rangle$ with 6 – 7 distinct features. The distribution found by Prentice &

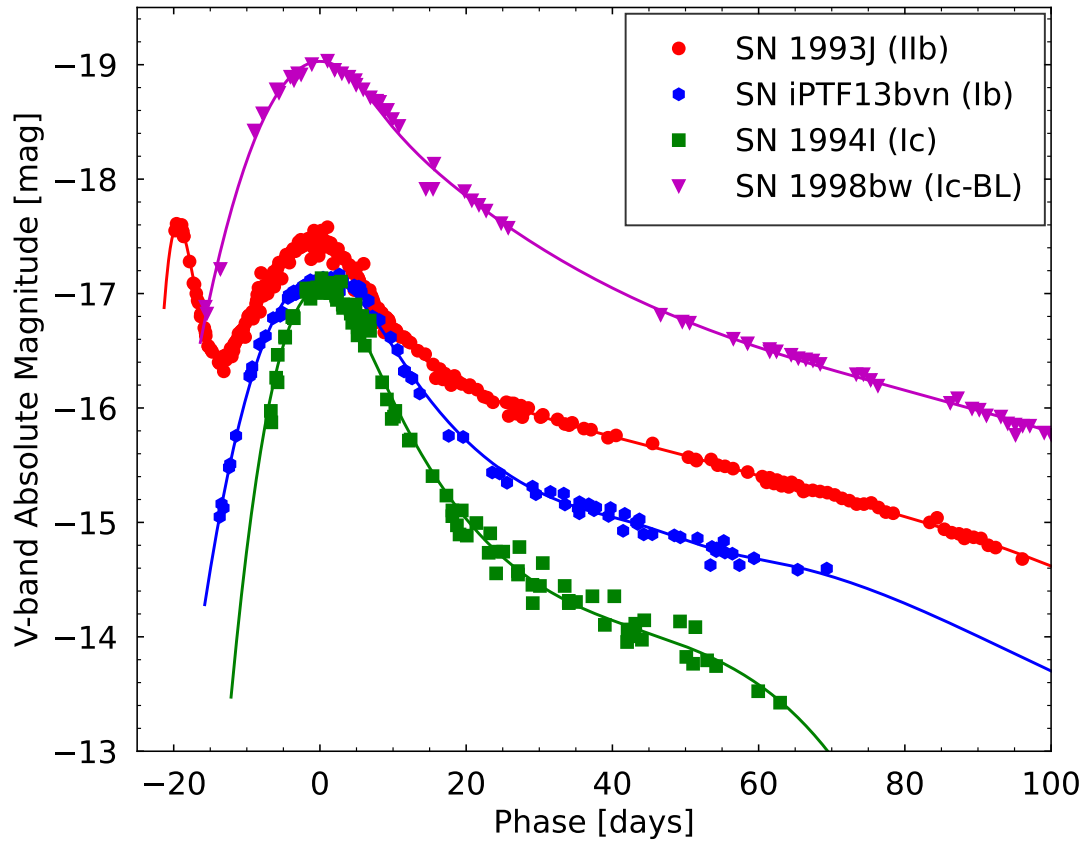


FIGURE 1.6: V-band observations of SN 1993J (I Ib), SN 2008D (Ib), SN 1994I (Ic) and SN 1998bw (Ic-BL). All light curves are given in rest frame, shifted to V-band peak and corrected for both galactic and host galaxy extinction. A spline has been fitted to each light curve to interpolate over epochs lacking observations.

Mazzali (2017) seems to suggest a bimodal distribution within the helium-poor SE-SNe, although it a greater number of events are required to confirm this distribution, which may require multiple formation channels to achieve.

1.2.3 Photometric evolution

1.2.3.1 SNe I Ib, Ib and Ic

In addition to their spectral diversity, SE-SNe exhibit a range of photometric properties both within each classification and between the different types of SE-SNe themselves. The V-band light curves of SN 1993J (I Ib), SN 1994I (Ic), SN 1998bw (Ic-BL) and SN iPTF13bvn are shown in Figure 1.6. SE-SNe have been observed to follow a trend

of brighter peak time luminosities as the degree to which their progenitor has been stripped increases (Prentice et al., 2016; Lyman et al., 2016). As such SNe Iib are generally considered the dimmest of the SE-SNe classification, for example the template SN Iib SN 1993J peaked at pseudo-bolometric luminosity of $L_{\text{peak}} \approx 3.0 \times 10^{42} \text{ erg s}^{-1}$ (Richmond et al., 1996), whilst GRB-SNe Ic the brightest, such as SN 2016jca which had a maximum luminosity of $L_{\text{peak}} \approx 5.8 \times 10^{42} \text{ erg s}^{-1}$ (Ashall et al., 2019). The increase in bolometric peak is associated with a greater mass of ^{56}Ni synthesised by the explosion which powers the bolometric light curve of CC-SNe well into the nebular phase (Arnett, 1996).

Along with the ^{56}Ni powered peak observed in all SE-SNe, some SNe can exhibit an initial bright peak several days prior to the main ^{56}Ni peak. This initial peak is the result of shock interaction caused as the propagating shock reaches the stellar surface at which point the optical density becomes low enough for the trapped photons to escape as a burst of intense light (Grassberg et al., 1971; Falk, 1978; Chevalier, 1992). This shock breakout peak lasts for several days before declining until the ^{56}Ni powered light curve becomes dominant. This initial bright shock breakout peak is not observed in all types of SNe Iib, a clear shock cooling tail is seen with SN 1993J (Lewis et al., 1994), see < -13 photometry of SN 1993J in Figure 1.6, while SN 2011dh only displayed a small shock cooling feature within its bluer bands (Arcavi et al., 2011; Ergon et al., 2014) and SN 2008ax did not display any strong shock breakout phase (Pastorello et al., 2008). The presence and duration of the shock breakout peak has been directly related to the compactness of the progenitor (Chevalier & Soderberg, 2010), with progenitors that possessed an extended hydrogen envelope exhibiting a shock breakout phase and those with compact envelopes have been seen to lack this pre-peak photometric feature.

1.2.3.2 SNe Ic-BL and GRB-SNe

While the evolution of the light curves for SNe Iib, SNe Ib and SNe Ic are expected to be primarily powered by the decay of ^{56}Ni and its daughter product ^{56}Co , it has been observed that this does not hold true for all SNe Ic-BL and especially GRB-SNe. For a portion of these hydrogen/helium poor events the mass of ^{56}Ni required to power the

light curve clashes with the expected amount of mass ejected by the explosion. One such example is GRB 111209A/SN 2011kl which would have had to synthesised a mass of ^{56}Ni of $M_{\text{Ni}} \approx 1.0 M_{\odot}$ which accounts for $\sim 1/3$ of the total mass ejected by the event (Greiner et al., 2015). The value of M_{Ni} required for these events is far higher than those expected for standard SE-SNe. To account for this increased luminosity, while keeping the M_{Ni} at values similar to that of other SE-SNe, additional energy from a central engine known as a magnetar has to be invoked (Wheeler et al., 2000; Thompson et al., 2004). The magnetar central engine has been used to explain the light curves of several SNe Ic-BL such as SN 1997ef and SN 2007ru (Wang et al., 2016), with magnetar powered hydrodynamical simulations by Barnes et al. (2018) and Shankar et al. (2021) robustly recreating the photometric and spectroscopic properties of SNe Ic-BL.

Along with their bright peak time luminosity, GRB-SNe display a prompt emission in the high photon energy regime before plateauing for $10^2 - 10^5$ seconds before declining over the course of several days, commonly called the GRB afterglow, before rising again to the SN peak, for example see the light curve evolution of SN 2016jca (Ashall et al., 2019). This GRB afterglow is dominated primarily by synchrotron radiation from the high energy electrons that are accelerated to relativistic velocities as they are swept up by the GRB jet (Meszaros et al., 1994; Daigne & Mochkovitch, 1998). This afterglow emission is initially dominant at X-ray wavelengths before down scattering to longer wavelengths. The afterglow follows a power law function of the form;

$$f(\nu) \propto t^{-\alpha} \nu^{-\beta}, \quad (1.3)$$

where α is the temporal decay index and β is the spectral decay index. The temporal decay index has been found to exhibit a broken power law shape if early enough photometry is acquired, which takes the form;

$$f(t) \propto \begin{cases} F_a \left(\frac{t}{T_a}\right)^{-\alpha_1} t < T_a \\ F_a \left(\frac{t}{T_a}\right)^{-\alpha_2} t \geq T_a \end{cases} \quad (1.4)$$

T_a is the epoch of break, F_a is the flux at T_a . The parameters α_1 and α_2 are the temporal decay index before and after T_a respectively, an example of the break in the temporal

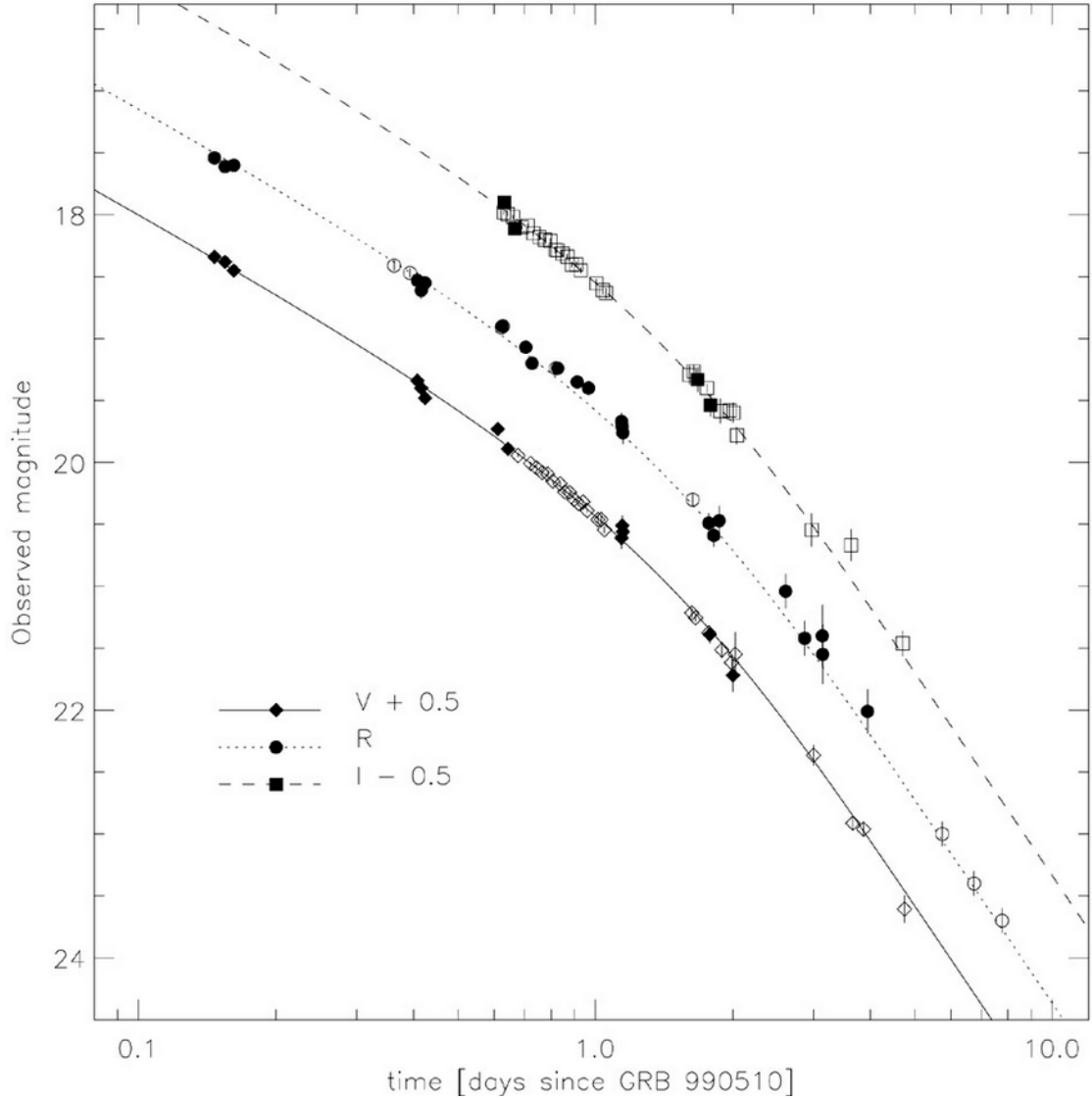


FIGURE 1.7: The early time, $t < 10$ days from GRB detection, VRI -band photometry of GRB 990510 fit with a broken power law ($\alpha_1 = 0.82 \pm 0.02$, $\alpha_2 = 2.18 \pm 0.05$ and a break at day 1.2 ± 0.08), image taken from [Harrison et al. \(1999\)](#).

decay and differing α 's is given in Figure 1.7. Through the study of multiple GRB-SNe, it has been found that α_1 tends to cluster around $\alpha_1 = 0.5$ while α_2 exhibits a much sharper decline having a value of $\alpha_2 = 1.2 - 1.4$ ([Vecchio et al., 2016](#); [Dainotti et al., 2022](#)), while β is typically at values around $\beta = 0.7$ ([Dainotti et al., 2022](#)). Once fit the afterglow can be extrapolated to late times, after the SN contribution becomes dominant, and removed from the photometry in order to extract the SN component of the GRB-SNe.

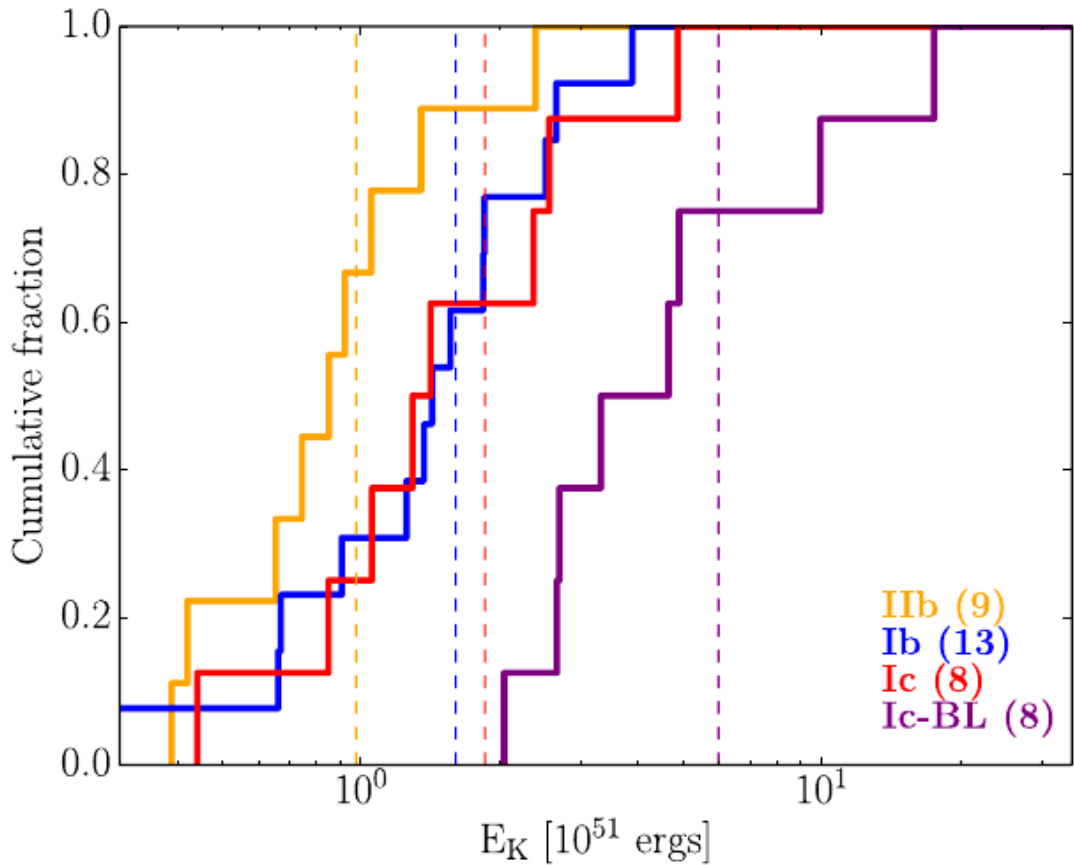


FIGURE 1.8: Cumulative distribution of the E_k for SE-SNe found from fitting the bolometric light curve during the photospheric phase. The average values of E_k are shown by the dashed lines and are as follows; SNe IIb(9) = 1.0 ± 0.6 erg, SNe Ib(13) = 1.6 ± 0.9 erg, SNe Ic(8) = 1.9 ± 1.3 erg and SNe Ic-BL(8) = 6.0 ± 5.0 erg. Figure taken from Lyman et al. (2016).

1.2.4 Kinetic energy distribution across SE-SNe

In addition to brighter peak luminosity SE-SNe also exhibit an increase in their kinetic energy as they become more stripped, as shown in Figure 1.8. Several different studies of SE-SNe have found that, through the use of an Arnett-like modelling; SNe IIb tend to explode with lower energies around $\sim 0.9 \pm 0.5 \times 10^{51}$ erg, such as SN 1993J (Woosley et al., 1994) and SN 2011hd (Bufano et al., 2014), while SNe Ib and Ic were found to cluster around $1.72 \pm 1.1 \times 10^{51}$ erg (Richardson et al., 2006; Cano, 2013; Taddia et al., 2015; Lyman et al., 2016; Taddia et al., 2018). The distribution of kinetic energies of SE-SNe varies drastically between the different studies with some finding that SNe Ib possess a greater average kinetic energy (Richardson et al., 2006; Taddia et al., 2018)

while others showing SNe Ic having higher average kinetic energies (Taddia et al., 2015; Lyman et al., 2016). The results from these studies are greatly impacted by the sample size of SE-SNe used and may suggest that SNe Ib and Ic undergo very similar formation channels. In contrast to the other SE-SNe, both SNe Ic-BL and GRB-SNe have been found to explode with kinetic energies between a few $\times 10^{51}$ to several $\times 10^{52}$ erg (Drout et al., 2011; Cano, 2013; Lyman et al., 2016), with GRB-SNe possessing the highest kinetic energies of all SE-SNe.

1.3 SE-SNe formation channels

SE-SNe as a group originate from stars that, during their life, have been stripped of part or all of their outer envelope. The degree of stripping that the SE-SN progenitor undergoes determines its spectroscopic features, with progenitors that have undergone a limited amount of stripping resulting in a SNe I Ib. Those progenitors stripped of their hydrogen envelope exploding as a SNe Ib and lastly progenitors that have been stripped of all their hydrogen and helium, leaving a bare Carbon/oxygen star, ultimately exploding as a SNe Ic/Ic-BL. The question then becomes, ‘What process can remove the hydrogen envelope in the case of SNe I Ib/Ib as well as the helium envelope in the case of SNe Ic from the high mass progenitor star prior to it undergoing core-collapse?’ There are currently a number of different formation channels that are expected to result in a stripped progenitor depending on if the progenitor was a single star (Meynet & Maeder, 2003; Eldridge & Tout, 2004; Georgy et al., 2009; Elias-Rosa et al., 2011) or binary star system (Yoon et al., 2010; Kuncarayakti et al., 2013, 2018).

1.3.1 Single Star Model

For single star progenitor models, these progenitors are expected to originate from high mass stars that have progressed through their evolution into the supergiant phase where they eject their outer envelope via strong stellar winds prior to exploding as a Wolf-Rayet star (Castor et al., 1975; Maeder & Lequeux, 1982; Heger et al., 2003; Eldridge

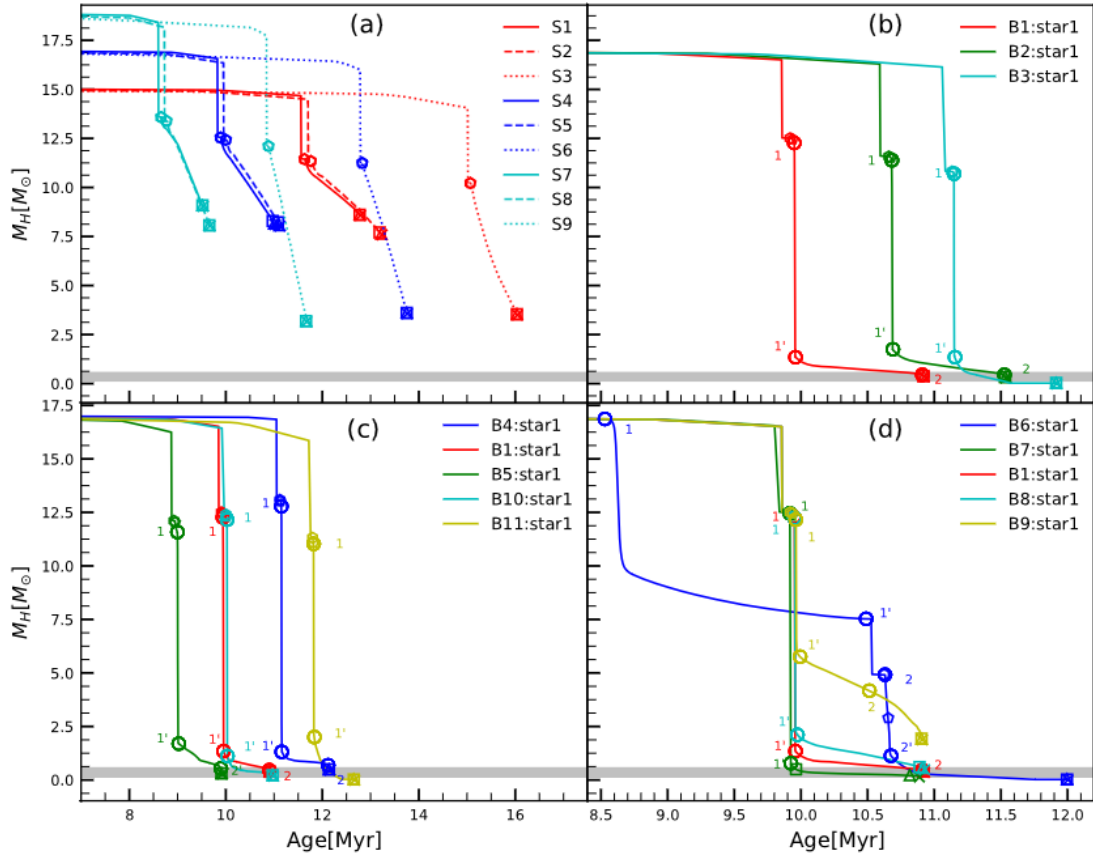


FIGURE 1.9: Time evolution of hydrogen envelope (M_H) for several single star models with masses ranging from 16–25 M_\odot and binary star systems with a 17 M_\odot primary and 15 M_\odot companion of varying orbital period. Shaded region is the expected hydrogen mass required to form a SNe IIb. Panel (a): Single star models with various rotational velocities and initial masses, panel (b): Binary models with an orbital period of 300 days and differing convective overshooting parameters, panel (c): Binary models with various initial rotational velocities and metallicities in the binary system with orbital period of 300 days and panel (d): Binary models with variable orbital periods. Figure taken from Long et al. (2022). Model parameters are given in Table 1 of Long et al. (2022).

& Tout, 2004; Groh et al., 2013a). These winds and the subsequent mass-loss rate of these massive stars originate from the line driven emission as a consequence of the stars high metallicity (Cassinelli, 1979; Abbott, 1982; Eldridge & Vink, 2006; van Loon, 2006). The winds seen in these high mass stars are formed as energetic photons are repeatedly re-absorbed by the high opacity transferring momentum to the wind material before their eventual final emission from the wind (Lucy & Abbott, 1993; Gräfener et al., 2017). In addition to the line driven wind found in high metallicity stars, high mass stars that possess relatively low metallicity are expected to experience a similar amount of mass loss through rotational stripping (Heger et al., 2000; Maeder & Meynet,

2003, 2008). The relation between progenitor mass-loss and metallicity suggests that as the metallicity decreases for a stellar population, the proportion of SNe Ic relative to SNe Ib should also fall. However, the single star models, both rotating and non-rotating, [Georgy et al. \(2009, 2012\)](#) showed that for various metallicities the ratio of different SNe type was not significantly affected until very low metallicities are reached. In addition, the observed SNe derived from single star models displayed a strong dependence with the initial mass, where it was seen that SNe IIb originated from lower mass stars while SNe Ib/c were produced by higher mass stars ([Georgy et al., 2009, 2012](#); [Groh et al., 2013b](#)).

1.3.2 Binary Star Model

While the single star progenitor model can, and has, been invoked to explain the formation of SE-SNe, an alternative formation channel has been put forth in the form of a binary star system ([Podsiadlowski et al., 1992](#); [Eldridge et al., 2008](#); [Yoon et al., 2010](#)). The stripping of the progenitors outer envelope occurs during the later phase, where mass is transferred from the primary star to its companion star. The transfer of mass is expected to occur during one of three stages, based on the evolutionary stage of the primary star; Case-A, during the hydrogen burning phase, Case-B, after the exhaustion of core hydrogen, and Case-C, after the exhaustion of core helium burning ([Kippenhahn & Weigert, 1967](#); [Lauterborn, 1970](#)). During one of these phases the primary star inflates to fill its Roche lobe; the volume of space surrounding a star, where orbiting material is gravitationally bound to the star which was first described analytically by [Paczynski \(1971\)](#) and refined by [Eggleton \(1983\)](#). Once the primary star has filled its Roche lobe, mass is lost from the first Lagrangian point and accreted onto the companion star. If stable mass transfer occurs then primary star loses mass at a steady rate as the Roche lobe radii decreases whilst mass is lost from the star ([Podsiadlowski et al., 1992](#); [Soberman et al., 1997](#)), which results in a hydrogen deficient primary star ([Laplace et al., 2021](#)). However, if the transfer of mass is unstable, the energy transferred to the companion star by the accretion of matter occurs at such a rate that the companion is swallowed by the primary star and a common envelope is formed around the two stars ([Paczynski,](#)

1976; Ivanova et al., 2013). This can either lead to the merger of the two stellar cores or the ejection of the common envelope and the formation of tightly bound stripped binary stars. At this point one of two channels are available for the common envelope binary system. The first is the ejection of the common envelope, which is brought about as the in-falling stars transfer energy to the envelope via frictional forces between the stars and common envelope (Paczynski, 1971). This leads to a tightly bound system containing a combination of evolved and unevolved core stars, which can then go on to explode as a SE-SNe (Podsiadlowski et al., 2010; Ivanova et al., 2013; Margutti et al., 2017). The second result of a common envelope phase is the merger of the two stellar cores resulting in unique objects such as a Thorne-Zytkow object; a degenerate core surrounded by a hydrogen rich envelope (Thorne & Zytkow, 1977).

1.3.3 Single Star vs Binary Progenitor Models

The question now becomes whether the single star and binary system progenitor models for SE-SNe can explain the observed rates of the different types of CC-SNe. Single star models have been shown to possess a mass loss rate great enough to account for the degree of stripping that SN Ib/c progenitors must undergo and has been invoked to explain several SE-SNe such as SN 2006jc (Foley et al., 2007; Pastorello et al., 2007), SN 2013cu (Gal-Yam et al., 2014; Groh, 2014). However, the expected mass range for single star progenitors and the observed rate of SE-SNe is in direct conflict with the number of high mass stars expected from the standard initial mass function (Smith et al., 2011). This incongruity strongly suggests that single star progenitors cannot account for all SE-SNe. Recently there has been work on a non-universal IMF, which may work to alleviate the disparity between SE-SNe rates and the number of high mass stars (Li et al., 2023), although not enough to completely rule out the need for binary formation channels for SE-SNe. In addition to the conflict between the rates of high mass stars and SE-SNe, it has shown that a significant portion of O-type massive stars end their lives in binary systems that have, at some point in their evolution, undergone stripping through binary interaction (Sana et al., 2012; Moe & Di Stefano, 2017).

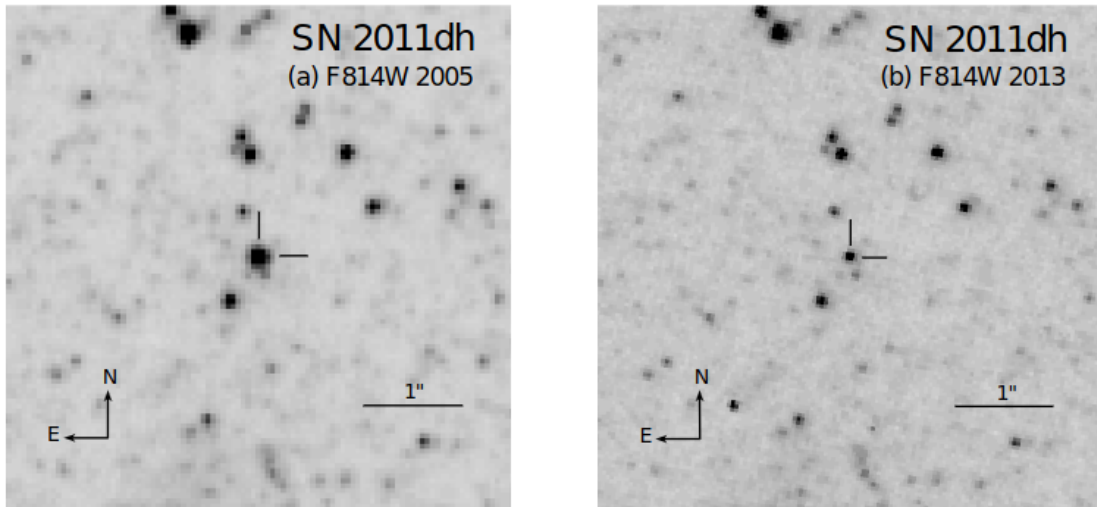


FIGURE 1.10: Two HST images taken at the site of SN 2011dh, where (a) is an archival HST ACS F814W taken in 2005 and (b) is a HST WFC3 F814W image taken in 2013 ~ 1.75 years post explosion, taken from [Van Dyk et al. \(2013\)](#). Location of SN 2011dh marked by the tickmarks. Comparison of the two images show a clear decrease in flux at the site of SN 2011dh due to the destruction of its progenitor, although SN 20011dh was still too luminous to determine the presence of a binary companion.

[Yoon et al. \(2017\)](#) produced a grid of $10 - 18 M_{\odot}$ stars that were evolved through binary interaction to final masses between $3 - 8 M_{\odot}$, which is in agreement with the final masses found from the study of SE-SNe light curves ([Lyman et al., 2016](#); [Taddia et al., 2018](#); [Prentice et al., 2019](#)), supporting the case of the binary formation channel. While these models can reproduce the stripping required for Type IIb and Ib SNe they were unable to remove enough of the helium layer required for the formation of SNe Ic. In addition [Long et al. \(2022\)](#) found that their single star models were incapable of removing enough hydrogen to result in a SNe IIb let alone any H-poor SE-SNe while their binary star models could reduce to a hydrogen fraction low enough to explode as both a SN IIb and SN Ib. The evolution of both the surface hydrogen mass fraction (upper) and helium core mass (lower) of several single star and binary star models from [Long et al. \(2022\)](#) are given in Figure 1.9. [Sravan et al. \(2019\)](#) suggests that the rates of SNe IIb can be accounted for at low metallicity solely with binary systems, although only if low transfer efficiency is assumed to stop the stars undergoing a common envelope phase. While their binary models can account for the rates of SNe IIb at low metallicity, the combined rates of their single star and binary models can only account for around half the observed rates of SNe IIb. Additionally, [Zapartas et al. \(2021\)](#) recently found

that models of single stars fail to explode, instead collapsing directly into a black hole, if stripped of all their outer hydrogen envelope unless higher wind strengths are invoked.

1.3.4 Observational Evidence of SE-SNe Progenitors

While the multiple formation channels and stripping mechanisms of SE-SNe progenitors have been known for multiple decades, there have been a low little confirmed detections of pre-explosion progenitor stars. This is primarily due to the lack of archival data covering the field of SNe prior to core-collapse and the lack of high resolution images of these sites. Of the small number of SE-SNe progenitors reported in the literature, they are typically identified by comparing the archival pre-explosion images and post-explosion imaging taken years after the SN has faded, for an example of this see Figure 1.10. This comparison enables the identification of the stellar properties of the likely progenitor star, which can then be fit with stellar evolution models to determine the formation channel with the highest likelihood for that event. In addition, the comparison of archival observations can be used to determine the presence of a companion star that survived the explosion of the progenitor star. This image comparison process was done with the stereotypical SNe Iib SN 1993J, which resulted in the detection of a companion star (Maund et al., 2004; Maund & Smartt, 2009; Fox et al., 2014) and agree with theoretical models suggesting that the progenitors of SN 1993J was a K-class star (Aldering et al., 1994; Van Dyk et al., 2002).

In addition to SN 1993J several other SE-SNe have had potential progenitor detections including several Type Iib SNe, SN 2011dh (Van Dyk et al., 2013; Maund, 2019), SN 2013df (Van Dyk et al., 2014) and SN 2016gkg (Kilpatrick et al., 2017), and two SNe Ib, SN Ib iPTF13bvn (Bersten et al., 2014; Folatelli et al., 2016) and SN 2019yvr (Kilpatrick et al., 2021). Of the progenitor detections discussed above the properties of the pre-explosion images for the majority SNe Iib progenitors are best explained by stellar evolution models that invoke binary interaction. The preference of the binary formation channel for SNe Iib has been further strengthened by the detection of several surviving companions, such as with SN 2001ig (Ryder et al., 2018). Along with the detections of progenitors and/or their companion stars for SNe Iib and Ib, there have

been tentative detections in pre-explosion imaging of the progenitor for the Type Ic SN SN2017ein, suggesting the event originated from a single star with a mass in the range of $60 - 70 M_{\odot}$ (Van Dyk et al., 2018; Kilpatrick et al., 2018; Xiang et al., 2019). However, Teffs et al. (2021) found that the ejecta mass predicted for SNe2017ein, through the modelling of photospheric and nebular phase observations using a radiation transfer code, were in conflict with the proposed progenitor mass found from studying pre-explosion images. Late time imaging of SN2017ein after the SN has fully faded will provide further information and confirm the mass of its progenitor.

1.4 Thesis statement

The analysis of these events, SNe that bridge the gap between the existing classifications of SE-SNe, is crucial in expanding and understanding the parameter space of SE-SNe properties. In the following chapters I will discuss the analysis of several transitional SE-SNe and their position within the parameter space of SE-SNe.

In Chapter 2, I study the photometric and spectroscopic evolution of SN2020cpg a SN Ib that displayed a high and low hydrogen velocity, which was published in Medler et al. (2021). Then in Chapter 3, I discuss the analysis of the photometric evolution and optical spectroscopy of SN2020acat, a fast rising SN IIb, and compare it to other SNe IIb showing it was an outlier in regard to the evolution of its light curve. This work was published in Medler et al. (2022). Alongside the optical spectroscopic evolution, I discuss in Chapter 4, the Near-Infrared observations taken for SN2020acat in particular focusing on the emergence of a flat-topped helium profile. This work was published in Medler et al. (2023). Then in Chapter 5, I present the investigation into the SN component of GRB 190829A/SN2019oyw and its placement among the parameter space of GRB-SNe. I then investigate the relation between the ejecta mass and kinetic energy of different He-poor SE-SNe. Finally in Chapter 6, I will offer a summary of the intermediate SE-SNe presented in this thesis and propose ideas for future work based on these new SE-SNe.

Chapter 2

The intermediate H-rich SN 2020cpg

2.1 Introduction

SNe Ib are the explosions of stars that have been stripped of their hydrogen envelope prior to core-collapse. The removal of their hydrogen envelope results in a spectral evolution that is dominated by the presence of helium lines during the photospheric phase (Filippenko, 1997). The question as to how much hydrogen can be hidden within the helium envelope of SNe Ib has been a topic of research for several decades (Elmhamdi et al., 2006; Hachinger et al., 2012; Prentice & Mazzali, 2017; Gilkis & Arcavi, 2022). While observations and analysis have mainly focused on the minimum amount of hydrogen needed to form a SNe Iib, the observation of helium dominated events are required to tackle this problem from the point of view of SNe Ib.

In this chapter the photometric and spectroscopic evolution for SN 2020cpg, a Type Ib SN with a thin hydrogen layer, over the course of ~ 130 days is presented. SN 2020cpg was initially classified with the Supernova Identification code SNID (Blondin & Tonry, 2007) as a Type Ib SN, from the spectrum obtained on 19/02/2020 with the Liverpool Telescope (LT; Steele et al., 2004). However, follow-up spectral observations suggests that SN 2020cpg displayed $H\alpha$ features as seen in Type Iib SNe. In Section 2.2.2 the $BgVri$ -band photometry for SN 2020cpg from the first 130 days after the explosion is presented. These observations were obtained through various Las Cumbres Observatory

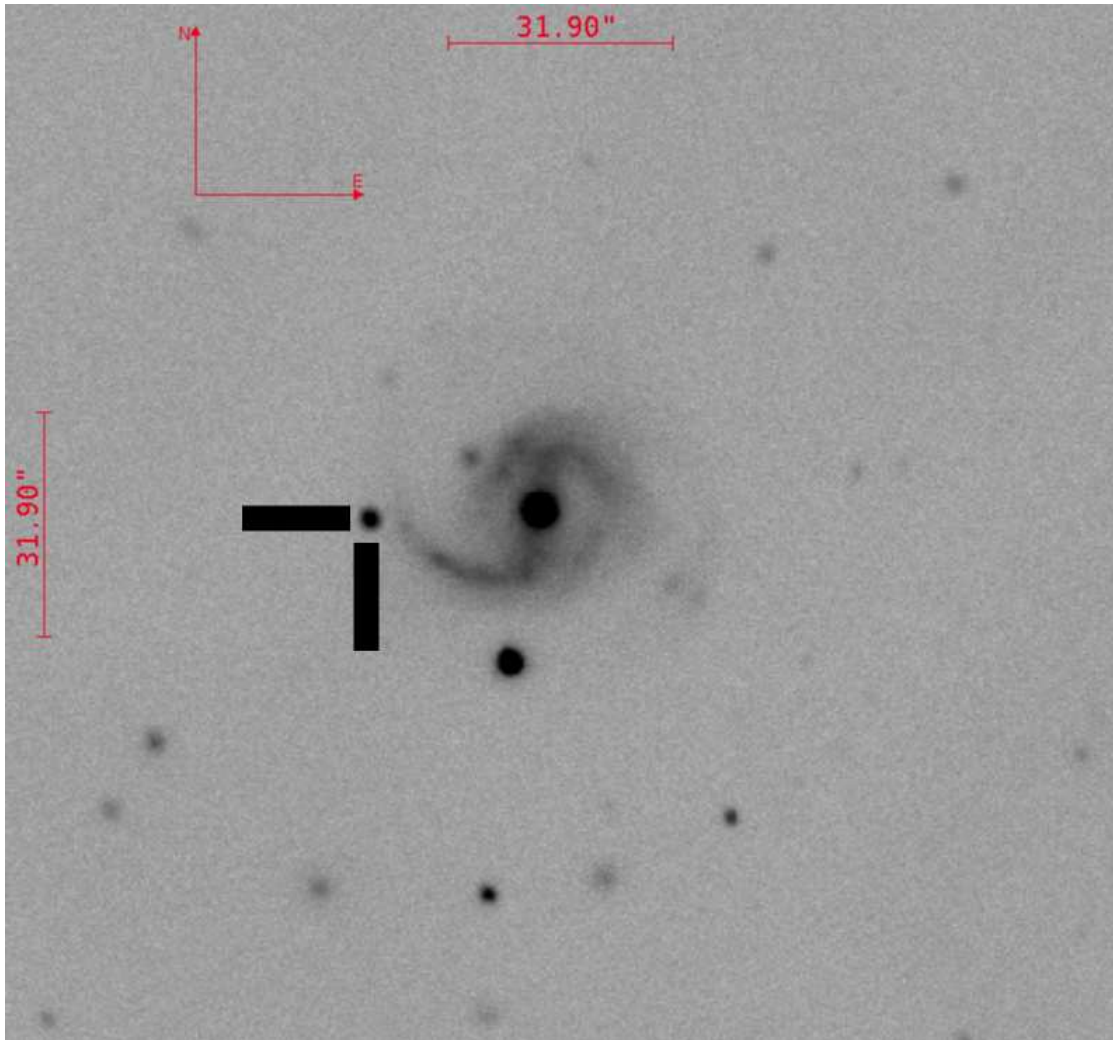


FIGURE 2.1: Image of SN 2020cpg and the host galaxy, obtained by combining LCO observations in $BgVri$ filters on 20/02/2020, stacked and aligned using AstroImageJ (Collins et al., 2017). The field of view is 2.6×2.4 arcmin².

Global Telescope network telescopes (LCO; Brown et al., 2013), as part of the Global Supernova Project (GSP; Howell & Global Supernova Project, 2017). The spectroscopic observation of SN 2020cpg are presented in Subsection 2.2.3. In Section 2.3 the construction of the pseudo-bolometric light curve and use of the Arnett-like model used to obtain the physical parameters are discussed. The analysis of the light curves for the $BgVri$ -band photometry and pseudo-bolometric light curve, along with physical properties obtained by an Arnett-like model are shown in Section 2.4.1 and 2.4.2. Then in Section 2.4.3, the evolution of the $H\alpha$, $He\ I$ and $Fe\ II$ line velocities are presented, along with a comparison of SN 2020cpg spectra with other well followed SNe Ib/IIf. In

Section 2.5 a discussion of the potential presence of a hydrogen envelope and the spectral modelling done to determine its presence. In addition, the use of hydrodynamical models in obtaining more realistic explosion parameters and a comparison to the results with those produced by the Arnett-like model is discussed. Finally, in Section 2.6 a summary of the analysis performed on SN 2020cpg is given, with final estimates for the physical parameters and a value of the progenitors initial mass presented. Work from this chapter was published in Medler et al. (2021). I carried out all work presented in this chapter except obtaining and reducing the observations, information on the different groups involved is given in Section 2.2, and the photospheric phase modelling which was carried out by Jacob Teffs.

2.2 Observations and Data Reduction

2.2.1 Explosion date and Host Galaxy

SN 2020cpg was first detected on 15/02/2020 (MJD = 58894.54) by Nordin et al. (2020) on behalf of the Zwicky Transient Facility (ZTF; Bellm et al., 2018). The last non-detection of SN 2020cpg, on 06/02/2020 (MJD = 58885.52), predates the ZTF discovery by 9 days. To place a better constraint on the explosion date of SN 2020cpg the pseudo-bolometric light curve model was modified to include the explosion date as a parameter, see Section 2.3.2. From this fit an explosion date of 08/02/20, MJD = 58887.7 ± 2.1 days, was obtained which is used throughout the rest of this work. SN 2020cpg was associated with the galaxy SDSS J135219.64+133432.9 and was located 1.14" South and 24.07" West from the galaxy centre, just off the outer end of the host galaxy's western spiral arm, as seen in Figure 2.1. Using the cosmological parameters of $H_0 = 73.0 \pm 5.0$ km/sec/Mpc, $\Omega_{\text{matter}} = 0.27$ and $\Omega_{\text{vacuum}} = 0.73$ gives a redshift distance of 158.6 ± 11.1 Mpc, with the distance calculation based on the local velocity field model from Mould et al. (2000). The host redshift of $z = 0.037$, implies a distance modulus of $m - M = 36.05 \pm 0.15$ mag.

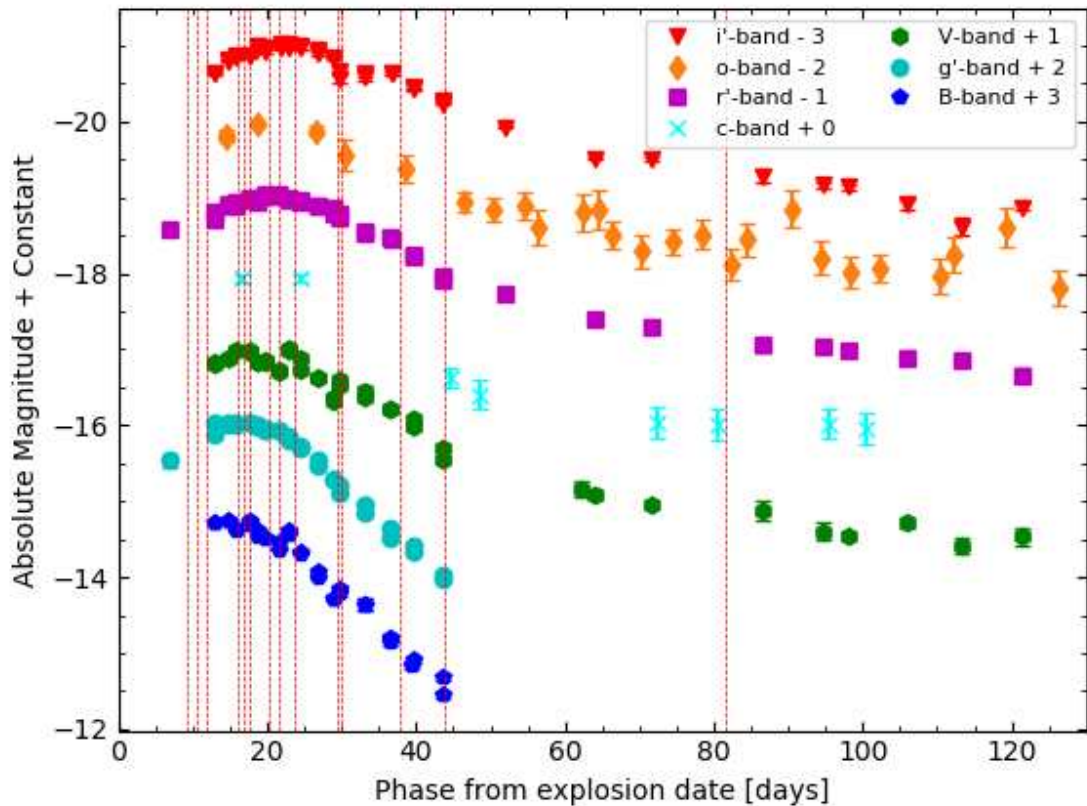


FIGURE 2.2: [Absolute magnitude photometry of SN 2020cpg obtained over the ~ 130 day follow-up campaign.] The absolute magnitude photometry of SN 2020cpg in the $BgVri$ -bands along with the ATLAS c and o -band covering ~ 130 days from the explosion date. The individual band light curves have been corrected for extinction, shifted by a constant magnitude and are shown in rest frame. The red dashed lines denote the epochs at which spectra were taken.

2.2.2 Photometry

The initial g and r -band photometry was obtained by ZTF using the ZTF-cam mounted on the Palomar 1.2m Samuel Oschin telescope several days ($t[\text{MJD}] \approx 58894.5$) before continuous follow-up occurred. This photometry was run through the automated ZTF pipeline (Masci et al., 2019) and is presented on Lasair transient broker (Smith et al., 2019)¹. After the discovery, the $BgVri$ -bands were followed by the Las Cumbres Observatory Global Telescope network (LCO; Brown et al., 2013) and reduced using the BANZAI pipeline (McCully et al., 2018). Full $BgVri$ -band photometry was obtained until 23/03/2020 from which point only Vri -band photometry could be obtained. Observations were obtained from a combination of 1 m telescopes from the

¹<https://lasair.roe.ac.uk/object/ZTF20aanvmdt/>

Siding Spring Observatory (code: COJ), the South African Astronomical Observatory (code: CPT), the McDonald Observatory (code: ELP) and the Cerro Tololo Interamerican Observatory (code: LSC). Both c and o -band photometry were also obtained by the Asteroid Terrestrial-impact Last Alert System (ATLAS; [Smith et al., 2020](#)) and reduced through the standard ATLAS pipeline ([Tonry et al., 2018](#)). The $BgVri + co$ -band absolute light curve from the follow-up campaigns are shown in [Figure 2.2](#). The photometry has been corrected for reddening using a Milky Way (MW) extinction of $E(B - V)_{\text{MW}} = 0.025 \pm 0.001$ mag, obtained using the Galactic dust map calibration of [Schlafly & Finkbeiner \(2011\)](#) and extinction factor $R_V = 3.1$. The host galaxy extinction was taken to be negligible relative to MW extinction, as there was no noticeable Na I D $\lambda\lambda$ 5890, 5896 lines at the SN rest frame, (e.g. [Poznanski et al., 2012](#)). Also it should be noted that, as seen in [Figure 2.1](#), SN 2020cpg was located far from the Galactic centre where the effect of dust is likely reduced. All uncorrected LCO photometry is given in [Tables A1 and B1](#), while the ATLAS photometry is in [Table C1](#).

2.2.3 Spectroscopy

Spectra from multiple telescopes were obtained over an 80 day period post explosion and reduced through standard means available within each observatory pipeline. The classification spectrum of SN 2020cpg ([Poidevin et al., 2020](#)) was obtained with the LT, on 19/02/2020 using the Spectrograph for the Rapid Acquisition of Transients (SPRAT; [Piascik et al., 2014](#)) and was reduced by the LT automatic pipeline ² (see [Barnsley et al., 2012](#), for details on the pipeline). Several later spectra were also obtained using the LT. Additional spectra for SN 2020cpg were obtained by the advanced Public ESO Spectroscopic Survey for Transient Objects (ePESSTO+) ³ ([Smartt et al., 2015](#)) using the ESO Faint Object Spectrograph and Camera mounted on the New Technology Telescope (NTT) (EFOSC2; [Buzzoni et al., 1984](#)). ePESSTO+ data were reduced as described in [Smartt et al. \(2015\)](#). The Alhambra Faint Object Spectrograph and Camera (ALFOSC) mounted on the Nordic Optical Telescope (NOT; [Djupvik & Andersen, 2010](#)) provided

²<http://telescope.livjm.ac.uk/TelInst/Inst/SPRAT/>

³www.pessto.org

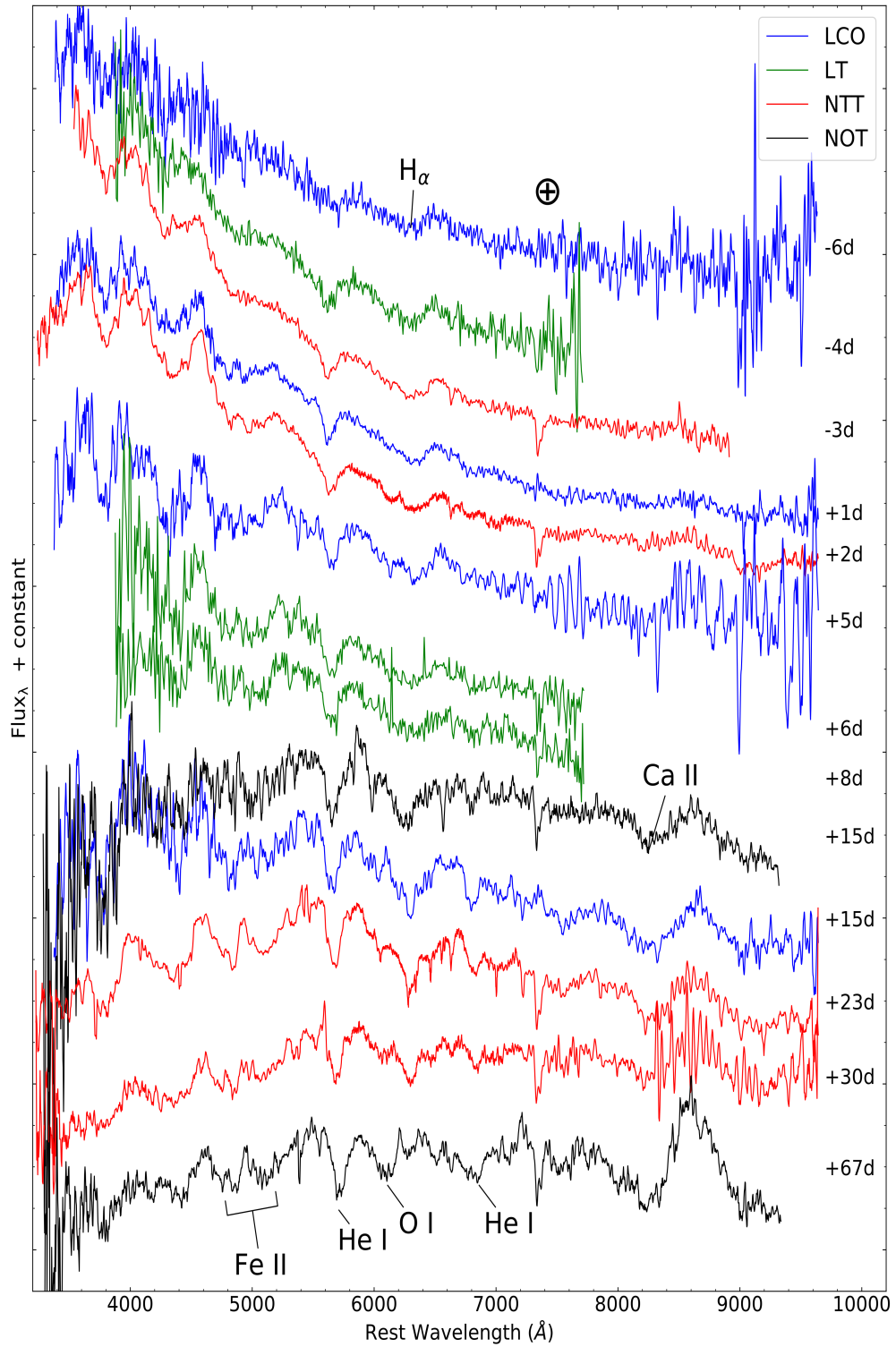


FIGURE 2.3: Spectroscopic evolution of SN 2020cpg with details of the observations given in Table 2.1. The epochs on the right side are relative to B_{max} in rest frame. The $H\alpha$, He I, Fe II, Ca II and O I features have been noted along with the main telluric feature at 7600, \oplus . The spectra have been binned to reduce the noise.

TABLE 2.1: Details of the spectroscopic observations of SN 2020cpg. Phase from both the predicted explosion date ($\text{Phase}_{\text{exp}}$) and the date of B_{max} ($\text{Phase}_{B_{\text{max}}}$) are given in rest-frame.

Date	$\text{Phase}_{\text{exp}}$ [Days]	$\text{Phase}_{B_{\text{max}}}$ [Days]	Telescope + Instrument	Range [Å]
17/02	+9	-6	FTS en12	3500 - 10000
19/02	+11	-4	LT SPRAT	4000 - 8000
20/02	+12	-3	NTT EFOSC2	3685 - 9315
24/02	+16	+1	FTN FLOYDS	3500 - 9000
25/02	+17	+2	NTT EFOSC2	3380 - 10320
28/02	+20	+5	FTS en12	3500 - 10000
29/02	+21	+6	LT SPRAT	4000 - 8000
02/03	+23	+8	LT SPRAT	4000 - 8000
09/03	+30	+15	NOT ALFOSC	3200 - 9600
09/03	+30	+15	FTN FLOYDS	3500 - 10000
17/03	+38	+23	NTT EFOSC2	3380 - 10320
23/03	+44	+30	NTT EFOSC2	3380 - 10320
30/04	+82	+67	NOT ALFOSC	3200 - 9600

several spectra of SN 2020cpg, which were reduced by the Foscgui pipeline ⁴. Multiple spectra were taken by the LCO 2 m Faulkes Telescope South (FTS) at COJ and Faulkes Telescope North (FTN) at the Haleakala Observatory (code: OGG). The observation of additional spectra was attempted after two and a half months post explosion, however SN 2020cpg was too dim at this point for the available telescopes to obtain good quality spectra. All spectra have been binned to improve the S/N ratio, and de-reddened, assuming a standard $R_V = 3.1$ and the $E(B - V)$ given in Section 2.2.1. All spectra can be seen in Figure 2.3. The details on the phase from B -band max, observatory and instrument alongside the observed range are given in Table 2.1.

2.3 Method

2.3.1 Pseudo-bolometric Light curve

The $BgVri$ -band photometry of SN 2020cpg was used to construct a pseudo-bolometric light curve, shown in Figure 2.4, using the pseudo-bolometric light curve code of Nicholl

⁴<http://graspa.oapd.inaf.it/foscgui.html>

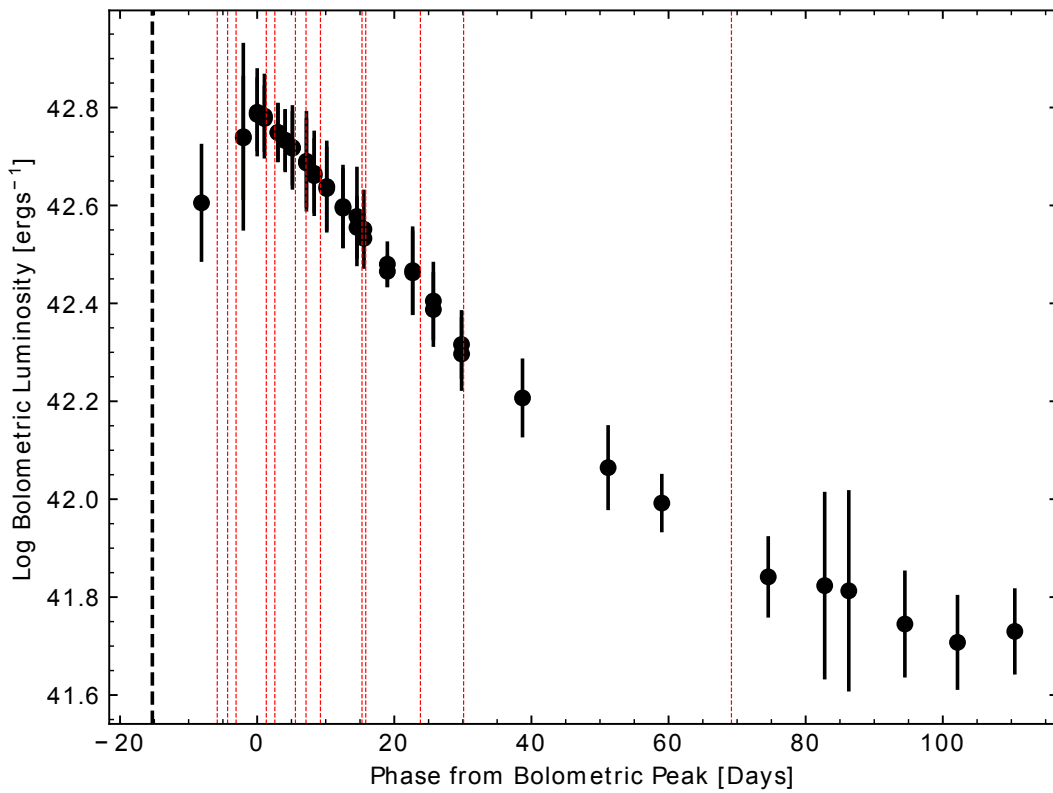


FIGURE 2.4: The pseudo-bolometric light curve of SN 2020cpg constructed from the *BgVri* photometry. Luminosity is shown relative to days from the peak of the pseudo-bolometric light curve in rest-frame and follows approximately 120 days from explosion. The red dashed lines indicate the epochs where spectra were taken and the black dashed line is the yielded explosion date.

(2018). To account for the lack of UV or NIR observations, the missing luminosity was approximated by extrapolating the blackbody spectral energy distributions that were fit to the *BgVri*-bands into the UV and NIR regions. The UV and NIR contributions to the pseudo-bolometric light curve are relatively small at peak time, contributing $\sim 10 - 20\%$ and $\sim 15 - 25\%$ respectively, compared to the optical contribution, which accounts for $\sim 50 - 60\%$ of total flux near bolometric peak (Lyman et al., 2014). As such the extrapolation to the UV and NIR bands does not introduce a significant error to the bolometric light curve.

Along with the pseudo-bolometric light curve of SN 2020cpg, pseudo-bolometric light curves for SN 1993J (Richmond et al., 1994; Barbon et al., 1995; Richmond et al., 1996), SN 2003bg (Hamuy et al., 2009), SN 2008ax (Pastorello et al., 2008; Tsvetkov et al., 2009), SN 2009jf (Sahu et al., 2011; Bianco et al., 2014), SN 2011dh (Tsvetkov et al.,

2012; Sahu et al., 2013; Brown et al., 2014), iPTF13bvn (Brown et al., 2014; Fremling et al., 2016; Folatelli et al., 2016), SN2013ge (Drout et al., 2016), 2015ap (Prentice et al., 2019) and SN2016gkg (Brown et al., 2014; Arcavi et al., 2017; Bersten et al., 2018) were also constructed. The comparison between these SE-SNe is shown in Figure 2.6. These SE-SNe were chosen as they all have comprehensive coverage over the first ~ 100 days post explosion, they all have well defined explosion dates and photospheric velocities both of which are required for the Arnett-like model used to obtain physical parameters. For these SE-SNe, any UV and NIR data available were excluded when constructing the pseudo-bolometric light curve ensuring the effects of the UV and NIR extrapolation did not greatly influence the comparison between the SE-SNe. Where SNe lacked Sloan Digital Sky Survey (SDSS) filters the corresponding Johnson-Cousins (J-C) filters were used to cover a similar wavelength range allowing for a more accurate comparison between the pseudo-bolometric light curves.

2.3.2 Physical parameters

The bolometric luminosity of a SN is intrinsically linked to several physical parameters, those being the mass of nickel synthesised during the explosion, the amount of material ejected from the outer layers of the progenitor and the kinetic energy of the ejected mass. This relation was first formulated for Type Ia SNe by Arnett (1982) who assumed that all the energy that powers the bolometric light curve originated from the decay of $^{56}\text{Ni} \rightarrow ^{56}\text{Co}$ and the decay of $^{56}\text{Co} \rightarrow ^{56}\text{Fe}$. While the model was initially formulated for SNe that do not undergo a hydrogen recombination phase, such as those seen in SE-SNe Ib/c and SNe I Ib, it has been used regularly for multiple types of SNe. This is done by ignoring the recombination phase and restricting the fitting to the rise and fall of the peak of the bolometric light curve that is powered by radioactive activity, as done in Lyman et al. (2016). The Arnett-like model also assumes that all ^{56}Ni is located in a point at the centre of the ejecta, that the optical depth of the ejecta is constant throughout the evolution of the light curve, the initial radius prior to explosion is very small and that the diffusion approximation used for the model is that of photons. While these assumptions are acceptable, the approximation of constant opacity has a severe effect

on the diffusion timescale which is dependent on the estimated ejecta mass and kinetic energy of the SN. The effect of neglecting the time-dependent diffusion on the ^{56}Ni mass was discussed by [Khatami & Kasen \(2019\)](#), who concluded that this results in an overestimation of the ^{56}Ni mass. Through alternative modelling methods it was seen that the ^{56}Ni mass was overestimated by the Arnett-like model by $\sim 30 - 40\%$ (see, [Dessart et al., 2016](#); [Woosley et al., 2021](#)).

Initially the Arnett-like model was used to determine the physical parameters of SN 2020cpg and compare the results to several other SE-SNe. In the Arnett-like model the kinetic energy and ejecta mass have a strong dependence on the diffusion timescale, τ_m , of the bolometric light curve, which is given as;

$$\tau_m = \left(\frac{\kappa_{\text{opt}}}{\beta c} \right)^{\frac{1}{2}} \left(\frac{6M_{\text{ejc}}^3}{5E_k} \right)^{\frac{1}{4}}. \quad (2.1)$$

Where M_{ejc} is the mass of ejected material and E_k is the kinetic energy of the supernovae. Also c is the speed of light, β is the constant of integration derived by [Arnett \(1982\)](#) that takes the value of $\beta \approx 13.8$ and κ_{opt} is the optical opacity of the material ejected by the SN. For the Arnett-like model a constant value of $\kappa_{\text{opt}} = 0.06 \pm 0.01 \text{cm}^2 \text{g}^{-1}$ was used. The value of κ_{opt} used in this work is consistent with the range of opacities, usually between $\kappa_{\text{opt}} = 0.05 - 0.08 \text{cm}^2 \text{g}^{-1}$ ([Drout et al., 2011](#); [Pignata et al., 2011](#)), used throughout the literature. The range of opacities that are used in the Arnett-like approach are derived from average values of a time varying opacity used in spectral modelling of well observed events. The κ_{opt} used in this work allows for a comparison of the fitting discussed above with previous work as a way to validate the model used and allows for a comparison between the derived physical parameters of SN 2020cpg and other SE-SNe. The degeneracy between the ejecta mass and kinetic energy was broken using the photospheric velocity the event obtained from the velocity of the Fe II 5169 Å line measured at maximum bolometric luminosity. This is the epoch when the outer ejecta has the largest contribution to the luminosity under the assumption of homogeneous density. The model was also adjusted to include the SN explosion date to allow for an improved fit and to place a constraint on the rise time of the SNe. For SNe

TABLE 2.2: Epoch of light curve maximum, rise time in rest-frame and peak absolute magnitude for the *BgVcroi* photometry bands for SN 2020cpg

Band	MJD_{\max}	Rise time (days)	m_{\max}	M_{\max}
<i>B</i>	58902.1	14.7 ± 2.5	18.38 ± 0.02	-17.75 ± 0.39
<i>g'</i>	58903.1	16.0 ± 2.1	18.05 ± 0.02	-18.04 ± 0.40
<i>V</i>	58904.7	17.0 ± 2.1	18.16 ± 0.02	-17.91 ± 0.38
<i>c</i>	58906.0	18.8 ± 2.3	18.10 ± 0.05	-17.97 ± 0.38
<i>r'</i>	58906.2	18.6 ± 2.1	18.06 ± 0.02	-18.00 ± 0.38
<i>o</i>	58908.3	21.1 ± 2.4	18.05 ± 0.05	-18.01 ± 0.39
<i>i'</i>	58909.2	22.0 ± 2.1	18.05 ± 0.02	-18.00 ± 0.38

with well observed pre-maximum and well defined explosion dates the literature values were used. The explosion date of SN 2020cpg was obtained by constraining the fitting to limit the potential explosion date to after the date of last non-detection and prior to the initial observation.

Due to the known problems with the Arnett-like model, an alternative method for determining the ejecta mass and kinetic energy of SN 2020cpg is discussed in Section 2.5.3. This method works by comparing the light curve properties and physical properties determined by hydrodynamical modelling of other SE-SNe, as done for SN 2010ah in Mazzali et al. (2013, here after PM13). This method re-scales the physical parameters of other SE-SNe using equation 2.1 under the assumption that the optical opacity of the two SNe are equivalent. This is physically a more robust assumption than a fixed opacity for all SE-SNe as adopted by the Arnett-like model. A comparison between the results obtained from the Arnett-like model and the light curve comparison model is presented later in Section 2.5.3.

2.4 Results

2.4.1 Multi-colour light curves

The early time rise of both the *B* and *V*-bands were missed in the follow-up campaign, however the peaks in both bands were observed, shown in Figure 2.2. The bluer bands peaked several days before the red bands, $t_{\text{blue}}^{\text{rise}} \approx 15$ days post explosion and $t_{\text{red}}^{\text{rise}} \approx$

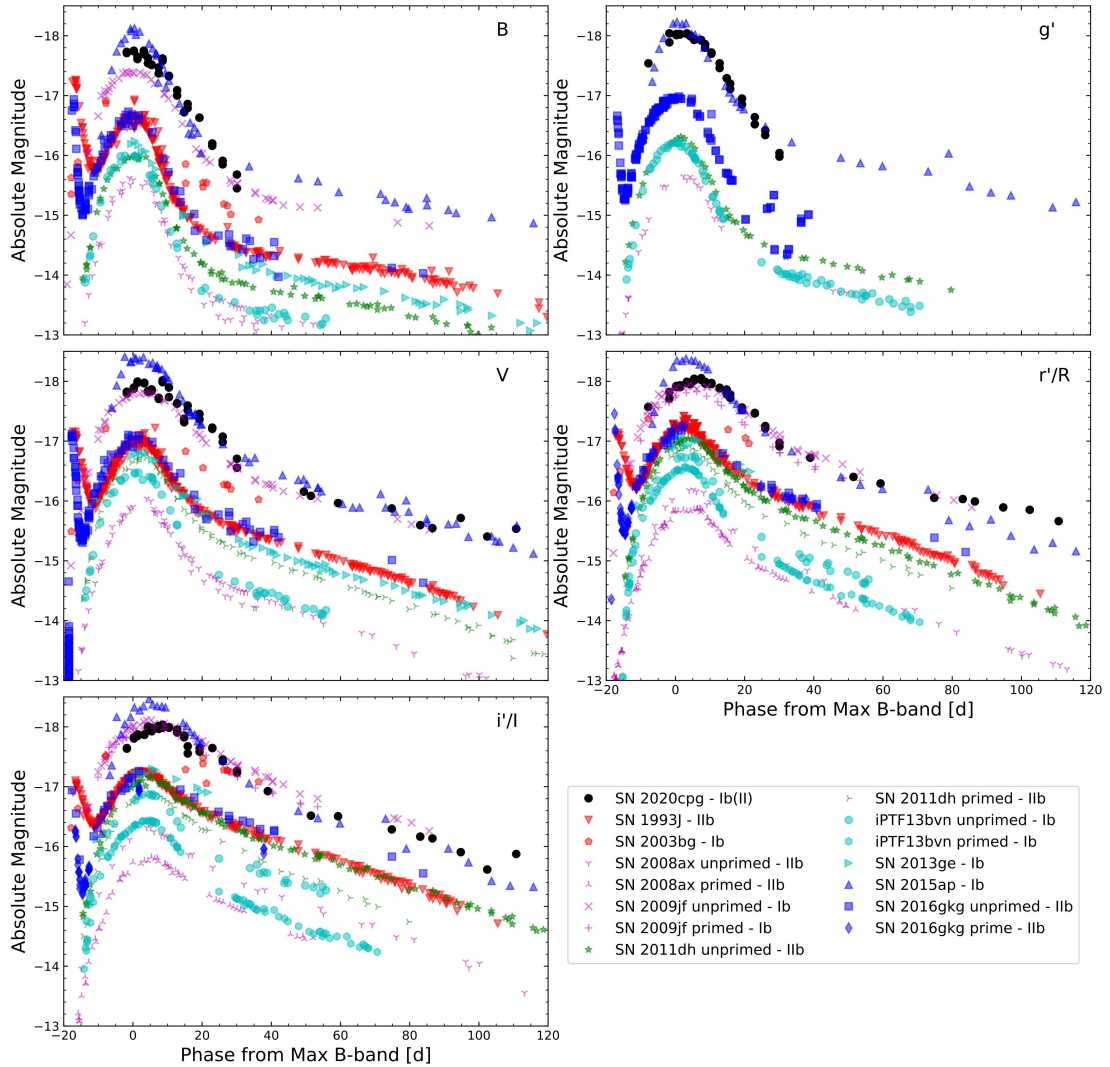


FIGURE 2.5: Comparison of the absolute magnitude light curves of several SNe Ib and IIb with SN 2020cpg. All photometry is relative to B_{\max} light which was either taken from the literature or by fitting a Gaussian to the B -band peak. The light curves have been corrected for time dilation as well as corrected for both Milky Way and host galaxy reddening when possible. Primed bands are SDSS photometry bands and unprimed are the Johnson-Cousins photometry bands. Error on absolute magnitudes not included.

19 days. Both the B and g -bands were followed for ~ 30 days by LCO before the photometry bands dropped below the brightness threshold required for follow-up. The brightness for the B and g -bands fell by ~ 2 magnitudes in the 30 days from the photometric peak as a result of the SN rapidly cooling. The remaining bands fell at a slower rate, dropping by roughly 1 magnitude in the same time period, before their decline slowed down as the light curve transitioned to the exponential tail produced by the radioactive decay ^{56}Co synthesised in the explosion. The ATLAS c -band was followed for approximately 100 days from the expected explosion date with the o -band

being followed for a further 30 days. The peaks in both bands were not well observed, especially in the c -band. As with the other bands the redder o -band declines at a slower rate just after maximum light when compared to the c -band. The ATLAS bands have a greater error associated with them compared to the $BgVri$ -bands, and as the ATLAS bands cover a similar wavelength range as the $BgVri$ they were not used when constructing the pseudo-bolometric light curve.

The light curves for He-rich CC-SNe display a variation within the evolution of their light curves due to the range of progenitor properties. As such the $BgVri$ -band photometry for SN 2020cpg was compared with those of SN 1993J, SN 2003bg, SN 2009jf, SN 2011dh, iPTF13bvn, SN 2013ge, SN 2015ap and SN 2016gkg. The absolute magnitude photometry for these SNe relative to SN 2020cpg is shown in Figure 2.5, with the details on each SN given in Table 2.3. SN 2020cpg is brighter than the majority of the other SNe that are compared here, with only SN 2009jf and SN 2015ap being of similar brightness. The B and g -bands evolve in a similar way to that of SN 2015ap while the other bands evolve more similar to SN 2009jf. Due to the lack of pre-maximum light observations it is not possible to determine if SN 2020cpg had a shock breakout cooling peak similar to that seen in several other SE-SNe, such as SN 1993J and SN 2016gkg.

2.4.2 pseudo-bolometric Light Curves

The pseudo-bolometric rise time for SN 2020cpg is $t_{\text{rise}}^{\text{bol}} \approx 16.0 \pm 2.5$ days. Once peak luminosity had been reached the light curve rapidly declines for the next ≈ 34 days before settling on the exponential tail. Due to lack of much pre-peak photometry the rise of the pseudo-bolometric light curve is not as well constrained as the post-peak light curve. SN 2020cpg reaches a peak luminosity of $\log(L_{\text{max}}) = 42.78 \pm 0.08$ [erg s^{-1}], which is higher than the average luminosity of Type IIb + Ib(II), which has a value of $\log(L_{\text{max}}) = 42.2_{-0.1}^{+0.4}$ [erg s^{-1}], and the average maximum luminosity of Type IIb + Ib(I), $\log(L_{\text{max}}) = 42.09 \pm 0.17$ [erg s^{-1}], as given in Prentice et al. (2019), showing that SN 2020cpg lies at the brighter end of the SE-SNe regime.

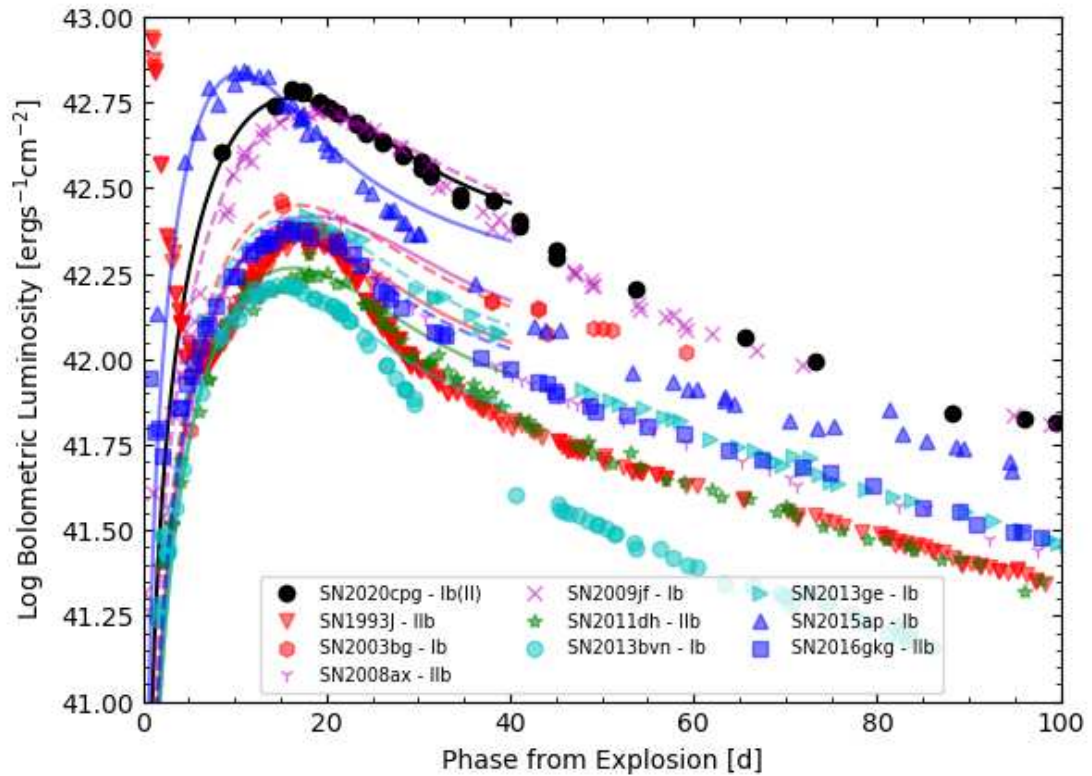


FIGURE 2.6: Pseudo-bolometric light curves of SN 1993J, SN 2003bg, SN 2008ax, SN 2009jf, SN 2011dh, iPTF13bvn, SN 2013ge, SN 2015ap, SN 2016gkg and SN 2020cpg covering a period of 100 days from their estimated explosion date. The Arnett-like model fit to the pseudo-bolometric light curves, detailed in Section 2.3.2, are shown as lines and were fitted out to ~ 40 days before they started to strongly diverge from the pseudo-bolometric light curves. The velocities used to break the degeneracy for each SN, along with the predicted physical parameters, are given in Table 2.4.

TABLE 2.3: Details for several historical Type Ib and IIb SNe which have been compared to SN 2020cpg. Sources- 1: Richmond et al. (1994), 2: Barbon et al. (1995), 3: Richmond et al. (1996), 4: Pastorello et al. (2008), 5: Hamuy et al. (2009), 6: Tsvetkov et al. (2009), 7: Sahu et al. (2011), 8: Tsvetkov et al. (2012), 9: Sahu et al. (2013), 10: Bianco et al. (2014), 11: Brown et al. (2014), 12: Fremling et al. (2016), 13: Folatelli et al. (2016), 14: Drout et al. (2016), 15: Arcavi et al. (2017), 16: Bersten et al. (2018) and 17: Prentice et al. (2019).

SN	Explosion date [MJD]	B_{\max} date [MJD]	Redshift	Distance [Mpc]	$E(B - V)_{\text{MW}}$ [mag]	$E(B - V)_{\text{Host}}$ [mag]	Source
1993J	49072.0	49093.48	-0.000113	2.9	0.069	0.11	1,2,3
2003bg	52695.0	52718.35	0.00456	20.25	0.018	-	5
2008ax	54528.8	54546.86	0.001931	5.1	0.0188	0.28	4,6
2009jf	55101.33	55120.91	0.0079	31	0.097	0.03	7,10
2011dh	55712.5	55730.82	0.001638	7.25	0.0309	0.05	8,9,11
iPTF13bvn	56458.17	56474.95	0.00449	19.94	0.0436	0.17	11,12,13
2013ge	56602.5	56618.93	0.004356	19.342	0.0198	0.047	14
2015ap	57270.0	57283.0	0.01138	50.082	0.037	-	17
2016gkg	57651.15	57669.67	0.0049	21.8	0.0166	0.09	11,15,16
2020cpg	58887.6	58902.07	0.037	158.6	0.0246	-	-

The pseudo-bolometric light curve of SN 2020cpg was then fit with the Arnett-like model using a photospheric velocity of $v_{\text{ph}} \approx 12500 \pm 1500 \text{ km s}^{-1}$ to break the degeneracy between the kinetic energy and ejecta mass. The value of v_{ph} was obtained from the average Fe II line velocities at peak light. The average value of the Fe II triplet was used instead of the commonly employed Fe II λ 5169 line due to the low signal to noise ratio within the Fe II region of the spectrum taken around peak luminosity. From the Arnett-like model fit to SN 2020cpg's pseudo-bolometric light curve a nickel mass of $M_{\text{Ni}} = 0.27 \pm 0.08 M_{\odot}$ was derived. The ejecta mass and kinetic energy given by the fit had a value of $M_{\text{ejc}} = 3.4 \pm 1.0 M_{\odot}$ and $E_{\text{k}} = 2.9 \pm 0.9 \times 10^{51} \text{ erg}$ respectively. This process was then repeated for the bolometric light curves of the other SE-SNe shown in Figure 2.6 and the derived physical parameters are given in Table 2.4. As expected the Arnett-like model deviates from the pseudo-bolometric light curves at later times ($t \gtrsim 40$ days) when the SNe start to transition into the nebular phase. Relative to the other SNe, SN 2020cpg has a high nickel mass similar to both SN 2009jf and SN 2015ap, shown in Table 2.4. The similar M_{Ni} between SN 2020cpg and both SN 2009jf and SN 2015ap is expected from their comparable peak luminosities. The ejecta mass and kinetic energy of SN 2020cpg is also higher than the majority of the SE-SNe studied here, suggesting that the progenitor of SN 2020cpg was a high mass star prior to the stripping of the outer envelope. However, due to the problems associated with the Arnett-like approach, an alternative approach to obtain the values for M_{ejc} and E_{k} is discussed in Section 2.5.3, the results of which are then used to estimate the progenitor mass.

2.4.3 Spectral Evolution and Comparison

At early times, the spectra of SN 2020cpg, shown in Figure 2.3, shows a large blue excess. The spectra rapidly cool until around +15 days from B_{max} . Prominent He I lines are present throughout the spectral evolution with the He I 5876 Å line being the most prominent and the 6678 Å line becoming stronger at around +23 days. Around +1 days post B_{max} the spectrum develops an absorption feature located in the H α region which persists for ~ 30 days. At earlier times during the spectral evolution, the H α feature is split into a high velocity and low velocity component which the merge into a single

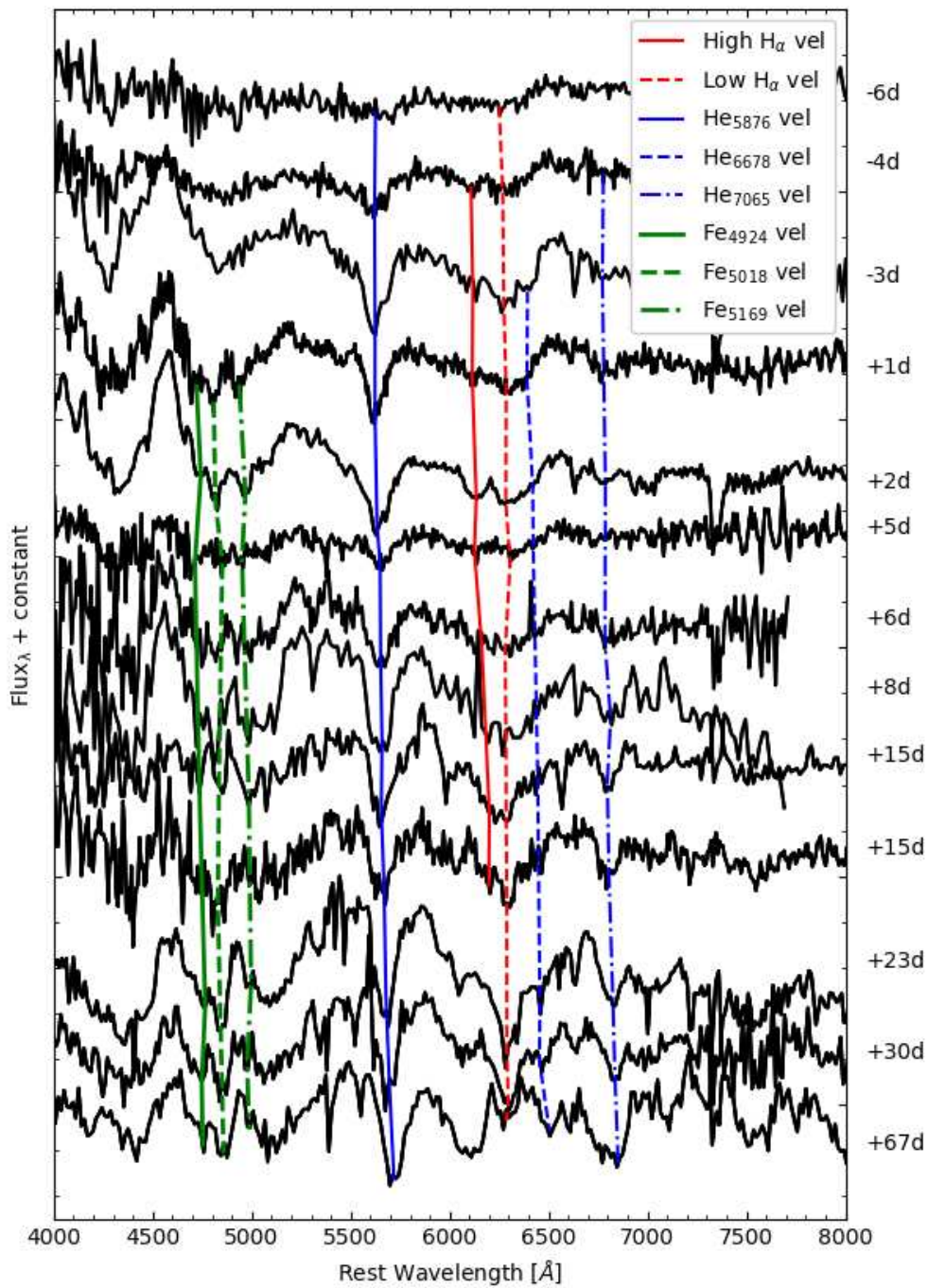


FIGURE 2.7: Evolution of SN 2020cpg spectra. The spectra have been plotted between 4000 – 8000 Å to highlight the regions where prominent H α , He I and Fe II features are visible. The different elements are shown by the different lines, with H α = red, He I = blue and Fe II = green, and different element lines given by different styles. Lines are only shown when line features are clearly visible within the spectra.

TABLE 2.4: Physical properties of several SE-SNe derived from the fitting of the Arnett-like model described in Section 2.3 and shown in Figure 2.6. The photospheric velocity used for each SN was taken from their discovery paper.

SN	v_{ph} [km s ⁻¹]	M_{Ni} [M _⊙]	M_{ejc} [M _⊙]	E_{k} [10 ⁵¹ erg]
1993J	8000 ± 1000	0.11 ± 0.03	2.0 ± 0.8	0.8 ± 0.3
2003bg	10000 ± 500	0.13 ± 0.04	2.8 ± 0.9	1.7 ± 0.5
2008ax	7500 ± 500	0.14 ± 0.04	2.6 ± 1.0	0.9 ± 0.3
2009jf	11000 ± 500	0.27 ± 0.09	4.0 ± 1.4	2.9 ± 1.0
2011dh	7000 ± 1000	0.09 ± 0.02	1.8 ± 0.5	0.5 ± 0.1
iPTF13bvn	8000 ± 1000	0.07 ± 0.02	1.7 ± 0.4	0.6 ± 0.2
2013ge	10500 ± 500	0.12 ± 0.03	2.7 ± 0.8	1.8 ± 0.5
2015ap	16000 ± 1000	0.22 ± 0.05	1.4 ± 0.4	2.2 ± 0.6
2016gkg	8000 ± 1000	0.10 ± 0.02	1.9 ± 0.4	0.7 ± 0.2
2020cpg	12500 ± 1200	0.27 ± 0.08	3.4 ± 1.0	2.9 ± 0.9

H α feature at later times. The presence of the H α line provides strong evidence that SN 2020cpg is not a standard Type Ib SN and may be an intermediate SN between the H-rich and H-poor SE-SNe. While the feature around 6300 Å may be interpreted as the presence of silicon, this is not likely, because it would imply that absorption from other silicon transitions, around 4100 and 5900 Å should be detected in this and later spectra which is not observed. Moreover, when identified as silicon, the line shift would indicate a velocity of 3000 km s⁻¹ which is far too slow for this epoch. These pieces of evidence alongside the lack of silicon in the spectra of other well observed Type Ib/c SNe gives strong evidence that the feature is the result of the presence of hydrogen within the outer envelope. Later, the spectral evolution shows the development of Fe II $\lambda\lambda$ 4924, 5018, 5169 lines, although it should be noted that the Fe II lines are located close to He I lines making the separation of these lines difficult, especially given the high noise in this region of the spectra.

The evolution of the line velocities for H α , He I $\lambda\lambda$ 5876, 6678, 7065 and Fe II $\lambda\lambda$ 4924, 5018, 5169 were determined by the fitting of a Gaussian to each feature to locate the minima. The line evolution of each elemental feature is shown in Figure 2.7. The line velocities derived from the Gaussian fits are given in Figure 2.8. The main source

of error for these elemental line velocities comes from the low S/N of the spectra, especially on the fringes where the Fe II line is located, which makes the fitting of the Gaussian more difficult. This results in an error derived from the Gaussian fitting of approximately 15%, with a negligible error associated with the redshift. For the H α feature, the minimum of the spectra feature can be split into two distinct high and low velocity components. The high velocity feature is visible from the second spectrum, -4 days, until approximately $+15$ days post B_{\max} , as shown by the solid red line in Figure 2.7. At this point the high velocity and low velocity components blend together in the later spectra to form a single H α feature. There is a clear separation between the high and low velocity H α components, with the low velocity remaining relatively constant in velocity with a decline of $\sim 2000 \text{ km s}^{-1}$ from $\sim 14500 \text{ km s}^{-1}$ to $\sim 12500 \text{ km s}^{-1}$ while the high velocity component drops by $\sim 5000 \text{ km s}^{-1}$ from $\sim 21000 \text{ km s}^{-1}$ to $\sim 16500 \text{ km s}^{-1}$ before the lines seem to merge into one constant H α feature. The He I $\lambda 5678$ feature remains strong throughout the spectral evolution while the He I $\lambda 6678$ feature, while not always visible due to high noise, follows the velocity evolution of He I $\lambda 5876$.

The signal to noise ratio in the Fe II region made finding the velocity evolution harder than for the other lines. The velocity of the He I and Fe II lines all follow a similar trend declining from $\sim 13000 \text{ km s}^{-1}$ to $\sim 10000 \text{ km s}^{-1}$. From the velocity evolution the peak-time photospheric velocity of SN 2020cpg was determined to have an average of $12500 \pm 1200 \text{ km s}^{-1}$, taken from the velocity of the He I and average Fe II features.

A spectral comparison between SN 2020cpg, the H-rich SN 2011dh, and the H-poor SN 2015ap SN, within the range $4000 - 9000 \text{ \AA}$ is shown in Figure 2.9, presenting the evolution of the hydrogen features and the line strength relative to standard SNe Ib and IIb. Both SN 2011dh and SN 2015ap were close, well observed, SE-SNe allowing for clear comparisons to SN 2020cpg. This is especially true of SN 2015ap, which photometrically appears similar to SN 2020cpg in both shape and luminosity. The epochs chosen were relative to the peak of the pseudo-bolometric light curve so that all SNe were at similar stages in their evolution. The epochs compared are $-5, 0, +5$ and $+30$ days relative to peak luminosity. The grey region in Figure 2.9 highlights the H α region. It is clear that early on the spectra of SN 2020cpg are more similar to those of SN 2015ap, especially in the He I lines velocity ($\sim 12000 \text{ km s}^{-1}$), and lack of a strong H α feature.

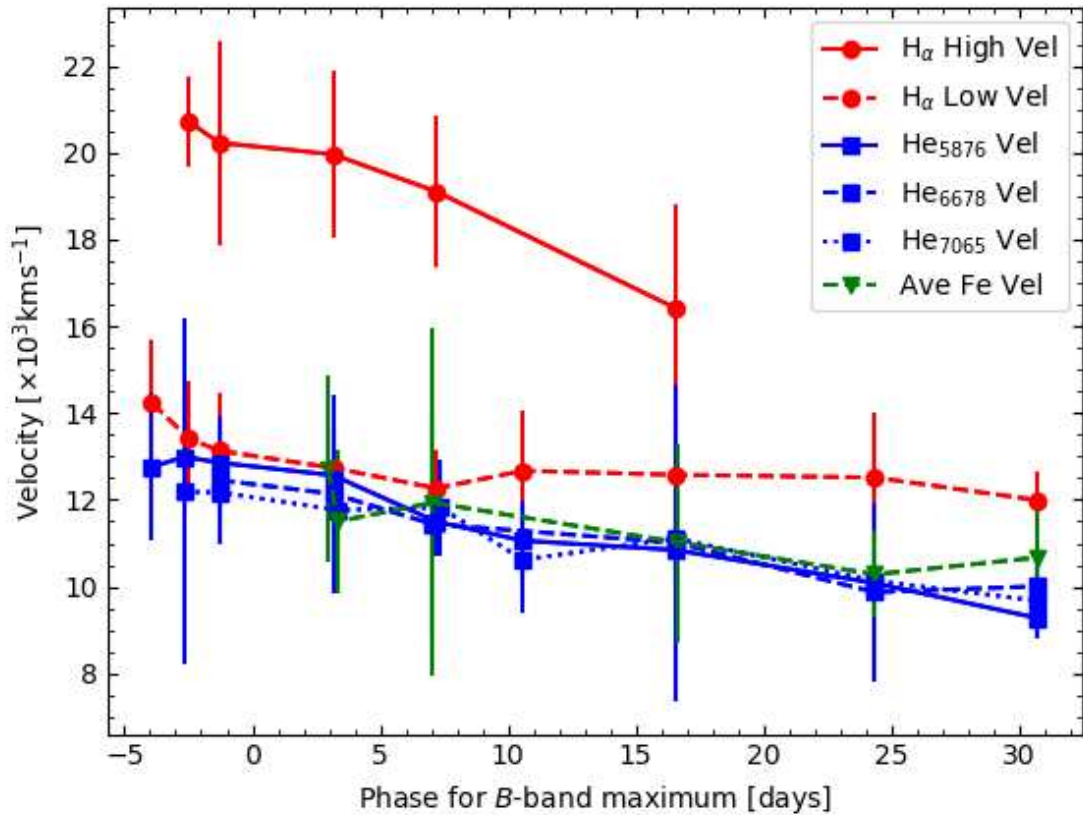


FIGURE 2.8: Line velocity evolution of H α , He I and Fe II from Gaussian fits to the spectra. The H α (red) is split into a high velocity and a low velocity component, shown as the solid line and dashed line respectively. The evolution of a selection of individual He I spectral lines (blue) are shown as separate curves. Due to the uncertainty in the Fe II lines (green), as a result of the noise in that region of the spectrum, the average line velocity is displayed. The plot is cut off at ~ 30 days due to the emergence of other lines around the H α region.

The He I $\lambda 6678$ feature, which can sometimes blend with the H α feature is not well defined in SN 2020cpg at any epoch and can only be clearly seen in plots b and d of Figure 2.9. As the spectra evolve, the He I features of SN 2015ap and SN 2020cpg deepen in a similar fashion, although the H α feature of SN 2020cpg also becomes deeper and more defined. The emergence of the H α feature results in the spectra of SN 2020cpg becoming more 2011dh-like and less like those of SN 2015ap. In the final plot, the spectrum of SN 2020cpg becomes very similar to that of SN 2011dh, especially in the H α region where there is a clear H α absorption feature that is not present in the SN 2015ap spectrum. Throughout the emergence of the H α feature its strength remains weaker than or similar to that of the He I $\lambda 5876$ peak, compared to the ratio of their strength seen in the SN IIb where the H α feature dominates throughout the spectra.

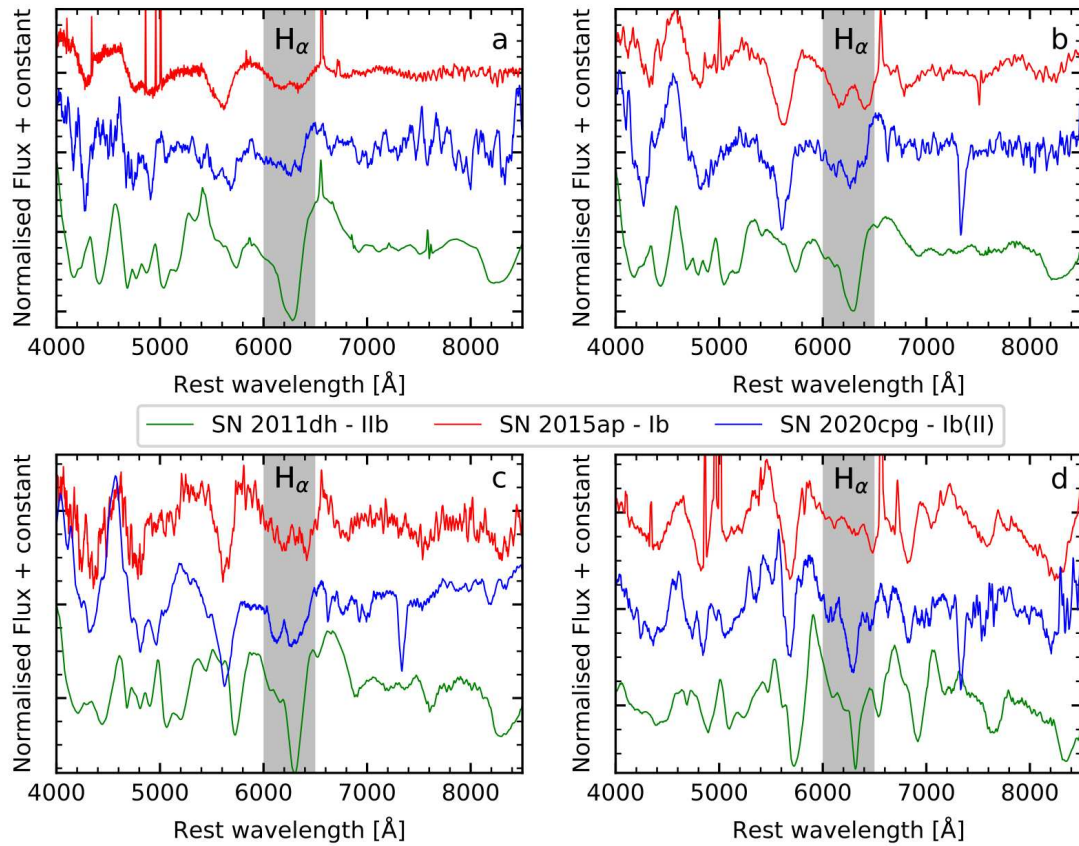


FIGURE 2.9: Comparison of SN 2020cpg (blue) with a characteristic SN Ib (SN 2015ap, red) and a characteristic SN IIb (SN 2011dh, green) at several epochs relative to pseudobolometric peak. The epochs shown are around a: -5 days, b: $+0$ days, c: $+5$ days, d: $+30$ days. The grey shaded area denote the region where the $H\alpha$ feature should be located if hydrogen is present within the outer envelope of the progenitor. The spectrum used for each of the plots along with the instrument used to obtain them are detailed in Table 2.5 and can all be found on WiseRep (Yaron & Gal-Yam, 2012).

From the classification scheme of Prentice & Mazzali (2017) and the strength of the $H\alpha$ feature relative to the He I peak, it seems that SN 2020cpg should be categorised as a Type Ib(II) SN.

2.5 Discussion

With a maximum luminosity of $6.03^{+1.21}_{-1.02} \times 10^{42}$ erg s $^{-1}$, SN 2020cpg is brighter than the average SE-SNe. Among the SNe considered here, only SN 2009jf and SN 2015ap have similar luminosities to SN 2020cpg. A comparison of the maximum luminosity of SN 2020cpg to the median peak luminosity of SNe Ib + Ib(II) and SNe IIb + IIb(I)

in [Prentice et al. \(2019\)](#) showed that SN 2020cpg is located at the brighter end of the luminosity range displayed by H-rich SNe. The rise time of SN 2020cpg is similar to most other SE-SNe, although the pseudo-bolometric light curve of SN 2020cpg is broader than many of the SNe shown in [Figure 2.6](#). The high pseudo-bolometric luminosity indicates a large amount of ^{56}Ni . An Arnett-like model fit yielded a total ^{56}Ni mass of $M_{\text{Ni}} = 0.27 \pm 0.08 M_{\odot}$. From the analysis of several SE-SNe performed by [Prentice et al. \(2019\)](#), the Arnett-like model derived mean nickel masses of $\langle M_{\text{Ni}} \rangle = 0.07 \pm 0.03 M_{\odot}$ for SNe I Ib + I Ib(I) and $\langle M_{\text{Ni}} \rangle = 0.09 \pm 0.06 M_{\odot}$ for SNe Ib + Ib(II). Therefore, SN 2020cpg produced roughly triple the mean nickel mass, placing it on the extreme end of SE-SNe.

Despite the similarity in mean ^{56}Ni between SNe I Ib + I Ib(I) and SNe Ib + Ib(II), [Prentice et al. \(2019\)](#) showed that SNe Ib + Ib(II) ^{56}Ni masses display a high mass tail, not seen in the SNe I Ib + I Ib(I), that extends to where SN 2020cpg resides. From the distribution of ^{56}Ni mass given by [Prentice et al. \(2019\)](#), it seems that SN 2020cpg behaves like H-poor SE-SNe. It should be noted that most neutrino-driven explosion models cannot produce M_{Ni} greater than $\sim 0.23 M_{\odot}$ ([Suwa et al., 2018](#)), although a study of literature M_{Ni} values done by [Anderson \(2019\)](#) found that $\sim 30\%$ of hydrogen-poor SE-SNe and $\sim 7\%$ of H-rich SE-SNe have ^{56}Ni masses that are greater $0.23 M_{\odot}$. This discrepancy arises from the assumptions of the Arnett-like model, see [Section 2.3.2](#), which result in an overestimation of the M_{Ni} . Taking into account this overestimation the M_{Ni} of SN 2020cpg is reduced to $\approx 0.16\text{--}0.19 M_{\odot}$, placing SN 2020cpg's M_{Ni} within, although close to, the upper limits of neutrino-driven explosion models. Given the uncertainty in the overestimation of M_{Ni} obtained by the Arnett-like model, the value given above for the M_{Ni} of SN 2020cpg is considered an upper-limit.

2.5.1 Hydrogen Envelope

As seen for the spectroscopic evolution of SN 2020cpg when compared to well observed Type Ib and I Ib SNe, there is strong evidence for the presence of a hydrogen envelope surrounding the progenitor of SN 2020cpg. The separation of the $\text{H}\alpha$ feature into a high velocity and a low velocity component suggests that the hydrogen is located in

TABLE 2.5: Spectral details for the spectra used in Figure 2.9, including the date the spectra were obtained and the instrument used to obtain them. All spectra shown in this table and Figure 2.9 are from the sources below; 1: [Arcavi et al. \(2011\)](#), 2: [Ergon et al. \(2014\)](#), 3: [Shivvers et al. \(2019\)](#), 4: [Prentice et al. \(2019\)](#).

SN	Plot	Date	Instrument	Source
2011dh	a	12/06/2011	FOS_1	1
	b	17/06/2011	ALFOSC	2
	c	25/06/2011	ALFOSC	2
	d	14/07/2011	ALFOSC	2
2015ap	a	15/09/2015	KAST	3
	b	20/09/2015	FLOYDS_S	4
	c	23/09/2015	FLOYDS_N	4
	d	20/10/2015	KAST	3
2020cpg	a	17/02/2020	COJ en12	-
	b	20/02/2020	EFOSC2	-
	c	23/02/2020	EFOSC2	-
	d	23/03/2020	EFOSC2	-

two distinct regions within the outer envelope of the progenitor star. A thin outer envelope and an inner section where the hydrogen and helium are thoroughly mixed together corresponding to the high and low velocity component respectively. While the two component $H\alpha$ features are not common among H-rich SE-SNe, it has been observed in other SNe, with SN 1993J displaying a clear double $H\alpha$ feature throughout the photospheric phase. The velocity of the high velocity component for SN 1993J does not seem as large as that for SN 2020cpg relative to the low velocity component. This suggests that the amount of hydrogen stripped from the progenitor of SN 2020cpg is greater than that of SN 1993J prior to the explosion, which is further supported by the weak $H\alpha$ feature seen in the spectral evolution of SN 2020cpg. The presence of a weak $H\alpha$ absorption feature provides evidence that SN 2020cpg is not a standard Type Ib SNe but rather a Type Ib(II).

2.5.2 Model Comparisons

By comparing the spectra of SN 2020cpg with model spectra, insight can be gained on the potential elemental composition of the outer layers prior to explosion. [Teffs et al. \(2020\)](#) calculated a set of synthetic SE-SNe models based on a single mass progenitor, with varying degrees of H/He stripping that produces several Type Ic/Ib/Iib analogue

SNe. [Teffs et al. \(2020\)](#) estimated the energy of a set of well observed Type IIb SNe by comparing synthetic and observed spectra at pre-, near- and post-peak luminosities.

A similar method is applied in this work to SN 2020cpg. The pre- and near-peak spectra of SN 2020cpg are very blue and with few strong features. The early synthetic Type IIb-like spectra in [Teffs et al. \(2020\)](#) are typically redder due to a stronger amount of Fe-group elements mixing, producing strong line blocking in the near UV. As such, the conditions in which the early spectra of SN 2020cpg are produced are beyond the scope of this comparison and can be explored in future work.

First a comparison between two spectra at approximately +15 and +30 days after *B*-band maximum to the Type IIb model from [Teffs et al. \(2020\)](#) is given in Figure 2.10, where the red spectra include the non-thermal effects on hydrogen and the black do not. These non-thermal effects arise from the interactions with energetic electrons that are created by the scattering of gamma-rays released from the decay chain of ^{56}Ni and ^{56}Co , ([Lucy, 1991](#)). This Type IIb model has an ejecta mass of $\sim 5.7 M_{\odot}$, with $1.3 M_{\odot}$ of helium and $0.1 M_{\odot}$ of hydrogen. For the earlier spectrum at the top of Figure 2.10 and when focusing on the $\text{H}\alpha$ and He I features, the best fit spectra was found to be that of a 5 foe model that does not include the non-thermal effects on H, where 1 foe is 1×10^{51} erg. The inclusion of non-thermal hydrogen produces a deep and broader $\text{H}\alpha$ line that is not reflected in the spectrum of SN 2020cpg. In the second spectrum considered, it was found that the 3 foe explosion model matches the spectrum of SN 2020cpg at this late phase. At this lower energy and later phase, the $\text{H}\alpha$ line is more narrow and when the non-thermal effects of hydrogen are not included, the 6000 – 6500 Å region is well reproduced.

As SN 2020cpg has been designated both as a Type Ib and a Type IIb, the helium rich, but hydrogen free, Type Ib models at the same epochs were also compared in Figure 2.10. For this, the "best fit" models that do not consider the non-thermal effects of hydrogen as black lines are also included in Figure 2.10. For the earlier spectrum, the 3 foe Ib model does a reasonable job of reproducing the 6000 – 6500 Å region without requiring H, but the $\text{He I } \lambda 6678$ line is stronger than in the observed spectrum. For

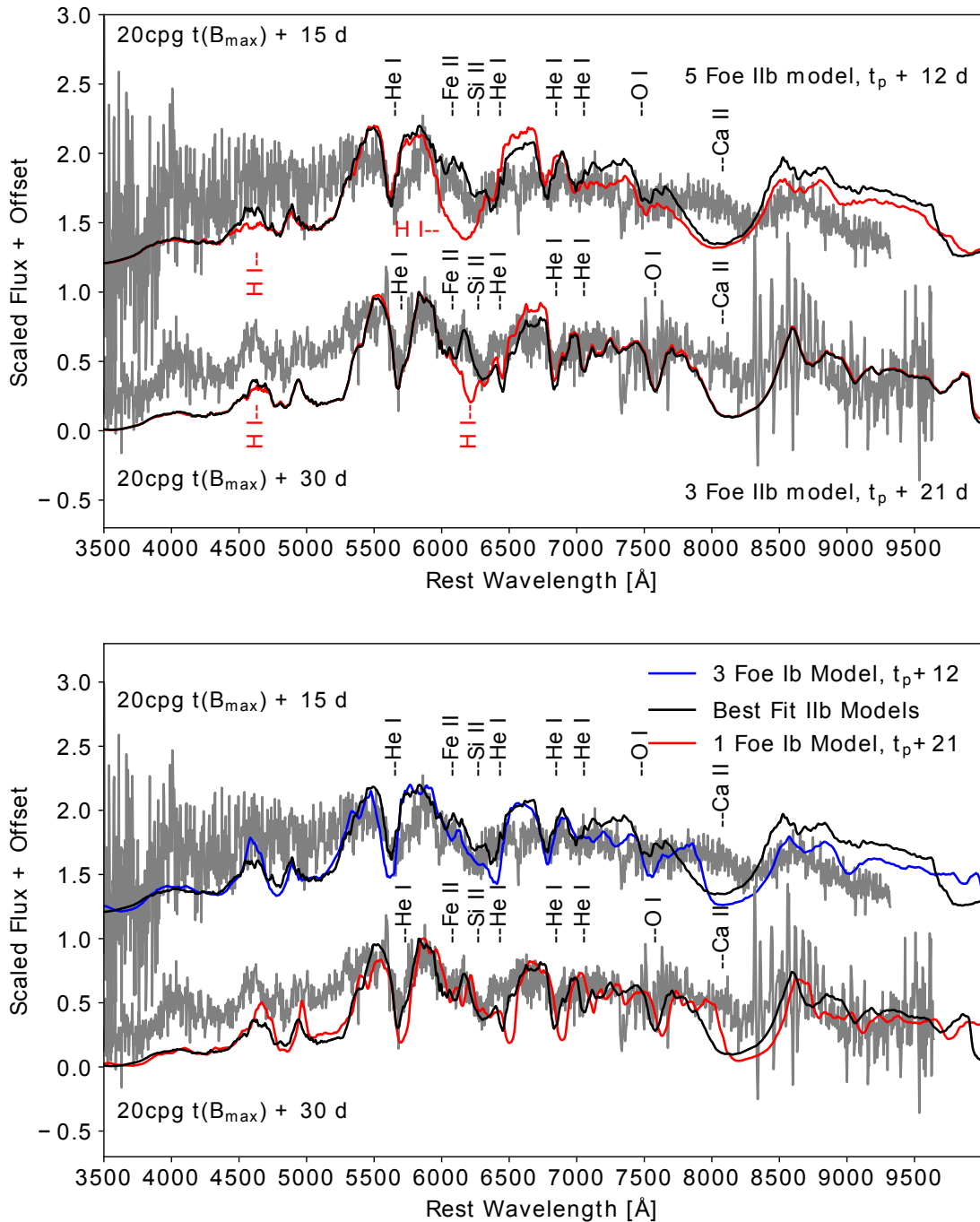


FIGURE 2.10: Top (a): Comparison of SN 2020cpg spectra with two different energy (3 and 5 foe) Type IIb models. Where t_p indicates the epoch of bolometric peak. The red model spectra include the non thermal effects of hydrogen while the black model spectra omit the non thermal effects. Both models include the non thermal effects on He. Several important contributing elements, in particular those near the $H\alpha$ line, are shown above their feature within the spectra. Bottom (b): SN 2020cpg spectra at +15 and +30 days from B -band maximum fit with a IIb-like model and with a Ib model with 3 foe of energy at a time of +12 days from t_p and 1 foe of energy at a time of +21 days respectively. The IIb model has an ejecta mass of $\approx 5.7 M_\odot$, with $1.3 M_\odot$ of helium and $0.1 M_\odot$ of hydrogen.

the later spectrum, the energy is reduced from the I Ib model again to 1 foe and also reproduces this 6000 – 6500 Å region.

From this modelling, several properties of the SN 2020cpg regarding its elemental composition can be inferred. The assumption that helium has non-thermal effects while hydrogen does not is unlikely to be physically viable. However, the mass of hydrogen in the I Ib model clearly produces too strong of an H α line. Not including any hydrogen in the model while maintaining a He-rich outer atmosphere results in strong He I λ 6678 and 7065 lines. The re-emission from the H α feature reduces the strength of the He I λ 6678 line while affecting the He I λ 7065 line less. The best fit I b models having low energy also suggests the He rich material is confined to lower velocities, such as those below a hydrogen rich shell as seen in the I Ib models. From the best fit models, a lower mass of hydrogen ($M_{\text{H}} < 0.1 M_{\odot}$) could result in a weaker H α feature but still produce enough re-emission to reproduce the 6000 – 6500 Å region in these late phases. A more detailed model would need to be calculated to derive a stronger estimate on the mass and distribution of H in SN 2020cpg.

At these two epochs, the photosphere has receded deep into the CO rich region of the ejecta as shown by the presence of the Ca II NIR triplet and the O I λ 7771. Early spectra of Type I Ib do not show these features as the abundances of these elements are lower in the H/He-rich shells. Both models are shown with (red line) and without (black line) the non thermal effects of hydrogen, but both include these effects on the helium. For the Type I Ib-like models at these epochs, the spectra that do not treat the non thermal effects of hydrogen, are better able to reproduce the observed spectral structure between 6000 – 6500 Å that would typically contain a strong H α feature. Due to the depth of the photosphere and the lack of a strong early H α feature, this suggests that the total H α mass is less than $0.1 M_{\odot}$, and that the distribution of the hydrogen is further out in the ejecta with respect to the photospheric velocity of the two epochs chosen.

The model shown at the top in Figure 2.10 is a 5 foe explosion, with the majority of the $0.1 M_{\odot}$ of hydrogen at velocities greater than $\approx 15000 \text{ km s}^{-1}$, while the 3 foe explosion in the lower model contains hydrogen at velocities greater than $\approx 12000 \text{ km s}^{-1}$. Both models favour both the estimated explosion energy from the Arnett fits in Section 2.4.2 and the

TABLE 2.6: SN parameters obtained from detailed hydrodynamic models and the resulting M_{ejc} and E_k for SN 2020cpg using the photospheric velocity obtained at the peak of the pseudo-bolometric light curve and the velocity at $t \sim 16$ days post explosion. The SNe are ordered by their types with the SNe with the least stripped progenitors at the top and most stripped at the bottom. Sources- 1: [Nomoto et al. \(1993\)](#), 2: [Mazzali et al. \(2002\)](#), 3: [Sauer et al. \(2006\)](#), 4: [Mazzali et al. \(2009\)](#), 5: [Tanaka et al. \(2008\)](#), 6: [Mazzali et al. \(2009\)](#), 7: [Mazzali et al. \(2017\)](#) a; rise time from the explosion to the pseudo-bolometric light curve peak b; width of pseudo-bolometric light curve taken from 0.25 mag below peak light c; photospheric velocity at epoch of peak light d; photospheric velocity at +16 days from explosion date (same epoch as when SN 2020cpg reached peak light).

SN	Type	M_{ejc} [M_{\odot}]	E_k [10^{51} erg]	Source	t (Lmax) _a [Days]	LC width _b [Days]	$v_{\text{ph}}(\text{max})_c$ [km s^{-1}]	2020cpg		2020cpg	
								M_{ejc} [M_{\odot}]	E_k [$\times 10^{51}$ erg]	M_{ejc} [M_{\odot}]	E_k [$\times 10^{51}$ erg]
03bg	IIb-Hyper	4.8 ± 0.5	5.0 ± 1.5	6	25.0 ± 2.0	34.0 ± 2.0	7000 ± 500	3.0 ± 1.0	11.0 ± 4.0	2.0 ± 1.0	4.0 ± 1.0
93J	IIb	3.7 ± 0.5	1.2 ± 0.1	1	19.0 ± 2.0	18.0 ± 2.0	7500 ± 100	7.0 ± 2.5	6.0 ± 1.0	5.0 ± 1.0	3.0 ± 1.0
08D	Ib	7.0 ± 0.5	6.0 ± 0.5	4	19.0 ± 2.0	24.0 ± 2.0	9500 ± 500	6.0 ± 2.0	9.0 ± 2.0	10000 ± 500	7.0 ± 1.0
08D	Ib	5.3 ± 1.0	6.0 ± 0.5	5	19.0 ± 2.0	24.0 ± 2.0	9500 ± 500	4.0 ± 2.0	9.0 ± 4.0	10000 ± 500	7.0 ± 3.0
04aw	Ic	4.0 ± 1.0	4.5 ± 1.5	7	16.0 ± 1.0	21.0 ± 2.0	11500 ± 500	4.0 ± 2.0	5.0 ± 2.0	11500 ± 500	5.0 ± 2.0
94I	Ic	1.2 ± 0.1	1.0 ± 0.5	3	12.0 ± 2.0	11.0 ± 2.0	10000 ± 500	4.5 ± 1.5	6.0 ± 3.0	9000 ± 1000	8.0 ± 5.0
02ap	Ic-BL	2.4 ± 1.2	4.0 ± 0.5	2	13.0 ± 2.0	18.0 ± 2.0	12500 ± 1250	3.0 ± 2.0	5.0 ± 1.0	9000 ± 100	12.0 ± 3.0

suggestion that some hydrogen is at high velocities. The He I $\lambda 6678$ line is relatively too strong for either epoch to match when non-thermal excitation of the hydrogen is not included. This suggests that a lower mass of hydrogen can still be responsible for some fraction of the 6000-6500 Å feature, likely coincident with Si II causing a re-emission of flux further redward, reducing the strength of the He I $\lambda 6678$ without affecting the He I $\lambda\lambda 5876, 7065$ and 7281 lines. However, for a full picture of how the hydrogen and helium are distributed and how much is present, a detailed stratified model would need to be produced, which is beyond the scope of this work.

2.5.3 Re-scaled Light curves

As mentioned in Section 2.3.2, the Arnett-like model is limited in its viability to obtain realistic ejecta mass and kinetic energy due to the assumption that the optical opacity is constant throughout the bolometric light curve and that the ejecta are optically thick. The problem with these assumptions is that helium is optically transparent at the temperatures reached surrounding the peak light phase of the light curve. In order to account for the effects of the helium layer on the ejecta mass and kinetic energy a detailed hydrodynamical model is required. However, this would not have been easily done with SN 2020cpg due to the lack of early time photometry and the low signal to noise ratio for the spectra. In order to estimate the physical parameters for SN 2020cpg equation 2.1 is transformed to obtain a ratio for the ejecta mass and kinetic energy between SN 2020cpg and other SE-SNe that have detailed hydrodynamical models:

$$\frac{E_{k1}}{E_{k2}} = \frac{\tau_{m1}^2 * v_{ph1}^3 * \kappa_1^{-1}}{\tau_{m2}^2 * v_{ph2}^3 * \kappa_2^{-1}}, \quad (2.2)$$

and

$$\frac{M_{ejc1}}{M_{ejc2}} = \frac{\tau_{m1}^2 * v_{ph1} * \kappa_1^{-2}}{\tau_{m2}^2 * v_{ph2} * \kappa_2^{-2}}. \quad (2.3)$$

Where τ_m is the diffusion time of the light curve, v_{ph} is the photospheric velocity at maximum light and κ is the optical opacity of the SN ejecta. Due to the difficulty

in determining κ it has been assumed that it evolves in a similar way for both SNe. This assumption holds strong for SNe of the same classification type due to the similar elemental structure between the two SNe and becomes weaker as different types of SN are compared to one another. However, as only SE-SNe are used to obtain the ejecta mass and kinetic energy of SN 2020cpg the problem that arises from the use of SNe with different opacities should be minimised.

Using this method SN 2020cpg is compared with SN 1993J (Nomoto et al., 1993), SN 1994I (Sauer et al., 2006), SN 2002ap (Mazzali et al., 2002), SN 2003bg (Mazzali et al., 2009), SN 2004aw (Mazzali et al., 2017) and SN 2008D (Mazzali et al., 2008; Tanaka et al., 2009), all SE-SNe that have undergone hydrodynamical modelling. Since several of the above SNe, including SN 2020cpg, lack early time photometric data, it was not always possible to determine τ_m . Instead the width of the pseudo-bolometric light curve taken from 0.25 mag below peak light is used as an alternative to τ_m . Due to the width of the light curve being influenced by both the ejecta mass and kinetic energy, as shown in equation 2.1, this allowed for a direct comparison between the widths of the light curves and physical properties of SN 2020cpg and the modelled SE-SNe. The details on photospheric velocity and light curve widths for each SN along with the M_{ejc} and E_k of SN 2020cpg given by equation 2.2 and equation 2.3 are shown in Table 2.6.

The physical parameters for SN 2020cpg were obtained using both the photospheric velocity at pseudo-bolometric peak, $v_{\text{ph}}(t = \text{max})$, for the individual SNe and the photospheric velocity at $t = 16$ days from the reported explosion date, $v_{\text{ph}}(t = 16)$. The $v_{\text{ph}}(t = \text{max})$ is used to break the degeneracy between the ejecta mass and the kinetic energy as it would be the velocity of the photosphere when all of the light has diffused through the ejecta. $v_{\text{ph}}(t = 16)$ was also used to compare the different SNe at the point when SN 2020cpg had reached maximum pseudo-bolometric light, allowing a direct comparison between SNe to be made. The values for the physical parameters obtained from comparisons with the hydrodynamical models are higher than those derived from using the Arnett-like model, as expected when comparing the Arnett-like model with hydrodynamical models. The main outlier in Table 2.6 is the properties predicted from

the SN 2003bg, a hypernova, which despite having a relatively high kinetic energy possessed a low photospheric velocity at pseudo-bolometric peak, resulting in a low ejecta mass and large kinetic energy.

There is a clear trend in the ejecta mass and kinetic energy obtained using the light curve comparison method which arises from the type of SN that SN 2020cpg is compared to, with the He-rich SE-SNe resulting in a generally larger values while the values obtained from He-poor SNe are noticeably lower. As SN 2020cpg is a He-rich SN, the physical parameters obtained from the Type Ib and Iib SNe are used to determine the values of the ejected mass, $M_{\text{ejc}} \sim 5.5 \pm 2.0 M_{\odot}$, and kinetic energy, $E_{\text{k}} \sim 9.0 \pm 3.0 \times 10^{51}$ erg, for SN 2020cpg. The value obtained using $v_{\text{ph}}(t = 16)$ for the ejecta mass was $\sim 4.0 \pm 1.5 M_{\odot}$ and a kinetic energy of $\sim 5.0 \pm 2.0 \times 10^{51}$ erg. It should be noted that the model given in PM13 is limited in scope and should not be expected to predict values of both M_{ejc} and E_{k} to a precision greater than $0.5 M_{\odot}$ and 1.0×10^{51} erg respectively. The values produced using $v_{\text{ph}}(t = \text{max})$ converge on the physical parameters with an average standard deviation of 1.85 while the $v_{\text{ph}}(t = 16)$ has an average standard deviation of 1.89. This suggests that using the photospheric velocity at pseudo-bolometric peak for each SN converge on a value better than the photospheric velocity at SN 2020cpg pseudo-bolometric peak. The values for the ejecta mass and kinetic energy produced by the light curve comparison are much higher than those predicted by the Arnett-like model, as expected due to the contribution of the helium envelope and the effect of having similar optical opacities. However, the ejecta mass derived from the light curve comparison method matches the value obtained by comparing the spectra of SN 2020cpg with the spectral models of [Teffs et al. \(2020\)](#), although the kinetic energy given by the modelling is lower than that predicted using the method from PM13.

The ejecta mass given by the spectral modelling and comparison with modelled SE-SNe has a value roughly double that given for Ib + Ib(II) and Iib + Iib(I) by [Prentice et al. \(2019\)](#) which take a mean value of $2.2 \pm 0.9 M_{\odot}$ and $2.7 \pm 1.0 M_{\odot}$ respectively. This places SN 2020cpg in the higher mass range of SE-SNe with only one H-rich and two H-poor SE-SNe having similar ejecta mass. The ejecta mass predicted by the Arnett-like model is closer to the mean values given by [Prentice & Mazzali \(2017\)](#) although still greater than the median, showing that by all standards SN 2020cpg was a more massive

event than the typical SE-SNe. The lower ejecta mass estimated by the Arnett-like model is expected, as this has been seen in several SNe such as SN 2008D which was estimated to have an ejecta mass of $2.9_{-0.6}^{+1.0} M_{\odot}$ from an Arnett-like approach (Lyman et al., 2016) and $\sim 5 - 7 M_{\odot}$ from hydrodynamic modelling (Mazzali et al., 2008; Tanaka et al., 2009). When compared to the ejecta masses of the H-rich SE-SNe, SN 2020cpg lies in the region that has been associated with an extended progenitor. As the ejecta mass obtained using the comparative method of PM13 and the spectral modelling of Teffs et al. (2020) are in close agreement, the light curve comparison method can be taken as a valid replacement for the Arnett-like model to obtain the ejecta mass when dealing with SE-SNe. This method will also improve in the future as more SE-SNe undergo hydrodynamical modelling.

From the light curve comparison method the derived kinetic energy takes a value of $\sim 9.0 \pm 3.0 \times 10^{51}$ erg which is greater than both the spectral modelling and the Arnett-like model. This kinetic energy place SN 2020cpg on the border of the Hypernovae, which are thought to have kinetic energies on the order of 10^{52} erg. The kinetic energy derived from spectral modelling tends towards a lower kinetic energy than the method described in PM13, however, larger than the kinetic energy estimated by the Arnett-like model which had a derived a kinetic energy of $\sim 2.9 \pm 0.9 \times 10^{51}$ erg. However, given the high ^{56}Ni mass the kinetic energy derived from the Arnett-like model is unlikely to be enough to synthesis the required amount of nickel.

From the derived ejecta mass, under the assumption that the progenitor did not collapse into a black hole but holds a $1.4 M_{\odot}$ neutron star, the progenitors core mass can be assumed to be $M_{\text{ejc}} + M_{\text{NS}} - M_{\text{outerenvelope}} = M_{\text{COcore}} \approx 6.0 \pm 2.0 M_{\odot}$. Here it has been assumed that the mass of the outer envelope was $\sim 1.5 M_{\odot}$. This core mass is just higher than the majority of SE-SNe investigated in Prentice & Mazzali (2017) which takes a mean value $< 5 M_{\odot}$. A core mass of $\sim 6.0 \pm 2.0 M_{\odot}$ is thought to originate from a progenitor with an initial mass of $18 - 25 M_{\odot}$, (Sukhbold et al., 2016).

As mentioned earlier with the Arnett-like model, the opacity for both SN 2020cpg and the comparison SN is neither constant nor the same. To this end, equation 2.1 is used to obtain an opacity for SN 2020cpg, which had a value of $\kappa_{\text{opt}} = 0.10 \pm 0.04 \text{ cm}^2 \text{ g}^{-1}$. The

TABLE 2.7: Opacities derived from the SN 2020cpg opacity. There seems to be a trend with the He-rich SNe having a lower opacity than the He-poor SNe.

SN	Type	Opacity [cm^2g^{-1}]
03bg	I Ib-Hyper	0.27 ± 0.19
93J	I Ib	0.06 ± 0.04
08D	I Ib	0.08 ± 0.06
08D	I Ib	0.13 ± 0.09
04aw	I Ic	0.13 ± 0.10
94I	I Ic	0.10 ± 0.08
02ap	I Ic-BL	0.19 ± 0.16

opacities of the other SE-SNe, obtained from the opacity of SN 2020cpg, shown in Table 2.7 are computed to determine the trends within the SE-SNe used in the comparison in this work and test the validity of the opacity determined for SN 2020cpg. As expected the He-rich SNe tend to have a lower opacity than the He-poor SNe, due to the fact that the helium present within the ejecta is virtually transparent to the optical photons. The opacity for SN 2008D has two values due to the different ejecta masses that was used. By looking at the opacities determined using the above method it is clear that a single time-independent value of the opacity should not be used for all types of SE-SNe, as done with the Arnett-like model discussed in Section 2.3.2.

2.6 Summary and Conclusions

The study of SN 2020cpg and the discovery of the weak hydrogen features within the otherwise SN Ib-like spectra shows formation channels between SNe Ib and IIb are not as rigid as previously thought. From the evolution of SN 2020cpg was compared to several other SE-SNe. Photometrically, SN 2020cpg looks very similar to the Type Ib SN 2009jf in peak luminosity, although the light curve of SN 2020cpg is slightly broader compared to SN 2009jf. Spectroscopically SN 2020cpg initially looked similar to the Type Ib SN, such as SN 2015ap, with the main difference being the presence of the weak $H\alpha$ feature within the spectra of SN 2020cpg. As the spectra evolve, the $H\alpha$ feature becomes more dominant until it rivals the $\text{He I } \lambda 5876$ feature in strength, making SN 2020cpg resemble more that of a Type IIb SN, such as SN 2011dh. Due to the weak $H\alpha$ feature that is shown within the spectra of SN 2020cpg a reclassification of SN 2020cpg to a Type Ib(II)

SN is suggested. The growing strength of the H α feature over time may be the result of a thin hydrogen envelope alongside mixing of hydrogen into the outer helium layers prior to explosion, which became more dominant as the photosphere receded through the mixed hydrogen/helium layer.

SN 2020cpg exploded producing an estimated Nickel mass of $\sim 0.3 \pm 0.1 M_{\odot}$ and from comparisons with hydrodynamic models of well studied He-rich SE-SNe an ejecta mass of $\sim 5.5 \pm 2.0 M_{\odot}$ and a kinetic energy of $\sim 9.0 \pm 3.0 \times 10^{51}$ erg. From spectral modelling the amount of helium expected within the ejecta is $1.3 M_{\odot}$ with a further $0.1 M_{\odot}$ of hydrogen contained within the outer envelope with a large majority of it existing above a velocity of $\approx 15000 \text{ km s}^{-1}$. From this modelling and the assumption that a neutron star remnant was formed, SN 2020cpg would have had a core mass of $M_{\text{core}} = 6.0 \pm 2.0 M_{\odot}$ which corresponds to a progenitor star with a initial mass of $M_{\text{ZAMS}} \sim 18 - 25 M_{\odot}$. Due to the distance to the host galaxy and the position of SN 2020cpg within the host galaxy, it is unlikely that there are any pre-explosion images of high enough quality to allow for the progenitor of SN 2020cpg to be determined. Further modelling of SN 2020cpg may give evidence for the progenitor however that is beyond the scope of this paper.

The use of the light curve comparison provides an alternative approach to the Arnett-like model in determining the ejecta mass and kinetic energy of new SE-SNe. This method accounts for the effects of the helium layer and the time dependency of the optical opacity, both of which are ignored in the Arnett-like approach. The method produces ejecta masses and kinetic energies that resemble those derived from comparison of optical spectra with spectral models, where as the Arnett-like approach seems to underestimate these values. Unlike the Arnett-like model, when used on SE-SNe the method described in PM13 requires several SNe of the same classification to constrain the ejecta mass and kinetic energy. This can lead to some outliers, like hypernovae, distorting the results. However as more SE-SNe undergo hydrodynamical modelling the constraining power of the light curve comparison method increase and the effect the outliers have is reduced. The results of the light curve comparison method for SN 2020cpg was tested by [Teffs et al. \(2022\)](#), whose spectral modelling found an ejecta mass of $\sim 7 \pm 2 M_{\odot}$ and a kinetic energy of $\sim 6 \pm 1 \times 10^{51}$ erg for SN 2020cpg. These values are in reasonable agreement with the parameters derived using the method from PM13 while showing

that the Arnett-like method clearly does not take into account the mass associated with the helium shell. The difference between the two methods arises from the use of both SNe I Ib and SNe I Ib in determining the ejecta mass and kinetic energy of SN 2020cpg. This clearly demonstrates the requirement to use SNe of similar classification when comparing the light curves of SE-SNe.

Chapter 3

The fast rising Type IIb SN 2020acat

3.1 Introduction

Transitioning away from the SNIb, as more and more hydrogen remains within the envelope of the SE-SNe progenitor, the SN transitions from a SNIb to a SNI Ib. The spectra of these events are dominated by predominantly hydrogen and helium during the photospheric phase, prior to transitioning to more SNIb-like spectra (Filippenko, 1997, 2000). These events bridge the gap between the H-rich SNI and the hydrogen-poor SE-SNe. Analysis of these events have suggested that there is a distinct difference between SNI and SE-SNe instead of a smooth continuum as the progenitor is stripped of its outer envelope (Pessi et al., 2019). The study of additional SNI Ib sheds light on the connection between SNI and SNI Ib.

In this chapter, the ultra violet (UV), optical and near infrared (NIR) observations of the Type IIb SN 2020acat are presented. Photometric coverage includes UV to NIR observations, while the spectra cover the optical observations. In Section 3.2, a discussion is had about the distance and reddening associated with the host galaxy of SN 2020acat, along with the explosion date. In Section 3.3, the acquisition of the UV to NIR photometric data and the spectral evolution of SN 2020acat are discussed. In Section 3.4, the analysis evolution of the UV - NIR photometric bands, along with the fast rising pseudo-bolometric light curve and the derived physical parameters of

SN 2020acat, as well as comparisons with other SNe I Ib are presented. Then, in Section 3.5, the spectroscopic evolution of SN 2020acat within the photospheric, transitional and early nebular phases are examined, alongside the line velocity evolution of the $H\alpha$, $H\beta$, He I 5867 and Fe II 5018. The optical spectra of SN 2020acat is compared with those of other well observed SNe I Ib. Then an analyse of the late time spectra and constraints are placed on the mass of oxygen synthesised by SN 2020acat. Finally, in Section 3.6, a summary of this analysis of SN 2020acat is given. The work presented in this chapter has been published in Medler et al. (2022). All work shown in this chapter was done by myself except obtaining and reducing the observations, details of which are given in Section 3.3, and the nebular phase spectral modelling which was done by Paolo Mazzali.

3.2 Host Galaxy and Explosion Date

SN 2020acat was discovered in the galaxy PGC037027 (Srivastav et al., 2020), a $W1 = 14.50 \pm 0.03$ mag galaxy (Cutri et al., 2013), at a redshift of $z = 0.007932 \pm 0.000150$. SN 2020acat was located 26.70" South and 19.90" West of galactic centre, at a projected distance of ~ 5.7 kpc. Figure 3.1 shows the location of SN 2020acat and the surrounding stars that were used for photometric calibration. Using the NASA/IPAC Extragalactic Database (NED ¹) default cosmology of $H_0 = 73.0 \pm 5 \text{ kms}^{-1}\text{Mpc}^{-1}$, $\Omega_{\text{matter}} = 0.27$ and $\Omega_{\text{vacc}} = 0.73$ (Spergel et al., 2007), the host galaxy distance was found to be 35.3 ± 4.4 Mpc, derived from the model based on the local velocity field given in Mould et al. (2000) using the terms for the influence of the Virgo Cluster, the Great Attractor and the Shapley Supercluster. The error associated with the distance modulus accounts for the error from the velocity field correction. An additional uncertainty on the distance is included relating to the low redshift of SN 2020acat, placing the host galaxy outside the Hubble flow regime. This uncertainty is on the order of 10% for SN 2020acat which arises from the peculiar velocity of the host galaxy and has been added in quadrature to the distance error. From the host galaxy distance, the implied distance modulus for SN 2020acat is $m - M = 32.74 \pm 0.27$ mag.

¹<https://ned.ipac.caltech.edu/>

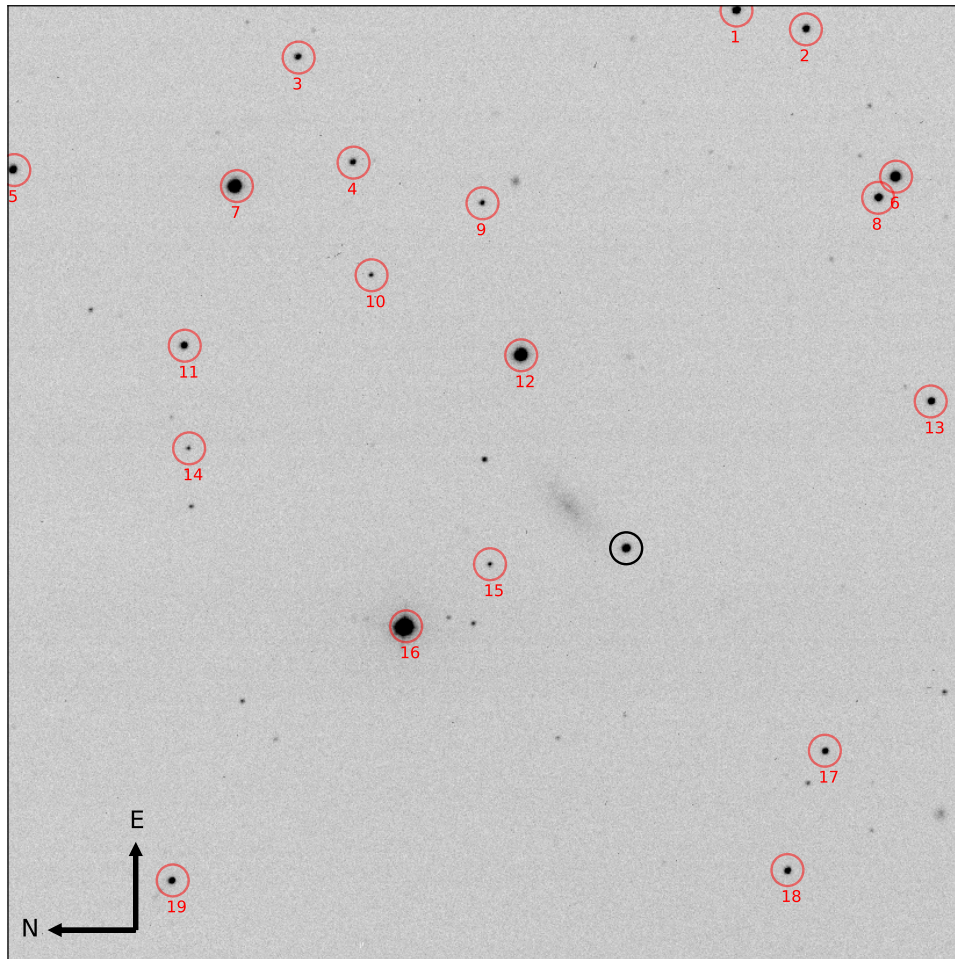


FIGURE 3.1: *ugriz* combined image of SN 2020acat (black) and surrounding standard stars (red), taken on 22/12/2020 during peak light using the Liverpool Telescope. The standard stars were used to calibrate the LT *ugriz* photometry.

The line of sight dust extinction of the host galaxy, $E(B - V)_{\text{host}}$, associated with SN 2020acat, is expected to be negligible. No strong, narrow interstellar Na I D lines were detected at the redshift of the host galaxy, see Section 3.5. This lack of strong Na I D lines, along with the position of SN 2020acat relative to its host galaxy, implies that $E(B - V)_{\text{host}}$ is negligible. The Milky Way (MW) extinction, $E(B - V)_{\text{MW}}$, takes a value of $E(B - V)_{\text{MW}} = 0.0207 \pm 0.0004$ mag, derived from the Schlafly & Finkbeiner (2011) dust map. Thus, the total extinction for SN 2020acat, $E(B - V)_{\text{tot}} = 0.0207 \pm 0.0004$ mag, is used throughout this work.

The first detection of SN 2020acat, taken on MJD = 59192.65 (09/12/20), occurred almost exactly two days after that last non-detection taken by the Asteroid Terrestrial-impact Last Alert System (ATLAS; Tonry et al., 2018; Smith et al., 2020) on MJD =

59190.61 (07/12/20). This last non-detection had a limiting magnitude of 19.33 mag in the ATLAS *o*-band, approximately ~ 0.78 mag dimmer than the initial observation. The last non-detection places a strong constraint on the explosion date and suggests that SN 2020acat was caught very early. From fitting the pseudo-bolometric light curve, see Section 3.4.3, an explosion date of $\text{MJD} = 59192.01 \pm 0.14$ was determined. This estimate is taken as the explosion date throughout this work.

3.3 Data Acquisition

3.3.1 Photometry

Photometry of SN 2020acat was obtained in the UV (*UVW2*, *UVM2*, *UVW1*, *u*, *U*), optical (*BgVriz*) and NIR (*JHK*) photometric bands, displayed in Figure 3.2 along with the ATLAS *c+o*-bands. SN 2020acat was initially detected by ATLAS on $\text{MJD} = 59192.65$ (09/12/20), and followed in the ATLAS *c + o*-bands for ~ 210 days. Additional optical follow-up of SN 2020acat in the *BgVriz*-bands was obtained from several telescopes over the campaign lasting ~ 230 days. These telescopes include the 2.0m Liverpool Telescope (LT; Steele et al., 2004), the 2.56m Nordic Optical Telescope with the Alhambra Faint Object Spectrograph and Camera (ALFOSC) and the 1.82m Copernico Asiago Telescope (CT) with AFOSC. Additional photometry was provided by the Palomar 1.2m Samuel Oschin telescope using the Zwicky Transient Facility camera (ZTF-cam; Bellm et al., 2018), the 67/92 cm Schmidt telescope at the Cima Ekar Observing Station and several telescopes as part of the Las Cumbres Observatory (Las Cumbres; Brown et al., 2013) through the Global Supernova Project (GSP Howell, 2019). All data reduction was done by automatic pipelines associated with each telescope group, with photometric magnitudes obtained through Point Spread Function (PSF) photometry. UV photometry of SN2020acat was obtained by the Neil Gehrels *Swift* Observatory (*SWIFT*; Roming et al., 2005) between 11/12/20 and 28/04/21. The UVOT data were reduced using the standard pipeline available in the HEASoft software package ² using the latest version of CALDB. Observation of every epoch was conducted using one or several orbits. To

²<https://heasarc.nasa.gov/lheasoft/>

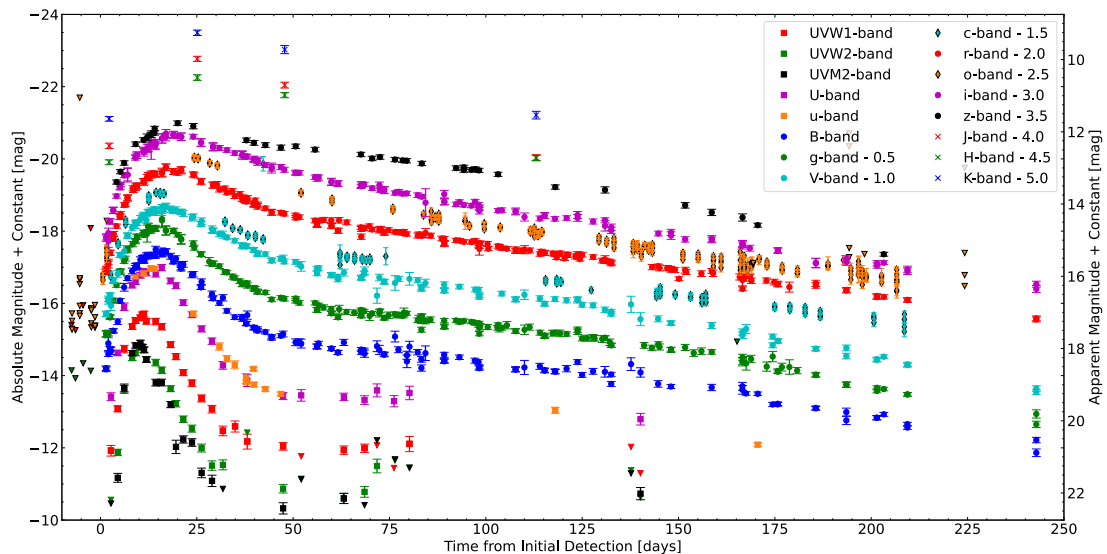


FIGURE 3.2: UV to NIR photometric observations of SN 2020acat, with phase relative to explosion date (MJD= 59192.01) and given in the rest frame. Each photometric band is given a marker signifying its location on the electromagnetic spectrum; UV = square, Optical = circle, and NIR = crosses. All photometric band limits are given by the solid triangles, with optical band limits having black outlines. Additionally, the ATLAS bands are given by the coloured diamonds with the black outline and are separate from the other optical bands due to the broad nature of the ATLAS filters.

improve the signal-to-noise ratio of the observation in a given band in a particular epoch, all orbit-date were co-added for that corresponding epoch using the HEASoft routine `uvotimsum`. The routine `uvotdetect` was also used to determine the correct position of the transient (which is consistent with the ground-based optical observations) and used the routine `uvotsource` to measure the apparent magnitude of SN 2020acat by performing aperture photometry. For source extraction a small aperture of radius 3.5'' was used, while an aperture of radius 100'' have been used to determine the background. The SN is located at the outskirts of its host, implying a negligible host contribution in the NUV bands. Moreover, as a small aperture has been used to extract the flux at the SN location, considerable host contribution is also not expected in the *SWIFT* optical ('U,B,V') bands. The NIR photometry was obtained by the 2.56m Nordic Optical Telescope (NOT; Djupvik & Andersen, 2010) equipped with NOTCAM through the NOT Unbiased Transient Survey 2 (NUTS2) and the 3.58m New Technology Telescope (NTT; Wilson, 1983) through the ESO Spectroscopic Survey for Transient Objects (ePESSTO+; Smartt et al., 2015) with SOFI (Moorwood et al., 1998).

All photometry have been corrected for reddening, although host galaxy image subtractions were not performed. The host galaxy of SN 2020acat lacked UV and optical observations prior to SN 2020acat making host subtraction not possible until after SN 2020acat has fully faded. However, this lack of host galaxy subtractions is not expected to affect the photometry of SN 2020acat due to its distance from galactic centre. The SWIFT photometry can be found in Table D1 while the LCO data is in Table E1, the data taken by the LT in Table H1. The Johnson-Cousin and SDSS band data from the AFOSC, ALFOSC, and Morivan instruments are in Table I1 and J1 respectively. Finally, the NIR photometry is given in Table K1.

3.3.2 Spectroscopy

SN 2020acat was classified as a Type I Ib SN on MJD = 59193.31 (10/12/2020) (Pessi et al., 2020) using the spectrum obtained by ePESSTO+ using the ESO Faint Object Spectrograph and Camera (EFOSC2; Buzzoni et al., 1984) mounted on the NTT. The classification spectrum was obtained ~ 1.3 days after the explosion. Further optical spectroscopic observations of SN 2020acat were obtained from ePESSTO+ using EFOSC2 with the NTT. Spectroscopic observations from ePESSTO+ were obtained with the blue grism, gr11 (3380 – 7520Å), and the red grism, gr16 (6015 – 10320Å). These EFOSC2 spectra were combined to form a single spectrum at each epoch with full optical coverage. Several additional spectra were obtained during the evolution of SN 2020acat using the Spectrograph for the Rapid Acquisition of Transients (SPRAT; Piascik et al., 2014) mounted on the LT, the Supernova Integral Field Spectrograph (SNIFS; Lantz et al., 2004) camera mounted on the Hawaii based UH88 telescope and via the NUTS2 programme using the ALFOSC mounted on NOT using grism 4. Further spectra were obtained through Las Cumbres using the FLOYDS spectrographs mounted on the 2 m Faulkes Telescope South (FTS) and the 2 m Faulkes Telescope North (FTN), based at the Siding Spring Observatory (COJ) and the Haleakala Observatory (OGG), respectively. Spectra were also obtained using the 1.82m Copernico telescope using AFOSC, with both the VPH7 and VPH6 gratings. All spectra were reduced in the standard procedure for each telescope. The spectroscopic follow-up campaign lasted for ~ 230 days before

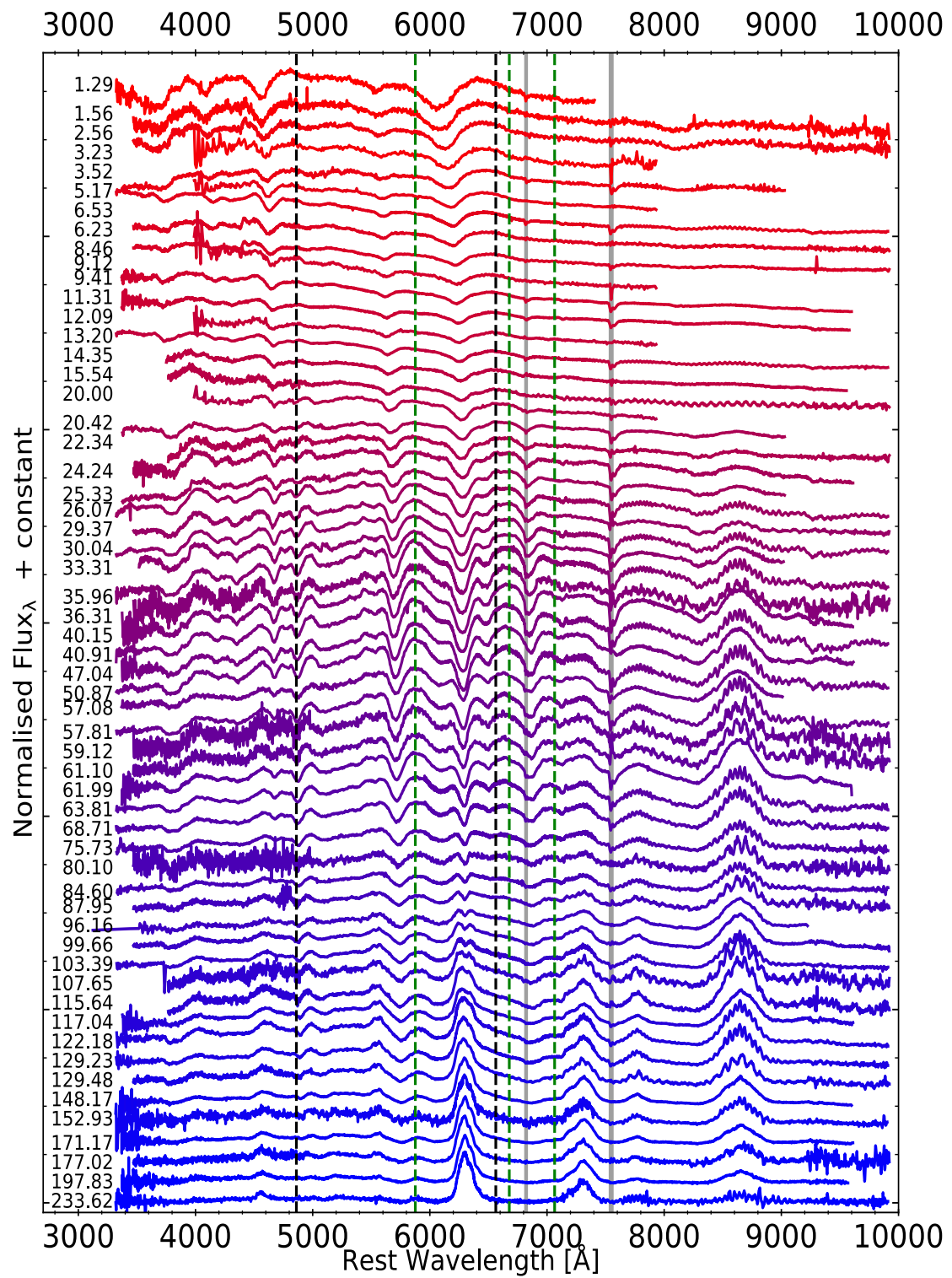


FIGURE 3.3: Spectroscopic evolution of SN 2020acat. Flux is normalised to H α feature or peak of the O I $\lambda\lambda$ 6300, 6363 feature depending on what was stronger at the time of observation. See Table 3.1 and Table 3.2 for the details on each spectrum. The phase of spectra is given on the left hand side. Both the hydrogen (black) and main optical helium (green) lines are given by the dashed lines at their rest wavelength, along with the telluric features which are denoted by the grey regions.

TABLE 3.1: Information on spectroscopic follow-up campaign for SN 2020acat. The epochs are relative to the explosion date (MJD = 59192.01) and are given in the rest frame. Wavelength range is also given in rest frame.

- a : Telescope and instrument;
 1. NTT = NTT using EFOSC2
 2. LasC = α : FTS using FLOYDS, β : FTN using FLOYDS
 3. LT = LT using SPRAT
 4. NOT = NOT using ALFOSC
 5. UH88 = UH88 using SNIFS
 6. ASI = CT using AFOSC

Spectrum	Epoch [days]	Observation date [UT]	Telescope ^{a}	Range [Å]
1	1.29	07:21:47 10/12/20	NTT	3323 - 7406
2	1.56	13:56:22 10/12/20	LasC _{α}	3470 - 9921
3	2.56	14:13:23 11/12/20	LasC _{α}	3470 - 9922
4	3.23	06:20:02 12/12/20	LT	3988 - 7931
5	3.52	13:23:36 12/12/20	UH88	3376 - 9028
6	5.17	05:20:31 14/12/20	LT	3988 - 7931
7	6.23	06:59:30 15/12/20	NTT	3323 - 9910
8	6.53	14:12:06 15/12/20	LasC _{α}	3471 - 9921
9	8.46	12:54:15 17/12/20	LasC _{α}	3470 - 9921
10	9.12	04:51:08 18/12/20	LT	3988 - 7931
11	9.41	11:53:10 18/12/20	NOT	3370 - 9600
12	11.31	09:51:05 20/12/20	NOT	3371 - 9580
13	12.09	04:47:46 21/12/20	LT	3988 - 7931
14	13.20	07:34:23 22/12/20	NTT	3323 - 9910
15	14.35	11:25:59 23/12/20	NOT	3751 - 9556
16	15.54	16:06:27 24/12/20	LasC _{β}	3769 - 9922
17	20.00	03:57:18 29/12/20	LT	3988 - 7931
18	20.42	14:18:10 29/12/20	UH88	3376 - 9028
19	22.33	12:35:17 31/12/20	LasC _{α}	3767 - 9922
20	24.24	10:30:45 02/01/21	NOT	3473 - 9612
21	25.33	12:54:04 03/01/21	UH88	3376 - 9028
22	26.07	06:54:28 04/01/21	NTT	3323 - 9910
23	29.38	14:46:34 07/01/21	LasC _{α}	3471 - 9921
24	30.04	06:56:26 08/01/21	NTT	3323 - 9910
25	33.31	13:54:24 11/01/21	UH88	3518 - 9019
26	35.96	06:05:24 14/01/21	NTT	3323 - 9910
27	36.31	14:31:12 14/01/21	LasC _{β}	3471 - 9922

TABLE 3.2: Continuation of spectral information from Table 3.1.

Spectrum	Epoch [<i>days</i>]	Observation date [<i>UT</i>]	Telescope ^{<i>a</i>}	Range [\AA]
28	40.15	11:34:23 18/01/21	ASI	3374 - 9610
29	40.91	05:54:07 19/01/21	NTT	3323 - 9910
30	47.04	10:09:25 25/01/21	NOT	3372 - 9615
31	50.87	06:53:36 29/01/21	NTT	3325 - 9911
32	57.08	12:59:24 04/02/21	UH88	3369 - 9010
33	57.81	06:40:43 05/02/21	NTT	3325 - 9912
34	59.12	14:29:24 06/02/21	LasC $_{\beta}$	3471 - 9921
35	61.10	14:11:41 08/02/21	LasC $_{\beta}$	3469 - 9922
36	61.99	11:50:35 09/02/21	NOT	3371 - 9601
37	63.81	07:52:36 11/02/21	NTT	3325 - 9911
38	68.71	06:16:37 16/02/21	NTT	3323 - 9910
39	75.73	08:17:39 23/02/21	NTT	3327 - 9911
40	80.09	17:49:21 27/02/21	LasC $_{\beta}$	3470 - 9921
41	84.60	06:41:28 04/03/21	NTT	3331 - 9911
42	87.95	15:46:53 07/03/21	LasC $_{\beta}$	3471 - 9920
43	96.16	10:15:06 16/03/21	ASI	3124 - 9224
44	99.66	11:03:20 19/03/21	LasC $_{\alpha}$	3470 - 9921
45	103.39	05:12:08 23/03/21	NTT	3327 - 9911
46	107.65	12:14:05 27/03/21	LasC $_{\beta}$	3767 - 9922
47	115.64	13:37:24 04/04/21	LasC $_{\beta}$	3768 - 9922
48	117.04	23:23:00 05/04/21	NOT	3376 - 9611
49	122.18	03:45:14 11/04/21	NTT	3327 - 9911
50	129.23	06:23:16 18/04/21	NTT	3323 - 9910
51	129.48	12:24:11 18/04/21	LasC $_{\beta}$	3470 - 9922
52	148.17	08:26:10 07/05/21	NOT	3370 - 9600
53	152.93	03:40:55 12/05/21	NTT	3318 - 9904
54	171.17	12:54:07 30/05/21	NOT	3373 - 9611
55	177.03	10:27:00 05/06/21	LasC $_{\beta}$	3471 - 9922
56	197.83	09:42:37 26/06/21	NOT	3373 - 9569
57	233.62	11:30:24 01/08/21	NTT	3319 - 9910

SN 2020acat was no longer observable. The spectroscopic evolution of SN 2020acat is shown in Figure 3.3, with the details on the spectroscopic observations given in Table 3.1 and Table 3.2.

3.4 Photometry Analysis

3.4.1 UV to NIR Light Curves

The UV bands of SN 2020acat were only followed for ~ 135 days before becoming too dim to observe. While the optical bands were followed for a total of ~ 250 days, with the NIR bands being observed a few times throughout the follow-up campaign. The rise of the UV and optical light curves was observed with a fast cadence. The close proximity of initial observation and the last non-detection, along with the depth of the limit in the ATLAS o -band, argues against the possibility of a long duration shock-cooling phase occurring prior to the observe rise, such as those seen in SN 1993J (Lewis et al., 1994), SN 2011dh (Arcavi et al., 2011) or SN 2016gkg (Arcavi et al., 2017). The lack of a long duration shock-cooling tail was also confirmed by the UV bands, which commonly show the cooling tail if it is indeed present. The UV bands of SN 2020acat, first observed ~ 2.5 days after the estimated explosion date, lack any deviation from the fast rise seen in the other redder bands, strongly implying a lack an extended shock-cooling tail.

The peaks of all but the NIR bands were well observed, allowing constraints to be placed on the epoch of maximum brightness and the value for peak magnitude in each band. The epoch of peak brightness in each band, t_{peak} , along with the rise time, peak apparent and absolute magnitudes are given in Table 3.3. The values of t_{peak} were determined by fitting a cubic spline to the each bands light curves around peak time. The error associated with the peak time is a combination of the error from the explosion date and the fitting of the cube spline. Unfortunately, the reduced number of observations in z -band around maximum light resulted in the value of t_{peak} having a greater error than the other bands. It should be noted that, due to the lack of any JHK -band data around

TABLE 3.3: Peak time, rise times, and both apparent and absolute peak magnitudes for the UV-optical photometry bands for SN 2020acat. The rise times are given in rest frame. The NIR bands (*JHK*) have insufficient data around peak and are excluded.

band	t_{peak} [<i>MJD</i>]	Rise time (t_r) [<i>days</i>]	m_{peak} [<i>mag</i>]	M_{peak} [<i>mag</i>]
<i>UVW2</i>	59202.20 ± 0.64	10.19 ± 0.40	18.20 ± 0.03	-14.72 ± 0.05
<i>UVM2</i>	59202.36 ± 0.64	10.35 ± 0.40	18.09 ± 0.04	-14.84 ± 0.05
<i>UVW1</i>	59203.54 ± 0.66	11.53 ± 0.42	17.32 ± 0.03	-15.64 ± 0.06
<i>u</i>	59204.77 ± 0.47	12.76 ± 0.20	15.89 ± 0.02	-16.95 ± 0.04
<i>U</i>	59204.88 ± 0.66	12.87 ± 0.41	15.83 ± 0.02	-17.01 ± 0.06
<i>B</i>	59207.19 ± 0.88	15.18 ± 0.75	15.42 ± 0.04	-17.40 ± 0.11
<i>g</i>	59208.06 ± 0.92	16.05 ± 0.82	15.16 ± 0.01	-17.65 ± 0.12
<i>V</i>	59208.65 ± 0.85	16.64 ± 0.71	15.18 ± 0.01	-17.62 ± 0.11
<i>r</i>	59210.20 ± 0.88	18.19 ± 0.75	15.09 ± 0.01	-17.70 ± 0.12
<i>i</i>	59212.17 ± 1.10	20.16 ± 1.18	15.14 ± 0.01	-17.64 ± 0.11
<i>z</i>	59213.09 ± 1.53	21.08 ± 2.29	15.23 ± 0.05	-17.44 ± 0.05

peak time, a spline could not be fitted without placing an extremely large uncertainty to the epochs of maximum light.

SN 2020acat has an incredibly fast rise time for a SNe IIb, with the UV bands peaking in ~ 10 days, while the optical bands peaking in $\sim 14 - 22$ days. This is faster than the average SNe IIb which reaches a peak in the UV bands in $\gtrsim 15$ days, with the optical bands reach peak in $\gtrsim 20$ days, as seen with SN 2008ax (Romíng et al., 2009) and SN 2011dh (Marion et al., 2014). The UV bands also display a very fast decline once they reach peak light, with an average decline in magnitude over the first 15 days from peak brightness, Δm_{15} , of $\Delta m_{15}^{UV} = 2.35 \pm 0.04$ mag. While the average Δm_{15} for the optical bands was $\Delta m_{15}^{opt} = 0.77 \pm 0.24$ mag, suggesting that the ejecta of SN 2020acat rapidly expanded and cooled scattering the light to lower energy bands. When compared to the Δm_{15} of 10 SNe IIb, with an average optical band decline of $\Delta m_{15}^{opt} = 0.92 \pm 0.22$ mag (Taddia et al., 2018), SN 2020acat declined in brightness at a slightly slower rate remaining brighter for longer. The *B*-band of SN 2020acat had a rise time of $B_{tr} = 15.18 \pm 0.75$ days, roughly 4 days faster than for SN 1993J ($B_{tr} = 18.97$ days, Richmond et al., 1994), SN 2008ax ($B_{tr} = 18.9$ days, Pastorello et al., 2008), SN 2011dh ($B_{tr} = 19.6$ days, Sahu et al., 2013) and SN 2011fu ($B_{tr} = 23.23$ days, Kumar et al., 2013). Interestingly, the *B*-band rise time of SN 2020acat lies between the B_{tr} values of Type II SNe (SNe II) ($B_{tr} = 8.3 \pm 2.0$

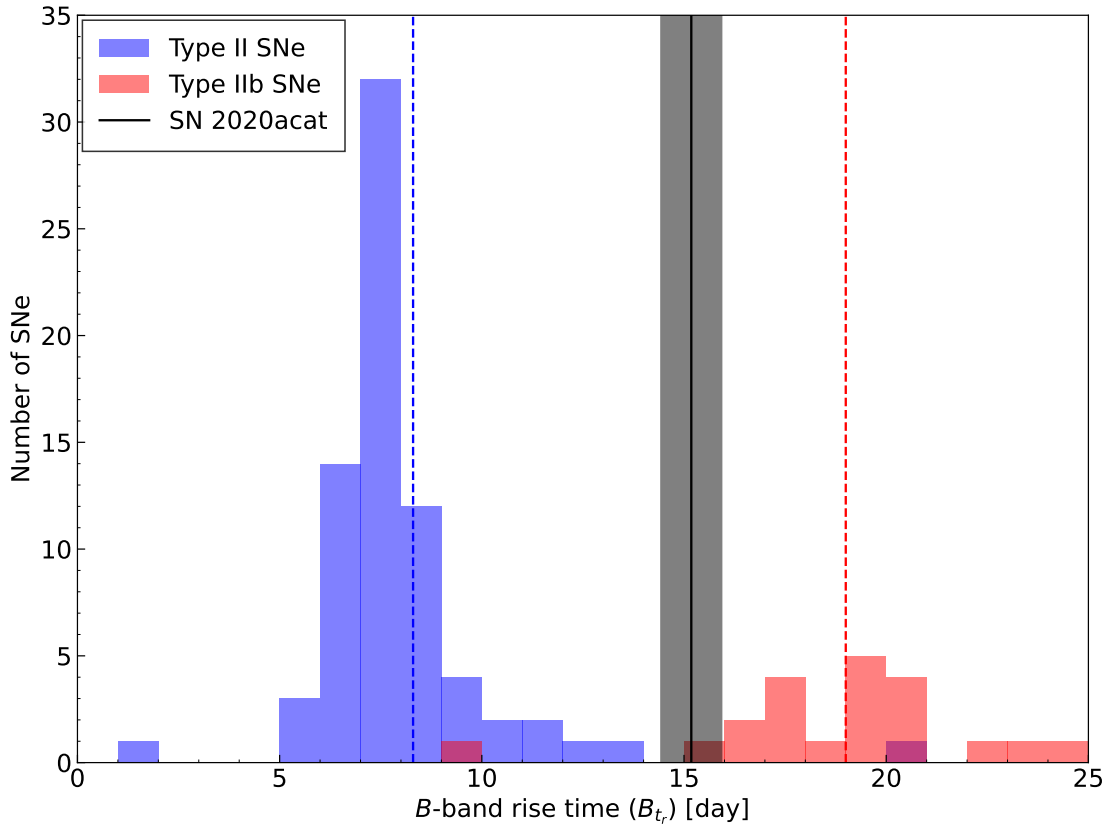


FIGURE 3.4: Comparison of the B -band rise time of SN 2020acat (black line, shaded region indicated uncertainty in rise time) to the rise time of several SNe II (blue) and SNe IIb (red). All rise times are given in rest frame. The B -band rise times are taken from Pessi et al. (2019). Dashed vertical lines indicated the average B -band rise times for each group.

days) and SNe IIb ($B_{tr} = 19.0 \pm 1.8$ days) found by Pessi et al. (2019) shown in Figure 3.4, suggesting that SN 2020acat was an outlier in hydrogen rich SE-SNe group and may have been a transitional event between the standard SNe II and the SNe IIb. The short rise time also places a strong constraint on the existence of any possible shock-cooling tail, a feature associated with progenitors that lack an extended radii, as was seen with hydrodynamical models (Bersten et al., 2012).

3.4.2 Colour Evolution

The $(UVW2 - V)$, $(UVM2 - V)$, $(UVW1 - V)$, $(U - B)$, $(B - V)$, $(g - r)$ ($r - i$) and $(i - z)$ colours of SN 2020acat are given in Figure 3.5. For the $(U - B)$ evolution, additional data was added using the $(u - g)$ and $(B - V)$ colours which forms a relation

with $(U - B)$, as given by [Jordi et al. \(2006\)](#), of;

$$(U - B) = \frac{(u - g) - (0.770 \pm 0.05)(B - V) - (0.72 \pm 0.04)}{(0.75 \pm 0.05)}. \quad (3.1)$$

It should be noted that equation 3.1 makes use of stellar colours to determine the relation parameters between the U and B -bands. However, when the colours derived from equation 3.1 were compared to the values of $(U - B)$ obtained from photometry there was little appreciable difference between the derived colour evolutions.

The colours obtained from the UV and optical photometry of SN 2020acat were all fit with a combination of a Gaussian function, to follow the initial decline and rise seen within the first few weeks, and a linear decay function, which fits to the late time colour decline and assumes a constant decline after the initial red peak around day ~ 35 . The evolution function is shown as a solid black line in Figure 3.5. Other SNe were not fit with the evolution function as they either did not follow the initial decline seen in SN 2020acat or lacked enough photometric data to fit the evolution function.

Initially, the colours of SN 2020acat start relatively red and rapidly become bluer within the first two weeks, reaching minima at around day $\sim 10 - 15$. After this blue minima, the colours evolve redward until they peak at $\sim 35 - 45$ days. The fast reddening seen during the weeks after the blue minima results from the cooling of the expanding ejecta and the shift in the peak of the blackbody emission to the redder bands. The reddening is also a result of line blanketing brought about by iron-group elements within the inner ejecta. Once the red peak is reached, all colours slowly decline over the next ~ 135 days. This decline is expected as the ejecta became optically thin after ~ 40 days allowing for trapped photons to escape the inner ejecta. The $(U - B)$ colour declines at a much faster rate, ~ 0.007 mag/day, compared to the other colours, with the $(B - V)$, $(g - r)$ and $(r - i)$ having a decline of ~ 0.004 , ~ 0.002 and ~ 0.003 mag per day, respectively. While the $(U - B)$ and $(B - V)$ colours follow a smooth decline at the late time ($t > 150$ days), both the $(g - r)$ and $(r - i)$ colours diverge from a linear decline. The $(g - r)$ colour starts to rapidly grow redder, while the $(r - i)$ colour evolution seems to rise at a slower pace. At this time, the effect of blackbody radiation has fully faded from the colour evolution and the reddening effect seen in both the $(g - r)$ and $(r - i)$ colours is likely

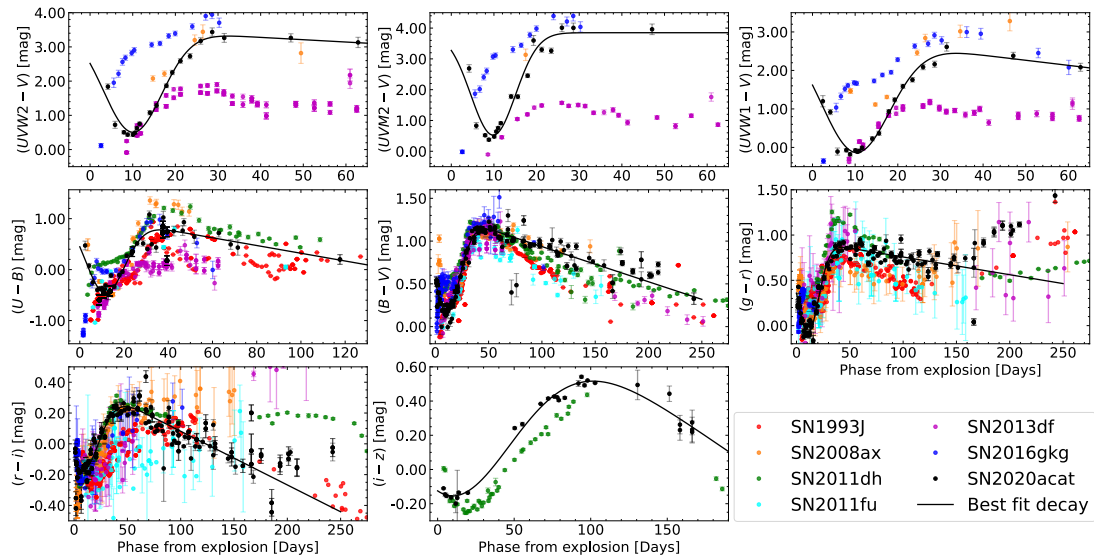


FIGURE 3.5: The $(UVW2-V)$, $(UVM2-V)$, $(UVW1-V)$, $(U-B)$, $(B-V)$, $(g-r)$, $(r-i)$ and $(i-z)$ colours of SN 2020acat (black) compared to the colours of SN 1993J (red), SN 2008ax (orange), SN 2011dh (green), SN 2011fu (cyan), SN 2013df (magenta), SN 2016gkg (blue). The colours of SN 2020acat were fit with a decay function (black line) which assumes a linear decline at late times, $\geq 35 - 45$ days. All SNe colours are given in the rest frame.

brought about by the emergence of the oxygen $\lambda\lambda 6300, 6363$ and calcium $\lambda\lambda 7292, 7324$ lines that dominate the spectra at this epoch. These emission lines roughly correspond to the central wavelengths of the r and i -band and dominate the contribution to the total flux in each band, thus drastically increasing the strength of these bands relative to the other photometric bands.

The multi-band colour evolution of SN 2020acat is compared to those of SN 1993J (Richmond et al., 1994; Barbon et al., 1995; Richmond et al., 1996), SN 2008ax (Pastorello et al., 2008; Tsvetkov et al., 2009; Taubenberger et al., 2011), SN 2011dh (Tsvetkov et al., 2012; Sahu et al., 2013; Brown et al., 2014; Ergon et al., 2014) and SN 2016gkg (Brown et al., 2014; Arcavi et al., 2017; Bersten et al., 2018). These SNe I Ib were chosen as comparison objects for SN 2020acat as they all possess comprehensive photometric and spectroscopic data around peak time, as well as into the late time when the hydrogen features have faded. The thoroughly documented nature of these events mean they have well known properties, allowing a comprehensive comparison between the results obtained from the Arnett-like model described below and the literature values. This is used as a test to validate the model used and thus the results obtained for SN 2020acat.

The colour evolutions of these SNe I Ib are also given in Figure 3.5, with details on each SN I Ib given in Table 3.4. For several SNe only Johnson-Cousins photometric bands were available for the redder (r to i) bands, such as SN 1993J. For these SNe a conversion to Sloan Digital Sky Survey (SDSS) red bands was done using equation 3.2 and 3.3 also from Jordi et al. (2006),

$$(g - r) = (1.646 \pm 0.008)(V - R) - (0.139 \pm 0.004), \quad (3.2)$$

and

$$(r - i) = (1.007 \pm 0.005)(R - I) - (0.236 \pm 0.003). \quad (3.3)$$

As with equation 3.1, it should be noted that the colours derived from equation 3.2 and equation 3.3 make use of stellar colours and should be taken as a way of obtaining the trend seen in the colour evolution for SNe that lack SDSS photometric bands.

While a comprehensive comparison of the colour evolution's of SN 2020acat can be done with the majority of the optical bands, the same cannot be said for the UV colours and the ($i - z$) evolution. This is due to the lack of UV and z -band data for several of these SN. The colour evolution of SN 2020acat initially follows the same trend as SN 2008ax, displaying an initial decline to a bluer colour before rising to a red peak within ~ 4 weeks of the explosion. This is expected for SNe that lack detection of a strong shock-cooling tail which is show as an initial very blue colour before becoming redder, such as SN 1993J. After the red maximum at ~ 4 weeks post-explosion, the colours of SN 2020acat follow the shape of SN 1993J and SN 2011dh, which both display a decline for several months before changing slope, although the rate of decline of SN 2020acat is much slower than the other SNe. At around $\sim 140 - 150$ days after explosion several SNe, including SN 2020acat, diverge from a linear decay in the ($g - r$) and ($r - i$) bands. The ($g - r$) colour of SN 2008ax also displays this increase, although the rise is at a much slower pace compared to both SN 1993J and SN 2020acat. The ($r - i$) colour evolution of SN 2020acat is quite similar to both SN 1993J and SN2011fu in the decline phase. Interestingly, the shape of the ($i - z$) colour evolution of SN 2020acat is very similar to

TABLE 3.4: Details for the SNe I Ib that are compared with SN 2020acat.

Sources: 1. Richmond et al. (1994), 2. Barbon et al. (1995), 3. Richmond et al. (1996), 4. Pastorello et al. (2008), 5. Tsvetkov et al. (2009) 6. Tsvetkov et al. (2012), 7. Sahu et al. (2013), 8. Kumar et al. (2013), 9. Brown et al. (2014), 10. Morales-Garoffolo et al. (2014b), 11. Van Dyk et al. (2014), 12. Arcavi et al. (2017), 13. Bersten et al. (2018).

SN	Explosion date [MJD]	Redshift	Distance [Mpc]	$E(B - V)_{\text{MW}}$ [mag]	$E(B - V)_{\text{Host}}$ [mag]	Source
1993J	49072.0	-0.00113	2.9	0.069	0.11	1,2,3
2008ax	54528.8	0.00456	20.25	0.022	0.278	4,5
2011dh	55712.5	0.001638	7.80	0.035	0.05	6,7,9
2011fu	55824.5	0.001845	74.5	0.068	0.035	8
2013df	56447.8	0.00239	21.4	0.017	0.081	10, 11
2016gkg	57651.2	0.0049	21.8	0.0166	0.09	12,13
2020acat	59192.01	0.007932	35.32	0.0207	-	-

that of SN 2011dh, despite the clear differences seen in the bluer colours. Although the overall ($i - z$) colour of SN 2020acat is redder than that of SN 2011dh and reaches the blue minima ~ 10 days before SN 2011dh.

3.4.3 Bolometric light curve

A pseudo-bolometric light curve was constructed using the UV - NIR photometric bands in order to obtain the physical parameters of SN 2020acat. The pseudo-bolometric light curve was constructed by integrating the flux of the UV - NIR bands and applying a blackbody correction. During epochs where NIR bands are missing, the magnitude is obtained by interpolating the points using a polynomial fit. Blackbody corrections were calculated by fitting the available spectral energy distribution (SED) with a blackbody function and extrapolating the blackbody function fit to the available bands out to the extremes of the UV and NIR regions when necessary. The coverage of both the UV and NIR regions during the photospheric phase is comprehensive enough to not require the extrapolation as any missing epochs can be obtained through interpolation of the available observations. However, at later times, especially once the UV bands becomes too dim for observations, this blackbody extrapolation is required to account for the missing bands. The blackbody extrapolation at late time is more heavily influenced by the evolution of the NIR light curve than the UV due to the lower temperature of the ejecta at this phase shifting the peak of the blackbody emission to longer wavelengths resulting in a smaller contribution from the UV. At this late phase the NIR light curves are expected

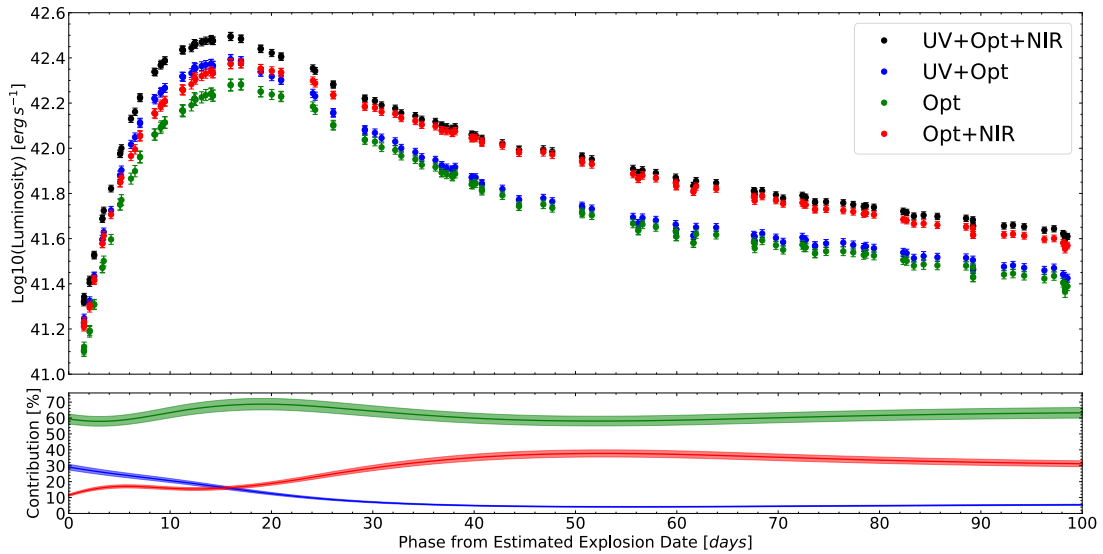


FIGURE 3.6: (Top) The Pseudo-bolometric light curve of SN 2020acat, along with the light curves constructed using the UV+optical, just optical and optical+NIR photometry. (Bottom) The contribution of the individual electromagnetic regions as a percentage of the pseudo-bolometric light curve, with UV = blue, Optical = green and NIR = red.

to evolves in a predictable way, as seen with other SNe IIb such as SN 2011dh (Ergon et al., 2014), and as such the extrapolation at this time does not add significant uncertainty to the bolometric light curve. The uncertainty associated with the pseudo-bolometric light curve was calculated using the uncertainty for the available photometry bands at each epoch, along with an uncertainty calculated from the fitting of the extrapolated SED and an additional uncertainty of 0.1 mag per 10 days applied to the extrapolated photometry bands. Further errors to account for the UV band extrapolations at late times were also added in quadrature to the total luminosity error.

To compare the contributions of the UV, optical and NIR regions to the total bolometric light curve, additional pseudo-bolometric light curves were constructed using the UV - optical, solely optical and optical - NIR photometry bands. These pseudo-bolometric light curves are presented in the top panel of Figure 3.6, while the contribution of each electromagnetic region to the complete pseudo-bolometric light curve given can be seen in the lower panel of Figure 3.6. The optical bands contribute the most to the total light curve throughout its evolution. Initially, the UV bands dominate over the NIR bands, before rapidly decline in strength as the NIR contribution increases, peaking at around ~35% and staying relatively constant until $\gtrsim 150$ days, when the NIR contribution

risers. The contribution from the NIR photometry bands shown in Figure 3.6 is initially slightly inflated due to the interpolation at early times resulting in an overestimation in the strength of the NIR bands. This lack of comprehensive photometric coverage for the NIR region resulted in an increase in the final error for the pseudo-bolometric light curve. However, the lack of NIR coverage at peak time is not expected to have a significant effect on the physical parameters derived from the pseudo-bolometric light curve due to the domination of the UV and optical bands at this epoch. The error of the pseudo-bolometric light curve was also influenced by the lack of UV bands at late times (≥ 60 days), although at this epoch the UV bands contribute little to the bolometric light curve ($\leq 10\%$ of total flux), and therefore is not expected to impose significant errors. The late time pseudo-bolometric light curve of SN 2020acat is likely suffers from an overestimation of the NIR bands during the period when they contribute significantly to the total light curve. While the pseudo-bolometric light curve constructed from the UV - NIR bands encapsulates the majority of photons emitted during the evolution of SN 2020acat, a small portion of light is unaccounted for associated with the bands outside the observed wavelength range. A full bolometric light curve of SN 2020acat is expected to have a slightly higher peak luminosity and more luminous late time due to the domination of the infrared bands during this epoch, as seen in Figure 3.6. Fitting of the full bolometric light curve during the photospheric phase would result in a slightly larger ^{56}Ni mass, and potentially a higher amount of ejecta mass and kinetic energy, compared to the pseudo-bolometric light curve. While an increase of the physical parameters is expected, the difference in physical parameters is not expected to be great enough to alter any of the conclusions derived from the analysis of pseudo-bolometric light curve.

The evolution of the pseudo-bolometric light curve of SN 2020acat, along with the light curves of SN 1993J, SN 2008ax, SN 2011dh, SN 2011fu, SN 2013df and SN 2016gkg are displayed in Figure 3.7, with the peak time evolution of each pseudo-bolometric light curve shown in the upper right. These SNe were used as comparison objects for SN 2020acat due to their comprehensive photometric coverage, which extends from the early time to well in to the nebular time phase. This allows for their pseudo-bolometric light curves to be compared with that of SN 2020acat during both the pre-maximum and post maximum phases, as well as at late time when ^{56}Co decay dominates the light

TABLE 3.5: Light curve details and physical parameters derived from fitting the pseudo-bolometric light curves for SN 2020acat and the other SNe IIb with the Arnett-like fit. Also shown are the literature values for the M_{Ni} , M_{ejc} and E_k of the different SNe IIb, these values were derived using the Arnett-like model and an optical opacity $\kappa = 0.06 \text{ cm}^2 \text{ g}^{-1}$.

SN	$\text{Log}(L_{\text{peak}})$ [erg s^{-1}]	t_{peak} [days]	v_{ph} [km s^{-1}]	This work			Literature		
				M_{Ni} [M_{\odot}]	M_{ejc} [M_{\odot}]	E_k [$\times 10^{51} \text{ erg}$]	M_{Ni} [M_{\odot}]	M_{ejc} [M_{\odot}]	E_k [$\times 10^{51} \text{ erg}$]
2020acat	42.49 ± 0.15	14.62 ± 0.27	10.0 ± 0.5	0.13 ± 0.03	2.3 ± 0.4	1.2 ± 0.3	-	-	-
1993J	42.37 ± 0.17	19.95 ± 0.32	8.0 ± 1.0	0.10 ± 0.03	1.9 ± 0.4	0.7 ± 0.2	0.10 ± 0.04	2.7 ± 0.8	1.3 ± 0.3
2008ax	42.38 ± 0.08	17.20 ± 0.27	7.5 ± 0.5	0.13 ± 0.04	2.5 ± 1.0	0.8 ± 0.3	0.10 ± 0.02	2.7 ± 0.5	1.2 ± 0.5
2011dh	42.15 ± 0.11	20.21 ± 0.54	6.5 ± 1.0	0.05 ± 0.01	2.2 ± 0.4	0.6 ± 0.1	0.07 ± 0.01	2.1 ± 0.5	0.8 ± 0.2
2011fu	42.49 ± 0.14	21.15 ± 0.73	8.0 ± 1.0	0.17 ± 0.03	3.4 ± 0.7	1.3 ± 0.3	0.15	3.5	1.3
2013df	42.38 ± 0.07	17.84 ± 0.30	8.0 ± 1.0	0.11 ± 0.02	1.5 ± 0.3	0.6 ± 0.1	0.11 ± 0.02	0.11 ± 0.30	0.8 ± 0.4
2016gkg	42.13 ± 0.02	18.47 ± 0.13	8.0 ± 1.0	0.06 ± 0.01	1.6 ± 0.3	0.6 ± 0.1	-	-	-

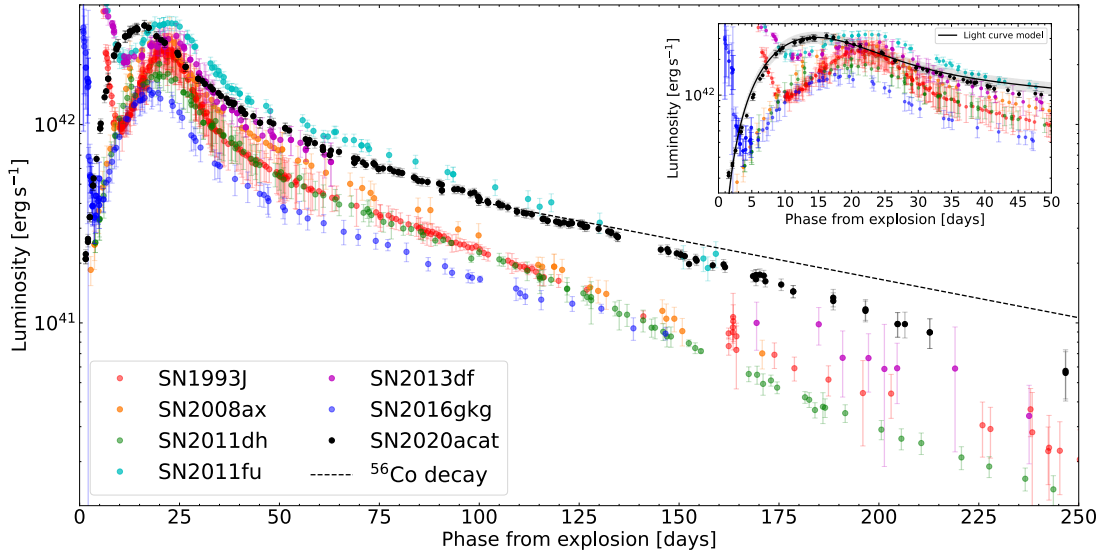


FIGURE 3.7: The pseudo-bolometric light curve of SN 2020acat, along with several other well observed SNe IIB over the first 250 days. The SNe shown in the plot are SN 1993J (red), SN 2008ax (orange), SN 2011dh (green), SN 2011fu (cyan), SN 2013df (magenta), SN 2016gkg (blue) and SN 2020acat (black). All SNe have been corrected for reddening as well as time dilation. The black dashed line displays the cobalt decay line that should dominate at late times for light curves powered solely by the decay of ^{56}Ni . The subplot (upper right) displays the initial 50 days of each pseudo-bolometric light curves. For SN 2020acat the Arnett-like fit is also displayed by the solid black line, along with associated errors for the model shown by the grey shaded region. The physical parameters of each SN IIB obtained from the Arnett-like fit are given in Table 3.5.

curve. All SNe shown in Figure 3.7 have also been thoroughly modelled and have well determined properties such as distance modulus, extinction and explosion date. This allows for a comparison and permits the placement of SN 2020acat within the property distribution space of SNe IIB. Also shown in Figure 3.7 is the decay slope of ^{56}Co , the source of power expected to dominate the late-time evolution of SNe. As expected, the decay of SNe IIB display a small spread at late time with all light curves significantly diverging from the slope of ^{56}Co decay (Wheeler et al., 2015), as predicted when there is an the absence of the full trapping of the gamma-rays released by the decay of ^{56}Co .

The pseudo-bolometric light curve of SN 2020acat peaks at a luminosity of $L_{\text{peak}} = 3.09_{-0.9}^{+1.28} \times 10^{42} \text{ erg s}^{-1}$, $\text{Log}(L_{\text{peak}}) = 42.49 \pm 0.15 [\text{erg s}^{-1}]$, with a rise time of $\sim 14.6 \pm 0.3$ days. The rise time of SN 2020acat is considerably faster compared to the other SNe IIB, which tend to have a rise time of ~ 20 days or longer, and was expected from the rapid rise seen in the UV and optical bands. The psuedo-bolometric light

curve of SN 2020acat lacks any shock-cooling tail seen in several of the other SNe IIB. While it may be possible that the shock-cooling phase of SN 2020acat was fully missed, this is unlikely to have happened. The extended duration of the shock-cooling phase combined with the luminous nature of the shock-cooling tail, which tends to outshine the peak of the ^{56}Ni powered peak of the light curve, makes it a very obvious feature of the light curves of SNe IIB when it is present. Thus, the lack of evidence for the light curve of SN 2020acat showing any dimming from an initial bright peak and the tight restriction on SN 2020acat's explosion date, make it likely that the shock-cooling phase of SN 2020acat was not prominent, a feature which is associated with SN from compact progenitors as was seen with SN 2008ax.

SN 2020acat displays a higher peak luminosity than the majority of SNe IIB shown in Figure 3.7. Among the SNe of our sample, only SN 2011fu is of similar brightness to SN 2020acat, with a peak luminosity of $\text{Log}(L_{\text{peak}}) = 42.49 \pm 0.17 [\text{erg s}^{-1}]$, while SN 2008ax has a similar luminosity to SN 2020acat, peaking at a luminosity of $\text{Log}(L_{\text{peak}}) = 42.38 \pm 0.57 [\text{erg s}^{-1}]$. Compared to the mean peak luminosity for SNe IIB given by [Prentice et al. \(2016\)](#), $\text{Log}(L_{\text{peak}}) = 42.36 \pm_{0.11}^{0.26} [\text{erg s}^{-1}]$, SN 2020acat is $\sim 0.12 [\text{erg s}^{-1}]$ brighter, suggesting that a larger than average amount of ^{56}Ni was synthesised during the explosion. The analysis done in [Prentice et al. \(2016\)](#) makes use of the same cosmology as used in Section 3.2 allowing for a comparison with SN 2020acat to be made.

However while a valid comparison to SN 2020acat can be made, it should be noted that there is an additional uncertainty in the luminosity of SN 2020acat and several comparison objects. This error arises from uncertainties in the distance modulus for events that lacked redshift independent distances and sit outside the Hubble Flow, as mentioned in Section 3.2. However, the uncertainty is not expected significantly alter the peak luminosities obtained for the SNe IIB shown here, as the bolometric corrections are the main contributor to the error for the pseudo-bolometric light curves.

An Arnett-like model ([Arnett, 1982](#)) was fit to the pseudo-bolometric light curves of SN 2020acat and the other SE-SNe to determine the mass of ^{56}Ni synthesised, as well as the mass of material ejected by the explosion (M_{ejc}) and the SNe kinetic energy

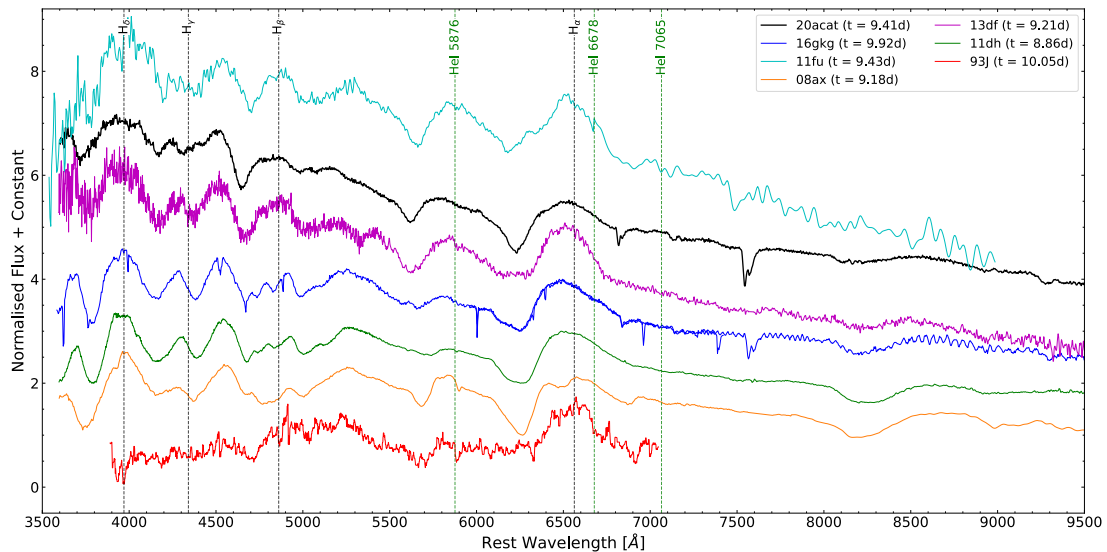


FIGURE 3.8: Spectroscopic comparison of SN IIb at around 9 days from explosion. All spectra have been corrected for redshift and extinction. The emerging hydrogen and helium features are marked at their rest wavelength.

(E_k). For the fitting of the Arnett-like model, an opacity of $\kappa = 0.06 \text{ cm}^2 \text{ g}^{-1}$ and a dimensionless form factor derived by Arnett (1982) of $\beta = 13.8$, were used for all SNe. An opacity of $0.06 \text{ cm}^2 \text{ g}^{-1}$ was used here as it has been established that a small optical opacity is needed for the modelling of the bolometric light curves for hydrogen rich SNe, and has been used in studies of Type IIb SNe (Lyman et al., 2016). The degeneracy between the ejecta mass and the kinetic energy was broken for each SN by using the photospheric velocity, v_{ph} . For SN 2020acat, the photospheric velocity had a value of $\sim 10000 \pm 1000 \text{ km s}^{-1}$. The method used to obtain the photospheric velocity discussed in Section 3.5.2. Additionally, the model used for SN 2020acat and the other SNe IIb was slightly modified to determine the estimated explosion date by fitting to the pre-peak photometric data. This was modified for those SNe that displayed a shock-cooling phase and produced values all within the error range given for the explosion date within the literature.

The Arnett-like model, shown in the upper right plot of Figure 3.7, is well fitted to the peak of the pseudo-bolometric light curve and the majority of the rise time. Although, it seems to underestimate the luminosity of the initial points, within less than 5 days from explosion, and starts to diverge away from the constructed pseudo-bolometric light curve at around 35 – 45 days after estimated explosion. The divergence at later times,

≥ 35 days, is expected as the light curve transitions away from being dominated by solely the decay of ^{56}Ni . Interestingly, the underestimation of the bolometric light curve at the earliest phase implies that the mass of ^{56}Ni is more mixed into the outer ejecta than what the model assumes. The main errors associated with the model arise from the error in the photospheric velocity, the error associated with the pseudo-bolometric light curve and the error within the estimated explosion data. From the fitting to the pseudo-bolometric light curve, the values for the physical parameters of SN 2020acat and the comparison SNe IIB, along with the peak luminosity and rise time for each event were determined. These values along with the photospheric velocity used to break the degeneracy between M_{ejc} and E_{k} , are given in Table 3.5. From the modelling of the SN 2020acat light curve, a ^{56}Ni mass of $M_{\text{Ni}} = 0.13 \pm 0.03 M_{\odot}$ was obtained, along with a ejecta mass of $M_{\text{ejc}} = 2.3 \pm 0.4 M_{\odot}$ and a kinetic energy of $E_{\text{k}} = 1.2 \pm 0.3 \times 10^{51}$ erg. It should be noted that in recent years there has been a lot of discussion in the validity of using an Arnett-like approach to obtain the value of the ^{56}Ni mass synthesised by CC-SNe. [Khatami & Kasen \(2019\)](#) discussed the effect of neglecting the time-dependent diffusion on the ^{56}Ni mass that Arnett-like models assume. Alternative models for CC-SNe have shown that the value of ^{56}Ni mass derived from the Arnett-like model is higher by $\sim 30 - 40\%$ than the results from recent modelling (see, [Dessart et al., 2016](#); [Woosley et al., 2021](#)). As such if the ^{56}Ni mass derived above for SN 2020acat is overestimated by $\sim 30 - 40\%$ then the final ^{56}Ni mass for SN 2020acat would be $M_{\text{Ni}} = 0.08 - 0.09 \pm 0.03 M_{\odot}$. However due to the prolific use of the Arnett-like model in the literature, when comparing the physical parameters of SN 2020acat with those of other SNe IIB, the uncorrected value of M_{Ni} will be used to give a more valid comparison.

The physical parameters obtained for SN 2020acat suggests that it was a high energy event, producing a large amount of both ^{56}Ni and ejecta. However, to get a comprehensive look at the physical parameters of SN 2020acat a comparison with a large study of SNe IIB is needed. From [Prentice et al. \(2019\)](#), a mean value of M_{Ni} and M_{ejc} of SNe IIB were determined to be $0.07 \pm 0.03 M_{\odot}$, and $2.7 \pm 1.0 M_{\odot}$ respectively. These physical parameters show that SN 2020acat produced a roughly average value for the ejecta mass while having a significantly higher value for the nickel mass, which would account for the brighter pseudo-bolometric light curve shown in Figure 3.7. However, when compared

to the analysis of SE-SNe done by Lyman et al. (2016), with values of $M_{\text{Ni}} = 0.11 \pm 0.04 M_{\odot}$, $M_{\text{ejc}} = 2.2 \pm 0.8 M_{\odot}$ and a kinetic energy of $1.0 \pm 0.6 \times 10^{51}$ erg, SN 2020acat synthesised slightly more nickel than the average SNe I Ib, an average amount of ejecta mass and a slightly higher kinetic energy. From both study comparisons it can be seen that SN 2020acat is an energetic event that produces a roughly average amount of ejecta for a SN I Ib.

The high energy derived for SN 2020acat, along with the value of M_{ejc} , supports the idea that the progenitor of SN 2020acat was an intermediate mass star with a M_{ZAMS} between $15 - 20 M_{\odot}$. The progenitor mass range of SN 2020acat was determined using the derived physical parameters, along with an assumed remnant mass of $1.5 - 2.0 M_{\odot}$, and the progenitor models described in Sukhbold et al. (2016). The value of the M_{ZAMS} predicted for SN 2020acat, while on the higher end of progenitor masses, is not out of the range of possibility for a SE-SNe (Zapartas et al., 2021). Deng et al. (2003) reported a similar progenitor $M_{\text{ZAMS}} \sim 20 - 25 M_{\odot}$, for SN 2002ap a Type Ic SNe that produced a similar amount of ejecta mass as SN 2020acat. A high mass progenitor, $M_{\text{ZAMS}} \sim 18 M_{\odot}$, was also suggested by Folatelli et al. (2015) for SN 2008ax. It was also shown by Lyman et al. (2016) that the observed distribution of ejecta masses for SE-SNe can be explained by progenitors with masses that range between $8 - 20 M_{\odot}$. As such an intermediate - high mass progenitor for SN 2020acat is not impossible, although it would require detailed hydrodynamic modelling to determine its validity, which is beyond the scope of this work.

3.5 Spectroscopic Analysis

Figure 3.3 shows the spectral evolution of SN 2020acat until the start of the nebular phase. The initial spectrum of SN 2020acat was obtained on 10/12/2020 (MJD = 59193.31), approximately 1 day after the estimated explosion date. Initially, the spectra of SN 2020acat displayed a blue continuum due to the high temperature of the material, before rapidly cooling. At around +20 days from explosion, the blue continuum had faded and the spectral line features become more dominant. The $H\alpha$ feature, along with

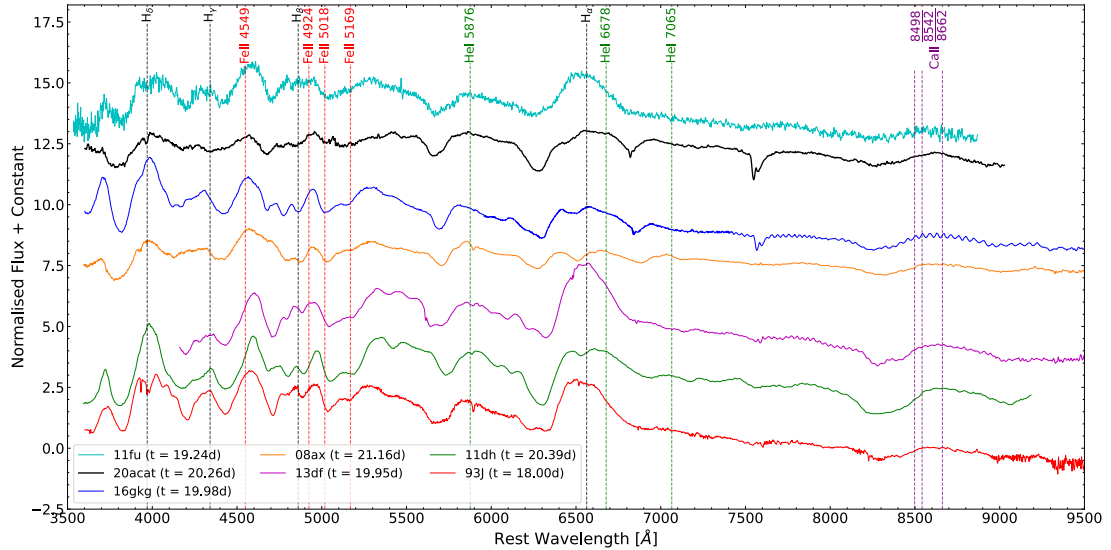


FIGURE 3.9: Spectral comparison of SN 2020acat with several well observed SNe I Ib roughly 20 days after explosion. Phase from explosion date for individual SNe are given in legend. All spectra are shown in rest frame and were normalised to the peak of the $H\alpha$ feature. SNe are ranked in terms of the $He\ I\ \lambda 5876$ line velocity and given in rest frame. Key photospheric phase lines are marked by the dashed lines and are given at their rest wavelength.

$H\beta$ and to a lesser degree $H\gamma$, dominate the spectra for the first ~ 100 days. Helium features are also clearly present, although they are not as strong as the hydrogen ones, as well as some ionised iron features. After ~ 100 days, the hydrogen features have almost fully faded from the spectra, leaving both oxygen and calcium to dominate the spectra of SN 2020acat, as the photosphere recedes deeper into the ejecta and the spectra transitions into the nebular phase.

3.5.1 Early Phase

3.5.1.1 Pre-maximum light

During the pre-maximum light phase, $\sim 0 - 20$ days after explosion, the $H\alpha$ feature displays a strong broad P-Cygni profile. While hydrogen features are clearly visible throughout the photospheric phase, the $He\ I\ \lambda\lambda 5876, 6678, 7065$ lines do not produce strong features until post-max light (~ 25 days after explosion), with the $5876\ \text{\AA}$ being the strongest of the $He\ I$ features, and the only one clearly visible in the pre-max spectra.

The 6678 Å feature is especially weak and seems to disappear when the H α feature is no longer visible.

In the blue region (< 6000 Å of the optical spectra, where the Fe II line features usually dominate, there is a strong absorption feature at ~ 4900 Å that is of similar depth to the H β feature at around ~ 20 days after the explosion. This feature is generally identified as Fe II $\lambda 5018$. However, it is generally observed alongside other Fe II lines, all of which display a similar strength. This is not what is observed in the spectra of SN 2020acat, where the Fe II 5018 feature broadly dominates over the other Fe II features. Also, the 4900 Å component is not broad enough to be a result of both the Fe II $\lambda\lambda 4924, 5018$ blending together, and there is a distinct weak absorption component between the H β line and the 4900 Å feature that has been associated with the Fe II $\lambda 4924$ line. The existence of a distinct Fe II $\lambda 4924$ feature, along with the fact that both the 4924 Å and 5169 Å components are not of similar strength relative to the 5018 Å line place strong doubt on the origins of the 4900 Å feature as the result of solely a Fe II line. The question remains on what is the element that causes the 4900 Å feature, within the spectra of SN 2020acat. This was tested by fitting the spectra of SN 2020acat with a continuum fit and adding an absorption component of different elements that possess a strong emission line just redward of the 4900 Å. Once the likely elements were identified, a line velocity was determined from the absorption minimum. The velocity was used to fit the features of the elements other optical lines found in different regions of the spectrum. If the additional features matched up with several other absorption features within the spectrum the element was considered a likely source of contribution to the 4900 Å feature. The process was repeated three times to determine if the elements presence existed within the spectra or if the initial presence was due to the noise within the spectrum. From this testing, the best elements that would have been able to create the 4900 Å feature are either helium, nitrogen or a combination of both, enhancing the already existing Fe II $\lambda 5018$ line. The helium line that would result in the 4900 Å feature is the He I $\lambda 5016$ line, which is significantly weaker than the He I $\lambda 5876$, with a weighted transition probability $g_k A_{ki}$ of 4.0116×10^7 and 4.9496×10^8 respectively (Gordon, 2006), thus making it unlikely that the He I $\lambda 5016$ line is the only line responsible for the 4900 Å feature. Along with helium, nitrogen also possesses multiple optical lines whose presence were

identified from fitting the spectra of SN 2020acat during the post-maximum brightness and the spectra observed between the photospheric phase and the nebular phase. These lines being the N II $\lambda\lambda$ 5005, 5680 and 5942 lines, which have equivalent transition probability to the He I λ 5876 line with a value of $g_k A_{ki}$ of 3.63×10^8 (Luo & Pradhan, 1989), 3.47×10^8 (Tachiev & Fischer, 2001) and 5.47×10^7 (Tachiev & Fischer, 2001) respectively. There also exists a weak N II line at 6482 Å however this line overlaps with the H α feature thus making the determination of its presence at early times, where the hydrogen Balmer features dominate, quite difficult. While the presence of additional nitrogen may enhance the broad nature of the 4900 Å feature, through the blending of several lines within the iron region of the SN 2020acat spectra, it should be noted that nitrogen does not have a strong emission. As such the presence of nitrogen alone is not enough to strongly alter the spectrum of SN 2020acat, unless unrealistic amounts of nitrogen were to be introduced. Therefore, while it is possible that nitrogen enhances the existing feature, the main cause of the 4900 Å feature is still thought to be a result of helium and iron.

The pre-maximum spectrum of SN 2020acat, taken on 18/12/2020, at around 9 days after explosion, was compared to the spectra of five SN I Ib, each taken at a similar epoch, in Figure 3.8. All spectra have been corrected for reddening, given in their rest wavelength, and normalised to the peak of the H α feature. Unfortunately, SN 1993J lacked full wavelength coverage at this epoch, covering a range of $\sim 4000 - 7000$ Å. However in this phase, as the major feature at wavelengths redder than 7000 Å is the Ca II feature the missing section of SN 1993J is not expected to be of great concern. Relative to the other SNe I Ib, SN 2020acat displays broader features for all lines seen at this epoch. SN 2020acat also displays strong hydrogen features compared to the other SNe. Unlike SN 2008ax, SN 2011dh and SN 2016gkg, SN 2020acat lacks strong iron features at around ~ 4800 Å instead showing a smooth emission from H β . The depth of the Ca II H&K feature within the spectrum of SN 2020acat is not as deep relative to some of the other SNe, being similar to both SN 2013df and SN 2016gkg.

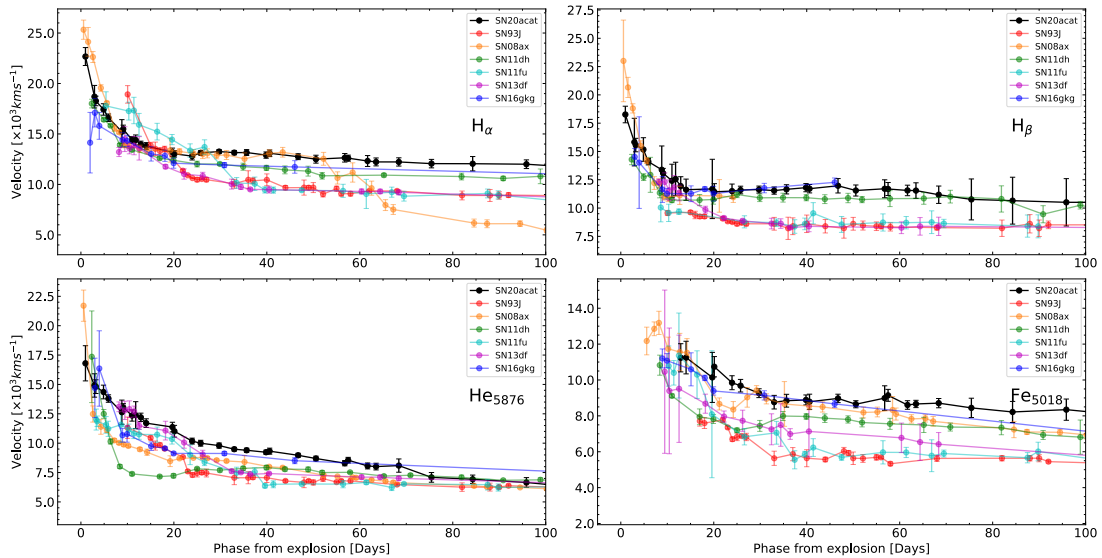


FIGURE 3.10: Line velocity evolution of the $H\alpha$, $H\beta$, $He\ I\ \lambda 5876$ and $Fe\ II\ \lambda 5018$ lines for SN 2020acat, which are compared to those of other SNe I**b**, over the first 100 days from explosion. It's clearly seen that SN 2020acat displays one of the highest line velocity of the SNe shown here.

3.5.1.2 Post-maximum light

The spectrum of SN 2020acat at ~ 20 days post explosion was also compared to the other SNe I**b** at a similar epoch, in Figure 3.9, which have been ranked by the $He\ I\ \lambda 5876$ maximum velocity. As expected, SN 2020acat displays a very blue-shifted helium feature with only the helium feature of SN 2011fu being bluer in wavelength. In all SNe spectra, the $He\ I\ \lambda 5876$ feature is strong and displays very similar shape in all except SN 1993J and SN 2013df. The $H\alpha$ feature, while present in all spectra at this epoch, varies significantly in both strength and broadness among the different SNe I**b** displayed in Figure 3.9. In SN 2020acat, the $H\alpha$ emission is quite broad, such that the $He\ I\ \lambda 6678$ feature is visible within the emission component P-Cygni $H\alpha$ profile, just blue of the peak. In all spectra, the $H\alpha$ P-Cygni absorption feature is deeper than $He\ I\ \lambda 5876$, although in the spectrum of SN 2008ax both features have a very similar depth. Unlike both SN 1993J and SN 2013df, SN 2020acat does not display a broad flat minimum in either the $H\alpha$ and $He\ I\ \lambda 5876$ features, showing that within SN 2020acat the hydrogen and helium existed within distinct shells and lack multiple high density regions as suggested for SN 1993J and SN 2013df (Sahu et al., 2013). All spectra also display clear NIR Ca II features. It should be noted that the line velocity of all major

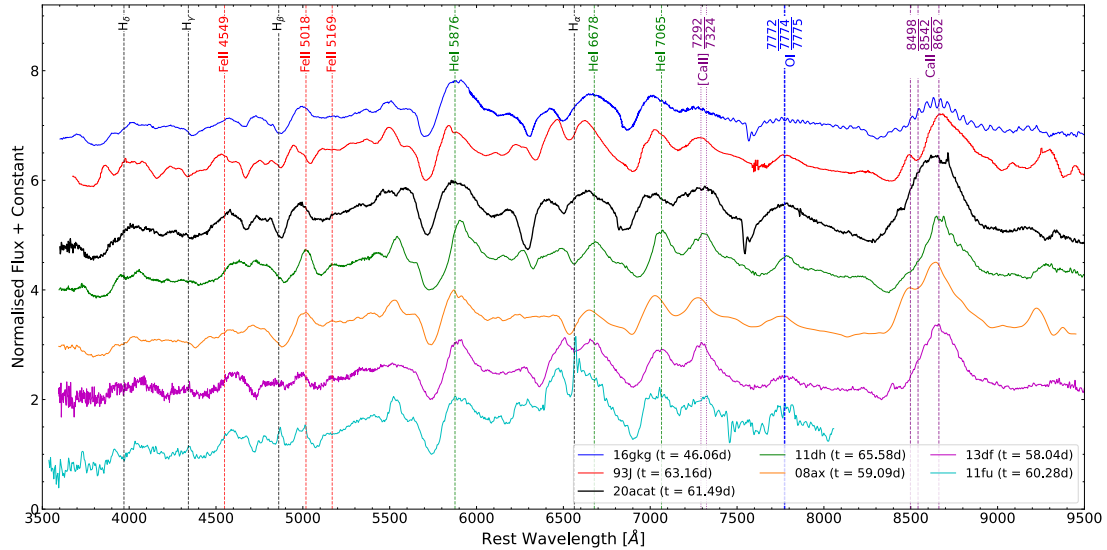


FIGURE 3.11: Spectral comparison of SN 2020acat with several well observed SNe I**b** roughly 60 days after their reported explosion date. All spectra are shown in rest frame and are ranked in terms of He I λ 5876 line velocity. Key transition phase element lines are marked at their rest wavelength, with allowed transitions shown as the dashed lines and forbidden lines shown as dotted lines.

features, in the ~ 20 day spectrum of SN 2020acat, are faster than those of other SNe at the same epoch, this can be clearly seen in Figure 3.10. The high velocity of all major features suggests that SN 2020acat was a very energetic event, likely originating from a high mass progenitor star.

3.5.2 Line Velocity Evolution

The expansion velocity of the ejected material in SN 2020acat was measured from the P-cygni profiles for the H α , H β , He I λ 5876 and Fe II λ 5018 lines within the spectra prior to day 100. This was determined by fitting the absorption minimum of the line profiles with a Gaussian function. The main error associated with the line velocity originates from the noise of the individual spectrum, along with a small error associated with fitting of the line features and the redshift correction. However, due to the high signal to noise ratio (S/N) of the spectra, the error at most epochs is not large for the H α , H β and He I λ 5876 lines.

Unlike the other lines, the Fe II λ 5018 line has an additional error associated with the origin of the 4900 Å feature. As mentioned in Section 3.5, identification of the Fe II

$\lambda 5018$ line is made difficult by the presence of helium and potentially nitrogen lines, and due to line blending, as well as the resolution of the spectra, it is not possible to determine the velocity minimum of each line individually. Despite that, it is expected that the velocity profile of the feature to be dominated by the Fe II $\lambda 5018$ line and have taken the minimum of the 4900 Å as the maximum velocity of the Fe II $\lambda 5018$ with an additional error of $\sim 20\%$ from the blending of the helium and possibly nitrogen lines. Due to the trouble with identifying the Fe II $\lambda 5018$ line, the line velocities other Fe II lines were used to check the obtained Fe II $\lambda 5018$ line velocity evolution with all lines showing an agreement with the velocity range derived for the Fe II $\lambda 5018$ line.

Along with the line velocity of the Fe II $\lambda 5018$ line, measuring the expansion velocity of the Fe II $\lambda 5169$ line is critical in determining the velocity of the photosphere as it moves through the expanding ejecta. Both [Hamuy et al. \(2001\)](#) and [Takáts & Vinkó \(2012\)](#) have shown that the evolution of the Fe II lines closely follow the evolution of the photosphere, especially compared to other lines seen during the photospheric phase such as the Balmer lines ([Dessart & Hillier, 2005](#)). Due to the nature of the Fe II region discussed in Section 3.5.1.1 and the noise within the spectra of SN 2020acat, determining the velocity of the Fe II $\lambda 5169$ line at maximum light resulted in a large velocity uncertainty. Despite that a photospheric velocity, based on the Fe II $\lambda 5169$ line, of $v_{\text{ph}} \sim 10000 \pm 1000 \text{ km s}^{-1}$ was determined from the peak time spectrum, taken ~ 15.5 days after explosion.

The velocity evolution of these lines was compared to the velocity evolution obtained from SN 1993J, SN 2008ax, SN 2011dh, SN 2011fu, SN 2013df and SN 2016gkg in Figure 3.10. Overall, the line velocities of elements identified in SN 2020acat are consistently higher when compared to other SE-SNe. The $H\alpha$ velocity initially is rivalled by only SN 2008ax at $\sim 22700 \text{ km s}^{-1}$, being $\sim 1000 \text{ km s}^{-1}$ higher than the other SNe. The $H\alpha$ and $H\beta$ velocities rapidly decline over the first ~ 20 days, before plateauing at around $\sim 13000 \text{ km s}^{-1}$ and $\sim 12000 \text{ km s}^{-1}$, respectively. Both the $H\alpha$ and $H\beta$ of SN 2020acat display a slight increase in their velocity of $\sim 500 \text{ km s}^{-1}$ at around ~ 30 days. This increase likely results from the fitting of the spectra as there is no physical reason seen within either the spectra or light curve that would account for this increase in velocity. The He I $\lambda 5876$ feature of SN 2020acat starts at ~ 16800

km s^{-1} and steadily declines for ~ 70 days, remaining higher than the other SE-SNe, until SN 2020acat starts to transition into the nebular phase. The Fe II $\lambda 5018$ line velocity of SN 2020acat remains faster than other SNe throughout the spectroscopic evolution.

3.5.3 Transition into the Nebular phase

Between $\sim 50 - 120$ days after the explosion, the spectrum of SN 2020acat undergoes a drastic change as the Balmer lines become narrower and more shallow, and the photosphere recedes deeper into the expanding ejecta. Along with the fading of the hydrogen features, the line velocity of most elements drops at a much slower rate than during the photospheric phase, falling by $\sim 2000 \text{ km s}^{-1}$ during this period, although the H α and H β lines drop at a slower pace only decreasing by $\sim 1000 \text{ km s}^{-1}$. The He I lines increase in strength relative to the H α line, and become the dominant feature as the spectrum transitions into that of a SN Ib. While this is happening, the NIR Ca II $\lambda\lambda 8498, 8542, 8662$ feature also becomes stronger, along with the weak absorption component of the Ca II H&K lines. Towards the end of this phase the [Ca II] lines $\lambda\lambda 7291, 7324$, along with the allowed O I $\lambda 7773$ feature, start to appear showing the spectrum is transitioning into the nebular phase.

The spectrum of SN 2020acat at ~ 60 days is compared with spectra of the other SNe Ib at a similar epoch, although the spectrum of SN 2016gkg is ~ 15 days earlier than the rest due to the limited late time observations, in Figure 3.11. Despite the late time, the absorption component of the H α feature in the SN 2020acat is much deeper than in the other SNe Ib. This deep hydrogen feature suggests that a large amount of hydrogen is still present at the depth of the photosphere at around ~ 60 days after the explosion. The presence of strong hydrogen features at this epoch may result from the progenitor having hydrogen mixed throughout the outer envelope and into parts of the inner envelope prior to collapse. The H α feature is also still significantly broader than those seen for other SNe Ib.

Although the H α feature remains broad in SN 2020acat, the He I velocities have dropped to within the velocity distribution given by the other SNe Ib. Overall, the spectrum of

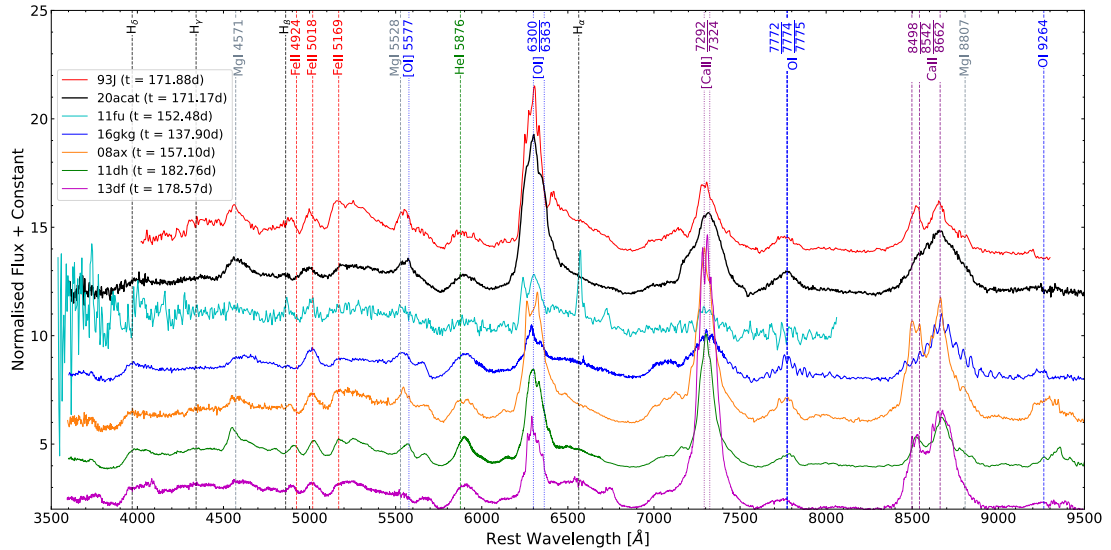


FIGURE 3.12: Spectral comparison of SN 2020acat with several SNe IIB around day ~ 170 . Phase from explosion date are given in legend and all spectra are shown in rest frame. SNe are ordered with respect to the flux ratio of the [O I] and [Ca II] nebular features. Key nebular phase line features are marked at their rest wavelengths, with allowed transitions shown as the dashed lines and forbidden lines shown as dotted lines.

SN 2020acat at this epoch is similar to that of SN 2016gkg, which still displays a relatively strong $H\alpha$ feature. Although, it should be noted that the spectrum of SN 2016gkg is ~ 15 days earlier than that of SN 2020acat, which can drastically change the strength of the $H\alpha$ feature and thus would affect the similarity between these two SNe. The $H\alpha$ and He I $\lambda 5876$ features within all spectra are of similar widths and all SNe display strong Ca II features in the NIR region, with both SN 1993J and SN 2008ax displaying a double peaked profile. The region within the spectra of SN 2020acat between $4800 - 4900 \text{ \AA}$ displays both a noticeable $H\beta$ and a broad feature within the Fe II portion of the region. This strong feature at this epoch is unlikely to result of solely Fe II lines and as discussed in Section 3.5.1.1 is expected to be enhanced by the presence of helium and possible nitrogen. If the $\sim 4900 \text{ \AA}$ feature is indicative to the presence of nitrogen in the spectra of SN 2020acat, it is expected that there should be other N II features detected, including the N II $\lambda\lambda 5680, 6611$ lines. These lines can be associated with weak features seen in the ~ 60 day spectrum of SN 2020acat in Figure 3.11, at ~ 5500 and 6450 \AA respectively. The feature potentially produced by the N II $\lambda 5680$ line is located blue of the [O I] $\lambda 5577$ feature, which produces a strong emission feature in all spectra except for SN 2013df and SN 2020acat. The potential N II 6611 \AA feature could be associated with a weak

absorption feature between the $H\alpha$ peak and the He I $\lambda 6678$ absorption minima. The 6611 Å feature is significantly weaker than the 5680 Å and 4900 Å features, likely due to a combination of the hydrogen and helium dominating the spectrum in this region. All of these absorption features are associated with nitrogen corresponding to a line velocity of $\sim 8000 \pm 500 \text{ km s}^{-1}$, suggesting that, if present, they all result from the same nitrogen-containing shell. [Jerkstrand et al. \(2015\)](#) discuss models that display strong N II within the late time (> 100 days). In order to determine the existence of potential N II lines, more detailed modelling of the spectrum at these epochs are required, which is beyond the scope of this work.

3.5.4 Nebular Phase

At around ~ 120 days after the explosion of SN 2020acat, the spectrum transitions into the nebular phase. During this phase, the $H\alpha$ feature completely disappears and the He I features decrease in strength. While this is happening, both the [O I] $\lambda\lambda 6300, 6363$ and the [Ca II] $\lambda\lambda 7291, 7323$ doublets become stronger and dominate the spectrum. The spectrum of SN 2020acat at ~ 170 days was compared to several SNe IIb at the same epoch, see Figure 3.12. Once again, the spectrum of SN 2016gkg differs significantly in phase compared to the other SNe. All the spectra of the SNe shown in Figure 3.12 are dominated by either the [O I] $\lambda\lambda 6300, 6363$ or the [Ca II] $\lambda\lambda 7291, 7324$ feature at this epoch. Mg I] $\lambda 4571$, O I $\lambda\lambda 7772, 7774$ and the NIR Ca II are also all identified within the spectrum of SNe IIb at this epoch. During this phase, the spectrum of SN 2020acat appears most similar to that of SN 1993J, both dominated by the [O I] feature over the [Ca II] feature. Both of these SNe lack a spectral feature at around 5700 Å that is present in the SNe that are dominated by [Ca II]. While they are similar SN 2020acat does not display a double peak in the Ca II NIR feature seen in SN 1993J, along with several other SNe IIb, instead possessing a single Ca II NIR peak seen also in SN 2016gkg. Another difference between SN 2020acat and SN 1993J is the lack of a small feature around 6400 Å associated with $H\alpha$. Which suggests that hydrogen in SN 2020acat, while mixed deep into the outer layers of the progenitor star as indicated by the strong $H\alpha$ visible at earlier

epochs, is unlikely to penetrate deep into the inner layers or exist in a thick circumstellar medium.

Both the [O I] and [Ca II] features observed within nebular time spectra can be used to probe the asymmetrical nature of the ejecta, as done with SN 2003bg by [Mazzali et al. \(2005\)](#). The evolution of the shape of both the [O I] and [Ca II] peaks in the spectra of SN 2020acat are shown in [Figure 3.13](#). The spectrum on day 117.04 still displays the remnant of an H α feature, seen by the flat-topped profile that would not be present if only [O I] was emitting in that region. Once the H α feature has fully faded from the spectrum, at ~ 130 days, the [O I] feature displays a strong symmetric shape. When compared with the [O I] features of other SE-SNe, the [O I] of SN 2020acat does not display a strong double peak feature, and appears more similar to both SN 2011fu and SN 2013df. Instead, the nebular spectra of SN 2020acat display a small bump on the red side of the peak, which is due to the [O I] $\lambda 6363$ line. The centroid of the [O I] peak is aligned with the 6300 Å while the centroid of the [Ca II] peak is slightly shifted by ~ 1000 km s $^{-1}$, which seems to move towards zero velocity as the spectra evolve. The [Ca II] feature is broader than those of other SNe IIb by several thousand km s $^{-1}$, likely a result of the high explosion energy causing a large dispersion in the calcium velocity distribution.

3.5.5 Oxygen mass and [Ca II]/[O I] ratio

[Fransson & Chevalier \(1989\)](#) suggested that the ratio between the flux of the [Ca II] $\lambda\lambda 7291, 7324$ and the [O I] $\lambda\lambda 6300, 6363$ lines provides a good way of estimating whether the progenitor had a large or small main-sequence mass. This is due to the assumption that the flux of the oxygen emission region is directly related to the mass of oxygen formed throughout the evolution of the progenitor star, while the flux of the calcium emitting region is dependent solely on the mass of calcium synthesised during the explosion, and thus not effected by the mass of the progenitor during its life cycle. Therefore, a large ratio, $[\text{Ca II}] / [\text{O I}] \gtrsim 1$, is expected to be the result of the progenitor having a small main-sequence mass. It was shown by [Elmhamdi et al. \(2004\)](#) that the $[\text{Ca II}] / [\text{O I}]$ ratio within the spectrum at late enough times (> 150 days) is expected

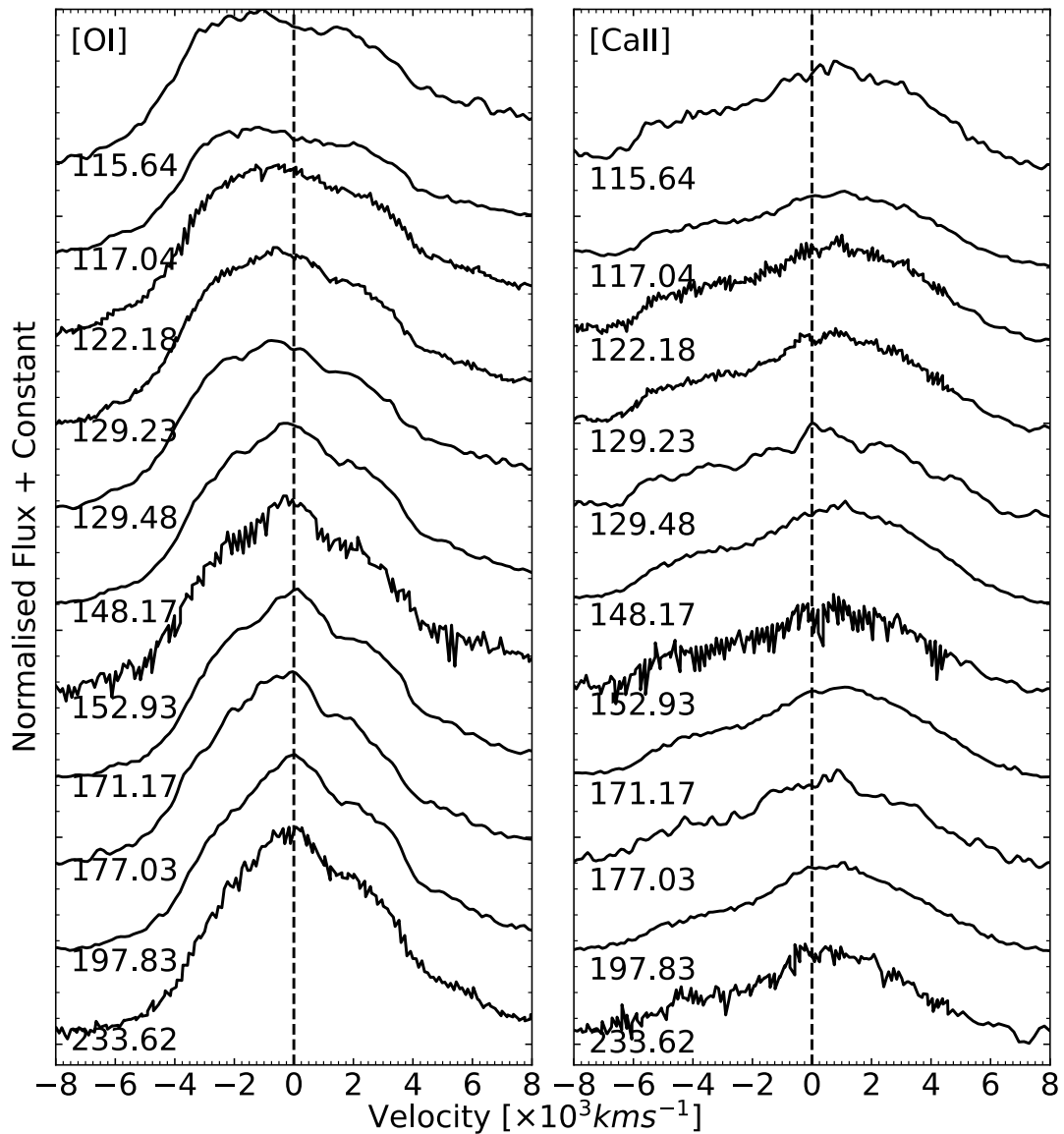


FIGURE 3.13: Line profile of [O I] $\lambda\lambda 6300, 6363$ (left) and [Ca II] $\lambda\lambda 7292, 7324$ (right) within the late time spectra of SN 2020acat. The dashed lines are the emission velocities corresponding to 6300 \AA and 7291 \AA lines. The epoch from estimated explosion date for each spectrum is given in rest frame.

to stay stable over very long periods. For SN 2020acat, at ~ 170 days the $[\text{Ca II}]/[\text{O I}]$ ratio was found to be ~ 0.5 , similar to that seen for SN 1993J and SN 2011fu at similar epochs, which suggests that the progenitor of SN 2020acat had a large M_{ZAMS} . However, it should be noted that this method is not a robust tool for obtaining M_{ZAMS} . The ratio between the [Ca II] $\lambda\lambda 7292, 7324$ and [O I] $\lambda\lambda 6300, 6363$ varies strongly among the different SNe IIb displayed in Figure 3.12, with SN 2008ax, SN 2011dh and SN 2013df all displaying a stronger forbidden calcium feature relative to the oxygen peak. SN 1993J,

SN 2011fu, SN 2016gkg and SN 2020acat on the other hand, all show a stronger oxygen feature which dominates over the calcium, although with SN 2016gkg the peaks of the oxygen and calcium features are very similar at ~ 140 days. Caution however, should be taken with the spectrum of SN 2016gkg which was obtained ~ 30 days earlier than the other SNe and thus by day 170 may have a drastically different ratio, especially given the proximity to unity that the $[\text{Ca II}]/[\text{O I}]$ ratio had at ~ 140 days.

From the nebular phase spectra of SN 2020acat, an estimation of the oxygen mass can be made, which can provide insight into the expected progenitor mass. The relationship between the observed $[\text{O I}]$ emission peak and the mass of oxygen was described by [Uomoto \(1986\)](#), which is expected to hold within a high density limit ($N_e \geq 10^6 \text{cm}^{-3}$), and is given by:

$$M_{\text{O}} = 10^8 F([\text{O I}]) D^2 \times \exp\left(\frac{2.28}{T_4}\right), \quad (3.4)$$

where M_{O} is the mass of neutral oxygen in M_{\odot} , $F([\text{O I}])$ is the flux of the $[\text{O I}] \lambda\lambda 6300, 6363$ peak in $\text{ergs}^{-1}\text{cm}^{-2}$, D is the distance in Mpc and T_4 is the temperature of the oxygen emitting region of the spectrum in units of $10^4 K$. The temperature of the $[\text{O I}]$ region can be determined by the ratio of fluxes between $[\text{O I}] 5577 \text{ \AA}$ and the $[\text{O I}] \lambda\lambda 6300, 6363$ lines. However, determining the flux of the $[\text{O I}] 5577 \text{ \AA}$ peak is not easy, as it can blend with Fe II lines, distorting the flux value of the peak. As such, a temperature of $T_4 = 0.4K$ was used, which arises from the assumption that within the oxygen emitting region during the nebular phase the density is high and the temperature is low ([Elmhamdi et al., 2004](#)). Using this low temperature, along with a $F([\text{O I}]) = 8.41 \times 10^{-14} \text{ erg s}^{-1} \text{ cm}^{-2}$ derived from the spectrum taken at ~ 170 days post explosion, results in an oxygen mass of $M_{\text{O}} = 3.13 \pm 0.07 M_{\odot}$. This is a large oxygen mass given the ejecta mass derived from the light curve. However, realistically the flux of oxygen is not constant over time as the SN fades and the spectra transitions further into the nebular phase. As such, different oxygen masses can be obtained as the spectra evolve, the values of which are given in Table 3.6. Due to the changing nature of the oxygen flux as SN 2020acat fades, the value of M_{O} derived from the spectrum taken on day ~ 171 can be considered an upper limit to the oxygen mass.

TABLE 3.6: Mass of oxygen obtained from the late time spectra of SN 2020acat using equation. 3.4. The flux from the spectrum taken 171.17 days from explosion is taken as an upper limit to the mass of oxygen. The error associated with each epoch is given in the parenthesis.

Phase [days]	Flux [$\times 10^{-14} \text{erg s}^{-1} \text{cm}^{-2}$]	M_{O} [M_{\odot}]
171.17	8.407	3.13 (0.14)
177.02	7.406	2.76 (0.10)
197.83	7.691	2.87 (0.12)
233.62	2.590	0.97 (0.04)

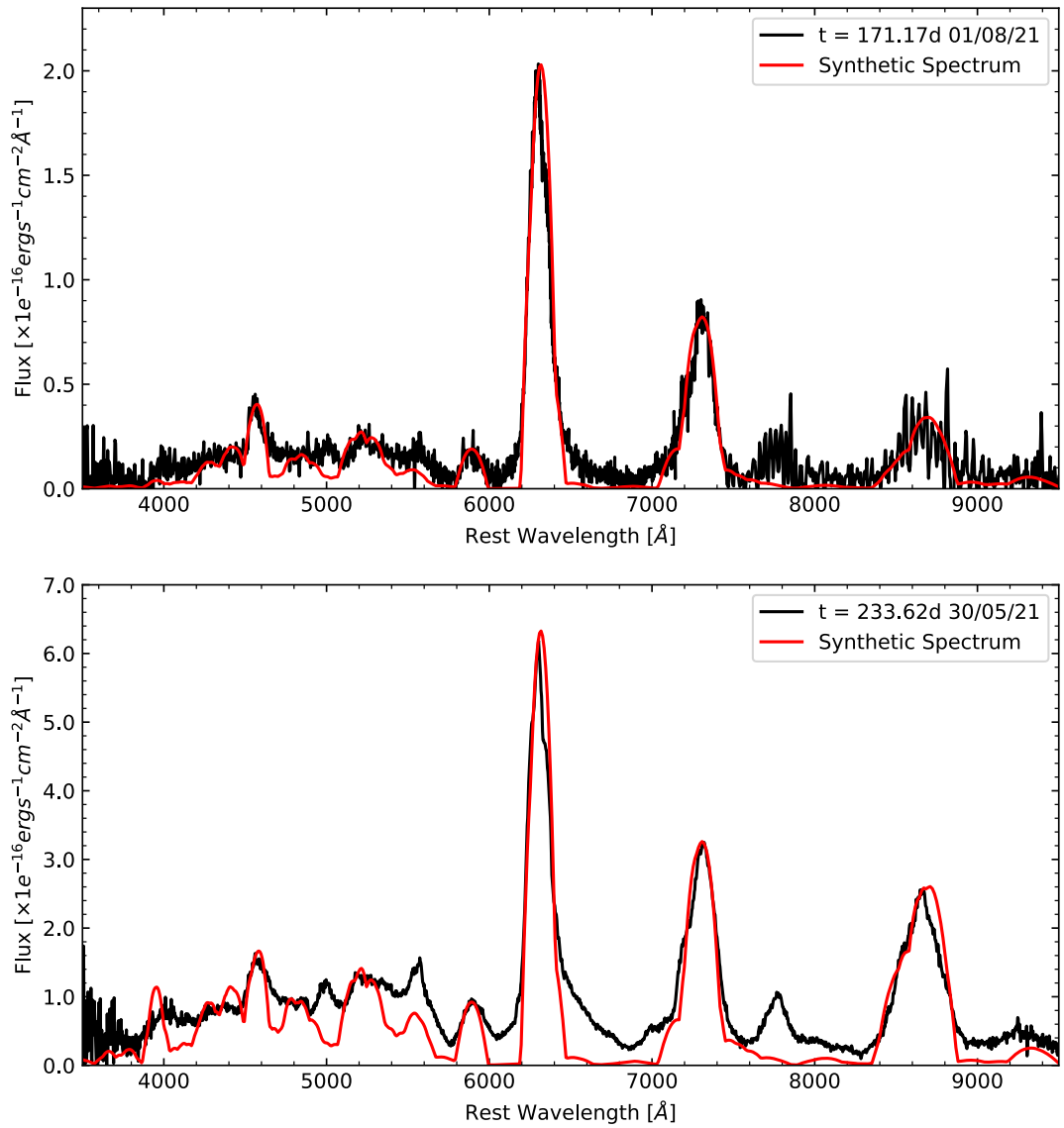


FIGURE 3.14: Nebular phase spectra (black) of SN 2020acat, taken at \sim 171.17 (top) and 233.62 (bottom) days post explosion, along with the one-zone nebular model (red) of Mazzali et al. (2001).

Two of the nebular spectra of SN 2020acat ($t = 171.17$ and $t = 233.63$) were modelled using our SN nebular spectrum synthesis code (e.g., [Mazzali et al., 2007](#)). Briefly, the code computes the emission of gamma rays and positrons by the radioactive decay of ^{56}Ni and ^{56}Co , and computes their deposition in the expanding SN ejecta, using a gamma-ray opacity $\kappa_{\text{gamma}} = 0.027 \text{gcm}^{-2}$ and a positron opacity $\kappa_{e^+} = 7 \text{gcm}^{-2}$. Following the prescriptions of [Axelrod \(1980\)](#), the deposited energy is utilised to heat the gas via collisional processes. Heating is then balanced by cooling via radiation in mostly forbidden lines. Ionization and recombination rates are balanced and the level populations within different ions is computed in non-local thermodynamic equilibrium (NLTE). The SN nebula is expected to be optically thin at late times and radiation transport is not performed. For SN 2020acat a simple one-zone version of the code is used, which allows the basic parameters of the inner ejecta to be determined without making assumptions about the density distribution. Clearly, because of such an approach, our results must be regarded as approximate. For the two spectra at ~ 231 and 170 days after explosion, a distance modulus $\mu = 32.74$ mag and a total reddening $E(B - V) = 0.0207$ mag was used to determine the spectral luminosity. The outer boundary velocity for the part of the nebula that contributes to the emission was set at 5100 km s^{-1} , based on the width of the emission lines. Given that a stratified model of the ejecta was not used, it should be expected that deposition efficiency decreases with time faster than in the real SN. This means that at later epochs somewhat larger values of the masses are required to fit the spectrum ([Mazzali et al., 2001](#)). Figure 3.14 shows the two observed spectra and the corresponding synthetic spectra. The main emission features are [O I] 6300,6363 Å, Mg I] 4570 Å, and Ca II] 7291,7324 Å. Weaker lines include [O I] 5577 Å, which is sensitive to recombination, the [O I] recombination line near 7773 Å, which is not reproduced in our model as the recombination emission, Na I D, and several [Fe II] lines, mostly near 5200 Å, which are important to determine the abundance of ^{56}Ni are not considered. The mean masses of the elements that contribute to the spectra are $M_{^{56}\text{Ni}} = 0.10 \pm 0.02 M_{\odot}$, $M_{\text{O}} = 1.0 \pm 0.10 M_{\odot}$, $M_{\text{C}} = 0.20 \pm 0.05 M_{\odot}$, $M_{\text{Ca}} = 0.045 \pm 0.005 M_{\odot}$, $M_{\text{Mg}} = 0.0012 \pm 0.0004 M_{\odot}$, $M_{\text{Na}} = 0.0008 \pm 0.0001 M_{\odot}$. Small amounts of Si and S were also included for consistency, but these elements do not produce strong lines in the optical range. The spectra do not appear to be fully nebular. In particular, a feature near

5000 Å may still have a P-Cygni profile from Fe II multiplet 42 lines. The ejected mass within the boundary velocity is $1.5 \pm 0.15 M_{\odot}$. This indicates a moderately massive CO core ($\sim 3 M_{\odot}$ under the assumption of a neutron star remnant), and is consistent with previous results for stripped-envelope SNe (e.g., [Mazzali et al., 2021](#), Figure 14), indicating a progenitor zero-age main sequence mass of $\sim 20 M_{\odot}$.

3.6 Conclusions

SN 2020acat was a well observed SN I Ib, with a highly constrained explosion date, that was thoroughly observed in the UV to NIR photometric regions during peak time, and extensive optical follow-up during the transition into the nebular phase. Spectroscopically SN 2020acat was followed for ~ 230 days resulting in a comprehensive optical campaign from pre-maximum light to the start of the nebular phase. The follow-up campaign was unfortunately halted as SN 2020acat moved into Solar conjunction and was too faint to be observed once it reappeared. The comprehensive photometric and spectroscopic data set gives SN 2020acat one of the best follow-up campaigns available for a SN I Ib caught within a few days of its explosion.

SN 2020acat displays a very fast rise, reaching the peak of the pseudo-bolometric light curve in ~ 15 days, more rapidly than other SNe I Ib. The fast rising pseudo-bolometric light curve, and the underestimation of the light curve model used in Section 3.4.3, may result from ^{56}Ni being mixed into the outer layers of the ejecta releasing trapped photons at a much faster rate than the standard SNe I Ib. However, more detailed modelling of the pseudo-bolometric light curve is required to determine the distribution of ^{56}Ni within the ejecta of SN 2020acat. Along with the fast rising pseudo-bolometric light curve SN 2020acat lacks any early time decline which is normally associated with the shock-cooling tail, which is also seen in its early time UV and optical light curves. While it might be possible that the shock-cooling phase was completely missed in the early time observations, the dim initial observation as well as the shape of the rising light curves and the tight constraint on the estimated explosion date, all suggest that SN 2020acat lacked any evident shock-cooling phase. The lack of an extended shock-cooling phase

strongly implies that the progenitor of SN 2020acat was a compact object that lacked an extended hydrogen envelope.

Modelling of the pseudo-bolometric light curve showed that SN 2020acat produced a mass of ^{56}Ni of $M_{\text{Ni}} = 0.13 \pm 0.03 M_{\odot}$ along with an ejecta mass of $M_{\text{ejc}} = 2.3 \pm 0.4 M_{\odot}$ and a kinetic energy of $E_{\text{k}} = 1.2 \pm 0.3 \times 10^{51}$ erg. When compared to other SNe I Ib, SN 2020acat was found to have synthesised a larger amount of ^{56}Ni , and produced a slightly larger ejecta mass and kinetic energy, implying that SN 2020acat originated from a more massive star than the average hydrogen rich SE-SNe. From the derived physical parameters, assuming a remnant mass of $\sim 1.5 - 2.5 M_{\odot}$, and using the set of progenitor models described in [Sukhbold et al. \(2016\)](#), a progenitor mass range of $M_{\text{ZAMS}} \approx 15 - 20 M_{\odot}$ was determined for SN 2020acat. This progenitor mass range agrees with the derived M_{ZAMS} obtained from analysis of the nebular phase spectra, which obtained a M_{ZAMS} of $\sim 20 M_{\odot}$, which together suggest that SN 2020acat likely originated from a relatively massive star.

Spectroscopically, SN 2020acat shows strong hydrogen features throughout its evolution into the nebular phase, covering the first ~ 100 days, at which point oxygen, along with calcium, starts to dominate the spectra. The clear presence of hydrogen well into the start of the nebular phase suggests that SN 2020acat possessed either a very dense thin hydrogen envelope prior to explosion or the hydrogen was mixed deep into the outer layers through some means of convection. In addition to the deep hydrogen signature within the spectra of SN 2020acat, the spectral feature usually associated with the Fe II $\lambda 5018$ line was seen to be much stronger than the surrounding Fe II lines. From analysis of the spectra at multiple epochs around peak time, it was determined that the feature was likely enhanced by the presence of a combination of helium and nitrogen within the ejecta. While the helium line that could have enhanced this feature has been reported prior, the presence of nitrogen is not expected in the spectra of SNe I Ib. One possible explanation for the origin of the nitrogen is if the progenitor of SN 2020acat was a massive enough star, then some nitrogen may still remain from the helium burning stage and appears in the spectra as weak N II features. Future work on modelling the evolution of SN 2020acat is required to investigate the potential presence of nitrogen in its spectra at early epochs.

Chapter 4

The flat-top shape of the NIR He profile of SN 2020acat

4.1 Introduction

While observations at optical wavelengths are vital due to the domination of the flux, observations at longer wavelengths are crucial for a comprehensive study of a SNe. The NIR region, between 9500 – 22000 Å, provides coverage of a critical region for the study of the helium shell within SE-SNe, especially during the late phase when the flux from the NIR region dominates the bolometric light.

Here the NIR spectra of SN 2020acat obtained throughout the optical follow-up campaign ([Medler et al., 2022](#)) are presented. Firstly in Section 4.2, an overview of the analysis done on SN 2020acat is given, discussing the results obtained from the photometry and optical spectra. In Section 4.3, the acquisition of the NIR spectra and discuss the evolution of the NIR spectra of SN 2020acat are discussed. In Section 4.4, the presence and origin of flat-topped P-Cygni profiles seen within other SNe are considered. In Section 4.5, the structure of the NIR helium features seen in SN 2020acat are analysed. Then in Section 4.6, look is taken at other SNe Iib NIR spectra to determine how unique the flat-topped helium structure is within other SNe Iib. Finally in Section 4.7, the conclusions from analysis of the NIR spectra of SN 2020acat and other SNe Iib are

given. Work from this chapter is published in [Medler et al. \(2023\)](#). The work in this chapter was primarily done by myself, except for the observations and data reduction which were done by Melissa Shahbandeh, and Ben Shapee and the spectral modelling done by Jacob Teffs.

4.2 SN 2020acat optical analysis

SN 2020acat was a rapidly rising SN I Ib caught within ~ 1 day of explosion on December 9th 2020 ($\text{MJD}_{exp} = 59192.01$) at a redshift of $z = 0.0079$ ([Medler et al., 2022](#)). SN 2020acat underwent a thorough follow-up campaign with photometric observations ranging from the Ultra-Violet (UV) to NIR bands, along with comprehensive optical spectroscopic coverage. Analysis showed that SN 2020acat had a very fast rise time for a SNe I Ib, reaching a bolometric peak of $L_{peak} = 3.09^{+1.28}_{-0.90} \times 10^{42} \text{ erg s}^{-1}$ in 14.6 ± 0.3 days, approximately 4–5 days faster than typical SNe I Ib. [Medler et al. \(2022\)](#) estimated that SN 2020acat had a ^{56}Ni mass of $M_{\text{Ni}} = 0.13 \pm 0.02 M_{\odot}$, along with an ejecta mass of $M_{\text{ejc}} = 2.3 \pm 0.3 M_{\odot}$, and a kinetic energy of $E_k = 1.2 \pm 0.2 \times 10^{51} \text{ erg}$. While the ejecta mass is average for SNe I Ib, both the ^{56}Ni mass and the E_k produced by SN 2020acat are slightly larger (see [Lyman et al., 2016](#); [Prentice et al., 2019](#)). The optical spectra of SN 2020acat initially displayed prominent hydrogen and helium lines, with a strong $\text{H}\alpha$ signature lasting for ~ 100 days. In the nebular phase, oxygen emission dominates over calcium. Finally, from analysis of photometry and spectra [Medler et al. \(2022\)](#) suggested that SN 2020acat originated from a compact progenitor with an initial mass of M_{ZAMS} between 15 – 20 M_{\odot} .

4.3 NIR Spectra

The NIR spectra of SN 2020acat were obtained using the Near-Infrared Echellette Spectrometer (NIREs: [McLean et al., 1998](#)) mounted on the 10m Keck 2 telescope based at

TABLE 4.1: Observational details for the NIR spectra of SN 2020acat. Phase is given from explosion date ($\text{MJD}_{exp} = 59192.01$) and given in rest frame. Air mass is the average air mass over the observation period.

UT date	MJD	Phase [days]	Instrument	Telluric STD	Air Mass	Exposure [s]
24 – 12 – 2020	59207.66	15.53	NIRES	HIP54815	1.16	1200
23 – 02 – 2021	59268.33	75.72	NIRES	HIP54815	2.54	1200
22 – 04 – 2021	59326.33	133.27	NIRES	HD asdf	1.16	1200
24 – 05 – 2021	59358.34	165.02	NIRES	HD asdf	1.37	1200

the W. M. Keck Observatory in Hawaii¹. The NIR spectra were reduced using the reduction software SpeX² (Rayner et al., 2003; Cushing & Vacca, 2004) and were corrected for telluric effects using AV0 standard stars and the package Xtellcor (Vacca & Cushing, 2003). Details on individual spectra are given in Table 4.1, with the phase given relative to the explosion date taken from Medler et al. (2022). The evolution of the NIR spectra of SN 2020acat is shown in Figure 4.1, where all spectra have been corrected for redshift and normalised to the average continuum flux of the spectrum.

Initially, the day 15.53 spectrum displays a predominantly featureless continuum with only the hydrogen $Pa\beta$ 1.2838 μm and He I 1.0830 μm and 2.0581 μm features visible. At this phase there is also a small noisy feature redwards of the He I 1.0830 μm peak. This is associated with the O I 1.1290 μm . As SN 2020acat evolves, features of heavier elements become more pronounced, with the O I 1.1290 μm , Ca II 1.1839 μm and 1.1950 μm lines, along with the Mg I 1.1828 μm , 1.4878 μm and 1.5033 μm lines, emerging in the day 75.72 spectrum. At this epoch the helium features start to transition from a smooth P-Cygni profile into a more flat-topped shape. Along with the change in shape, the two features develop a small peak-like feature just redward of the emission wavelength. The presence of these small peaks in both features dismisses the possibility that the peak by the He I 1.0830 μm line is the result of either the $Pa\gamma$ line or other elements. As the spectra evolve further, the O I 1.1290 μm and Mg I 1.5033 μm lines become narrower. By day 133.27 both helium features display a flat-topped profile, while continuing to exhibit the small red peaks. The He I 1.0830 μm peak exhibits a slight slope, declining from the blue edge of the flat-top, with the He I 2.0581 μm feature

¹<https://www.keckobservatory.org/>

²<http://www2.lowell.edu/users/massey/manual.pdf>

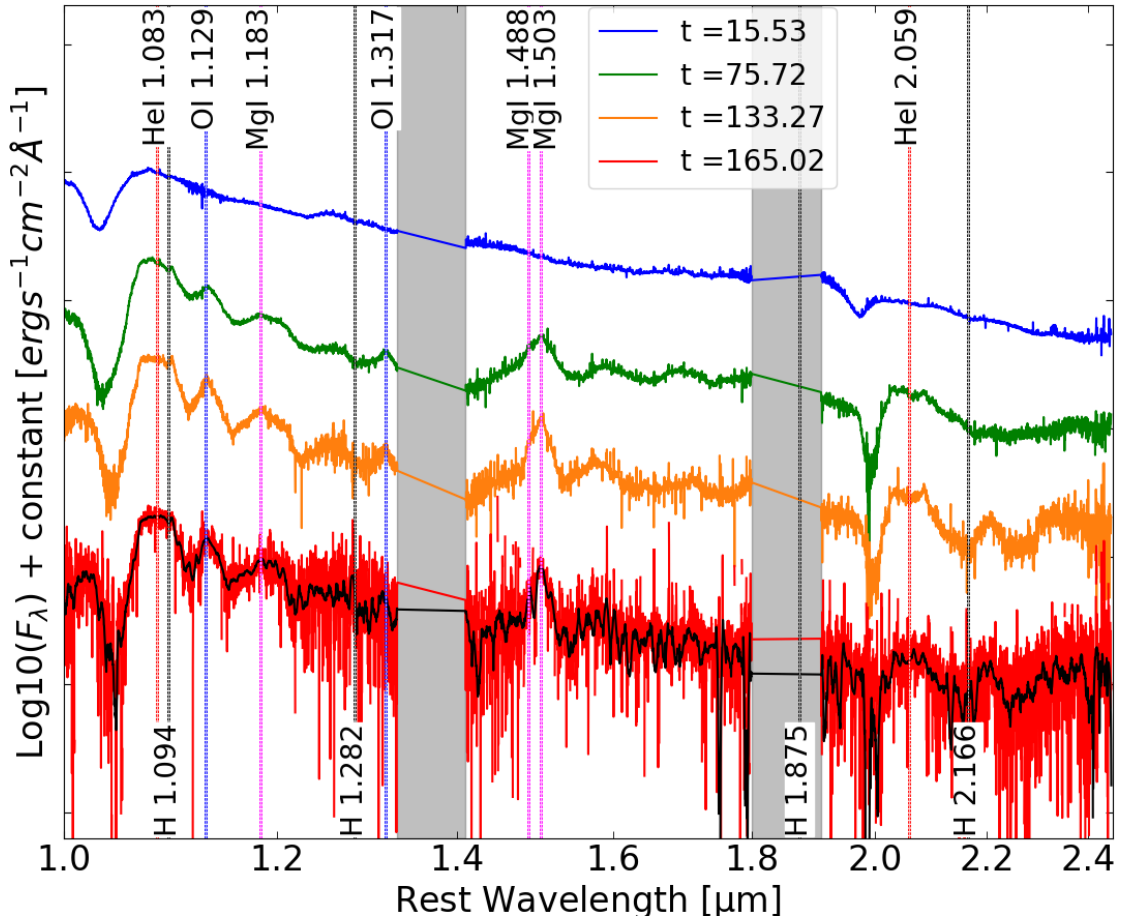


FIGURE 4.1: NIR spectroscopic evolution of SN 2020acat, corrected for redshift with telluric contamination (shaded regions) removed. The main emission lines are given by dashed lines. Phases are given relative to explosion date and given in rest frame. The black spectrum shows the smoothed day 165.02 spectrum, allowing a better view of spectral features.

displaying a more symmetrical top centred on the rest wavelength of the emission line. At this epoch an additional feature emerges around $2.2 \mu\text{m}$, which may be associated with the Na I $2.2090 \mu\text{m}$ line. Unfortunately the spectrum taken on day 165.02 had a very low signal to noise ratio (S/N), making the identification of any weak lines quite difficult. A Savitzky-Golay smoothing filter was applied to this spectrum using the python SciPy (Virtanen et al., 2020) function `savgol_filter`³, which allowed the weaker features of the spectrum to be shown more clearly. As with the other late time spectra, clear features of He I $1.0830 \mu\text{m}$ and $2.0581 \mu\text{m}$, O I, and Mg I were seen, along with the $2.2 \mu\text{m}$ feature.

³https://docs.scipy.org/doc/scipy/reference/generated/scipy.signal.savgol_filter.html

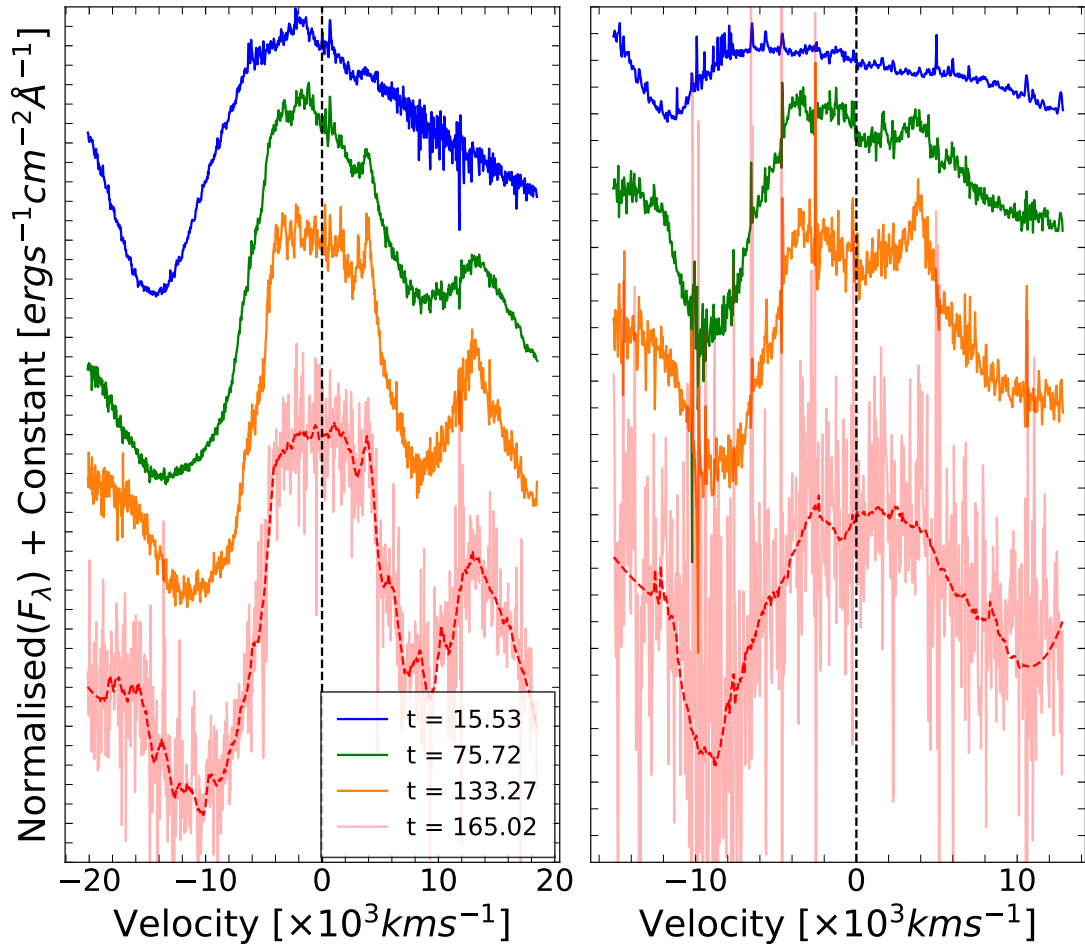


FIGURE 4.2: Velocity evolution of the He I 1.0830 μm and 2.0581 μm lines. The flat-top feature of the He I 1.0830 μm line develops the day 75 and 133 spectra, while the He I 1.0830 μm and 2.0581 μm line develops earlier between the day 15 and 75 spectra.

4.4 Flat-topped P-Cygni profiles

P-Cygni profiles are spectral features formed from the combination of a strong blue-shifted absorption component, created by material moving towards the observer absorbing light originating from deeper within the material, and an emission peak around the emission wavelength, produced by the expanding ejecta moving in all directions (Fransson, 1984). However not all P-Cygni profiles display the symmetric emission peak centred around the rest wavelength of the line. Friesen et al. (2012) modelled the behaviour of resonance-scattering line profiles resulting in the development of both the commonly seen P-Cygni and a diversity of other line profile shapes. They found that the shape of the emission peak was strongly influenced by the optical depth of the emission

TABLE 4.2: Line velocity of the He I 1.0830 μm and 2.0581 μm lines derived from fitting the absorption minimum with a Gaussian fit. Associated errors obtained from fitting errors and noise within the spectra.

Phase [days]	He I 1.0830 μm velocity [$\times 10^3 \text{ km s}^{-1}$]	He I 2.0581 μm velocity [$\times 10^3 \text{ km s}^{-1}$]
15.53	14.4 ± 0.4	11.7 ± 0.5
75.72	13.3 ± 0.9	9.3 ± 1.0
133.27	11.4 ± 0.9	8.7 ± 0.9
165.02	10.7 ± 0.9	8.6 ± 3.6

region, with the flatter peaks emerging as optical depth was decreased. Flat-topped P-Cygni profiles have been observed in the late time spectra of the Type II-pec SN 1987A (Bevan, 2015) and the NIR [Fe II] 1.257 μm and 1.644 μm lines of the Type Ia SN 2003hv (Motohara et al., 2006). In these cases, the flat-topped regions were associated with a low dust optical depth and a central region of iron-peak elements lacking enough ^{56}Ni to power the iron line emission respectively. While the underlying physics of these flat-top regions may be similar, the physical conditions of each case are drastically different. The lack of ^{56}Ni -rich ejecta associated with SN 2003hv is unlikely to cause the flat-topped profiles in SN 2020acat due to the drastically different explosion mechanisms of SNe Ia and SNe IIb. However the physics of the flat-topped models described by Bevan (2015), where there is a central region of low optical depth, may explain the shape of the helium NIR lines seen in SN 2020acat.

4.5 Helium 1.0830 & 2.0581 μm Features

Of all the NIR lines discussed in Section 4.3, the helium lines display the most drastic change as SN 2020acat evolves. The evolution of the He I 1.0830 μm and 2.0581 μm features is shown in Figure 4.2, with the corresponding line velocity given in Table 4.2. In the earliest spectrum both helium features display broad P-Cygni profiles, as expected from spherically symmetric ejecta expanding at high velocity. The He I 1.0830 μm line displayed a faster overall velocity, falling from 14400 to 10700 km s^{-1} , compared to the He I 2.0581 μm line, which declined from 11700 km s^{-1} to 8600 km s^{-1} . It should be noted that the final velocity of the He I 2.0581 μm line has a much greater uncertainty

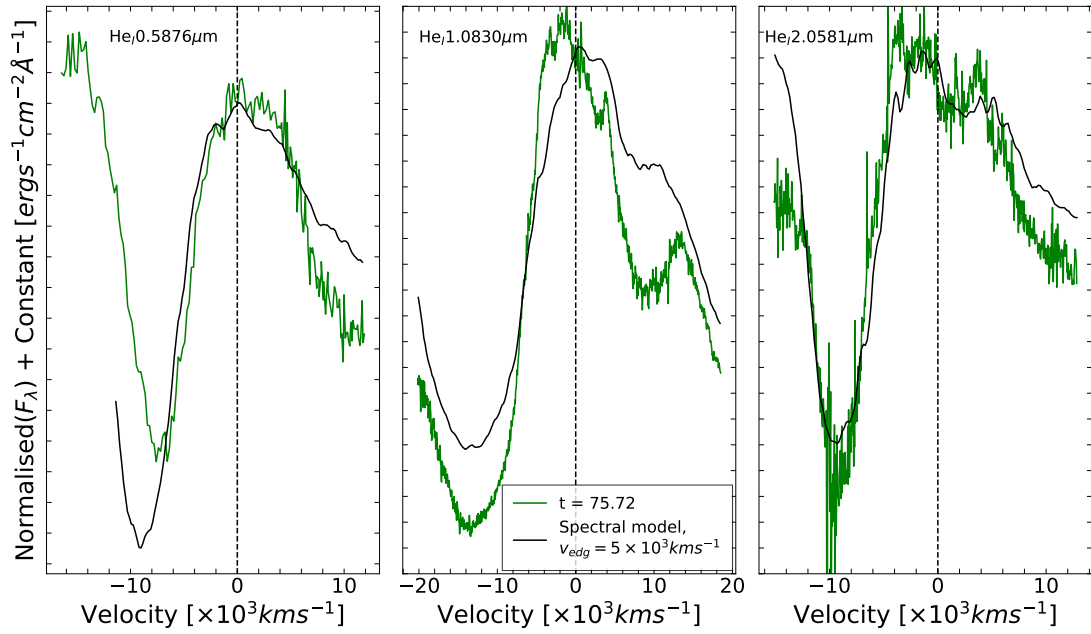


FIGURE 4.3: The spectral model constructed by fitting the photospheric phase optical spectra and extended into the NIR region. The emission from the helium shell below $\sim 5000 \text{ km s}^{-1}$ was included in an attempt to reproduce the flat-top shape that starts to emerge in the NIR features around ~ 75 days post explosion.

compared to the other velocities due to the spectrum's very low S/N at this epoch. The He I 2.0581 μm line velocity declines rapidly between days 15.53 and 75.72, roughly twice the decline seen in the He I 1.0830 μm line velocity during this period. This is likely due to the weakness of the He I 2.0581 μm compared to the He I 1.0830 μm line. However, after the initial rapid decline the two line velocities continue to evolve at a similar pace.

Along with the broad nature of the profiles, the initial spectrum's emission peaks are both blue-shifted by several tenths of a micron with respect to the rest wavelength. As the spectrum evolves the peaks of the He I lines shift closer to their rest wavelengths and become flatter in shape. This is first seen clearly in the day 133.27 spectrum, where the features appear flat-topped with distinct cutoffs on either side of the lines' rest wavelength, and is still visible in the day 165.02 spectrum. The presence of a small peak just red of both He I lines is also interesting. This small peak was originally interpreted as resulting from the *Pa* γ 1.094 μm line. However, a small peak is also seen near He I 2.0581 μm , at a similar displacement from the emission line, in a region with no associated hydrogen or heavy element emission lines. This strongly suggests that

TABLE 4.3: v_{edg} obtained from fitting the flat-topped He I 1.0830 μm and 2.0581 μm emission peaks.

Phase	He I 1.0830 μm	He I 2.0581 μm
[days]	v_{edg} [$\times 10^3 \text{ km s}^{-1}$]	v_{edg} [$\times 10^3 \text{ km s}^{-1}$]
75.72	4.0 ± 0.5	3.9 ± 0.5
133.27	3.7 ± 0.5	3.9 ± 0.5
165.02	3.6 ± 1.0	3.6 ± 1.0

the small peaks are not due to different emission lines, and instead mark the start of the helium emission shell, placing a strong constraint on the lower limit of the helium shell velocity.

The day 75 spectrum was compared with a synthetic spectrum in Figure 4.3. This model is a modified version of the model described in Teffs et al. (2020), where helium was removed below a velocity of 5000 km s^{-1} , that was fit to photospheric phase spectra evolves out to ~ 75 days post explosion. The synthetic spectrum was computed using a Montecarlo SN spectrum synthesis code (Mazzali, 1993; Lucy, 1999; Mazzali, 2000) and includes a non-thermal module for the treatment of He I (Hachinger et al., 2012). Unfortunately the depth of the He I 0.5876 μm and 1.0830 μm absorption features are not well fit in the synthetic spectrum, however the aim of the modelling was to reproduce the shape of the NIR helium lines while maintaining the standard P-Cygni profile of the He I $\lambda 5876$ line this is of little concern. The synthetic spectrum is able to reasonably reproduce the flat-topped P-Cygni profile of both NIR Helium features while producing the expected P-Cygni profile that was observed in the optical spectra, Medler et al. (2022). While the synthetic spectrum reproduces the small red peak seen in both Helium lines, a feature expected as a result of a sharp inner cut-off of the helium shell, the model fails to reproduce the He I 1.0830 μm feature in detail. This is likely caused by the contribution of other lines in this region such as C I, Si II.

The widths of the flat-topped peaks were determined by fitting a Super-Gaussian function to the He I 1.0830 μm and 2.0581 μm peaks. The fit allows for the edges of the flat-top to be determined, while also fitting to the shape of the emission profile outside this region. It was assumed that the peaks are symmetrical around the rest wavelength once the flat-topped shape emerged. The edge velocities, v_{edg} , of the helium lines

are given in Table 4.3, with errors arising from the fitting of the Gaussian and the S/N of the spectra. As SN 2020acat evolves, the width of the flat-top decreases as ejecta expand and the density of the emitting helium shell appears to decrease slightly, although this is within the uncertainty of the measurement. The existence of a minimum helium velocity indicates that the helium shell was not mixed down into the inner ejecta. To investigate the possibility of a non-mixed helium shell, the velocity of the [O I] 6300, 6363 feature are compared with the width of the flat-topped He I 1.0830 μm and 2.0581 μm features. This comparison allows for the boundary between the inner helium shell and the shell of O-rich material to be probed. At both epochs the Full-Width Half-Maximum (FWHM) of the [O I] emission peak coincides with the v_{edg} of the helium shell to within $\sim 100 \text{ km s}^{-1}$ (see Figure 4.4). The lack of overlap between the helium and oxygen velocities strongly implies that the bulk of the two shells were not mixed prior to explosion.

4.6 SNe I Ib Helium Structure

The flat-topped He I 1.0830 μm and 2.0581 μm features seen in the late time spectra of SN 2020acat imply a cut off to the helium shell at low velocity. The question arises whether this feature is unique to SN 2020acat or if it was seen in other SNe I Ib. At early times ($t < 60$ days), when the majority of NIR observations are obtained (Shahbandeh et al., 2022), SN 2020acat does not clearly show flat-topped helium features as the photosphere had not yet receded deep enough into the inner ejecta. As such, only SN 2008ax (Taubenberger et al., 2011) and SN 2011dh (Ergon et al., 2015) possess observations, with high enough S/N, to allow for good comparisons with SN 2020acat. The late-time He I 1.0830 μm and 2.0581 μm features of SN 2020acat are compared with those of SN 2008ax and SN 2011dh, obtained 11 – 06 – 2008 and 16 – 12 – 2011 respectively, in Figure 4.5. It should be noted that the NIR spectrum of SN 2011dh does not extend to the He I 2.0581 μm line, so only SNe 2008ax and 2020acat are displayed in Figure 4.5 (right panel).

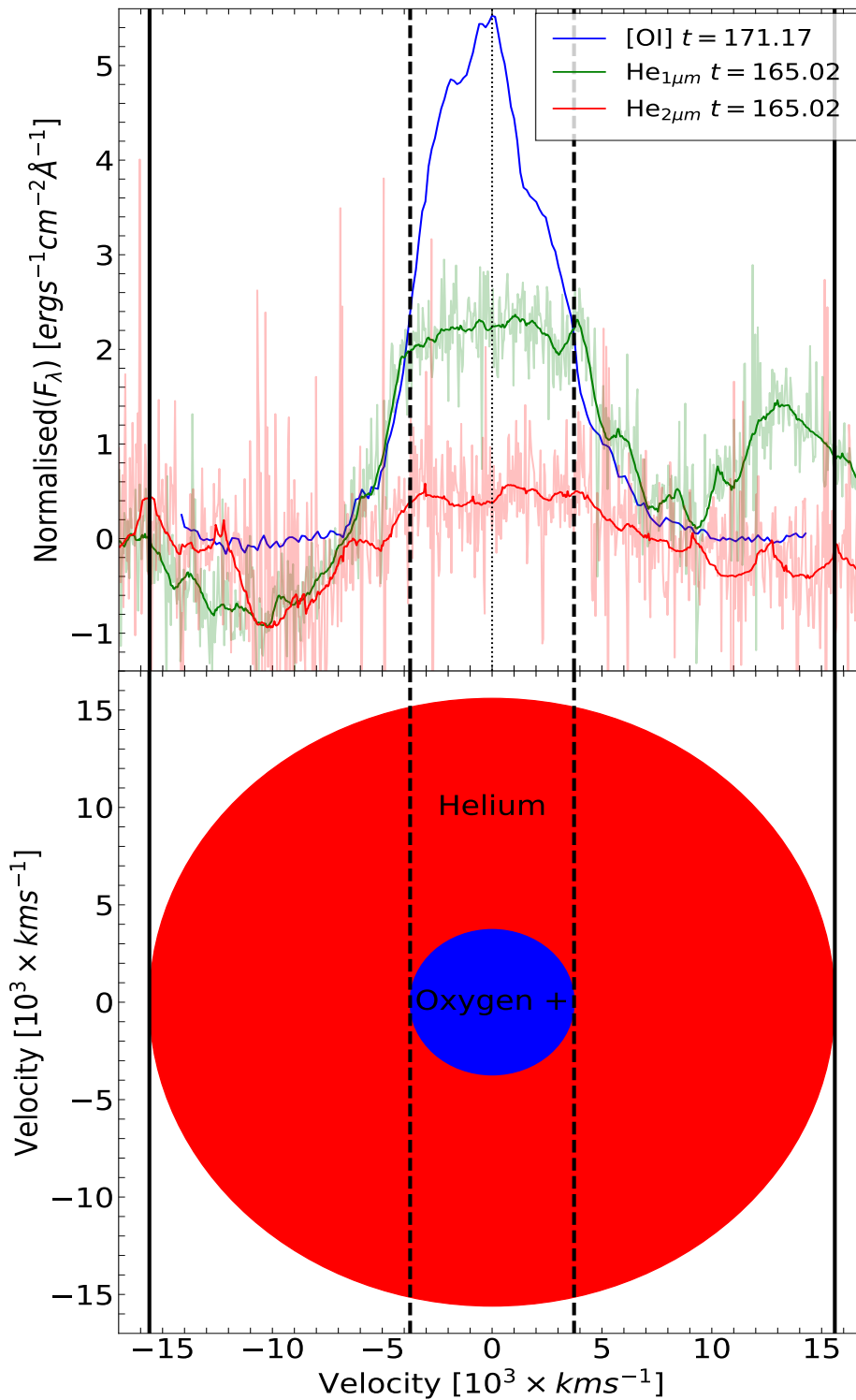


FIGURE 4.4: Top: Comparison of the late time [O I] 6300, 6363 peak and the smoothed NIR He I features. All features have been scaled to the continuum. The solid, dashed and dotted vertical lines correspond to the Helium shell v_{edg} , the FWHM of the [O I] feature and the emission wavelength of each feature respectively. Bottom: Structure of the He/O-rich shells in the progenitor of SN 2020acat, under the assumption of optically thin ejecta, corresponding to the velocities derived from the spectra.

SN 2008ax seems to also display these narrow flat-topped NIR helium profiles, while SN 2011dh displays only a strong emission profile. When compared to SN 2020acat, the He I 1.0830 μm feature of SN 2008ax exhibits a more prominent slope along the top of the feature peaking at the blue edge of the flat-top. On the other hand, the He I 2.0581 μm line shows more of a symmetric double peak centred on the emission line, similar in nature to the line seen in the day 133.27 spectrum of SN 2020acat, although significantly narrower. It was initially suggested that the shape of the He I 1.0830 μm and 2.0581 μm lines in SN 2008ax may result from a non-uniform distribution of ^{56}Ni within the ejecta (Taubenberger et al., 2011). However, Maurer et al. (2010) suggested that the cause of flat-top shape seen in SN 2008ax was instead the result of a torus-shaped distribution of helium, along with an additional asymmetry along the line of sight to induce the strong blue peak seen in the He I 1.0830 μm line. Their models confined the majority of heavy elements to within the core with some mixing between the inner elements and the bottom of the helium shell.

The question remains what could cause the helium features to display flat-topped shapes in SNe 2008ax and 2020acat, but not in SN 2011dh. The flat-topped profiles may be explained by stellar evolution, where the He shell does not mix with the inner regions which have a much higher molecular weight. However, there are several possibilities that could give rise to flat-topped profiles, including asphericity in the explosion which could lead to element mixing in velocity space (e.g. Mazzali et al., 2005). The observed line profiles would then depend on the orientation of the line of sight. The small number of SNe I Ib with late time NIR spectra, however, means that this suggestion is speculative in nature and requires a more extensive data set to determine its validity.

4.7 Conclusions

SN 2020acat displays interesting NIR spectra, which are dominated by the NIR helium lines and at later times display strong oxygen and magnesium lines. The He I features display a curious evolution, transitioning from a standard P-Cygni profile during the photospheric phase into a more flat-topped shape at late times. From the width of the

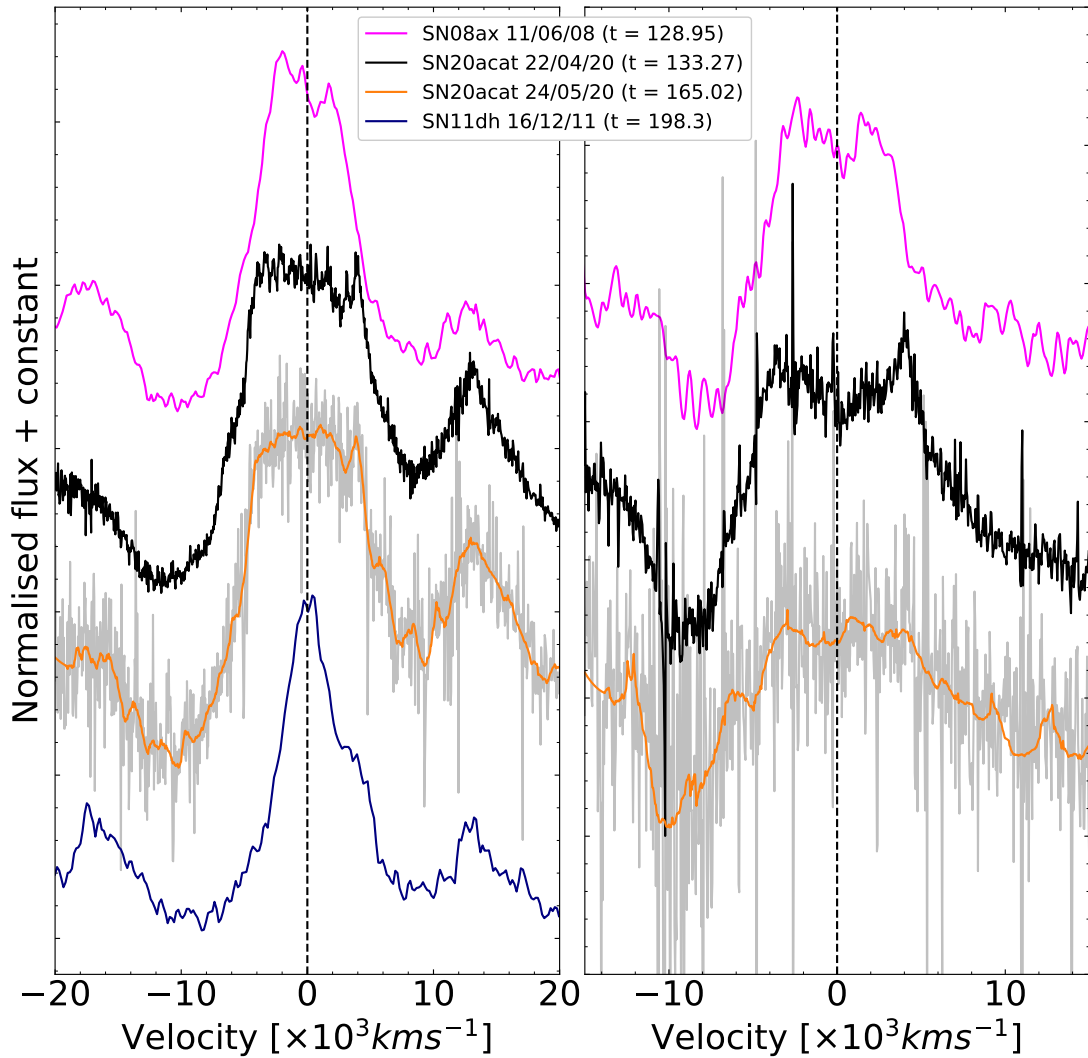


FIGURE 4.5: Comparison of the He I 1.0830 μm (left) and the He I 2.0581 μm (right) feature within the late time spectra of SN 2008ax (magenta), SN 2011dh (blue) and SN 2020acat (black and orange).

two flat-topped peaks a lower limit on the velocity of the helium shell was obtained. Fitting the flat-top features revealed a minimum velocity of the helium shell of around $\sim 4.0 \pm 0.5 \times 10^3 \text{ km s}^{-1}$, which seem to slightly decline to a final velocity of $\sim 3.6 \pm 1.0 \times 10^3 \text{ km s}^{-1}$ roughly 90 days later. The shape of these features are thought to originate from a lack of emitting helium within the ejecta material brought about by a low optical depth within the central region of the ejecta. Through a comparison with the [O I] 6300, 6363 emission peak it was found that there is a lack of overlap between the helium and oxygen features, strongly suggesting that there is little or no mixing between the He/O-rich shells.

Once the flat-topped helium features were identified, a comparison with other SNe I Ib NIR spectra was done to determine if the features were unique to SN 2020acat. Due to the lack of late-time NIR observations for SNe I Ib, only SN 2008ax and SN 2011dh possessed spectra that could be compared with SN 2020acat. While SN 2008ax displayed a similar flat-topped feature, although significantly smaller in width, SN 2011dh displayed a sharp emission profile expected for spherically symmetric ejecta. A non-spherically shaped helium shell is likely to be the origin for the flat-topped profile seen in SN 2008ax and SN 2020acat, which may be linked to the structure of their progenitors. If the feature is indeed linked to the nature of the SNe progenitor, it may be used to determine the structure of the progenitor of events with limited observations, so long as late time NIR spectra are obtained. However, due to the limited number of SE-SNe NIR spectra, a larger sample of NIR spectra is currently needed to confirm the connection between progenitor structure and shape of the NIR helium feature.

Chapter 5

The study of SN 2019oyw and an initial inspection of the $M_{\text{ejc}}/E_{\text{k}}$ relation in He-poor stripped-envelope supernovae.

5.1 Introduction

In contrast to the minimal stripping that SNe IIb undergo prior to core-collapse, SNe Ic have all of its hydrogen and at least the majority of its helium envelope removed before exploding. They have been stripped down to their O-rich shell and exhibit distinct oxygen and calcium lines throughout their spectral evolution (Filippenko, 1997). In addition to being dominated by heavier elements, SNe Ic can display line velocities, kinetic energies and ejecta masses vastly higher than those seen in other SE-SNe (Taddia et al., 2018; Prentice et al., 2019). For the SNe Ic that possess the largest kinetic energy, a significant portion of them are detected in conjuncture with GRB. The connection between those SNe Ic-BL that are associated with a GRB and those that lack a GRB detection has been suggested to result from a delay in the launching of the jet from a compact central engine (Fan et al., 2011). However, Nakar (2015) has suggested that this transition can be explained by the failure of the jet to break through the outer envelope of the

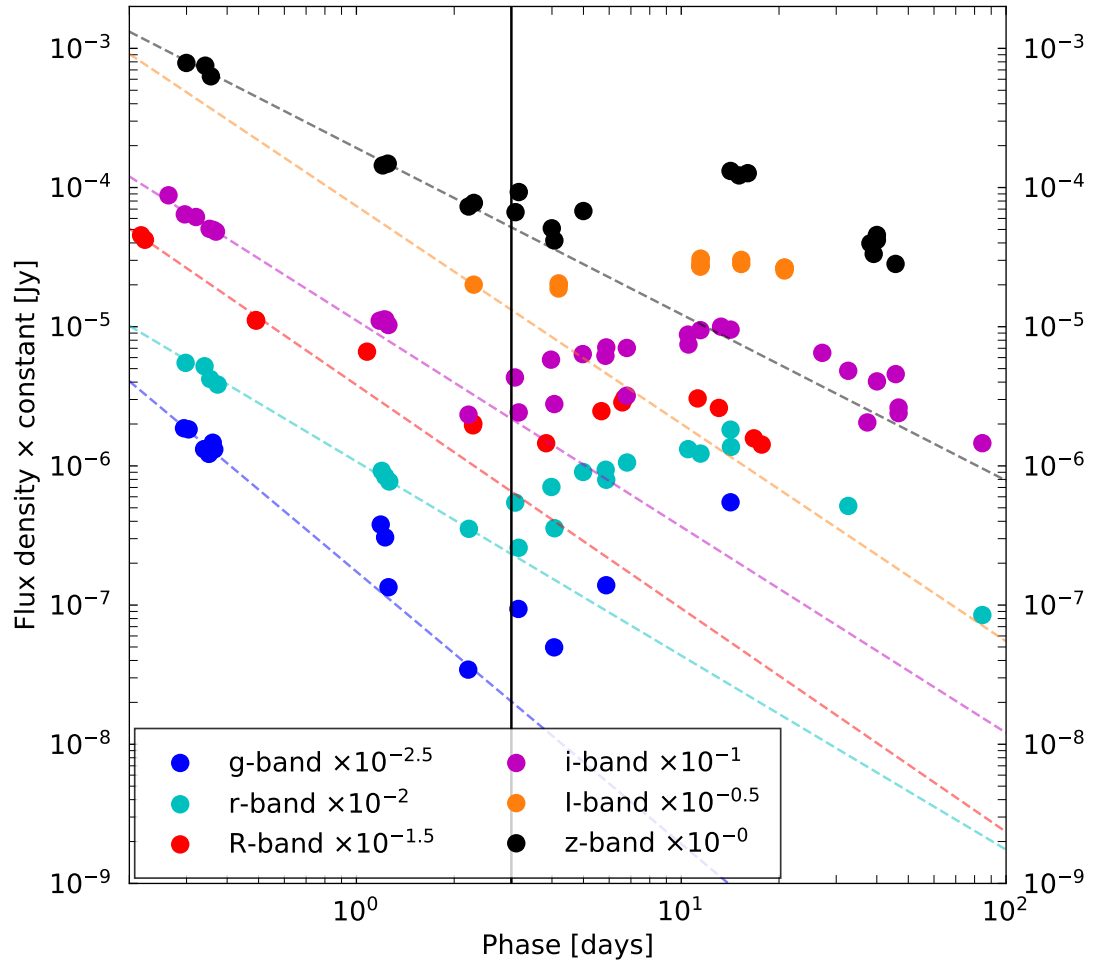


FIGURE 5.1: Photometric observations of GRB 190829A/SN 2019oyw. Each band has been corrected for extinction, redshift, shifted by a constant value and are shown in the rest phase frame. The uncertainty for the observations are not shown for clarity. The dashed lines indicate the power law fit to the GRB afterglow which dominates $t < 3$ days post detection. The solid vertical line denotes the transition between GRB afterglow and SN being the dominant component to the light curve.

progenitor. An analysis of the evolution of the energy-mass relation from standard SNe Ic to GRB-SN can shed light on the population of He-poor SE-SNe.

In this chapter the photometric and spectroscopic observations of SN 2019oyw covering a ~ 90 day period are presented. Initially a brief discussion of the GRB component of SN 2019oyw is presented in Section 5.2. Then in Section 5.3, a discussion about the properties of the optical photometry obtained from GRB 190829A/SN 2019oyw along with the removal of the GRB afterglow is given. From the corrected photometry the pseudo-bolometric light curve of SN 2019oyw is discussed in Section 5.4 to the peak luminosity and rise time of SN 2019oyw, which is then compared to other GRB-SNe.

Then in Section 5.5, the analysis of the spectra of SN 2019oyw is presented, a comparison of the evolution of SN 2019oyw with other SNe Ic-BL is shown and a new classification for SN 2019oyw is discussed. In Section 5.4 the physical parameters of SN 2019oyw determined through the use of several methods are discussed. After that an examination of the energy-mass relation for He-poor SE-SNe is given in Section 5.7. Finally Section 5.8 gives a summary of the photometric and spectroscopic analysis of SN 2019oyw. The work within this chapter is primarily my own, with the exception of the observations and data reduction which was taken by multiple groups and is discussed in more detail in Section 5.3.

5.2 The GRB associated with SN 2019oyw

SN 2019oyw was discovered coincident with GRB 190829A, a long-duration GRB that was initially observed by the *Fermi* satellite on the 29th of August 2019 at 19 : 55 : 53 UT (MJD 58724.66) (Fermi GBM Team, 2019). GRB 190829A was also detected by the Burst Alert Telescope (BAT) aboard the *Swift* satellite approximately 1 minute after the *Fermi* detection (Dichiara et al. (2019)). From the BAT observations it was determined that GRB 190829A possessed a T_{90} , the time between 5% and 95% of the counts are observed, with a value of $T_{90} = 58.2 \pm 8.9$ s (Lien et al., 2019).

GRB 190829A displayed two peaks within the GRB light curve, one around the initial detection and a second stronger peak around 50s later (Hu et al. (2021)). The time-averaged spectrum from the initial *Swift* observation was best fit with a cut-off power law with a photon index of $\alpha = -1.56^{+0.07}_{-0.08}$ and a peak energy cut-off of $E_{\text{p}} = 123.51^{+56.14}_{-31.61}$ keV. For the second burst the time-averaged spectrum was best fit with a *Band*-function peaking at an energy of $E_{\text{p}} = 11.23^{+0.30}_{-0.32}$ keV while possessing a low-energy spectral index of $\alpha = -0.23^{+0.26}_{-0.24}$ and a high-energy index of $\beta = -2.53^{+0.01}_{-0.01}$ (Hu et al. (2021)). The low-energy spectral index found in the second burst is far lower than the expected limit for synchrotron radiation, $\alpha = -1.5$, a feature that is seen in other GRBs, such as GRB 080916C and GRB 080825C (Wang & Dai (2021)). The double peaked nature of the emission from GRB 190829A was also observed in events such as GRB 180728A,

with Wang et al. (2019) proposing the use of a Binary-driven hypernova type II model (BdHN II) as the cause of the observed light curve as an alternative to the collapsar model.

After 4.09 days from the initial detection the spectrum of GRB 190829A displayed an underlying SN component that greatly resembles that of GRB 980425/SN 1998bw. The question over whether the similarity between GRB 190829A/SN 2019oyw and GRB 980425/SN 1998bw remains at later epochs, during the SN dominated phase, is discussed below.

5.3 Photometry

Multi-band optical photometry of SN 2019oyw was obtained from the 2.0m Liverpool Telescope (LT) using the IO:O camera, the 8.2m Very Large Telescope (VLT) using the FORS2 acquisition camera. Additional *R*-band photometry was obtained using the Crimean Astrophysical Observatory (CrAO) using 2.6m ZTSh telescope, the Simeiz Observatory located at Mt. Koshka using the 1.0m Zeiss-1000 telescope, and the Maidanak Observatory using 1.5m AZT-22 telescope. The *R*-band observations were used to obtain the temporal decay index for the *I*-band to remove the afterglow contribution, the process of which is explained below. These observations range from hours after the initial detection of GRB 190829A to several months post explosion. All data have been reduced using standard pipelines, corrected for both host and galactic extinction using a total extinction of $E(B - V) = 1.089$ taken from (Chand et al., 2020), and presented in rest frame in Figure 5.1 alongside the observations from (Hu et al., 2021). The additional photometry of GRB 190829A/SN 2019oyw presented here are given in Table L1 without corrections for extinction, k-correction and GRB afterglow.

5.3.1 GRB afterglow

The *grRiz*-band observations taken prior to 3 days post detection, which were all dominated by the GRB afterglow, were fit with a single power law function. The fit in each band was weighted with the uncertainty related to the observations, to determine

TABLE 5.1: Optical band temporal flux decay indices, α_{opt} , from fitting a single power law model to the *grRiz*-band photometry obtained prior to 3 days post GRB, both those values found from this work and those taken from [Hu et al. \(2021\)](#).

band	α_{opt}	literature α_{opt}
<i>g</i>	1.96 ± 0.06	1.77 ± 0.08
<i>r</i>	1.39 ± 0.06	1.45 ± 0.01
<i>R</i>	1.48 ± 0.09	-
<i>i</i>	1.48 ± 0.08	1.53 ± 0.13
<i>z</i>	1.20 ± 0.02	1.25 ± 0.01

the temporal flux decay indices, α_{opt} , of GRB 190829A, the results of which are given in Table 5.1. The lack of *I*-band afterglow photometry prohibited the fitting of a power law model. Instead, the difference between the *r* and *R*-band α values was used, in conjunction with the *i*-band α_i value, to determine a value for α_I . This was done because of the similarity in central wavelength and coverage between the SDSS and the Johnson-Cousins filters for the *r/R*-band and the *i/I*-bands. We do not expect this to add significant error to the SN *I*-band light curve as a result of the well covered afterglow region of the *r*, *R* and *i*-bands of SN 2019oyw. The temporal flux decay indices found for the optical photometry of SN 2019oyw are in agreement with the average temporal decay index found for the *griz*-bands in [Hu et al. \(2021\)](#). The trend seen in the α_{opt} of SN 2019oyw, as wavelength increases α_{opt} decreases is expected as the peak of the synchrotron radiation transitions to longer wavelengths as the GRB fades. The break from this trend seen with the α_r may result from additional $\text{H}\alpha$ flux that dominates the *r*-band region of the electromagnetic spectrum. While irregular a similar trend for the evolution of α_{opt} was also seen by [Hu et al. \(2021\)](#) as shown in Table 5.1. The average value of α_{opt} found for SN 2019oyw, $\alpha_{\text{opt}} \approx 1.5$ is slightly greater than the average value, $\alpha_{\text{opt}} \approx 1.2 \pm 0.1$ found from the analysis of 87 GRB-SNe by [Dainotti et al. \(2022\)](#) although still within the distribution seen with other GRB-SNe. The post-break optical photometry was then corrected for the extrapolated GRB afterglow to determine the magnitude of the SN 2019oyw light curves. Once the photometry was corrected for both the GRB contribution and redshift, a low order polynomial was fit to the photometry between day 3 and 40 to determine the rise time and peak magnitude of each band, both of which are given in Table 5.2. The lack of comprehensive coverage around and post peak in several bands lead to a large uncertainty on the determined light curve

TABLE 5.2: Rise time and peak magnitudes of $rRiIz$ -bands obtained from the fitting of a low order polynomial. The g -band is not included as the lack of post peak observations made the fit unreliable. Rise time is in rest phase from initial detection.

band	rise time [days]	peak apparent [mag]
r	16.32 ± 1.24	18.37 ± 0.49
R	10.31 ± 0.75	18.80 ± 0.26
i	17.22 ± 1.33	18.79 ± 0.55
I	15.52 ± 1.14	18.84 ± 0.32
z	17.12 ± 1.32	18.64 ± 0.54

parameters.

5.3.2 Photometry of SN 2019oyw

The absolute magnitude r -band light curve of SN 2019oyw was compared with the R -band light curve of the typical SNe Ic-BL SN 1998bw from [Clocchiatti et al. \(2011\)](#), shown in Figure 5.2, with the addition of a SN 1998bw R -band light curve re-scaled in time to fit the available epochs of SN 2019oyw. SN 2019oyw was found to possess a similar peak time magnitude to SN 1998bw, with a maximum absolute magnitude value of $M_{\text{rmax}} \approx -19.17 \pm 0.56$ mag compared to $M_{\text{Rmax}} \approx -19.02 \pm 0.1$ mag. Figure 5.2 indicates that SN 2019oyw had a slightly faster rise time compared to SN 1998bw, at 16.32 ± 1.24 and 18.0 days respectively. However, the lack of comprehensive coverage around the r -band maximum, primarily during the decline phase, gives a large uncertainty to the rise time of the r -band.

5.4 Pseudo-Bolometric light curve

The photometry of SN 2019oyw was used to construct a pseudo-bolometric light curve of SN 2019oyw. For bands that lack comprehensive coverage, the missing epochs were determined using an interpolation method that fit an intermediate-order polynomial to the available bands in order to interpolate the photometry at epochs between observations. For bands that lack late-time coverage the photometry were extrapolated out to i -band

epochs using a constant decay. For these epochs additional uncertainty is added based on the length of time from last observation. While not negligible, this additional uncertainty does not significantly increase the uncertainty of the pseudo-bolometric light curve. The photometry magnitudes were then fit with a low-order polynomial to obtain the spectral energy distribution of SN 2019oyw between 3,000 – 10,000 Å and integrated to obtain the pseudo-bolometric light curve. The method used to extrapolate underpopulated photometry bands added an additional uncertainty, which increased by a constant of 0.1 mag/day for each day from the last observation. While at early times, around bolometric maximum, the uncertainty from the extrapolation does not contribute a significant amount relative to the intrinsic uncertainty of the observations, later times the contribution from the extrapolation does significantly contribute to the uncertainty of the pseudo-bolometric due to the lack of late time observations. The pseudo-bolometric light curve of SN 2019oyw is shown in Figure 5.3 alongside several other SNe Ic-BL, SN 1998bw (Galama et al., 1998; McKenzie & Schaefer, 1999), SN 2006aj (Pian et al., 2006; Ferrero et al., 2006; Bianco et al., 2014) and SN 2009bb (Pignata et al., 2011). The comparison pseudo-bolometric light curves were constructed using available B to z -band photometry correcting for changes in cosmology and integrated between 3,000 – 10,000 Å.

Through fitting the pseudo-bolometric light curve, SN 2019oyw was found to have a maximum luminosity of $\log_{10}(L_{\text{Ps-Bol}}) = 42.7 \pm 0.1 [\text{ergs}^{-1}]$ with a rise time of $t_{\text{r}} = 17 \pm 2$ days. When compared to other SNe Ic-BL, SN 2019oyw was very similar to the light curve of SN 1998bw with a similar light curve width, although SN 2019oyw possessed a slightly dimmer peak luminosity and similar rise time. The rise of SN 2019oyw was slightly sharper than SN 1998bw due to the removal of the GRB 190829A afterglow, which dominates the light curve at early times up until day $\sim 7 - 9$. Despite the initial appearance of difference in the sharpness of their light curve rises both SN 1998bw and SN 2019oyw have a similar rise time from half peak luminosity, at $\sim 7.1 \pm 0.7$ and $\sim 7.4 \pm 0.9$ days respectively. While the pseudo-bolometric light curve of SN 2019oyw and SN 1998bw display similar evolution, the monochromatic light curves of SN 2019oyw do not all follow a similar evolution, as shown by Figure 5.2.

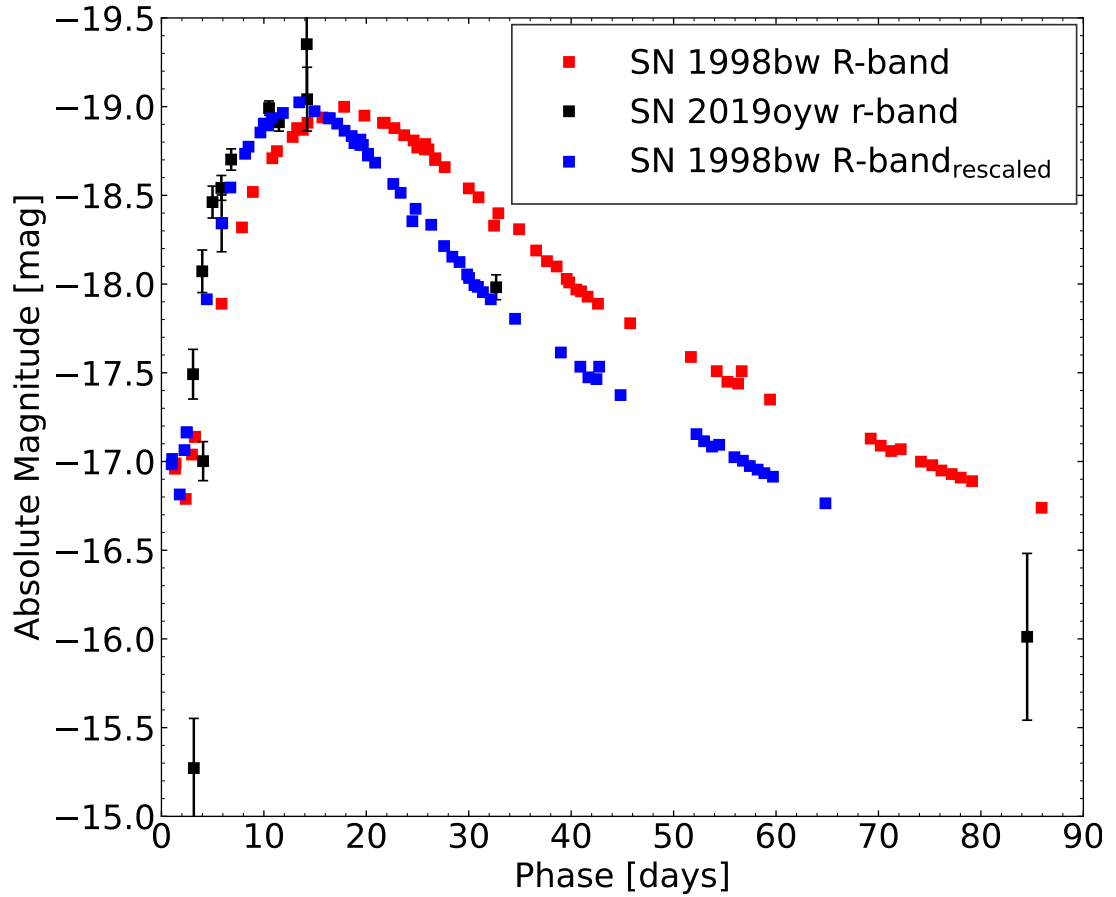


FIGURE 5.2: Comparison between the r -band of SN 2019oyw (black) and the R -band of SN 1998bw (red). Also included is the R -band light curve of SN 1998bw (blue) re-scaled to fit the r -band of SN 2019oyw. All light curves have been corrected for extinction, with a k -correction applied and are shown in their rest frame.

5.5 Spectroscopy

Several optical spectra that cover ~ 1 month from the GRBs initial detection have been obtained for SN 2019oyw, all of which are shown in Figure 5.4. The spectra presented here were provided by both Grand Telescope Canarias (GTC) and the VLT and have been reduced in the standard methods for each telescope. All spectra have been corrected for reddening, using the extinction value of $E(B - V) = 1.089$ used in Hu et al. (2021) and are all given in the rest frame. In addition, all spectra presented here have been flux calibrated using the r -band photometry interpolated to the epoch of spectral observation. Information on each spectrum is given in Table 5.3. The spectra shown in Figure 5.4 are constrained to between $4500 - 9000 \text{ \AA}$. The flux at wavelengths shorter than 4500 \AA has

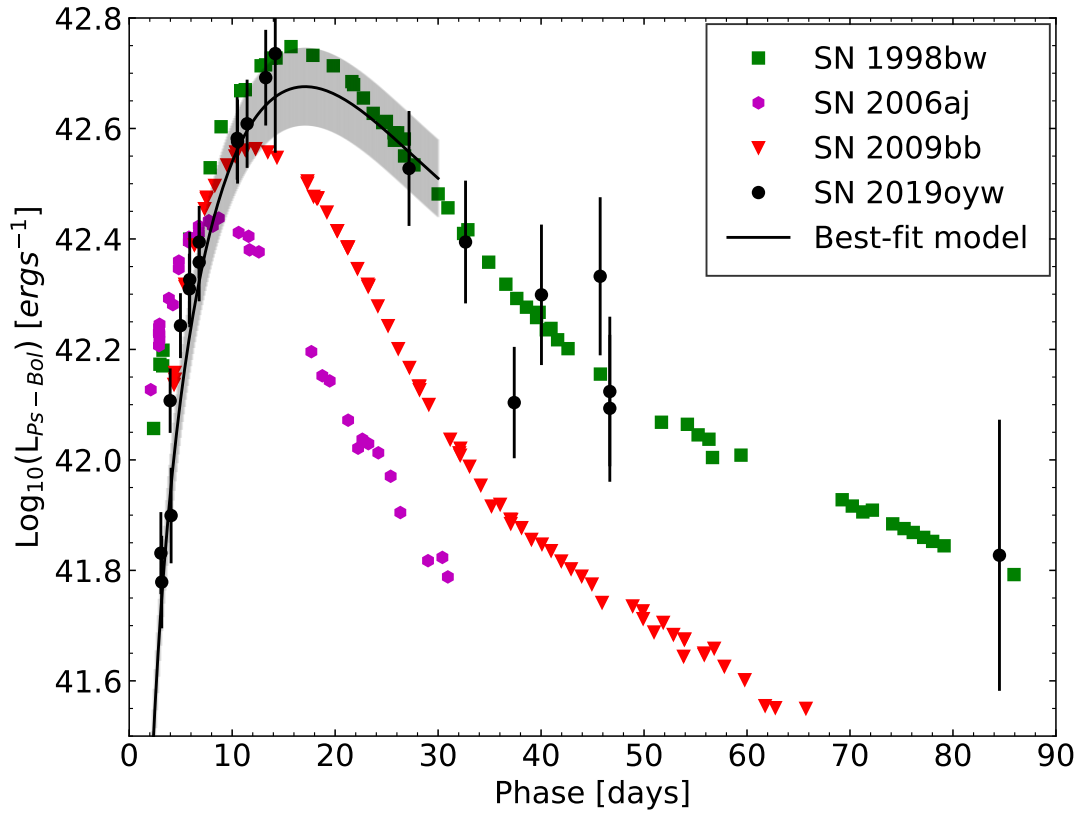


FIGURE 5.3: Pseudo-bolometric light curves of several SNe Ic-BL, covering the first 90 days since their explosion. The black solid line is a best fit Arnett-like model to the light curve of SN 2019oyw fit using a standard optical opacity of $0.06 \text{ cm}^2 \text{ g}^{-1}$, the results of which are given in Table 5.4.

TABLE 5.3: Information for spectra of SN 2019oyw. Phase is relative to the GRB explosion date and given in rest frame. Wavelength range is in rest frame.

Date	Phase ^a [days]	Telescope	Instrument	range [Å]
2019-09-10.19	10.54	GTC	OSIRIS	3426 – 9468
2019-09-11.22	11.48	VLT	FORS2	2946 – 11125
2019-09-15.34	15.31	VLT	FORS2	2947 – 8922
2019-09-21.27	20.79	VLT	FORS2	2946 – 8922
2019-09-28.16	27.19	GTC	OSIRIS	3426 – 9468

^a Phase from explosion date (MJD = 58724.83)

been cut from Figure 5.4 as the S/N of all spectra rapidly decline below 4500 Å and as such have been cut for clarity. Furthermore, a Savitzky-Golay filter (Savitzky & Golay, 1964) has been applied to each spectrum, using a second order polynomial and window of $\lambda - \lambda/100 < \lambda < \lambda + \lambda/100$, in order to reduce the noise of the spectra especially within the blue region. Strong galaxy lines, cosmic rays and the main telluric feature at $\lambda 7600$ have been removed from the spectrum by interpolating the flux within the region using a spline fit to the surrounding spectrum.

5.5.1 Spectral Evolution and line velocities

The early spectra, ~ 10 days after GRB detection, displays a strong peak around ~ 5000 Å, associated with the blending of the Fe II lines. Unfortunately, the low S/N in the 4500 – 5500 Å region shown in Figure 5.4 makes line identification within this region quite difficult, even after the application of the Savitzky-Golay filter. A broad emission feature around ~ 8200 Å produced by the merging of the near infrared Ca II lines is also observed throughout the spectral evolution. This Ca II feature is initially very broad, covering any traces of O I 7774 Å features. However, as SN 2019oyw evolves the Ca II NIR-triplet absorption minima declines in velocity and by approximately day 20 the O I feature can be isolated from the calcium feature. Along with the Fe II and Ca II lines a clear Si II feature is seen to emerge in the spectrum around ~ 6300 Å around day 10 which is seen in all later spectra.

As with the Fe II feature, the Ca II NIR-triplet exhibits a similar shift in the wavelength of the blended emission peak as SN 2019oyw evolves. Initially the absorption feature around 7700 Å is seen to be dominated solely by the calcium NIR lines, with the feature being replicated with a single Gaussian fit and a maximum velocity of $\sim 33.1 \pm 2.1 \times 10^3$ km s⁻¹. The absorption minima of this feature gradually shifts to longer wavelengths over the next $\sim 5 - 10$ days before becoming broader in the day 20 spectrum. At this point the minima of the absorption feature widens to a width that cannot be explained solely by the absorption feature of the NIR Ca II triplet and the O I 7774 Å starts to contribute significantly. At earlier times the emission from the O I $\lambda 7774$ lines were blanketed by the high velocity Ca II NIR-lines. The absorption feature around ~ 7800 Å

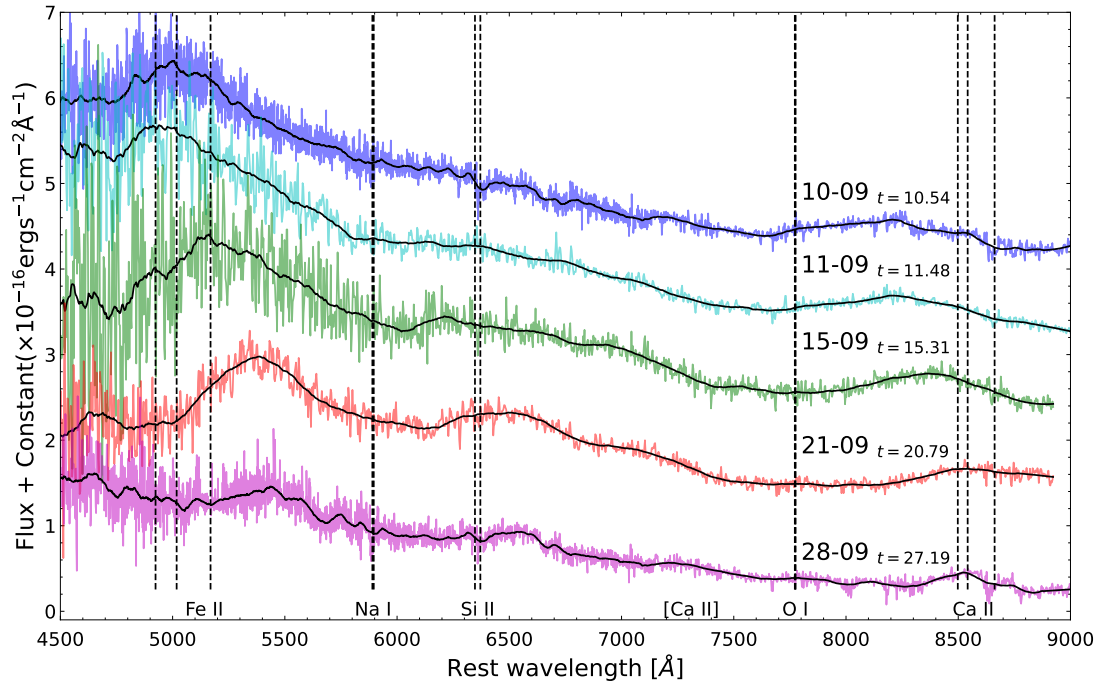


FIGURE 5.4: Spectral evolution of SN 2019oyw. All spectra have been dereddened using an $E(B - V) = 1.089$, normalised to the flux at the r -band effective wavelength, shifted upwards vertically by multiples of 10^{-16} and are shown at rest wavelength. Dates, phases and additional spectral information are reported in Table 5.3. A Savitzky-Golay filter was applied to all spectra, solid black line. The rest wavelength of the Fe II, Na I, Si II, O I, [Ca II] and Ca II emission lines are shown by the vertical dashed lines.

in the spectrum of SN 2019oyw, associated with the Ca II NIR-triplet, initially displays a large amount of blending with the O I $\lambda 7774$ feature, making the identification of the absorption minima difficult and as such a velocity at this epoch can not be defined. Based on the spectral evolution of SN 2019oyw, the calcium velocity is likely to follow that of SN 1998bw, especially at early times. By day 20 the Ca II feature had become separate from the O I feature and was found to possess a corresponding velocity of $13.9 \pm 2 \times 10^3$ km s $^{-1}$, a similar velocity to SN 1998bw at this epoch.

Studying the evolution of the absorption features allows the line velocities of various elements and more importantly the photospheric velocity of SN 2019oyw to be determined. However, it is well known that line velocities of SN Ic-BL can be notoriously difficult to determine due to the broad absorption features within the spectra, especially in SNe that have low S/N such as SN 2019oyw. Extracting line velocities is especially difficult at earlier times when there is significant blending between the spectra features of multiple species moving at high velocity. Despite this problem with line blending

there are several species that can be isolated and their velocities determined. A Gaussian function was fit to the absorption features associated with each line to determine their velocity. While the low S/N of the spectra is expected to increase the uncertainty of the Gaussian fit it does not significantly contribute to the uncertainty. Comparing the velocities derived from fitting the unsmoothed and smoothed spectrum it was found that the velocities differ by a maximum of $\sim 1.7\%$. Therefore the average from the smoothed and unsmoothed spectra was taken as the reported velocity to decrease the uncertainty of the line velocity at each epoch.

The strong Si II feature around $\sim 6300 \text{ \AA}$ was fit in all spectra and the Si II line velocities of SN 2019oyw are shown in Figure 5.5 alongside several other SNe Ic-BL. Excluding SN 2013dx the Si II line velocities of the other SNe Ic were determined through the fitting of available spectra prior to 30 days post explosion. Initially the Si II feature of SN 2019oyw had a velocity of $25.5 \pm 6.7 \times 10^3 \text{ km s}^{-1}$ around day 10 which rapidly declined to a final velocity of $8.3 \pm 2.1 \times 10^3 \text{ km s}^{-1}$ by day 27. The evolution of the Si II $\lambda 6355 \text{ \AA}$ line is commonly used as the tracer for the photospheric velocity, v_{ph} , within SNe Ic-BL, although Parrent et al. (2016) considered that the identification of the Si II $\lambda 6355 \text{ \AA}$ line may be influenced by other trace elements within the region. While it has been suggested that the Fe II $\lambda 5169$ line works as a better tracer of the photospheric velocity Branch et al. (2002), the low S/N of the iron region alongside the strong blending effects that influences the Fe II lines within SNe Ic-BL prohibits the identification of individual Fe II lines within the spectra of SN 2019oyw. Thus, the velocity evolution of the Si II $\lambda 6355 \text{ \AA}$ line was used to trace the photospheric velocity of SN 2019oyw throughout this work. The velocity of the Si II line was fit with an exponential decay function and used to determine v_{ph} corresponding to the peak time of the pseudo-bolometric light curve. From the fitting it was found that v_{ph} had a value of $v_{\text{ph}} = 14.8 \pm 2.8 \times 10^3 \text{ km s}^{-1}$ at pseudo-bolometric maximum. When compared to other SNe Ic-BL, the photospheric velocity of SN 2019oyw initially possess a value similar to that of SN 1998bw and declines in a similar manner. However, at post-peak times the velocity of SN 2019oyw rapidly declines, reaching a velocity comparable to those observed in SN 2006aj and SN 2013dx.

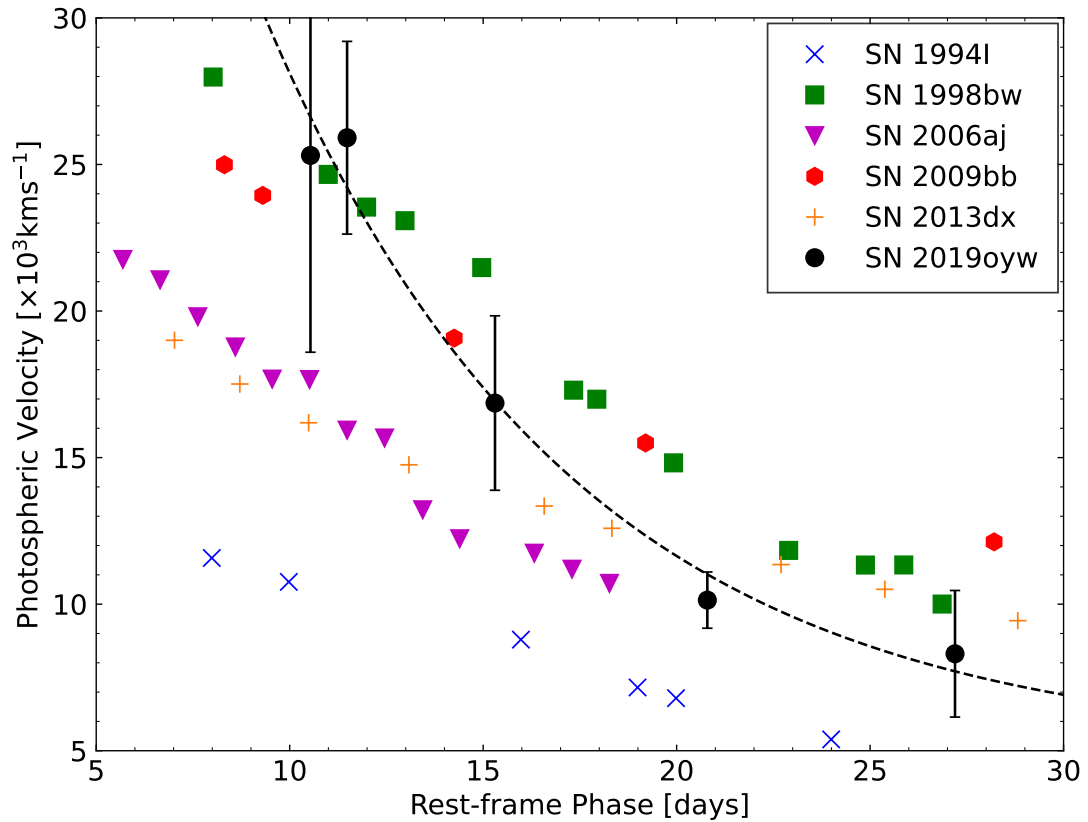


FIGURE 5.5: Evolution of the photospheric velocity v_{ph} of several H/He-poor SNe are shown. v_{ph} is measured from the absorption minima of the Si II $\lambda 6355$ feature. The velocities for all SNe except SN 2013dx were determined by fitting the available spectra with a Gaussian function to find the absorption feature. The velocity of SN 2013dx was taken the spectroscopic models from [Mazzali et al. \(2021\)](#).

5.5.2 Spectral Comparison

Spectroscopically, SN 2019oyw appears as a typical SN Ic-BL, exhibiting strong Fe II, Ca II and Si II lines with broad absorption features at all epochs. Figure 5.6 displays the day 10 and 11 spectra of SN 2019oyw which are compared to the spectra of SN 1998bw ([Patat et al., 2001](#)), SN 2006aj ([Pian et al., 2006](#)) and SN 2009bb ([Pignata et al., 2011](#)), obtained at similar epochs. Of the SNe compared in Figure 5.6, SN 2019oyw most strongly resembles SN 1998bw. Both SNe display a peak flux around 5000 \AA associated with Fe II lines before a decline in flux towards the Si II feature. The peak of the Fe II feature seen in SN 2019oyw was offset bluewards from the peak of SN 1998bw by $\sim 90 \text{ \AA}$, although the low S/N of the iron region makes identification of the peak difficult. In addition, the day 11 spectrum shows a clear Si II feature similar in shape to that

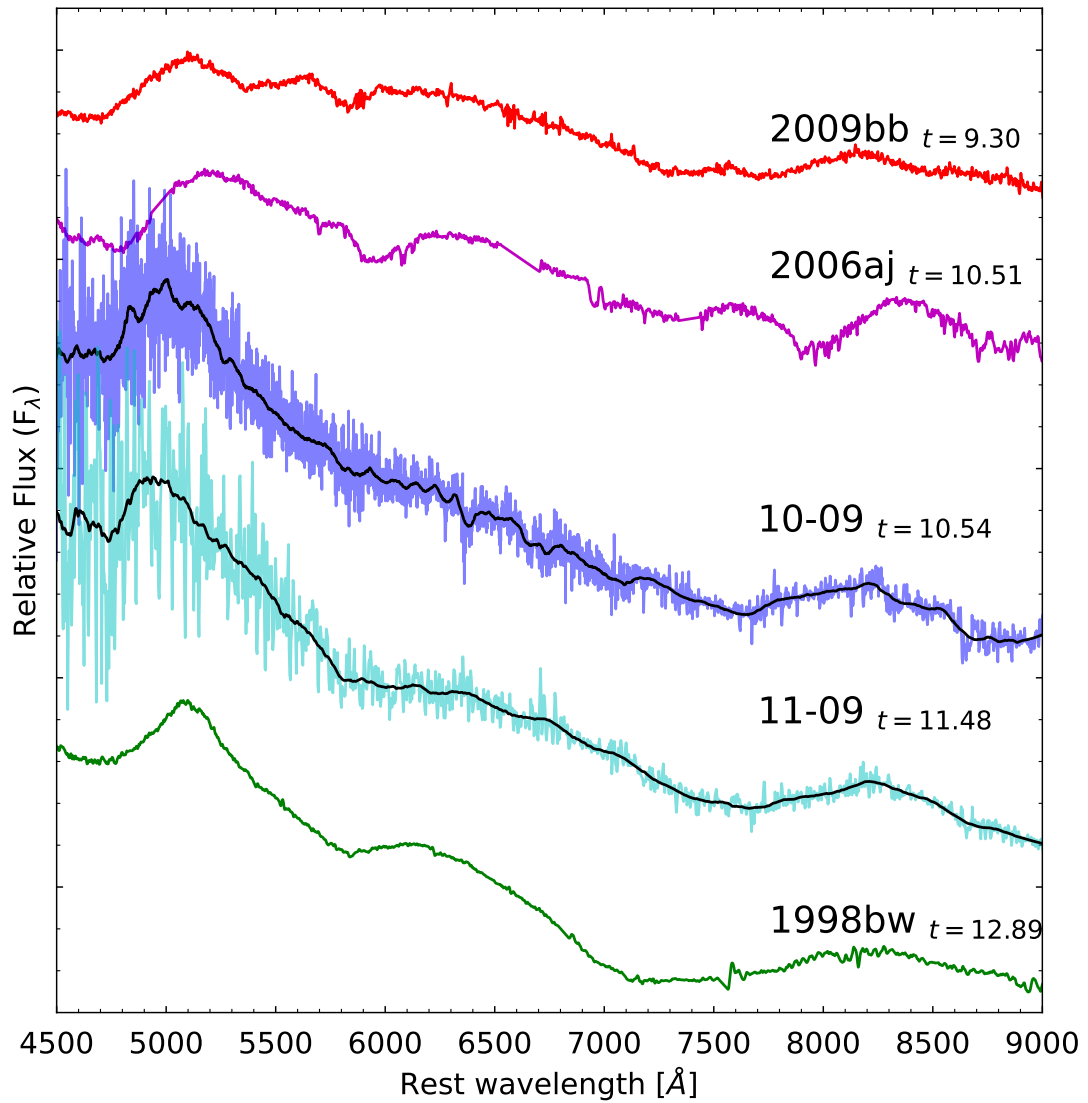


FIGURE 5.6: Comparison of several SNe Ic-BL spectra obtained around 10 days post explosion. All spectra shown in rest wavelength and have been shifted vertically an arbitrary amount.

of SN 1998bw at velocities observed in both SN 1998bw and SN 2009bb. A broad absorption feature around 7800 Å, associated with the Ca II NIR-triplet, was seen in both SN 1998bw and SN 2019oyw at similar velocities. Initially the feature in both SNe displayed a high velocity while lacking the strong emission feature connected with the O I $\lambda 7774$ line as seen in SN 2006aj.

The later spectrum of SN 2019oyw, at around 20 days post detection, is also compared to other SNe Ic-BL all observed at similar epochs, in Figure 5.7. At this epoch SN 2019oyw is observed to be similar to both SN 1998bw and SN 2006aj. SN 2019oyw displays a

Fe II emission peak at a similar wavelength as SN 2006aj. While SN 2019oyw appears similar to SN 2006aj at later times, especially below $\sim 7000 \text{ \AA}$ it displays a broad Ca II NIR feature while lacking the strong O I $\lambda 7774$ feature seen in both SN 2006aj and SN 2009bb. In addition to the lack of O I feature, which was also seen in SN 1998bw at this epoch, SN 2019oyw possesses a similar Si II absorption feature to that seen in SN 1998bw.

As noted in Section 5.5.1 the peak of the Fe II feature shifts to larger wavelengths as SN 2019oyw evolves due to the changing opacities within the 5000 \AA region. This shift in peak wavelength is also seen in the other SNe Ic-BL, although the rate at which the shift occurs is seen to differ between the events. The Fe II peak seen in SN 2006aj, while initially not as blueshifted as the Fe II peak in SN 2019oyw, displays a similar evolution over time shifting to the rest wavelength of the Fe II $\lambda 5363$ line around ~ 16 days, see Figure 5.8. In comparison the emission peak of the Fe II feature of SN 1998bw takes ~ 26 days after explosion. This might indicate that SN 2019oyw possessed a density profile more similar to that of SN 2006aj than SN 1998bw.

5.5.3 Re-classification

Prentice & Mazzali (2017) suggested that SNe Ic can be further divided into different categories depending on the average number of absorption features in the $4000 - 8000 \text{ \AA}$ region of the photospheric phase spectra. The spectra of SN 2019oyw during this phase show signs of a blended Fe II feature, alongside a clear Si II absorption and finally a blended O I/Ca II feature. The features identified and their strong blending result in SN 2019oyw being reclassified as a SNe Ic-3/4. The low S/N of the spectra makes it difficult to accurately identify the number of spectral absorption features, especially those seen in the region between $4000 - 5000 \text{ \AA}$, which is heavily influenced by the blending of the Fe II lines. The uncertainty in the Fe II region does not drastically change the classification of SN 2019oyw as the spectra above 5000 \AA possess a low enough S/N to clearly identify the key absorption features mentioned by Prentice & Mazzali (2017). To test the new classification for SN 2019oyw the spectra were smoothed using a window of $\lambda - \lambda/10 < \lambda < \lambda + \lambda/10$, to remove the majority of the noise within the spectrum while

keeping the broad absorption features typical of SNe Ic-BL. The local minima were then found for these smoothed spectra across a wavelength region of 4000 – 8000 Å and clustered in three main regions, those associated with the blended Fe II lines, the isolated Si II line and the Ca II NIR triplet, confirming the initial classification of SN 2019oyw as a SNe Ic-3/4, with the uncertainty in the classification arising from the low S/N in the region between 5600–5900 Å making the identification of the Na I line uncertain. As discussed in Section 5.5.2, the spectral evolution of SN 2019oyw is very similar, especially around peak time, to the evolution of SN 1998bw, which was classified as a Ic-3. The similarity between these two SNe includes the initial low number of blended absorption features observed during the pre-peak time and the increased number of separate features seen during the post peak phase. In their classification scheme [Prentice & Mazzali \(2017\)](#) also use the photospheric velocity derived from the velocity evolution of the Si II line and the time taken for the light curve to decline to half peak luminosity, $t_{1/2}$, as further ways to further differentiate SNe. However, given the light curve similarity between SN 2019oyw and SN 1998bw discussed in Section 5.4 the value of $t_{+1/2}$ for SN 2019oyw is not expected to differ drastically from that of SN 1998bw.

5.6 Explosion Parameters

5.6.1 Light curve comparison

The explosion parameters of GRB-SNe, the mass of material ejected, M_{ejc} , and their kinetic energy, E_{k} , are known to be much greater than those associated with SNe Ic ([Sahu et al., 2018](#); [Mazzali et al., 2021](#)). These parameters can be determined in multiple ways, with the primary methods being the use of hydrodynamical modelling of the observed spectra ([Nakamura et al., 2001](#); [Deng et al., 2003](#); [Ashall & Mazzali, 2020](#); [Mazzali et al., 2021](#)) and the semi-analytical modelling of the SNe bolometric light curve ([Arnett, 1982](#)). One big difference between the two methods is the treatment of the optical opacity, κ_{opt} . In the hydrodynamical models the opacity evolves with time as the ejecta expands while the semi-analytical model assumes a constant value of κ_{opt} at all times, centralised ^{56}Ni and a spherically symmetric ejecta. The use of a

constant κ_{opt} results in the semi-analytical approach consistently producing lower values of the explosion parameters when compared to those determined via detailed modelling (Lyman et al., 2016). In addition to these two methods, a third way of estimating the SNe explosion parameters is to compare the properties a SN with those of a hydrodynamically modelled SN to obtain a ratio of M_{ejc} and E_{k} between the two SNe, as was done with both SN 2010ah (Mazzali et al., 2013) and SN 2020cpg (Medler et al., 2021), the results of which produce values for the explosion parameters more similar to those derived from spectral modelling (Mazzali et al., 2013; Teffs et al., 2022) than the values obtained through an semi-analytical approach. Using the relation between the shape of the SN light curve and the kinetic energy detailed in Arnett (1982), the relationship between the kinetic energy of two SNe is given by:

$$\frac{E_{\text{k}1}}{E_{\text{k}2}} \propto \left(\frac{t_{\text{bol}1}}{t_{\text{bol}2}} \right)^2 \left(\frac{v_{\text{ph}1}}{v_{\text{ph}2}} \right)^3 \left(\frac{\kappa_{\text{opt}1}}{\kappa_{\text{opt}2}} \right)^{-1}, \quad (5.1)$$

where t_{bol} is the width of the light curve at three quarters of the peak luminosity. While the ratio of ejecta masses for the SNe is given as:

$$\frac{M_{\text{ejc}1}}{M_{\text{ejc}2}} \propto \left(\frac{t_{\text{bol}1}}{t_{\text{bol}2}} \right)^2 \left(\frac{v_{\text{ph}1}}{v_{\text{ph}2}} \right) \left(\frac{\kappa_{\text{opt}1}}{\kappa_{\text{opt}2}} \right)^{-1}. \quad (5.2)$$

For SNe of a similar classification it is assumed that the evolution of κ_{opt} is sufficiently similar as to be negligible in determining the explosion parameters using the light curve comparison. While this does increase the uncertainty in the final values, the error associated with the photospheric velocity and light curve width will be more significant.

The light curve comparison method was used to compare the explosion parameters between SN 2019oyw and both SN 1998bw and SN 2006aj. These SNe Ic-BL were used as they had each undergone hydrodynamic modelling to determine their ejecta mass and kinetic energy. In addition to all having been previously modelled, SN 1998bw was used for a comparison due to the photometric and spectroscopic similarities with SN 2019oyw especially at early times, $t < 20$ days. While SN 2006aj is not photometrically similar to SN 2019oyw, SN 2006aj displays a post peak spectrum not dissimilar to that of

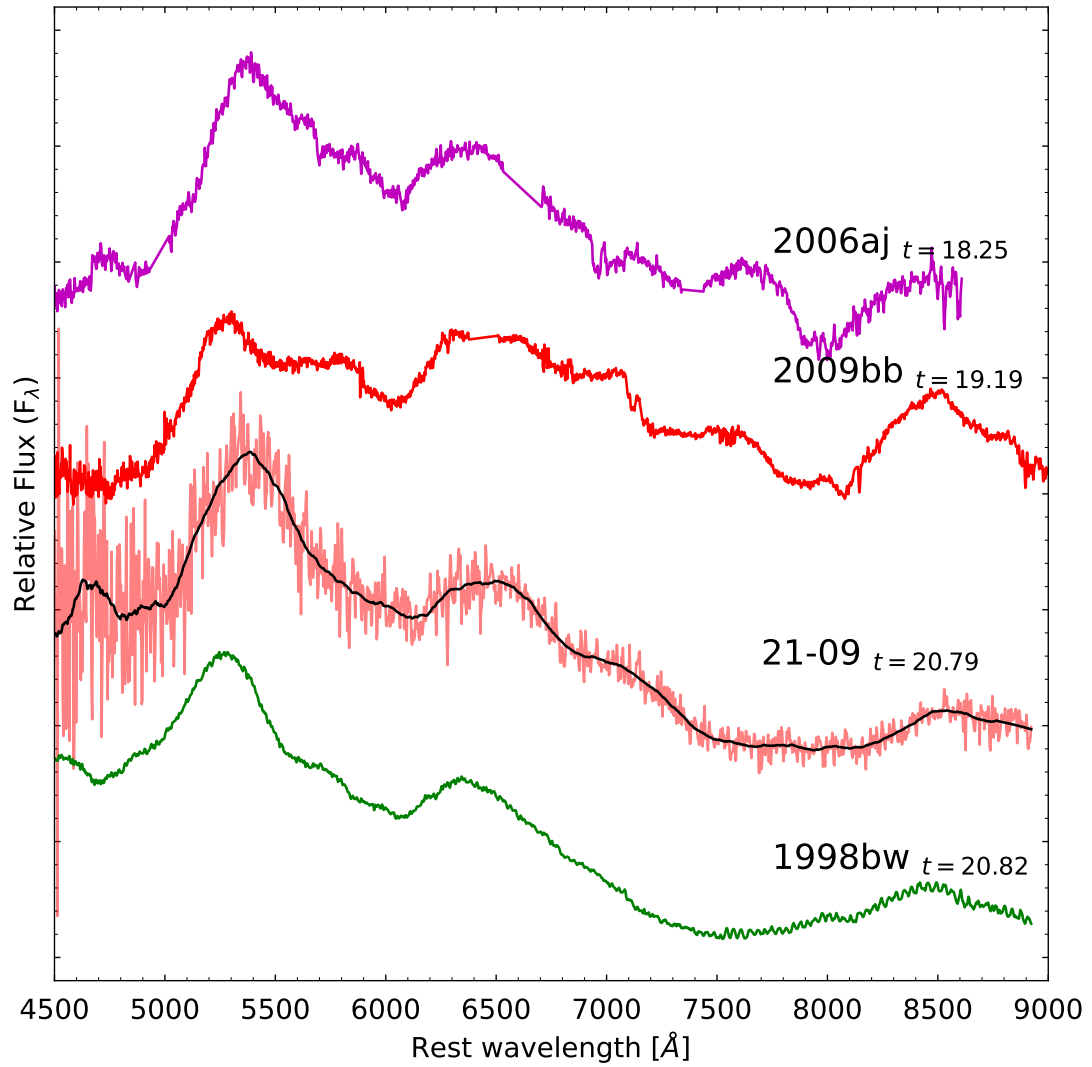


FIGURE 5.7: Spectra of several SNeIc-BL obtained around 20 days post explosion, similar to Figure 5.6.

SN 2019oyw and a convergence is seen in their late time velocities around this epoch, $t \geq 20$ days, see Figure 5.5.

The SNe were compared at several different epochs as an analog for the different ejecta structures and to account for the evolution of SN 2019oyw as it declined in velocity. The velocities used for the comparison were the photospheric velocity at the peak time for each individual SNe, the SNe velocity when SN 2019oyw was at bolometric peak, the early phase at $t = 10$ days where SN 2019oyw possessed a velocity similar to that of SN 1998bw and finally the velocity at 20 days after explosion when SN 2019oyw transitioned to a slower velocity closer to that of SN 2006aj. The average results for

the light curve comparison with SN 1998bw, SN 2006aj and SN 2013dx are given in Table 5.4. The average explosion parameters, weighted by the uncertainty given by the hydrodynamic models, from all the light curve comparisons give an ejecta mass for SN 2019oyw of $M_{\text{ejc}} = 10 \pm 3 M_{\odot}$ and a kinetic energy of $E_{\text{k}} = 19 \pm 8 \times 10^{51}$ erg. The physical parameters of He-poor SE-SNe, 1 SNe Ic, 5 SNe Ic-BL and 6 GRB-SNe including SN 2019oyw, are shown in Figure 5.9. Compared to the physical parameters of other He-poor SE-SNe derived by hydrodynamic modelling, SN 2019oyw lies within the expected region dominated by GRB associated SNe, possessing a high energy and ejecta mass. The physical parameters of SN 2019oyw, derived from light curve comparison method, shows a similar ejecta mass as other GRB-SN, placing it between SN 2013dx and SN 1998bw, while it exploded with a relatively low energy for a GRB-SN, roughly 40% that of SN 1998bw.

5.6.2 Semi-Analytical light curve model

In addition to the light curve comparison method discussed above, another way to determine the physical parameters of a SN is through the fitting of the bolometric light curve, first detailed in Arnett (1982). This approach, although common in the literature, possesses several problems when used for core-collapse SNe, with the main problem occurring due to the treatment of the ^{56}Ni synthesised by the explosion and the evolution of the κ_{opt} . This is especially prevalent with high energy events such as those of GRB-SNe which tend to have values of M_{ejc} and E_{k} much higher than those found from the Arnett-like model (Iwamoto et al., 1998; Mazzali et al., 2013; Ashall et al., 2019; Prentice et al., 2019). As such we are cautious when giving the physical parameters, primarily M_{ejc} and E_{k} , determined for SN 2019oyw using the Arnett-like model. Despite the problems associated with the Arnett-like approach, we give here the best-fit light curve model of SN 2019oyw for the purpose of comparing it to other GRB-SNe.

The model were fit to the pseudo-bolometric light curve of SN 2019oyw, using a standard optical opacity for SE-SNe of $\kappa_{\text{opt}} = 0.06 \text{ cm}^2 \text{ g}^{-1}$ which was fit to the pseudo-bolometric light curve over a 28 day period between days 5 and 33. Later epochs were not fit with the

Arnett-like model due to the larger uncertainties associated with the late time pseudo-bolometric light curve, as discussed in Section 5.4, and the large disagreement seen between the light curve of the Arnett-like model and late time luminosities, brought about by transition from an optically thick ejecta during the photospheric phase to the optically thin ejecta in the nebular phase. A photospheric velocity of $14.8 \pm 2.8 \times 10^3 \text{ km s}^{-1}$, determined from the Si II line, see Section 5.5.1, was used to break the degeneracy between the ejecta mass and kinetic energy of SN 2019oyw. The best-fit model extended out to 30 days is presented in Figure 5.3, with a 1σ error shown by grey shaded region.

The best-fit model for the pseudo-bolometric light curve captures the rapid rise of the light curve reasonably well, although the lack of peak time photometry has resulted in an under luminous fit to the peak of the pseudo-bolometric light curve. At late time, when SN 2019oyw starts to transition into the nebular phase, ($t \sim 40$), the model drastically diverges from the pseudo-bolometric light curve. However, this difference is expected and as such epochs at this phase are not used for the fitting.

The best-fitting model of the pseudo-bolometric light curve suggests that SN 2019oyw synthesised a mass of ^{56}Ni , M_{Ni} , of $0.21 \pm 0.04 M_{\odot}$, along with an ejecta mass of $M_{\text{ejc}} = 3.5 \pm 0.9 M_{\odot}$ and possessed a kinetic energy of $E_{\text{k}} = 4.6 \pm 1.3 \times 10^{51} \text{ erg}$. These physical parameters, derived from the fitting of the pseudo-bolometric light curve are around average when compared to other SNe Ic-BL fit with an Arnett-like model (Lyman et al., 2016; Taddia et al., 2019), although slightly lower than the mean ejecta mass of GRB-SNe found by (Prentice et al., 2019).

It should be noted that the restricted range of photometric bands used to construct the pseudo-bolometric light curve shown in Figure 5.3, along with the lack of post-peak g -band photometry, resulted in an under-luminous bolometric light curve for SN 2019oyw. At early times the UV and blue optical bands contribute a large percentage to the total flux, with the U/u -band contributing around $20 \pm 3\%$ (Prentice et al., 2016). In addition, the NIR bands are expected to also contribute $\sim 14 \pm 3\%$ of the total flux for SNe Ic-BL at bolometric peak (Prentice et al., 2016). Adjusting for the missing bands would push SN 2019oyw up to a peak luminosity of $\log_{10}(L_{\text{Bol}}) = 42.9 \pm 0.4 [\text{erg s}^{-1}]$ which would increase the value of M_{Ni} to $0.35 \pm 0.21 M_{\odot}$. This increase in the value of M_{Ni} from

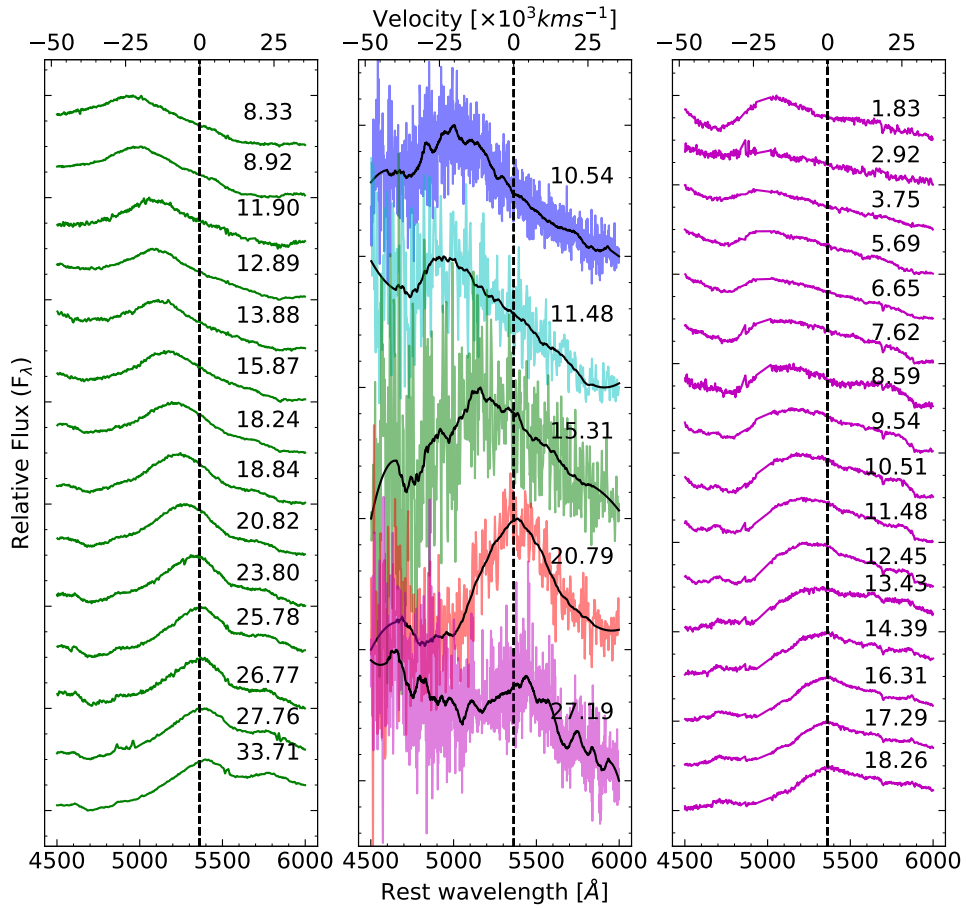


FIGURE 5.8: Evolution of the blue-shifted Fe II peak of SN 1998bw (left), SN 2019oyw (middle) and SN 2006aj (right). Phase relative to explosion date is noted above each spectrum. Rest wavelength and velocity relative to the Fe II $\lambda 5363$ line are shown on the bottom and top respectively. SN 2019oyw displays a shift in the Fe II peak at a rate between that seen in SN 1998bw and SN 2006aj.

adjusting the peak luminosity to account for the missing photometric bands now places SN 2019oyw close to the average M_{Ni} found for SNe Ic-BL (Lyman et al., 2016; Prentice et al., 2016).

5.6.3 Model comparisons

The values for the physical parameters of SN 2019oyw derived from the Arnett-like model are significantly lower than those found from the comparison of the light curve properties. The discrepancy between the values derived from Arnett-like light curve

fitting and those obtained by hydrodynamic modelling has been found in several GRB-SNe. For example, the spectral modelling of SN 1998bw (Iwamoto et al., 1998) found an ejecta mass twice that of the value derived from the Arnett-like approach and a kinetic energy up to five times greater than that derived from light curve modelling (Lyman et al., 2016). The difference between the two methods described above is likely due to the assumptions that are made in the Arnett-like, such as the central region of ^{56}Ni rich material and the use of a constant opacity and photospheric velocity throughout the light curve evolution. Given the similarities in the peak pseudo-bolometric luminosities between SN 2019oyw and SN 1998bw, the value derived for M_{Ni} from the Arnett-like fit of SN 2019oyw should be taken to be a lower limit, with the increased value of $0.35 \pm 0.21 M_{\odot}$ taken as a more likely value for the true amount of ^{56}Ni synthesised. The two methods used for determining the explosion parameters of SN 2019oyw are clearly in conflict. The ejecta mass of SN 2019oyw determined by the two methods differ by a factor of ~ 2.5 , while the kinetic energy differ by a factor of 3 – 5. When compared to other GRB-SNe, the parameters of SN 2019oyw derived using the light curve comparison method agree with the highly energetic nature of other events, as shown in Figure 5.9. Given the similarities in the photometric and spectroscopic properties between SN 2019oyw and SN 1998bw, we take the values of ejecta mass and kinetic energy to be those derived from the light curve comparison method, $10 \pm 3 M_{\odot}$ and $19 \pm 8 \times 10^{51}$ erg respectively, as the most likely values for SN 2019oyw placing it well within the GRB-SNe region of Figure 5.9, giving SN 2019oyw a $E_{\text{k}}/M_{\text{ejc}}$ ratio of ≈ 2 . This $E_{\text{k}}/M_{\text{ejc}}$ ratio is in agreement with the distribution of $E_{\text{k}}/M_{\text{ejc}}$ as a function of average number of spectra features shown by Prentice & Mazzali (2017). The $E_{\text{k}}/M_{\text{ejc}}$ ratio determined from the Arnett-like method, ≈ 1.4 , is in disagreement with the trend found by Prentice & Mazzali (2017) and would require a greater number of spectral features than those found in Section 5.5.

Given the ejecta mass value and a black hole remnant of $\sim 3 M_{\odot}$, giving a CO core mass of $\sim 10 - 15 M_{\odot}$, a single star progenitor for SN 2019oyw would be expected to have a Zero Age Main Sequence mass of $M_{\text{ZAMS}} = 35 - 45 M_{\odot}$, based on the models of stripped Wolf-Rayet stars presented by Meynet & Maeder (2005) and comparisons to the expected progenitor mass of other GRB-SNe (Iwamoto et al., 1998; Deng et al., 2005). Unfortunately, the uncertainty in the ejecta mass value of SN 2019oyw makes it

TABLE 5.4: Explosion properties of SN 2019oyw derived from equations 5.1 and 5.2, Comp, and the parameters obtained from the best-fit light curve model fit to the pseudo-bolometric light curve, Best-fit.

Method	M_{Ni} [M_{\odot}]	M_{ejc} [M_{\odot}]	E_{k} [$\times 10^{51}$ erg]
Comp ¹	-	8.7 ± 2.3	24.4 ± 9.8
Comp ²	-	8.8 ± 2.4	15.6 ± 6.3
Comp ³	-	13.7 ± 3.8	22.8 ± 9.1
Best-fit ⁴	0.21 ± 0.04	3.5 ± 0.9	4.6 ± 1.3

¹ Comparison with SN 1998bw using $t_{\text{bol}} = 17$ days

² Comparison with SN 2006aj using $t_{\text{bol}} = 9$ days

³ Comparison with SN 2013dx using $t_{\text{bol}} = 15$ days

⁴ Model of SN 2019oyw pseudo-bolometric light curve

difficult to place a tight constraint on the progenitor mass, as such we have taken an initial mass range of $35 - 45 M_{\odot}$ as a conservative value for the progenitor of SN 2019oyw. Comparing the expected progenitor M_{ZAMS} of SN 2019oyw to those of other GRB-SNe, shown in Figure 5.10, shows that SN 2019oyw lies well within the parameter space of other GRB-SNe in a location similar to that of SN 1998bw.

5.7 Mass and Energy relation

When compared to other SE-SNe, GRB-SNe typically cluster at very large kinetic energies, a few $\times 10^{52}$ erg, much higher than those seen in other SNe Ic (Cano, 2013; Mazzali et al., 2014). Alongside their high energies, GRB-SNe are expected to eject large amounts of material, approximately $\sim 1.3 - 1.4$ times greater than SNe Ic-BL that are not associated with a GRB (Cano, 2013; Prentice et al., 2019). Given the differences in E_{k} and M_{ejc} between the two types of SNe Ic-BL a question arises over whether there is a continuous relationship in E_{k} and M_{ejc} parameter space at low orders, $E_{\text{k}} < 1 \times 10^{52}$ erg and $M_{\text{ejc}} < 5 M_{\odot}$ where SNe Ic and most SNe Ic-BL exist, all the way to the higher orders, $E_{\text{k}} > 1 \times 10^{52}$ erg and $M_{\text{ejc}} > 5 M_{\odot}$ which is dominated by GRB-SNe and a few SNe Ic-BL. In order to test if there is a continuous relation between the low and high order He-poor SNe, the physical parameters of several SNe Ic, derived through the hydrodynamical modelling, were fit with a single power law function which takes the form;

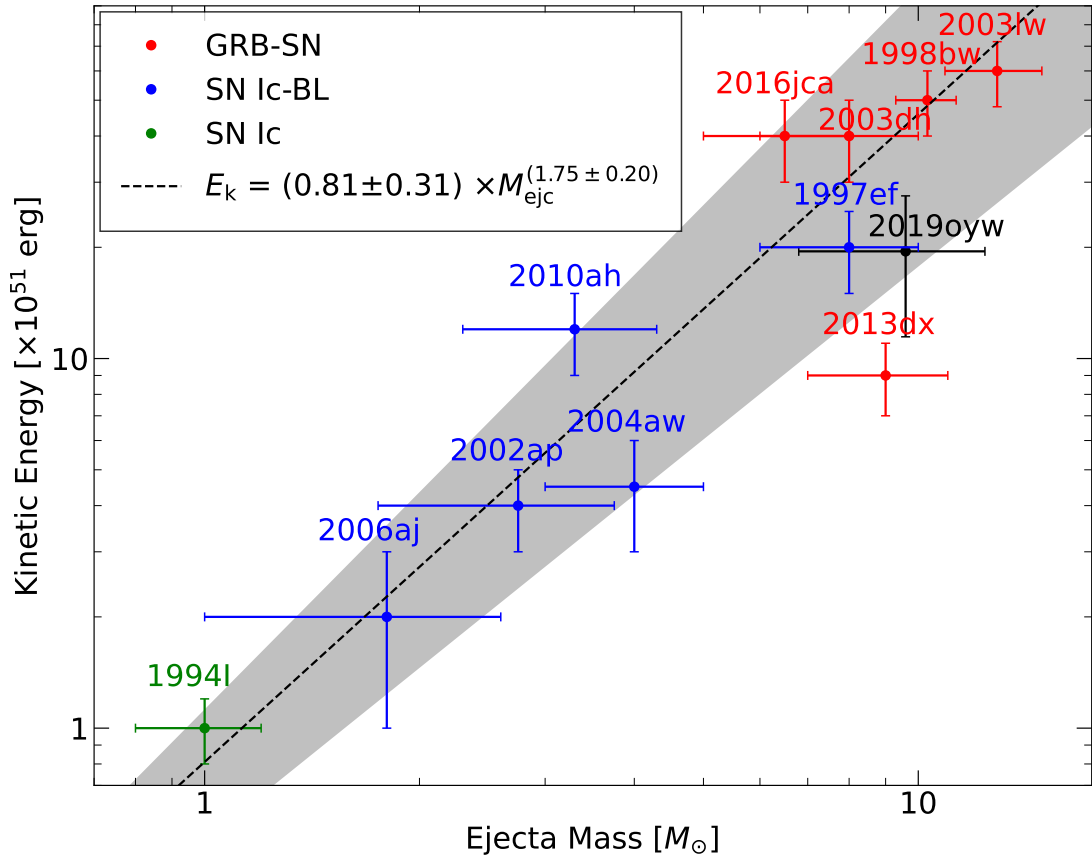


FIGURE 5.9: Ejecta mass vs kinetic energy of several He-poor SE-SNe. GRB-SNe are in red, non-GRB associated SNe Ic-BL are in blue and the standard SNe Ic is given in green. SN 2019oyw (black) displays a slightly large ejecta mass for the kinetic energy derived from light curve comparisons. Included is the best fit single power law function, with the 1σ uncertainty given by the shaded region.

$$E_{\text{k}}[\times 10^{51}\text{erg}] = A \times M_{\text{ejc}}^B[M_{\odot}]. \quad (5.3)$$

Where A is the amount of material ejected by the explosion with a given energy having units of $10^{51}\text{erg}/M_{\odot}$ and B is the exponent, both of which are derived from the fitting.

It should be noted that the kinetic energies in Figure 5.9 have not been corrected for the effects of asphericity. When the effect of asymmetrical ejecta, determined through the modelling of late-time nebular spectra, is taken into account the kinetic energies of GRB-SNe have been shown to reduce by a factor of 2 – 3 depending on the asphericity of each event (Maeda et al., 2002; Mazzali et al., 2005). The reduction in the kinetic energies of GRB-SNe would place them all around $1 - 2 \times 10^{52}\text{erg}$ which are similar to the energy expected from a millisecond magnetar (Mazzali et al., 2014). The reduction

to the GRB-SNe kinetic energies that is expected from correcting for asphericity, would result in a lower value for the exponent in eqn. 5.3. However, given the need for late-time spectroscopic observations, the degree of asphericity is not well constrained for many GRB-SNe and as such is not taken into account in the kinetic energies of GRB-SNe used for the fitting of eqn. 5.3.

The function given by equation 5.3 were fit using the kinetic energies and ejecta masses of 1 SNe Ic, 5 SNe Ic-BL and 5 GRB-SNe, which were taken from (Mazzali et al., 2021) and references therein. For the fitting of equation 5.3, SN 2019oyw was not included due to the uncertainty in determining its explosion properties. The best-fit power law function is shown in Figure 5.9, with the 1σ uncertainty given by the shaded region. The fit shows a clear relationship between the kinetic energy and ejecta mass for all types of He-poor CC-SNe. From the fit it was found that constant of proportionality had a value of $A = 0.81 \pm 0.31$ while the exponent had a value of $B = 1.75 \pm 0.20$.

While the best-fit is able to capture a relationship between E_{k} and M_{ejc} for the majority of SNe Ic shown in Figure 5.9, both SN 2013dx and SN 2010ah, lie outside the 1σ uncertainty. For SN 2013dx it has been shown that the kinetic energy is significantly lower than other GRB-SN of a similar ejecta mass (Mazzali et al., 2021). This difference between the energy-mass relation for SN 2013dx has been suggested to arise from the central engine lacking sufficient energy to fully accelerate the ejecta to the velocities typical of GRB-SNe (Mazzali et al., 2021). A range of values for the physical properties of SN 2013dx have been reported, with an $M_{\text{ejc}} = 3 - 19$ and E_{k} between $8 - 35 \times 10^{51}$ erg (D’Elia et al., 2015; Toy et al., 2016; Volnova et al., 2017; Mazzali et al., 2021). Due to the uncertainty in its physical parameters, SN 2013dx was removed from the fitting sample to determine if it had any significant effect on the values of A and B . However, the removal of SN 2013dx does not significantly alter the parameters derived from the best fit, changing by a maximum of 11%. While SN 2013dx seems to lie well outside the best-fit, SN 2010ah is not far outside of the 1σ uncertainty and displays significant overlap between the uncertainties associated from the hydrodynamical modelling and the best-fit function. A Spearman’s rank test was performed on the best-fit function shown in Figure 5.9 to determine the effectiveness of the function in capturing continuous distribution between the populations of SNe Ic-BL and GRB-SNe. The data was split

into two groups containing the SNe Ic-BL and the GRB-SNe, SN 1994I was not included in the test due to the low number of standard SNe Ic. The fit to the whole data set had a Spearman's rank correlation coefficient of 0.87, while just the SNe Ic-BL and GRB-SNe sets had correlation coefficient values of 0.90 and 0.52 respectively. The high value for the correlation coefficient of the whole data set shows the whole distribution of He-poor SNe can be reasonably captured by a continuous power law function. The SNe Ic-BL also display a strong correlation between the power law function and the distribution of SNe Ic-BL. What is of interest is that the coefficient for GRB-SNe shows that while the fit definitely captures the general trend seen with the kinetic energies of GRB-SNe, the fit fails to fully capture the distribution of GRB-SNe. This break from a single power law for GRB's that possess low kinetic energies could suggest that there might be a lower limit cut-off for the ejecta masses produced by GRB-SNe. This lower limit in the ejecta mass would therefore place a lower limit on the progenitor masses of GRB-SNe, below which GRB-SNe may not occur.

Unfortunately, the low number of objects, especially those considered standard SNe Ic, may have resulted in an under fitting at low energies. Additionally, the current parameter space for GRB-SNe seems to suggest a broader distribution than that seen in SNe Ic-BL not associated with a GRB. As such, the relation between kinetic energy and ejecta mass for He-poor SE-SNe found in this work is tentative and increasing the number of He-poor SNe that have undergone detailed hydrodynamic modelling will improve the identification of any underlying trends within the He-poor SN class.

5.8 Conclusion

We have shown the photometric and spectroscopic evolution of SN 2019oyw, the SN component of GRB-SN 190829A. SN 2019oyw displays a pseudo-bolometric evolution very similar to that of SN 1998bw with a similar rise time, $\sim 17 \pm 2$ days. In addition to the similar rise time, SN 2019oyw also peaked at a pseudo-bolometric luminosity comparable to that of SN 1998bw, around $\sim 5.0^{+0.8}_{-0.7} \times 10^{42} \text{ergs}^{-1}$. Although the lack of photometry surrounding peak time places a sizable uncertainty on this peak luminosity.

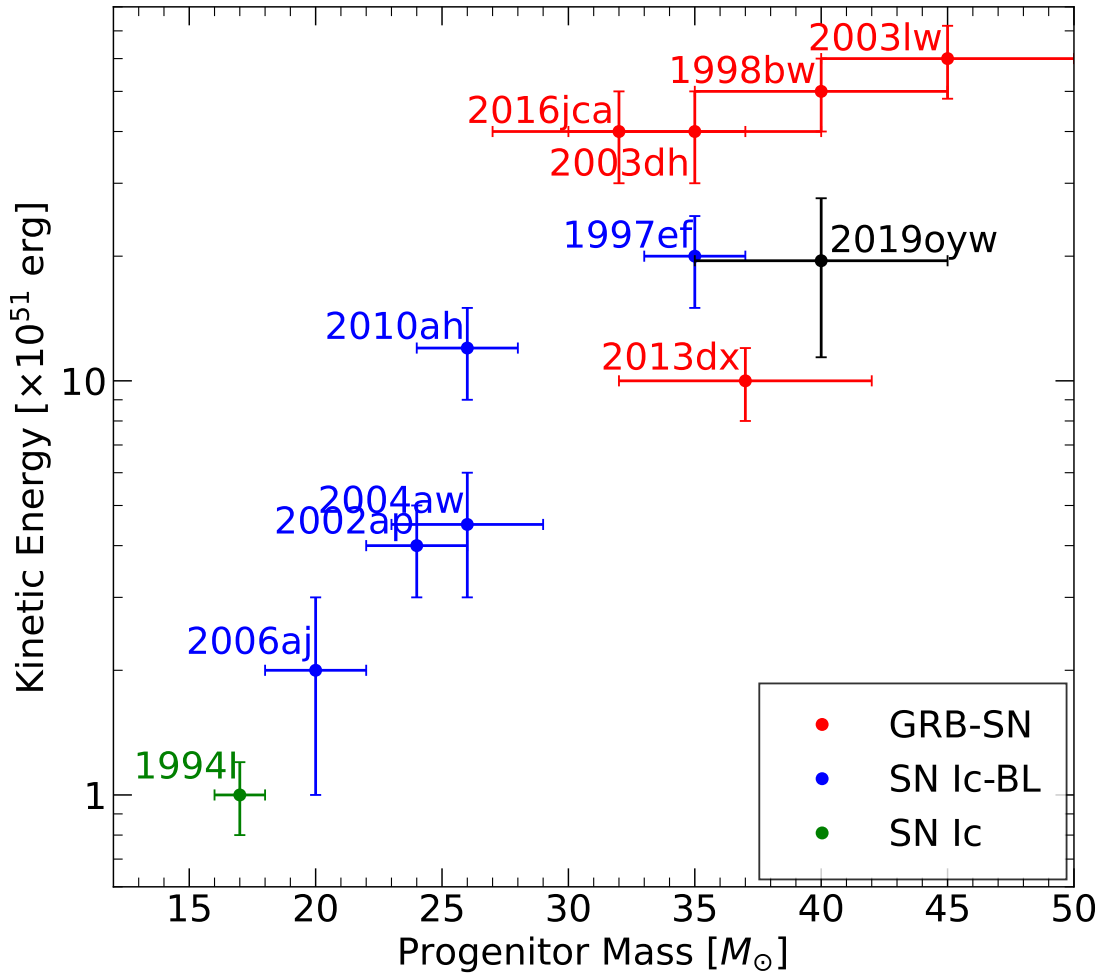


FIGURE 5.10: Expected progenitor mass vs the kinetic energy of several He-poor SE-SNe. SN 2019oyw lies almost on top of SN 1997ef seemingly on the lower edge of the GRB-SNe region. Colour scheme is the same as Figure 5.9.

Fitting to the available pseudo-bolometric light curve showed that SN 2019oyw synthesised a ^{56}Ni mass of $0.21 \pm 0.04 M_{\odot}$, which when adjusted for missing photometric bands using average correction factors for the UV and NIR contributions, increased to $M_{\text{Ni}} = 0.35 \pm 0.21 M_{\odot}$ similar to other GRB-SNe. From a comparison of the pseudo-bolometric light curve properties of SN 2019oyw to other SNe Ic-BL that have undergone hydrodynamic modelling, we suggest that SN 2019oyw ejected $\sim 10 \pm 3 M_{\odot}$ of material with a kinetic energy of $\sim 19 \pm 8 \times 10^{51}$ erg. Relative to other GRB-SNe, SN 2019oyw ejected a comparable amount of material while possessing a kinetic energy that lies towards the lower end of the energy distribution seen with GRB-SNe. Based on stellar evolution models the final mass of SN 2019oyw corresponds to an initial progenitor mass of $35 - 45 M_{\odot}$. Spectroscopically SN 2019oyw possessed a very similar evolution

to that of SN 1998bw, displaying blended iron and oxygen/calcium features throughout the photospheric phase. While similar, the evolution of the Fe II peak suggests that SN 2019oyw may have possessed a shallower density profile than SN 1998bw, which is also suggested by the evolution of the photospheric velocity derived from the Si II line. Based on the spectroscopic features associated with SN 2019oyw we assign it a classification of SN Ic-3/4. This new classification is additionally supported by the energy/mass ratio found for SN 2019oyw which fits the trend found by [Prentice & Mazzali \(2017\)](#).

Finally, the relationship between the ejecta mass and Kinetic energy of several hydrodynamically modelled He-poor SE-SNe was explored and fit with a single power law function. This relation was found to be best captured by a single power law of the form;

$$E_{\text{k}} [\times 10^{51} \text{erg}] = 0.81 \pm 0.31 \times M_{\text{ejc}}^{1.75 \pm 0.20} [M_{\odot}]$$

The best-fitting mass-energy function was able to capture the evolution from the standard SNe Ic to the high energy/mass of the GRB-SNe, suggesting that a continuous mass-energy relation holds across the different types of He-poor SNe that are not associated with a GRB, as well as the majority of GRB-SNe. This also includes SN 2019oyw which was found to lie within the 1σ uncertainty region, although close to the lower limit on the uncertainty, based on the kinetic energy and ejecta mass determined using the light curve comparison method given in Section 5.6.1. The function shown in Figure 5.9 reasonably reproduces the energy/mass distribution seen in SNe Ic-BL not associated with GRBs. However, the distribution of GRB-SNe is not as well captured by equation 5.3, which suggests that GRB-SNe exhibit a much larger diversity within their explosion properties compared to other SNe Ic-BL that are not associated with GRBs. This may result from multiple formation channels for GRB-SNe with distinct central engines and that not all GRB-SNe possess similar progenitors to SNe Ic-BL. However, the low number of events, especially of standard SNe Ic, used here to find the energy-mass relation places a large uncertainty on the relationship. Through an increased effort to determine the explosion parameters of He-poor SE-SNe using hydrodynamical models, it can be tested whether the continuous relationship between kinetic energy and ejecta mass found in Section 5.7 holds true for other He-poor events or if there is a discontinuity between the different types.

Chapter 6

Conclusions and Future Work

6.1 Conclusions

In Chapter 2, I discussed the analysis of SN 2020cpg, a SN Ib that displayed $H\alpha$ features within its spectra around bolometric peak. The analysis of this event showed that by ~ 7 days post B -band maximum weak $H\alpha$ feature, that possessed both a low and high velocity component, rivalled the He I $\lambda 5876$ feature transforming SN 2020cpg into a more SN I Ib-like event. The presence of this weak $H\alpha$ feature within the spectra of SN 2020cpg, a SE-SNe that should lack have been stripped of any hydrogen and are dominated by the presence of helium, shows that the transition between the H-rich SNe I Ib and H-poor SNe Ib is not as distinct as previously thought. The presence of hydrogen within the outer ejecta of SN 2020cpg was further evidenced by fitting of a I Ib-like spectral model to the post-peak spectrum of SN 2020cpg. This modelling suggested that SN 2020cpg possessed a hydrogen mass of $M_H < 0.1 M_\odot$, which was later reduced to $M_H = 0.08 M_\odot$, which places SN 2020cpg at the upper limit of hydrogen within SNe Ib as shown in Figure 6.1. As such, I suggest that SN 2020cpg should be reclassified as a Type Ib(II) SN, a type of SE-SNe that displays weak $H\alpha$ features where the absorption component dominates over the emission component of the P-Cygni profile. Compared to other SNe Ib that have been suggested to possess a small hydrogen

envelope, $M_{\text{H}} < 0.1 M_{\odot}$, SN 2020cpg seems to lie at the upper end of the distribution and overlap with several SNe classified as SNe I Ib.

Modelling the bolometric light curve of SN 2020cpg showed that it produced a $M_{\text{Ni}} \sim 0.3 \pm 0.1 M_{\odot}$. In addition, a robust method that can extract ejecta masses and kinetic energies of CC-SNe through the comparison of bolometric light curves new SNe with several other SE-SNe that have undergone hydrodynamical modelling has been demonstrated. This method has shown that SN 2020cpg possessed an ejecta mass of $5.5 \pm 2.0 M_{\odot}$ and a kinetic energy of $9.0 \pm 3.0 \times 10^{51}$ erg. The use of this method, as a way of obtaining valid estimates for SNe properties when spectral modelling is not possible, has been shown to produce values in reasonable agreement with the physical parameters determined from more detailed modelling. Given the ejecta mass determined above SN 2020cpg is expected to have possessed a progenitor ZAMS mass of $M_{\text{ZAMS}} = 18 - 25 M_{\odot}$. This progenitor mass of SN 2020cpg is much greater than the mass expected for a SN Ib if solely binary interaction is assumed to be the formation channel. This high M_{ZAMS} , alongside the presence of a thin layer of hydrogen, seems to suggest that a massive single star that was unable to fully strip its hydrogen envelope was the progenitor for SN 2020cpg. This is in agreement with a number of single star evolution models that are unable to fully remove their hydrogen envelope, suggesting that at least some SNe Ib originate from the single star formation channel.

Then in Chapter 3, I discussed the photometry and optical spectra of a the Type Ib SN, SN 2020acat, which displayed a fast rise time, reaching peak in ~ 15 days, see Figure 6.2. The fast rise time seen with SN 2020acat, significantly faster than typical SN Ib, may suggest that the radioactive ^{56}Ni synthesised by the explosion was more dispersed into the outer regions of the ejecta than typically assumed for SNe Ib, which is commonly assumed to be very localised to the central region of the ejecta. The comprehensive rise-time coverage, alongside deep non-detection less than 2 days prior to initial detection, allowed for tight constraints to be placed on the explosion date of SN 2020acat. The constraint on the explosion date and shape of the early time observations showed that SN 2020acat lacked a strong shock-cooling phase. The lack of a strong shock cooling phase indicates that the progenitor of SN 2020acat was a compact object and lacked an extended hydrogen envelope prior to explosion, similar to that seen with SN 2008ax

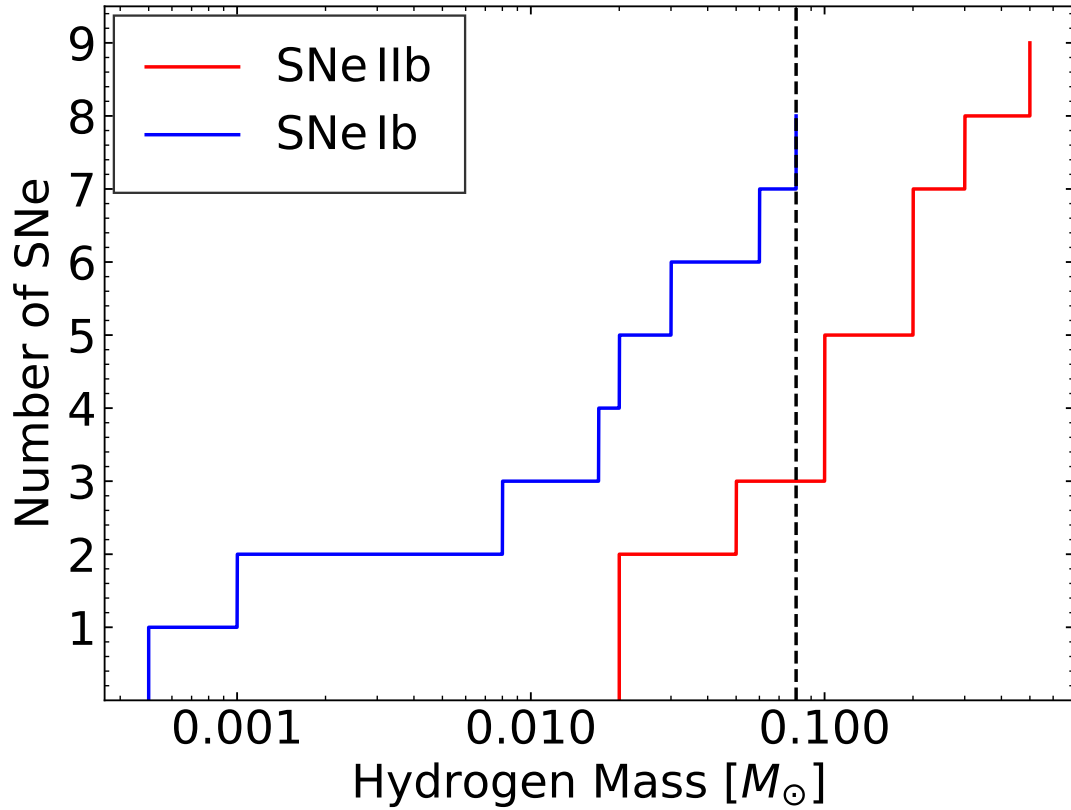


FIGURE 6.1: Distribution of hydrogen mass, M_{H} within the progenitor envelope of 9 SNe IIb and 8 SNe Ib derived from spectral modelling. The expected M_{H} of SN 2020cpg, $M_{\text{H}} = 0.08 M_{\odot}$ is shown by the dashed black line. The SNe used to construct this Figure are; SN 1983N (Elmhamdi et al., 2006), SN 1990I (Elmhamdi et al., 2006), SN 1993J (Wheeler et al., 1993), SN 1999dn (Spencer & Baron, 2010), SN 2000H (Elmhamdi et al., 2006), SN 2003bg (Mazzali et al., 2005), SN 2005bf (Folatelli et al., 2006), SN 2008D (Tanaka et al., 2009), SN 2008ax (Gilkis & Arcavi, 2022), SN 2011dh (Bersten et al., 2012), SN 2011fu (Morales-Garoffolo et al., 2015), SN 2011hs (Bufano et al., 2014), iPTF12os (Fremming et al., 2016), iPTF13bvn (Gilkis & Arcavi, 2022), SN 2013df (Morales-Garoffolo et al., 2014a), SN 2016gkg (Piro et al., 2017) and SN 2019yvr (Gilkis & Arcavi, 2022)

which also lacked a strong shock-cooling phase. Further analysis of the light curve of SN 2020acat showed it produced $0.13 \pm 0.03 M_{\odot}$ of ^{56}Ni , along with an ejecta mass of $M_{\text{ejc}} = 2.3 \pm 0.4 M_{\odot}$ and a kinetic energy of $E_{\text{k}} = 1.2 \pm 0.3 \times 10^{51}$ erg. The ejecta mass predicted for SN 2020acat implies an initial progenitor mass in the range of $15 - 20 M_{\odot}$, placing in within the upper range of progenitors that have undergone stripping via binary interaction which is typically between $10 - 20 M_{\odot}$.

From the spectral evolution, it was shown that SN 2020acat possessed distinctive strong hydrogen features well into the nebular phase, at which point oxygen and calcium,

dominate the spectra. The presence of clear hydrogen lines were observed well into the start of the nebular phase suggesting that SN 2020acat possessed either a very dense thin hydrogen envelope prior to explosion or the hydrogen was mixed deep into the outer layers through some means of convection. Analysis of the nebular phase spectra focused on the [O I]/[Ca II] flux ratio, which was found to be greater than unity suggesting that the progenitor of SN 2020acat was indeed a relatively high mass star, in agreement with the light curve analysis, although this analysis does not indicate a preference of binary or single star formation. In addition to the deep hydrogen signature observed within the spectra of SN 2020acat, the spectral feature associated with the Fe II λ 5018 line was seen to be much stronger than the surrounding Fe II lines. This enhanced Fe II λ 5018 line was likely enhanced by the presence of a combination of helium and potentially nitrogen within the ejecta. While the helium line that could have enhanced this feature has been reported prior, the presence of nitrogen is not expected in the spectra of SNe I Ib, with additional work being needed to confirm the presence of the weak N II lines.

Continuing on from the study of the optical data of SN 2020acat, in Chapter 4, I discussed the analysis of the NIR spectra of SN 2020acat. The NIR spectra showed an interesting evolution of the He I 1.0830 μ m and 2.0581 μ m lines which developed a flat-top shape after ~ 70 days after explosion. The He I 1.0830 μ m and 2.0581 μ m flat-top features displayed minimum boundary velocities of around $\sim 3.5 - 4.0 \times 10^3$ km s⁻¹. This flat-top shape is thought to arise from a central region of helium rich material with a low optical depth, prohibiting the emission of the helium He I 1.0830 μ m and 2.0581 μ m lines. Comparison with the optical [O I] λ 6300, 6363 emission peak showed that the majority of oxygen-rich material was located at velocities within the flat-top region boundaries, strongly suggesting that there is little or no mixing between the helium envelope and the oxygen-rich shell. After analysing the He I 1.0830 μ m and 2.0581 μ m feature other SNe I Ib that possessed NIR data were studied to determine if other hydrogen-rich SE-SNe exhibit this flat-top behaviour. Unfortunately, due to the lack of late-time observations of the NIR region, only SN 2008ax and SN 2011dh have NIR observations at phases similar to that of SN 2020acat. While SN 2008ax displayed a similar flat-top feature to SN 2020acat, as well as a lack of a shock-breakout phase, SN 2011dh exhibited only a sharp emission peak for the NIR helium lines as expected

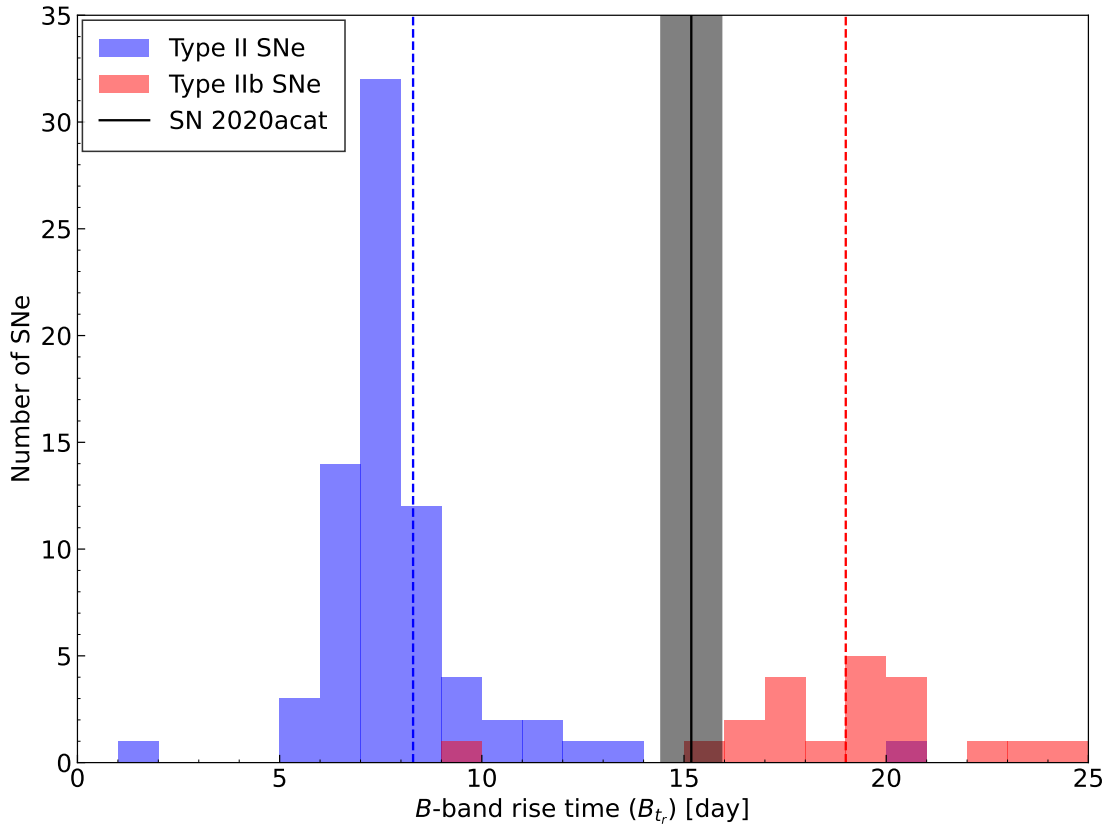


FIGURE 6.2: B -band rise time distribution of SNe II (blue) and SNe IIb (red) taken from Pessi et al. (2019), with the dashed vertical lines indicating the average B -band rise time for each group. The B -band rise time of SN 2020acat, $B_{tr} = 15.18 \pm 0.75$ days, is shown by the black solid line with the uncertainty given by the shaded region. All rise times are given in rest frame.

for a spherically symmetric ejecta. To account for the flat-top He I 1.0830 μm and 2.0581 μm features in both SN 2008ax and SN 2020acat a non-spherical helium shell is required, a property directly linked to the structure of the progenitor. Additional NIR observations of late-time SNe IIb are required to determine the percentage of SNe IIb that possess flat-top helium features and if there indeed is a link between the progenitor structure and the shape of the NIR helium profiles.

Finally in Chapter 5, I analysed the photometric and spectroscopic evolution of the SN component of GRB 190829A/SN 2019oyw. The pseudo-bolometric light curve of SN 2019oyw displays a very similar shape to that of the proto-typical SNIc-BL SN 1998bw. Correcting for the missing photometry bands, an upper limit on the mass of ^{56}Ni synthesised by SN 2019oyw, $M_{\text{Ni}} = 0.35 \pm 0.21 M_{\odot}$ was found, a mass similar to other GRB-SNe. Through a light curve comparison, using the method previously used

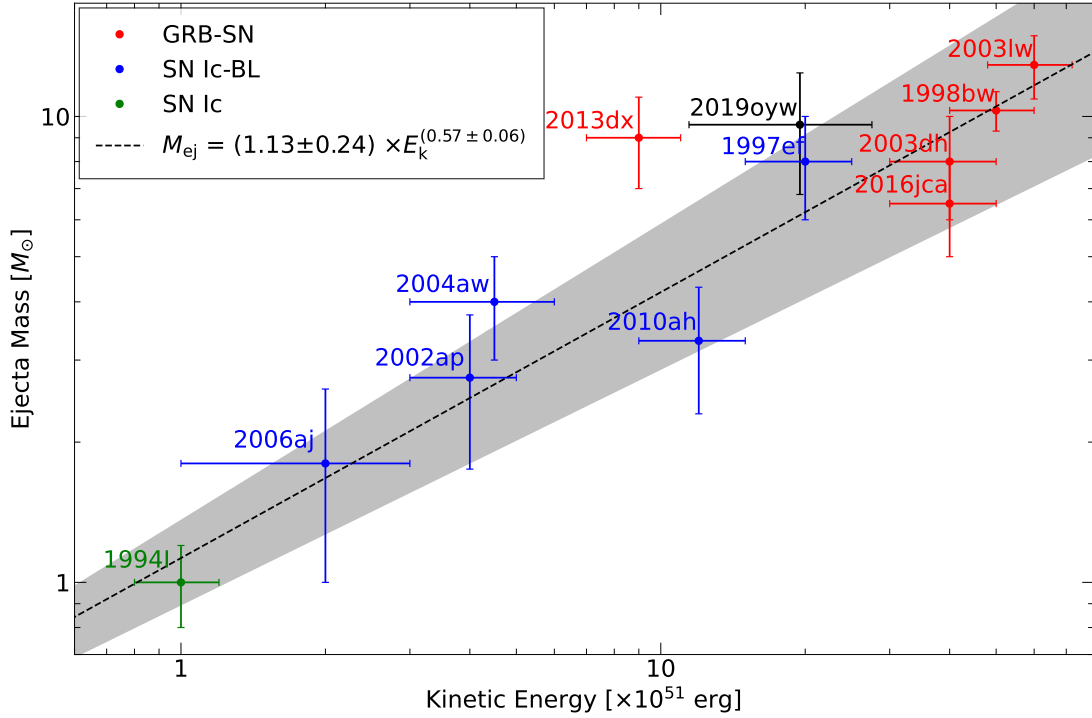


FIGURE 6.3: Single power-law function fit the the current distribution of ejecta masses and kinetic energies of He-poor SNe that have undergone hydrodynamic modelling. Uncertainty captures the majority of SNe, with the exception of SN 2013dx which was far less energetic than expected for the mass of ejecta it produced.

to determine the physical parameters of SN 2020cpg, a ejecta mass of $M_{ejc} = 10 \pm 3 M_{\odot}$ and kinetic energy of $E_k \sim 19 \pm 8 \times 10^{51}$ erg was determined for SN 2019oyw, which would correspond to a progenitor with an initial mass in the range of 35 – 45 M_{\odot} . Through analysis of the spectral evolution of SN 2019oyw a reclassification to a SN Ic-3/4 is suggested based on the number of blended absorption features seen within the pre- and peak-time spectra. This reclassification is supported by the energy/mass ratio of SN 2019oyw, $\sim 2 E_k/M_{ejc}$, agreeing with the trend found for other GRB-SNe and SNe Ic-BL. Lastly an analysis of the relationship between ejecta mass and kinetic energy was performed to determine if a smooth transition between the standard SNe Ic, Ic-BL and GRB-SNe can be found. The best-fit relation between the ejecta mass and kinetic energy was found to be;

$$E_k [\times 10^{51} \text{ erg}] = 0.81 \pm 0.31 \times M_{ejc}^{1.75 \pm 0.20} [M_{\odot}] \quad (6.1)$$

This function was found to capture the evolution of SNe Ic-BL very well as shown in

Figure 6.3. However the GRB-SNe sample display a greater dispersion in their explosion properties compared to the SNe Ic-BL sample. The inconsistency between the function and GRB-SNe sample may suggest that GRB-SN may originate from multiple formation channels and are not always a smooth continuation of the helium stripped SE-SNe at higher progenitor masses as previously thought. Unfortunately, the low numbers of well modelled helium-poor SE-SNe means the energy-mass relationship discussed in this work is not well constrained. An increased effort in modelling helium-poor SE-SNe, especially standard SNe Ic, is required to further study the energy-mass relationship to determine if it truly holds at the high energies where GRB-SNe are located.

As shown by the analysis of the SE-SNe events presented throughout this work, SE-SNe display a range of properties that cannot truly be captured by the rigid classical classifications that have been used throughout the literature. The spectral observations of SN 2020cpg which were found to display hydrogen features at early times runs in opposition to the properties expected in SNe Ib. The existence of hydrogen features within a SN Ib provides strong evidence that there is a smooth transition between SN I Ib and SN Ib as the progenitor becomes more stripped. This smooth transition, which has previously been discussed in the literature, has been in need of greater number of observations, which events like SN 2020cpg has provided. In addition, the analysis of the late-time NIR observations of the SNe I Ib, SN 2020acat has shown a way to distinguish SNe I Ib into two groups, those that exhibit flat-top NIR helium features and those that display sharp emission features which can be directly linked to the structure of their progenitor and potentially the presence of a shock-breakout phase. Finally the exploration of SN 2019oyw and the energy-mass relation between the helium-poor SE-SNe, has shown that while SNe Ic and SNe Ic-BL seem to exist on a smooth continuum, GRB-SNe are not as well constrained by this smooth evolution from high energy SNe Ic-BL to the energetic GRB-SNe. This finding suggests that GRB-SN are not solely a continuation of SNe Ic at higher energies but possess a lower limit to their ejecta masses independent of their kinetic energies. The dispersion seen in the kinetic energies of GRB-SNe may be the result of multiple formation channels for He-poor SE-SNe, with the presence of the GRB counterpart being dependent on the evolution the progenitor undergoes.

6.2 Future work

As shown throughout this work, SE-SNe displays a continuum of spectral and photometric properties that the historical classifications are not flexible enough to easily describe. This will only lead to confusion as the number of well observed transitional SE-SNe are discovered and observed increases through the work of increasingly comprehensive SN surveys that will occur in the coming future. As such, future work to model these transitional events is required to determine their explosion parameters, to fill out the parameter space of spectroscopic and photometric properties and if there is a smooth progression between the different types. A photometric and spectroscopic study of the observations of current hydrogen-rich is required to place constraints on the transition between type II SNe and SNe I Ib. This will provide context to determine if there are strong limits to the minimum amount of material that can be removed through the stripping processes that form SE-SNe. In addition continued observations of SNe I Ib at the NIR wavelengths during the nebular phase are required to determine the frequency of the flat-top helium feature, as well as the link between progenitor structure, shock-breakout phase and shape of the He I 1.0830 μm and 2.0581 μm .

Bibliography

Abbott D. C., 1982, ApJ, 259, 282

Afsariardchi N., Drout M. R., Khatami D. K., Matzner C. D., Moon D.-S., Ni Y. Q.,
2021, The Astrophysical Journal, 918, 89

Aldering G., Humphreys R. M., Richmond M., 1994, AJ, 107, 662

Anderson J. P., 2019, A&A, 628, A7

Arcavi I., et al., 2010, The Astrophysical Journal, 721, 777

Arcavi I., et al., 2011, ApJ Letters, 742, L18

Arcavi I., et al., 2017, ApJ Letters, 837, L2

Arnett W. D., 1977, ApJS, 35, 145

Arnett W. D., 1980a, ApJ, 237, 541

Arnett W. D., 1980b, in Ninth Texas Symposium on Relativistic Astrophysics. pp 366–
379

Arnett W. D., 1982, ApJ, 253, 785

Arnett W. D., 1996, Space Science Reviews, 78, 559

Ashall C., Mazzali P. A., 2020, MNRAS, 492, 5956

Ashall C., et al., 2019, Monthly Notices of the Royal Astronomical Society, 487, 5824

Axelrod T. S., 1980, PhD thesis, Univ. of California, Santa Cruz

- Baade W., Zwicky F., 1934, Proceedings of the National Academy of Science, 20, 254
- Barbon R., Benetti S., Cappellaro E., Patat F., Turatto M., Iijima T., 1995, A&AS, 110, 513
- Barkat Z., Rakavy G., Sack N., 1967, Phys. Rev. Lett., 18, 379
- Barnes J., Duffell P. C., Liu Y., Modjaz M., Bianco F. B., Kasen D., MacFadyen A. I., 2018, The Astrophysical Journal, 860, 38
- Barnsley R. M., Smith R. J., Steele I. A., 2012, Astronomische Nachrichten, 333, 101
- Begelman M. C., Li Z.-Y., 1992, ApJ, 397, 187
- Bellm E. C., et al., 2018, PASA, 131, 018002
- Bersten M. C., et al., 2012, ApJ, 757, 31
- Bersten M. C., et al., 2014, The Astronomical Journal, 148, 68
- Bersten M. C., et al., 2018, Nature, 554, 497
- Bertola F., 1964, Annales d'Astrophysique, 27, 319
- Bethe H. A., 1990, Rev. Mod. Phys., 62, 801
- Bethe H. A., Wilson J. R., 1985, ApJ, 295, 14
- Bethe H. A., Brown G. E., Applegate J., Lattimer J. M., 1979, Nuclear Physics A, 324, 487
- Bevan A. & Barlow M. J., 2015, MNRAS, 456, 1269
- Bianco F. B., et al., 2014, ApJS, 213, 19
- Blandford R. D., Znajek R. L., 1977, MNRAS, 179, 433
- Blondin S., Tonry J. L., 2007, ApJ, 666, 1024
- Bowers R., Wilson J. R., 1982, ApJ, 263, 366
- Branch D., et al., 2002, ApJ, 566, 1005

- Brown T. M., et al., 2013, PASA, 125, 1031
- Brown P. J., Breeveld A. A., Holland S., Kuin P., Pritchard T., 2014, Ap&SS, 354, 89
- Brunish W. M., Cox A. N., Becker S. A., Despain K. H., 1984, in Maeder A., Renzini A., eds, Observational Tests of the Stellar Evolution Theory Vol. 105, Observational Tests of the Stellar Evolution Theory. p. 89
- Bucciantini N., Thompson T. A., Arons J., Quataert E., Del Zanna L., 2006, Monthly Notices of the Royal Astronomical Society, 368, 1717
- Bufano F., et al., 2014, Monthly Notices of the Royal Astronomical Society, 439, 1807
- Burrows A., Lattimer J. M., 1986, ApJ, 307, 178
- Buzzoni B., et al., 1984, The Messenger, 38, 9
- Cano Z., 2013, MNRAS, 434, 1098
- Cassinelli J. P., 1979, Annual Review of Astronomy and Astrophysics, 17, 275
- Castor J. I., Abbott D. C., Klein R. I., 1975, ApJ, 195, 157
- Chand V., et al., 2020, ApJ, 898, 42
- Chandrasekhar S., 1931, ApJ, 74, 81
- Chen K.-J., Woosley S., Heger A., Almgren A., Whalen D. J., 2014, ApJ, 792, 28
- Chevalier R. A., 1992, ApJ, 394, 599
- Chevalier R. A., Soderberg A. M., 2010, ApJ, 711, L40
- Clocchiatti A., Wheeler J. C., 1997, ApJ, 491, 375
- Clocchiatti A., Suntzeff N. B., Covarrubias R., Candia P., 2011, AJ, 141, 163
- Colgate S. A., 1971, ApJ, 163, 221
- Colgate S. A., White R. H., 1964, Technical report, The hydrodynamic behavior of supernovae explosions. Lawrence Radiation Lab., Univ. of California, Livermore

- Colgate S. A., White R. H., 1966, *ApJ*, 143, 626
- Collins K. A., Kielkopf J. F., Stassun K. G., Hessman F. V., 2017, *AJ*, 153, 77
- Corsi A., et al., 2016, *ApJ*, 830, 42
- Corsi A., et al., 2023, *ApJ*, 953, 179
- Cushing M. C., Vacca W. D. & Rayner J. T., 2004, *PASA*, 116, 362
- Cutri R. M., et al., 2013, Explanatory Supplement to the AllWISE Data Release Products, Explanatory Supplement to the AllWISE Data Release Products
- Daigne F., Mochkovitch R., 1998, *Monthly Notices of the Royal Astronomical Society*, 296, 275
- Dainotti M. G., Levine D., Fraija N., Warren D., Sourav S., 2022, *The Astrophysical Journal*, 940, 169
- Deng J., Mazzali P. A., Maeda K., Nomoto K., 2003, *Nuclear Phys. A*, 718, 569–571
- Deng J., Tominaga N., Mazzali P. A., Maeda K., Nomoto K., 2005, *ApJ*, 624, 898
- Dessart L., Hillier D. J., 2005, *A&A*, 439, 671
- Dessart L., Hillier D. J., Livne E., Yoon S.-C., Woosley S., Waldman R., Langer N., 2011, *Monthly Notices of the Royal Astronomical Society*, 414, 2985
- Dessart L., Hillier J. D., Woosley S., Livne E., Waldman R., Yoon S.-C., Langer N., 2016, *MNRAS*, 458, 1618
- Dichiara S., et al., 2019, *GRB Coordinates Network*, 25552, 1
- Djupvik A. A., Andersen J., 2010, *Highlights of Spanish Astrophysics V*, p. 211
- Drout M. R., et al., 2011, *ApJ*, 741, 97
- Drout M. R., et al., 2016, *ApJ*, 821, 57
- Duncan R. C., Thompson C., 1992, *ApJ Letters*, 392, L9
- D’Elia V., et al., 2015, *A&A*, 577, A116

- Eggleton P. P., 1983, *ApJ*, 268, 368
- Eldridge J. J., Tout C. A., 2004, *Monthly Notices of the Royal Astronomical Society*, 353, 87
- Eldridge J. J., Vink J. S., 2006, *A&A*, 452, 295
- Eldridge J. J., Izzard R. G., Tout C. A., 2008, *MNRAS*, 384, 1109
- Elias-Rosa N., et al., 2011, *ApJ*, 742, 6
- Elias J. H., Matthews K., Neugebauer G., Persson S. E., 1985, *ApJ*, 296, 379
- Elmhamdi Danziger I. J., Cappellaro E., Della Valle M., Gouiffes C., Phillips M. M., Turatto M., 2004, *A&A*, 426, 963
- Elmhamdi A., Danziger I. J., Branch D., Leibundgut B., Baron E., Kirshner R. P., 2006, *A&A*, 450, 305
- Ergon M., et al., 2014, *A&A*, 562, A17
- Ergon M., et al., 2015, *A&A*, 580, A142
- Falk S. W., 1978, *ApJ Letters*, 225, L133
- Fan Y.-Z., Zhang B.-B., Xu D., Liang E.-W., Zhang B., 2011, *ApJ*, 726, 32
- Fermi GBM Team 2019, GRB Coordinates Network, 25551, 1
- Ferrero P., et al., 2006, *A&A*, 457, 857
- Filippenko A. V., 1997, *Annual Review of Astronomy and Astrophysics*, 35, 309
- Filippenko A. V., 2000, *AIP Conference Proceedings*, 522, 123
- Filippenko A. V., et al., 1995, *ApJ Letters*, 450, L11
- Folatelli G., et al., 2006, *ApJ*, 641, 1039
- Folatelli G., Bersten M. C., Kuncarayakti H., Benvenuto O. G., Maeda K., Nomoto K., 2015, *ApJ*, 811, 147

- Folatelli G., et al., 2016, *The Astrophysical Journal Letters*, 825, L22
- Foley R. J., Smith N., Ganeshalingam M., Li W., Chornock R., Filippenko A. V., 2007, *ApJ Letters*, 657, L105
- Fowler W. A., Hoyle F., 1964, *ApJS*, 9, 201
- Fox O. D., et al., 2014, *ApJ*, 790, 17
- Fraley G. S., 1968, *Ap&SS*, 2, 96
- Fransson C., 1984, *A&A*, 132, 115
- Fransson C., Chevalier R. A., 1989, *ApJ*, 343, 323
- Fremling C., et al., 2016, *A&A*, 593, A68
- Friesen B., Baron E., Branch D., Chen B., Parrent J. T., Thomas R. C., 2012, *ApJS*, 203, 12
- Gal-Yam A., et al., 2006, *ApJ*, 639, 331
- Gal-Yam A., et al., 2014, *Nature*, 509, 471
- Galama T. J., et al., 1998, *Nature*, 395, 670
- Galama T. J., et al., 1999, *A&AS*, 138, 465
- Georgy C., Meynet G., Walder R., Folini D., Maeder A., 2009, *A&A*, 502, 611
- Georgy C., Ekström S., Meynet G., Massey P., Levesque E. M., Hirschi R., Eggenberger P., Maeder A., 2012, *A&A*, 542, A29
- Gilkis A., Arcavi I., 2022, *Monthly Notices of the Royal Astronomical Society*, 511, 691
- Gordon D., 2006, *High Precision Calculations for Helium*. Springer New York, New York, NY, pp 199–219, doi:10.1007/978-0-387-26308-3_11
- Gräfener G., Owocki S. P., Grassitelli L., Langer N., 2017, *A&A*, 608, A34

- Grassberg E. K., Imshennik V. S., Nadyozhin D. K., 1971, *Astrophysics and Space Science*, 10, 28
- Greiner J., et al., 2015, *Nature*, 523, 189
- Groh J. H., 2014, *A&A*, 572, L11
- Groh J. H., Georgy C., Ekström S., 2013a, *A&A*, 558, L1
- Groh J. H., Meynet G., Georgy C., Ekström S., 2013b, *A&A*, 558, A131
- Hachinger S., Mazzali P. A., Taubenberger S., Hillebrandt W., Nomoto K., Sauer D. N., 2012, *Monthly Notices of the Royal Astronomical Society*, 422, 70
- Hamuy M., et al., 2001, *ApJ*, 558, 615
- Hamuy M., et al., 2009, *ApJ*, 703, 1612
- Hansen C. J., Kawaler S. D., Trimble V., 2012, *Stellar interiors: physical principles, structure, and evolution*. Springer Science & Business Media
- Harrison F. A., et al., 1999, *ApJ Letters*, 523, L121
- Heger A., Langer N., Woosley S. E., 2000, *ApJ*, 528, 368
- Heger A., Fryer C. L., Woosley S. E., Langer N., Hartmann D. H., 2003, *ApJ*, 591, 288
- Howell D., 2019, in *American Astronomical Society Meeting Abstracts #233*. p. 258.16
- Howell D. A., Global Supernova Project 2017, in *American Astronomical Society Meeting Abstracts #230*. p. 318.03
- Hu Y.-D., et al., 2021, *A&A*, 646, A50
- Hurley K., et al., 2002, *GRB Coordinates Network*, 1252, 1
- Ivanova N., et al., 2013, *A&ARv*, 21, 59
- Iwamoto K., et al., 1998, *Nature*, 395, 672
- Janka H.-T., 2001, *A&A*, 368, 527

- Janka H.-T., Buras R., Kitaura Joyanes F. S., Marek A., Rampp M., Scheck L., 2005, Nuclear Physics A, 758, 19
- Janka H.-T., Langanke K., Marek A., Martínez-Pinedo G., Müller B., 2007, Physics Reports, 442, 38
- Jerkstrand Ergon M., Smartt S. J., Fransson C., Sollerman J., Taubenberger S., Bersten M., Spyromilio J., 2015, A&A, 573, A12
- Jordi Grebel E. K., Ammon K., 2006, A&A, 460, 339
- Khatami D. K., Kasen D. N., 2019, ApJ, 878, 56
- Kilpatrick C. D., et al., 2017, MNRAS, 465, 4650
- Kilpatrick C. D., et al., 2018, Monthly Notices of the Royal Astronomical Society, 480, 2072
- Kilpatrick C. D., et al., 2021, Monthly Notices of the Royal Astronomical Society, 504, 2073
- Kippenhahn R., Weigert A., 1967, Z. Astrophys., 65, 251
- Kouveliotou C., Meegan C. A., Fishman G. J., Bhat N. P., Briggs M. S., Koshtal T. M., Paciesas W. S., Pendleton G. N., 1993, ApJ Letters, 413, L101
- Kouveliotou C., et al., 1998, The Astrophysical Journal, 510, L115
- Kumar B., et al., 2013, MNRAS, 431, 308
- Kuncarayakti H., et al., 2013, The Astronomical Journal, 146, 30
- Kuncarayakti H., et al., 2018, A&A, 613, A35
- Lantz B., et al., 2004, in Mazuray L., Rogers P. J., Wartmann R., eds, SPIE Conference Series Vol. 5249, Optical Design and Engineering. p. 146, doi:10.1117/12.512493
- Laplace E., Justham S., Renzo M., Göteborg Y., Farmer R., Vartanyan D., de Mink S. E., 2021, A&A, 656, A58
- Lauterborn D., 1970, A&A, 7, 150

- Lewis J. R., et al., 1994, *Monthly Notices of the Royal Astronomical Society*, 266, L27
- Li J., Liu C., Zhang Z.-Y., Tian H., Fu X., Li J., Yan Z.-Q., 2023, *Nature*, 613, 460
- Lien A. Y., et al., 2019, *GRB Coordinates Network*, 25579, 1
- Long G., et al., 2022, *The Astrophysical Journal Supplement Series*, 262, 26
- Lucy L. B., 1991, *ApJ*, 383, 308
- Lucy L. B., 1999, *A&A*, 344, 282
- Lucy L. B., Abbott D. C., 1993, *ApJ*, 405, 738
- Luo D., Pradhan A. K., 1989, *J. Phys. B: At. Mol. Opt. Phys*, 22, 3377
- Lyman J. D., Bersier D., James P. A., 2014, *MNRAS*, 437, 3848
- Lyman J. D., Bersier D., James P. A., Mazzali P. A., Eldridge J. J., Fraser M., Pian E., 2016, *MNRAS*, 457, 328
- MacFadyen A. I., Woosley S. E., 1999, *ApJ*, 524, 262
- Madau P., della Valle M., Panagia N., 1998, *MNRAS*, 297, L17
- Maeda K., Nakamura T., Nomoto K., Mazzali P. A., Patat F., Hachisu I., 2002, *ApJ*, 565, 405
- Maeder A., Lequeux J., 1982, *A&A*, 114, 409
- Maeder A., Meynet G., 2003, in van der Hucht K., Herrero A., Esteban C., eds, *IAU symposium Vol. 212, A Massive Star Odyssey: From Main Sequence to Supernova*. p. 267
- Maeder A., Meynet G., 2008, in de Koter A., Smith L. J., Waters L. B. F. M., eds, *Astronomical Society of the Pacific Conference Series Vol. 388, Mass Loss from Stars and the Evolution of Stellar Clusters*. p. 3
- Margutti R., et al., 2017, *ApJ*, 835, 140
- Marion G. H., et al., 2014, *ApJ*, 781, 69

- Masci F. J., et al., 2019, PASA, 131, 018003
- Maund J. R., 2019, The Astrophysical Journal, 883, 86
- Maund J. R., Smartt S. J., 2009, Science, 324, 486
- Maund J. R., Smartt S. J., Kudritzki R. P., Podsiadlowski P., Gilmore G. F., 2004, Nature, 427, 129
- Maurer I., Mazzali P. A., Taubenberger S., Hachinger S., 2010, MNRAS, 409, 1441
- Mazzali P. A. & Lucy L. B., 1993, A&A, 279, 447
- Mazzali P. A., 2000, A&A, 363, 705
- Mazzali P. A., Nomoto K., Patat F., Maeda K., 2001, ApJ, 559, 1047
- Mazzali P. A., et al., 2002, ApJ Letters, 572, L61
- Mazzali P. A., et al., 2005, Science, 308, 1284
- Mazzali P. A., et al., 2007, ApJ, 670, 592
- Mazzali P. A., et al., 2008, Science, 321, 1185
- Mazzali P. A., Deng J., Hamuy M., Nomoto K., 2009, ApJ, 703, 1624
- Mazzali P. A., Walker E. S., Pian E., Tanaka M., Corsi A., Hattori T., Gal-Yam A., 2013, MNRAS, 432, 2463
- Mazzali P. A., McFadyen A. I., Woosley S. E., Pian E., Tanaka M., 2014, MNRAS, 443, 67
- Mazzali P. A., Sauer D. N., Pian E., Deng J., Prentice S., Ben Ami S., Taubenberger S., Nomoto K., 2017, MNRAS, 469, 2498
- Mazzali P. A., Pian E., Bufano F., Ashall C., 2021, MNRAS, 505, 4106
- McCully C., Volgenau N. H., Harbeck D.-R., Lister T. A., Saunders E. S., Turner M. L., Siiverd R. J., Bowman M., 2018, in Guzman J. C., Ibsen J., eds, SPIE Astronomical Telescopes + Instrumentation Vol. 10707, Software and Cyberinfrastructure for Astronomy V. SPIE, p. 141, doi:10.1117/12.2314340

- McKenzie E. H., Schaefer B. E., 1999, PASA, 111, 964
- McLean I. S., et al., 1998, in Fowler A. M., ed., *Astron Tel & Instr Proc Vol. 3354, Infrared Astronomical Instrumentation*. SPIE, p. 566
- Medler K., et al., 2021, *Monthly Notices of the Royal Astronomical Society*, 506, 1832
- Medler K., et al., 2022, *Monthly Notices of the Royal Astronomical Society*, 513, 5540
- Medler K., Mazzali P. A., Ashall C., Teffs J., Shahbandeh M., Shappee B., 2023, *MNRAS*, 518, L40
- Meszáros P., Rees M. J., Papathanassiou H., 1994, *ApJ*, 432, 181
- Metzger B. D., Thompson T. A., Quataert E., 2007, *ApJ*, 659, 561
- Meynet G., Maeder A., 2003, *A&A*, 404, 975
- Meynet G., Maeder A., 2005, *A&A*, 429, 581
- Meza N., Anderson J. P., 2020, *A&A*, 641, A177
- Minkowski R., 1941, PASA, 53, 224
- Miyaji S., Nomoto K., Yokoi K., Sugimoto D., 1980, *PASJ*, 32, 303
- Moe M., Di Stefano R., 2017, *ApJS*, 230, 15
- Moorwood A., Cuby J.-G., Lidman C., 1998, *The Messenger*, 91, 9
- Morales-Garoffolo A., et al., 2014a, *MNRAS*, 445, 1647
- Morales-Garoffolo A., et al., 2014b, *MNRAS*, 445, 1647–1662
- Morales-Garoffolo A., et al., 2015, *MNRAS*, 454, 95
- Motohara K., et al., 2006, *ApJ Letters*, 652, L101
- Mould J. R., et al., 2000, *ApJ*, 529, 786
- Müller B., 2019, *Annual Review of Nuclear and PARTICLE Science*, 69, 253
- Nakamura T., Mazzali P. A., Nomoto K., Iwamoto K., 2001, *ApJ*, 550, 991

- Nakar E., 2015, *ApJ*, 807, 172
- Nicholl N., 2018, *Research Notes of the AAS*, 2, 230
- Nomoto K., 1984, *ApJ*, 277, 791
- Nomoto K., Suzuki T., Shigeyama T., Kumagai S., Yamaoka H., Saio H., 1993, *Nature*, 364, 507
- Nordin J., Brinnel V., Giomi M., Santen J. V., Gal-Yam A., Yaron O., Schulze S., 2020, *Transient Name Server Discovery Report*, 2020-511, 1
- O'Connor E., Ott C. D., 2011, *The Astrophysical Journal*, 730, 70
- Paczyński B., 1971, *Annual Review of Astronomy and Astrophysics*, 9, 183
- Paczynski B., 1976, in Eggleton P., Mitton S., Whelan J., eds, *IAU Symposium Vol. 73, Structure and Evolution of Close Binary Systems*. p. 75
- Palmer D. M., et al., 2009, *GRB Coordinates Network*, 9204, 1
- Parrent J. T., Milisavljevic D., Soderberg A. M., Parthasarathy M., 2016, *ApJ*, 820, 75
- Pastorello A., et al., 2007, *Nature*, 447, 829
- Pastorello A., et al., 2008, *Monthly Notices of the Royal Astronomical Society*, 389, 955
- Patat F., et al., 2001, *ApJ*, 555, 900
- Pessi P. J., et al., 2019, *MNRAS*, 488, 4239
- Pessi P., et al., 2020, *Transient Name Server AstroNote*, 248, 1
- Pian E., et al., 2006, *Nature*, 442, 1011
- Piascik S. A., Steele I. A., Bates S. D., Mottram C. J., Smith R. J., Barnsley R. M., Bolton B., 2014, in Ramsay S. K., McLean I. S., Takami H., eds, *SPIE Astronomical Telescopes + Instrumentation Vol. 9147, Ground-based and Airborne Instrumentation for Astronomy V*. SPIE, p. 2703, doi:10.1117/12.2055117
- Pignata G., et al., 2011, *ApJ*, 728, 14

- Piro A. L., Muhleisen M., Arcavi I., Sand D. J., Tartaglia L., Valenti S., 2017, *ApJ*, 846, 94
- Podsiadlowski P., Joss P. C., Hsu J. J. L., 1992, *ApJ*, 391, 246
- Podsiadlowski P., Ivanova N., Justham S., Rappaport S., 2010, *Monthly Notices of the Royal Astronomical Society*, 406, 840
- Poidevin F., et al., 2020, *Transient Name Server Classification Report*, 2020-571, 1
- Popham R., Woosley S. E., Fryer C., 1999, *ApJ*, 518, 356
- Porter A. C., Filippenko A. V., 1987, *The Astronomical Journal*, 93, 1372
- Poznanski D., Prochaska J. X., Bloom J. S., 2012, *MNRAS*, 426, 1465
- Prentice S. J., Mazzali P. A., 2017, *MNRAS*, 469, 2672
- Prentice S. J., et al., 2016, *MNRAS*, 458, 2973
- Prentice S. J., et al., 2019, *MNRAS*, 485, 1559
- Pruet J., Woosley S. E., Buras R., Janka H.-T., Hoffman R. D., 2005, *The Astrophysical Journal*, 623, 325
- Puckett T., et al., 1994, *IAU Circ.*, 5961, 1
- Rakavy G., Shaviv G., 1967, *ApJ*, 148, 803
- Rampp M., Janka H.-T., 2000, *Astrophysical Journal*, 539, L33–L36
- Rayner J. T., Toomey D. W., Onaka P. M., Denault A. J., Stahlberger W. E., Vacca W. D., Cushing M. C., Wang S., 2003, *PASA*, 115, 362
- Richardson D., Branch D., Baron E., 2006, *AJ*, 131, 2233
- Richmond M. W., Treffers R. R., Filippenko A. V., Paik Y., Leibundgut B., Schulman E., Cox C. V., 1994, *AJ*, 107, 1022
- Richmond M. W., et al., 1996, *AJ*, 111, 327
- Roming P. W. A., et al., 2005, *Social Science Research*, 120, 95–142

- Roming P. W. A., et al., 2009, *ApJ*, 704, L118
- Ryder S. R., et al., 2018, *The Astrophysical Journal*, 856, 83
- Sahu D. K., Gurugubelli U. K., Anupama G. C., Nomoto K., 2011, *MNRAS*, 413, 2583
- Sahu D. K., Anupama G. C., Chakradhari N. K., 2013, *MNRAS*, 433, 2
- Sahu D. K., Anupama G. C., Chakradhari N. K., Srivastav S., Tanaka M., Maeda K., Nomoto K., 2018, *MNRAS*, 475, 2591
- Salvaterra R., et al., 2009, *Nature*, 461
- Sana H., et al., 2012, *Science*, 337, 444
- Sauer D. N., Mazzali P. A., Deng J., Valenti S., Nomoto K., Filippenko A. V., 2006, *MNRAS*, 369, 1939
- Savitzky A., Golay M. J. E., 1964, *Analytical Chemistry*, 36, 1627
- Schlafly E. F., Finkbeiner D. P., 2011, *ApJ*, 737, 103
- Shahbandeh M., et al., 2022, *ApJ*, 925, 175
- Shankar S., Mösta P., Barnes J., Duffell P. C., Kasen D., 2021, *Monthly Notices of the Royal Astronomical Society*, 508, 5390
- Sharon A., Kushnir D., 2020, *MNRAS*, 496, 4517
- Shivvers I., et al., 2017, *Publications of the Astronomical Society of the Pacific*, 129, 054201
- Shivvers I., et al., 2019, *MNRAS*, 482, 1545
- Smartt S. J., 2009, *Annual Review of Astronomy and Astrophysics*, 47, 63
- Smartt S. J., et al., 2015, *A&A*, 579, A40
- Smith N., Li W., Filippenko A. V., Chornock R., 2011, *Monthly Notices of the Royal Astronomical Society*, 412, 1522
- Smith K. W., et al., 2019, *Research Notes of the American Astronomical Society*, 3, 26

- Smith K. W., et al., 2020, PASA, 132, 085002
- Soberman G. E., Phinney E. S., van den Heuvel E. P. J., 1997, A&A, 327, 620
- Spencer J., Baron E., 2010, The Astrophysical Journal, 718, 957
- Spergel D. N., et al., 2007, ApJS, 170, 377
- Sravan N., Marchant P., Kalogera V., 2019, The Astrophysical Journal, 885, 130
- Srivastav S., et al., 2020, Transient Name Server AstroNote, 249, 1
- Steele I. A., et al., 2004, in Oschmann Jacobus M. J., ed., Society of Photo-Optical Instrumentation Engineers (SPIE) Conference Series Vol. 5489, Ground-based Telescopes. p. 679, doi:10.1117/12.551456
- Sukhbold T., Ertl T., Woosley S. E., Brown J. M., Janka H. T., 2016, ApJ, 821, 38
- Sutherland P. G., Wheeler J. C., 1984, ApJ, 280, 282
- Suwa Y., Tominaga N., Maeda K., 2018, MNRAS, 483, 3607
- Tachiev G., Fischer C. F., 2001, Canadian Journal of Physics, 79, 955
- Taddia F., et al., 2015, A&A, 574, A60
- Taddia F., et al., 2018, A&A, 609, A136
- Taddia F., et al., 2019, A&A, 621, A71
- Takahashi K., 2018, The Astrophysical Journal, 863, 153
- Takáts K., Vinkó J., 2012, MNRAS, 419, 2783
- Tanaka M., et al., 2009, ApJ, 692, 1131
- Taubenberger S., et al., 2011, MNRAS, 413, 2140
- Teffs J., Ertl T., Mazzali P. A., Hachinger S., Janka H.-T., 2020, Monthly Notices of the Royal Astronomical Society, 499, 730

- Teffs J. J., Prentice S. J., Mazzali P. A., Ashall C., 2021, *Monthly Notices of the Royal Astronomical Society*, 502, 3829
- Teffs J. J., Mazzali P. A., Medler K., Hachinger S., 2022, *MNRAS*, 517, 5678
- Thompson T. A., Chang P., Quataert E., 2004, *The Astrophysical Journal*, 611, 380
- Thorne K. S., Zytlow A. N., 1977, *ApJ*, 212, 832
- Tiengo A., et al., 2013, *Nature*, 500, 312
- Timmes F. X., Woosley S. E., Weaver T. A., 1995, *ApJS*, 98, 617
- Tonry J. L., et al., 2018, *PASA*, 130, 064505
- Toy V. L., et al., 2016, *ApJ*, 818, 79
- Tsvetkov D. Y., Volkov I. M., Baklanov P., Blinnikov S., Tuchin O., 2009, *Peremennye Zvezdy*, 29, 2
- Tsvetkov D. Y., Volkov I. M., Sorokina E., Blinnikov S., Pavlyuk N., Borisov G., 2012, *Peremennye Zvezdy*, 32, 6
- Uomoto A., 1986, *ApJ Letters*, 310, L35
- Usov V. V., 1992, *Nature*, 357, 472
- Uzdensky D. A., MacFadyen A. I., 2007, *The Astrophysical Journal*, 669, 546
- Vacca W. D., Cushing M. C. & Rayner J. T., 2003, *PASA*, 115, 389
- Valenti S., et al., 2008, *MNRAS*, 383, 1485
- Van Dyk S. D., Garnavich P. M., Filippenko A. V., Höflich P., Kirshner R. P., Kurucz R. L., Challis P., 2002, *PASA*, 114, 1322
- Van Dyk S. D., et al., 2013, *The Astrophysical Journal Letters*, 772, L32
- Van Dyk S. D., et al., 2014, *AJ*, 147, 37
- Van Dyk S. D., et al., 2018, *The Astrophysical Journal*, 860, 90

- Vecchio R. D., Dainotti M. G., Ostrowski M., 2016, *The Astrophysical Journal*, 828, 36
- Virtanen P., et al., 2020, *Nature Methods*, 17, 261
- Volnova A. A., et al., 2017, *MNRAS*, 467, 3500
- Wanajo S., Kajino T., Mathews G. J., Otsuki K., 2001, *The Astrophysical Journal*, 554, 578
- Wang K., Dai Z.-G., 2021, *Galaxies*, 9
- Wang L.-J., Han Y.-H., Xu D., Wang S.-Q., Dai Z.-G., Wu X.-F., Wei J.-Y., 2016, *The Astrophysical Journal*, 831, 41
- Wang Y., Rueda J. A., Ruffini R., Becerra L., Bianco C., Becerra L., Li L., Karlica P., 2019, *ApJ*, 874, 39
- Wheeler J. C., et al., 1993, *ApJ Letters*, 417, L71
- Wheeler J. C., Yi I., Höflich P., Wang L., 2000, *ApJ*, 537, 810
- Wheeler J. C., Johnson V., Clocchiatti A., 2015, *MNRAS*, 450, 1295
- Wilson J. R., 1980, in *Ninth Texas Symposium on Relativistic Astrophysics*. pp 358–365
- Wilson R. N., 1983, in Swings J. P., Kjaer K., eds, *ESO Conference and Workshop Proceedings Vol. 17, ESO Conference and Workshop Proceedings*. p. 173
- Wilson J. R., Mayle R., Woosley S. E., Weaver T., 1986, *Annals of the New York Academy of Sciences*, 470, 267
- Woosley S. E., 1993, *ApJ*, 405, 273
- Woosley S. E., Janka T., 2005, *Nature*, 1, 147
- Woosley S. E., Hartmann D. H., Hoffman R. D., Haxton W. C., 1990, *ApJ*, 356, 272
- Woosley S. E., Eastman R. G., Weaver T. A., Pinto P. A., 1994, *ApJ*, 429, 300
- Woosley S. E., Langer N., Weaver T. A., 1995, *ApJ*, 448, 315
- Woosley S. E., Sukhbold T., Kasen D. N., 2021, *ApJ*, 913, 145

- Xiang D., et al., 2019, *The Astrophysical Journal*, 871, 176
- Yaron O., Gal-Yam A., 2012, *PASA*, 124, 668
- Yoon S.-C., Woosley S. E., Langer N., 2010, *The Astrophysical Journal*, 725, 940
- Yoon S.-C., Dessart L., Clocchiatti A., 2017, *ApJ*, 840, 10
- Zapartas E., et al., 2021, *A&A*, 656, L19
- Zhang B., Mészáros P., 2001, *ApJ Letters*, 552, L35
- Zhang W., Woosley S. E., MacFadyen A. I., 2003, *ApJ*, 586, 356
- van Loon J. T., 2006, in Lamers H. J. G. L. M., Langer N., Nugis T., Annuk K., eds, *Astronomical Society of the Pacific Conference Series Vol. 353, Stellar Evolution at Low Metallicity: Mass Loss, Explosions, Cosmology*. p. 211 (arXiv:astro-ph/0512326), doi:10.48550/arXiv.astro-ph/0512326

Appendix

TABLE A1: Apparent $BgVri$ LCO Photometry of SN 2020cpg, no k-correction or extinction correction applied.

MJD_B	$B(err)$ [mag]	$MJD_{g'}$	$g'(err)$ [mag]	MJD_V	$V(err)$ [mag]
58900.362	18.39(0.02)	58894.544	18.55(0.09)	58900.367	18.25(0.02)
58900.364	18.37(0.02)	58900.371	18.05(0.01)	58900.369	18.28(0.02)
58902.316	18.35(0.02)	58900.374	18.20(0.01)	58902.322	18.20(0.02)
58902.319	18.36(0.02)	58902.326	18.08(0.01)	58902.324	18.18(0.02)
58903.337	18.49(0.02)	58902.328	18.06(0.01)	58903.343	18.10(0.02)
58903.34	18.45(0.02)	58903.346	18.06(0.01)	58903.345	18.08(0.02)
58905.101	18.35(0.02)	58903.349	18.07(0.01)	58905.238	18.10(0.02)
58905.233	18.39(0.02)	58905.242	18.05(0.01)	58905.24	18.11(0.02)
58905.236	18.41(0.02)	58905.245	18.06(0.01)	58906.256	18.24(0.02)
58906.251	18.47(0.02)	58906.26	18.10(0.01)	58906.258	18.25(0.02)
58906.254	18.56(0.02)	58906.263	18.09(0.01)	58907.277	18.21(0.02)
58907.272	18.59(0.02)	58907.281	18.14(0.01)	58907.279	18.24(0.02)
58907.274	18.58(0.02)	58907.283	18.16(0.01)	58909.253	18.35(0.02)
58909.248	18.63(0.02)	58909.256	18.16(0.02)	58909.255	18.37(0.02)
58909.25	18.73(0.02)	58909.259	18.17(0.02)	58910.336	18.09(0.02)
58910.331	18.48(0.02)	58910.34	18.29(0.02)	58910.338	18.06(0.02)
58910.333	18.52(0.02)	58910.342	18.23(0.02)	58912.105	18.18(0.02)
58912.1	18.77(0.02)	58912.109	18.37(0.02)	58912.107	18.34(0.02)
58912.102	18.78(0.02)	58912.111	18.39(0.02)	58914.389	18.45(0.02)
58914.383	19.01(0.02)	58914.392	18.63(0.02)	58914.39	18.44(0.02)
58914.386	19.10(0.02)	58914.395	18.55(0.02)	58916.355	18.76(0.02)
58916.35	19.38(0.04)	58916.359	18.80(0.02)	58916.357	18.70(0.02)
58916.352	19.37(0.04)	58916.361	18.80(0.02)	58917.323	18.48(0.02)
58917.313	19.31(0.05)	58917.331	18.89(0.02)	58917.327	18.56(0.02)
58917.318	19.24(0.05)	58917.336	18.98(0.02)	58920.62	18.62(0.06)
58920.61	19.47(0.09)	58920.627	19.24(0.02)	58920.623	18.71(0.06)
58920.615	19.47(0.09)	58920.632	19.14(0.02)	58924.184	18.87(0.04)
58924.174	19.94(0.06)	58924.192	19.45(0.02)	58924.188	18.85(0.04)
58924.179	19.90(0.06)	58924.197	19.57(0.02)	58927.094	19.09(0.04)
58927.084	20.25(0.06)	58927.102	19.75(0.02)	58927.098	19.00(0.04)
58927.089	20.19(0.06)	58927.107	19.67(0.02)	58931.054	19.37(0.04)
58931.044	20.65(0.05)	58931.062	20.11(0.02)	58931.058	19.52(0.04)
58931.049	20.42(0.05)	58931.067	20.05(0.02)	58949.708	19.92(0.12)
-	-	-	-	58951.685	19.99(0.08)
-	-	-	-	58959.235	20.11(0.05)
-	-	-	-	58974.207	20.20(0.15)
-	-	-	-	58982.144	20.48(0.15)
-	-	-	-	58985.538	20.53(0.07)
-	-	-	-	58993.431	20.36(0.09)
-	-	-	-	59000.823	20.67(0.14)
-	-	-	-	59008.891	20.54(0.15)

TABLE B1: Apparent *ri* LCO Photometry of SN 2020cpg, no k-correction or extinction correction applied.

MJD _{<i>r'</i>}	<i>r'</i> (<i>err</i>) [mag]	MJD _{<i>i'</i>}	<i>i'</i> (<i>err</i>) [mag]
58894.501	18.49(0.08)	58900.38	18.41(0.02)
58900.376	18.35(0.02)	58900.382	18.40(0.02)
58900.378	18.24(0.02)	58902.335	18.24(0.02)
58902.331	18.16(0.02)	58902.336	18.22(0.02)
58902.333	18.14(0.02)	58903.355	18.20(0.02)
58903.352	18.16(0.02)	58903.357	18.17(0.02)
58903.354	18.13(0.02)	58905.251	18.17(0.02)
58905.247	18.07(0.02)	58905.253	18.18(0.02)
58905.249	18.09(0.02)	58906.269	18.06(0.02)
58906.265	18.11(0.02)	58906.271	18.04(0.02)
58906.267	18.08(0.02)	58907.29	18.12(0.02)
58907.286	18.02(0.02)	58907.291	18.06(0.02)
58907.288	18.05(0.02)	58909.265	18.08(0.02)
58909.262	18.01(0.02)	58909.267	18.03(0.02)
58909.264	18.04(0.02)	58910.349	18.01(0.02)
58910.345	18.07(0.02)	58910.35	18.06(0.02)
58910.347	18.10(0.02)	58912.118	18.05(0.04)
58912.114	18.11(0.02)	58912.119	18.06(0.04)
58912.116	18.09(0.02)	58914.401	18.09(0.03)
58914.397	18.17(0.02)	58914.403	18.14(0.03)
58914.399	18.18(0.02)	58916.368	18.19(0.02)
58916.364	18.20(0.02)	58916.369	18.22(0.02)
58916.366	18.28(0.02)	58917.347	18.37(0.05)
58917.341	18.28(0.02)	58917.349	18.49(0.05)
58917.344	18.34(0.02)	58920.643	18.46(0.05)
58920.638	18.54(0.02)	58920.646	18.40(0.05)
58920.64	18.50(0.02)	58924.208	18.40(0.03)
58924.202	18.59(0.02)	58924.21	18.40(0.03)
58924.205	18.60(0.02)	58927.118	18.59(0.02)
58927.112	18.81(0.02)	58927.12	18.62(0.02)
58927.115	18.85(0.02)	58931.08	18.81(0.01)
58931.072	19.09(0.02)	58931.084	18.78(0.01)
58931.076	19.15(0.02)	58939.657	19.12(0.01)
58939.653	19.34(0.02)	58951.692	19.53(0.03)
58951.689	19.66(0.04)	58959.243	19.54(0.04)
58959.239	19.77(0.03)	58974.215	19.76(0.11)
58974.211	20.01(0.10)	58982.151	19.88(0.05)
58982.147	20.03(0.04)	58985.546	19.91(0.05)
58985.542	20.07(0.03)	58993.439	20.14(0.09)
58993.435	20.17(0.11)	59000.831	20.43(0.15)
59000.827	20.21(0.10)	59008.898	20.17(0.06)
59008.894	20.40(0.12)	-	-

TABLE C1: Apparent c+o band ATLAS photometry for SN 2020cpg. Photometry has not been corrected for either extinction or k-correction.

MJD _c	<i>c</i> (<i>err</i>) [mag]	MJD _o	<i>o</i> (<i>err</i>) [mag]	MJD _o	<i>o</i> (<i>err</i>) [mag]
58903.464	18.10(0.06)	58901.489	18.33(0.08)	58953.488	19.32(0.17)
58903.499	18.10(0.05)	58901.493	18.23(0.07)	58957.400	19.80(0.30)
58903.503	18.19(0.06)	58901.500	18.24(0.06)	58957.412	19.59(0.20)
58903.512	18.18(0.05)	58901.511	18.22(0.06)	58957.415	19.87(0.27)
58911.503	18.13(0.05)	58905.562	18.07(0.05)	58961.441	19.38(0.16)
58931.502	19.27(0.13)	58905.565	18.09(0.05)	58961.444	19.78(0.22)
58931.522	19.59(0.17)	58905.573	18.06(0.05)	58961.465	19.67(0.21)
58931.530	19.45(0.15)	58905.583	18.10(0.05)	58965.446	19.26(0.20)
58931.539	19.46(0.16)	58913.454	18.20(0.07)	58965.457	19.73(0.29)
58935.583	19.78(0.25)	58913.458	18.10(0.06)	58965.491	19.55(0.21)
58935.586	19.55(0.21)	58913.463	18.24(0.07)	58969.404	20.12(0.30)
58959.426	20.14(0.30)	58913.477	18.19(0.07)	58969.417	19.83(0.23)
58959.430	19.66(0.19)	58917.449	18.25(0.18)	58969.421	20.02(0.27)
58959.438	20.18(0.28)	58917.457	18.32(0.19)	58969.428	19.75(0.22)
58959.455	20.05(0.27)	58917.467	18.78(0.27)	58971.423	19.68(0.26)
58967.415	19.96(0.23)	58925.533	18.70(0.21)	58971.439	19.54(0.25)
58967.425	20.10(0.26)	58925.538	18.65(0.17)	58977.446	19.21(0.28)
58967.460	20.10(0.28)	58933.537	19.36(0.18)	58981.387	19.63(0.20)
58982.391	20.06(0.25)	58933.543	19.02(0.13)	58981.404	20.07(0.30)
58987.399	20.12(0.27)	58933.547	19.14(0.15)	58981.415	19.76(0.26)
-	-	58933.559	18.86(0.12)	58985.366	19.94(0.23)
-	-	58937.496	19.27(0.13)	58985.380	20.12(0.28)
-	-	58937.498	19.32(0.12)	58989.354	19.76(0.18)
-	-	58937.508	18.99(0.29)	58989.358	20.08(0.25)
-	-	58937.522	19.47(0.17)	58989.393	20.06(0.24)
-	-	58941.433	18.80(0.13)	58997.324	20.07(0.28)
-	-	58941.445	18.91(0.15)	58997.331	20.13(0.28)
-	-	58941.448	19.50(0.24)	58997.335	20.06(0.30)
-	-	58941.463	19.18(0.27)	58999.352	19.83(0.28)
-	-	58943.479	19.44(0.25)	58999.355	19.77(0.29)
-	-	58943.484	19.47(0.30)	59006.346	19.44(0.30)
-	-	58949.477	19.20(0.26)	59013.351	20.26(0.30)
-	-	58949.482	19.30(0.30)	59013.357	20.25(0.29)
-	-	58951.461	18.89(0.28)	59013.367	20.23(0.28)
-	-	58951.469	19.57(0.29)	59021.328	20.08(0.27)
-	-	58951.482	19.17(0.29)	59021.346	20.04(0.27)
-	-	58953.467	19.28(0.19)	59025.321	20.26(0.30)
-	-	58953.474	19.92(0.28)	59029.318	19.44(0.30)
-	-	58953.478	19.46(0.19)	59037.297	19.95(0.29)

TABLE D1: UV Swift

<i>MJD</i>	<i>UW2</i> (err) [mag]	<i>UM2</i> (err) [mag]	<i>UW1</i> (err) [mag]	<i>U</i> (err) [mag]	<i>B</i> (err) [mag]	<i>V</i> (err) [mag]	Source
59194.7642841482	22.361(-9)	22.474(-9)	20.954(0.25)	19.421(0.142)	18.143(0.097)	17.867(0.148)	Swift
59196.533506946	21.049(0.141)	21.762(0.232)	19.795(0.108)	18.211(0.07)	17.33(0.06)	16.988(0.08)	Swift
59198.2288194154	19.305(0.142)	19.274(0.139)	18.14(0.111)	16.933(0.093)	16.378(0.09)	16.359(0.149)	Swift
59200.3189431276	18.432(0.073)	18.309(0.064)	17.52(0.063)	16.333(0.052)	15.925(0.049)	15.705(0.059)	Swift
59201.1982194394	18.296(0.075)	18.098(0.067)	17.347(0.064)	16.232(0.055)	15.801(0.052)	15.636(0.064)	Swift
59202.460872812	18.121(0.074)	18.027(0.067)	17.276(0.064)	16.059(0.054)	15.616(0.05)	15.464(0.062)	Swift
59202.9660980227	18.132(0.069)	18.141(0.063)	17.191(0.059)	15.952(0.049)	15.577(0.046)	15.416(0.053)	Swift
59203.389043097	18.217(0.074)	18.212(0.068)	17.17(0.062)	15.97(0.052)	15.562(0.049)	15.371(0.058)	Swift
59204.0296705762	18.47(0.076)	18.488(0.071)	17.371(0.063)	15.997(0.051)	15.505(0.047)	15.491(0.058)	Swift
59206.4582486298	18.562(0.1)	19.126(0.114)	17.377(0.079)	16.019(0.064)	15.331(0.057)	15.261(0.077)	Swift
59208.0338656812	18.775(0.103)	19.124(0.114)	17.521(0.081)	15.848(0.06)	15.377(0.056)	15.264(0.073)	Swift
59210.3600122291	19.285(0.097)	19.735(0.108)	18.018(0.075)	16.217(0.054)	15.519(0.048)	15.194(0.055)	Swift
59211.7589494866	19.7(0.114)	20.905(0.318)	18.349(0.085)	16.35(0.057)	15.587(0.05)	15.221(0.057)	Swift
59213.6829899187	20.129(0.123)	20.7(0.155)	18.792(0.091)	16.819(0.06)	15.742(0.049)	15.313(0.054)	Swift
59215.9460654256	20.39(0.143)	20.784(0.167)	19.082(0.104)	17.153(0.066)	16.034(0.053)	15.433(0.057)	Swift
59218.4606308191	20.927(0.18)	21.626(0.248)	19.506(0.124)	17.545(0.075)	16.227(0.055)	15.526(0.059)	Swift
59221.1843525082	21.413(0.234)	21.846(0.305)	19.803(0.143)	17.884(0.086)	16.566(0.062)	15.749(0.065)	Swift
59224.037030507	21.393(0.249)	22.069(-9)	20.405(0.208)	18.555(0.123)	16.669(0.067)	15.899(0.072)	Swift
59227.2181480029	-	-	20.282(0.239)	-	-	-	Swift
59230.4050775736	20.499(-9)	-	20.701(0.348)	18.977(0.214)	17.149(0.11)	-	Swift
59239.7789964651	22.054(0.233)	22.61(0.339)	20.833(0.167)	19.406(0.122)	17.67(0.069)	16.553(0.064)	Swift
59244.5172300455	21.778(-9)	21.806(-9)	21.106(-9)	19.386(0.221)	17.936(0.135)	16.781(0.124)	Swift
59255.6692440499	22.325(0.29)	22.331(0.291)	20.937(0.192)	19.427(0.132)	17.904(0.081)	16.951(0.081)	Swift
59261.0783032858	22.142(0.298)	22.518(-9)	20.885(0.19)	19.515(0.162)	18.215(0.109)	16.896(0.091)	Swift
59264.3386622583	21.425(0.351)	20.725(-9)	20.803(-9)	19.248(0.247)	18.01(0.17)	17.59(0.236)	Swift
59268.9636908929	21.269(-9)	21.251(-9)	21.431(-9)	19.546(0.22)	17.743(0.165)	17.238(0.217)	Swift
59272.8370710846	21.468(-9)	21.487(-9)	20.768(0.358)	19.319(0.259)	18.022(0.171)	17.123(0.181)	Swift
59330.7752096895	21.542(-9)	21.639(-9)	20.847(-9)	19.94(-9)	18.506(0.218)	17.832(0.263)	Swift
59333.2481259101	22.293(-9)	22.2(0.348)	21.577(-9)	20.045(0.245)	18.735(0.161)	18.241(0.216)	Swift

TABLE E1: LCO BgVri

MJD_B	$B(\text{err})$ [mag]	MJD_g^*	$g^*(\text{err})$ [mag]	MJD_V	$V(\text{err})$ [mag]	MJD_r^*	$r^*(\text{err})$ [mag]	MJD_i^*	$i^*(\text{err})$ [mag]	Source
59236.78	17.75(0.03)	59236.79	17.21(0.02)	59236.78	16.61(0.03)	59236.79	16.27(0.05)	59236.79	16.05(0.10)	COJ
59236.78	17.78(0.03)	59248.65	17.49(0.04)	59236.78	16.62(0.03)	59236.79	16.27(0.05)	59236.79	16.00(0.09)	COJ
59248.64	18.01(0.05)	59248.65	17.50(0.04)	59248.64	16.84(0.04)	59248.65	16.59(0.04)	59248.65	16.30(0.07)	COJ
59248.64	18.02(0.06)	59300.58	18.08(0.04)	59248.65	16.97(0.03)	59248.65	16.61(0.06)	59300.59	17.25(0.06)	COJ
59300.58	18.66(0.05)	59300.59	18.08(0.04)	59300.58	17.69(0.04)	59300.59	17.30(0.05)	59300.60	17.22(0.07)	COJ
59300.58	18.65(0.06)	59325.60	18.47(0.03)	59300.58	17.69(0.05)	59300.59	17.34(0.05)	59325.60	17.67(0.08)	COJ
59325.59	18.79(0.05)	59325.60	18.48(0.03)	59325.59	18.10(0.03)	59325.60	17.66(0.04)	59325.61	17.75(0.08)	COJ
59325.59	19.05(0.07)	-	-	59325.59	18.03(0.04)	59325.60	17.69(0.04)	-	-	COJ
59194.08	17.93(0.24)	59194.08	18.16(0.11)	59194.08	17.68(0.06)	59194.08	17.71(0.09)	59194.09	18.05(0.21)	CPT
59194.08	18.23(0.04)	59197.12	16.45(0.02)	59194.08	17.74(0.08)	59194.09	17.65(0.07)	59194.09	17.83(0.15)	CPT
59197.11	16.75(0.02)	59197.12	16.45(0.03)	59197.11	16.46(0.03)	59197.12	16.39(0.04)	59197.13	16.56(0.05)	CPT
59197.11	16.75(0.02)	59199.09	15.79(0.03)	59197.11	16.47(0.03)	59197.12	16.40(0.04)	59197.13	16.54(0.05)	CPT
59199.09	16.13(0.02)	59199.09	15.85(0.03)	59199.09	15.92(0.03)	59199.10	15.89(0.04)	59199.10	16.21(0.16)	CPT
59208.10	15.46(0.03)	59208.10	15.02(0.17)	59199.09	15.93(0.03)	59199.10	15.86(0.04)	59199.10	16.22(0.18)	CPT
59208.10	15.46(0.04)	59208.10	14.98(0.17)	59208.10	15.15(0.05)	59208.11	15.16(0.08)	59208.11	15.21(0.10)	CPT
59209.13	15.40(0.05)	59209.13	15.30(0.09)	59208.10	15.16(0.05)	59208.11	15.19(0.08)	59208.11	15.21(0.10)	CPT
59209.13	15.39(0.04)	59209.13	15.29(0.09)	59209.13	15.12(0.04)	59209.14	15.03(0.06)	59209.14	15.17(0.08)	CPT
59211.09	15.66(0.03)	59211.10	15.32(0.03)	59209.13	15.11(0.05)	59209.14	15.02(0.06)	59209.14	15.08(0.08)	CPT
59211.09	15.66(0.02)	59211.10	15.30(0.03)	59211.09	15.23(0.03)	59211.10	15.14(0.04)	59211.10	15.10(0.05)	CPT
59213.09	15.83(0.02)	59213.12	15.55(0.10)	59211.10	15.25(0.03)	59211.10	15.15(0.04)	59211.11	15.12(0.06)	CPT
59213.09	15.86(0.03)	59213.13	15.53(0.10)	59213.12	15.27(0.04)	59213.13	15.09(0.05)	59213.13	15.17(0.07)	CPT
59213.12	15.76(0.04)	59229.09	16.78(0.03)	59213.12	15.27(0.04)	59213.13	15.11(0.06)	59213.13	15.17(0.07)	CPT
59213.12	15.75(0.04)	59229.09	16.78(0.05)	59229.09	16.19(0.03)	59229.10	15.88(0.06)	59229.10	15.68(0.08)	CPT
59229.09	17.20(0.03)	59233.10	16.99(0.04)	59229.09	16.22(0.03)	59229.10	15.88(0.06)	59229.10	15.65(0.07)	CPT
59229.09	17.25(0.04)	59233.10	16.99(0.03)	59233.09	16.42(0.03)	59233.10	16.06(0.05)	59233.10	15.86(0.07)	CPT
59233.09	17.58(0.03)	59254.13	17.70(0.04)	59233.10	16.44(0.04)	59233.10	16.10(0.05)	59233.11	15.82(0.06)	CPT
59233.09	17.54(0.04)	59254.13	17.70(0.03)	59254.13	17.13(0.05)	59254.14	16.78(0.04)	59254.14	16.46(0.05)	CPT
59254.12	18.18(0.03)	59275.96	18.04(0.05)	59254.13	17.06(0.03)	59254.14	16.78(0.04)	59254.14	16.46(0.05)	CPT
59254.12	18.18(0.03)	59275.96	17.74(0.14)	59275.95	17.35(0.06)	59281.95	17.15(0.05)	59281.95	16.96(0.07)	CPT
59272.16	18.26(0.13)	59281.94	17.97(0.03)	59275.96	17.39(0.06)	59281.95	17.12(0.04)	59281.95	16.97(0.07)	CPT
59272.16	18.43(0.21)	59281.95	17.95(0.03)	59281.94	17.45(0.03)	59291.10	17.18(0.09)	59291.11	17.21(0.08)	CPT
59275.95	18.37(0.08)	59291.10	18.15(0.03)	59281.94	17.45(0.03)	59291.10	17.28(0.19)	59291.11	17.14(0.06)	CPT
59275.95	18.61(0.09)	59291.10	17.98(0.10)	59291.09	17.62(0.04)	59316.80	17.48(0.06)	59316.80	17.33(0.09)	CPT
59281.93	18.43(0.03)	59316.79	18.04(0.07)	59291.09	17.58(0.03)	59316.80	17.44(0.08)	59316.80	17.41(0.09)	CPT
59281.94	18.41(0.03)	59316.79	18.10(0.07)	59316.79	17.72(0.06)	59359.92	18.14(0.19)	59359.93	18.17(0.10)	CPT
59291.09	18.59(0.04)	59359.92	18.81(0.09)	59316.79	17.69(0.05)	59359.93	18.06(0.08)	59359.93	18.13(0.10)	CPT
59291.09	18.62(0.04)	59359.92	18.91(0.10)	59359.91	18.68(0.10)	59436.78	19.24(0.07)	59436.78	19.25(0.10)	CPT
59316.78	18.45(0.05)	59367.82	18.79(0.18)	59359.91	18.59(0.09)	59436.77	19.21(0.07)	59436.78	19.38(0.12)	CPT
59359.90	19.12(0.14)	59436.76	20.38(0.17)	59367.81	18.72(0.06)	-	-	-	-	CPT
59359.91	19.22(0.16)	59436.77	20.67(0.13)	59367.82	18.96(0.06)	-	-	-	-	CPT
59367.80	19.62(0.05)	-	-	59436.78	20.26(0.08)	-	-	-	-	CPT
59436.77	20.96(0.17)	-	-	59436.78	20.16(0.10)	-	-	-	-	CPT
59436.77	20.61(0.10)	-	-	-	-	-	-	-	-	CPT
59193.50	18.62(0.05)	59193.51	18.15(0.08)	59193.51	18.09(0.06)	59193.52	17.92(0.08)	59193.52	17.94(0.08)	ELP
59193.50	18.65(0.06)	59193.51	18.17(0.08)	59193.51	18.10(0.05)	59193.52	17.89(0.08)	59193.52	17.97(0.09)	ELP
59194.52	18.08(0.03)	59194.53	17.67(0.03)	59194.52	17.57(0.03)	59194.54	17.38(0.04)	59194.54	17.50(0.05)	ELP
59194.52	18.08(0.03)	59194.54	17.70(0.03)	59194.52	17.58(0.03)	59194.54	17.40(0.04)	59194.54	17.51(0.05)	ELP
59201.55	15.78(0.03)	59201.56	15.47(0.03)	59201.56	15.57(0.03)	59201.57	15.55(0.05)	59201.57	15.68(0.06)	ELP
59201.55	15.77(0.03)	59201.56	15.47(0.03)	59201.56	15.58(0.03)	59201.57	15.53(0.05)	59201.57	15.67(0.06)	ELP
59204.50	15.52(0.03)	59204.50	15.20(0.05)	59204.50	15.27(0.04)	59204.51	15.26(0.05)	59204.51	15.48(0.07)	ELP
59204.50	15.48(0.04)	59204.50	15.18(0.05)	59204.50	15.29(0.04)	59204.51	15.25(0.05)	59204.51	15.47(0.07)	ELP
59221.45	16.68(0.03)	59221.46	16.22(0.04)	59221.45	15.79(0.03)	59221.46	15.52(0.05)	59221.46	15.46(0.07)	ELP
59221.45	16.68(0.03)	59221.46	16.21(0.04)	59221.45	15.80(0.04)	59221.46	15.51(0.05)	59221.46	15.43(0.08)	ELP
59195.35	17.58(0.02)	59195.36	17.24(0.02)	59195.35	17.17(0.03)	59195.36	17.00(0.04)	59195.37	17.21(0.07)	LSC
59195.35	17.59(0.03)	59195.36	17.23(0.02)	59195.35	17.19(0.03)	59195.36	17.00(0.04)	59195.37	17.20(0.07)	LSC
59203.35	15.64(0.02)	59203.36	15.36(0.03)	59203.36	15.43(0.03)	59203.37	15.43(0.05)	59203.37	15.55(0.07)	LSC
59203.36	15.64(0.02)	59203.37	15.36(0.03)	59203.36	15.43(0.03)	59203.37	15.43(0.05)	59203.37	15.60(0.08)	LSC

TABLE F1: Table above cont

MJD_B	$B(\text{err})$ [mag]	MJD_g^*	$g^*(\text{err})$ [mag]	MJD_V	$V(\text{err})$ [mag]	MJD_r^*	$r^*(\text{err})$ [mag]	MJD_i^*	$i^*(\text{err})$ [mag]	Source
59206.34	15.51(0.02)	59206.35	15.23(0.03)	59206.35	15.26(0.03)	59206.35	15.21(0.04)	59206.36	15.39(0.08)	LSC
59206.34	15.50(0.02)	59206.35	15.25(0.02)	59206.35	15.24(0.03)	59206.35	15.22(0.04)	59206.36	15.41(0.08)	LSC
59218.31	16.38(0.02)	59218.32	15.96(0.03)	59218.31	15.61(0.03)	59218.32	15.41(0.04)	59218.32	15.32(0.07)	LSC
59218.31	16.37(0.02)	59218.32	15.95(0.02)	59218.31	15.60(0.03)	59218.32	15.43(0.04)	59218.32	15.33(0.07)	LSC
59252.42	18.07(0.03)	59252.42	17.59(0.02)	59252.42	17.01(0.03)	59252.43	16.65(0.04)	59252.43	16.41(0.07)	LSC
59252.42	18.08(0.02)	59252.42	17.59(0.02)	59252.42	17.03(0.03)	59252.43	16.64(0.04)	59252.43	16.42(0.07)	LSC
59260.22	18.18(0.03)	59260.22	17.65(0.03)	59260.22	17.08(0.03)	59260.23	16.94(0.05)	59260.23	16.49(0.06)	LSC
59260.22	18.10(0.02)	59260.23	17.66(0.03)	59260.22	17.10(0.03)	59260.23	16.73(0.04)	59260.23	16.49(0.06)	LSC
59266.21	18.23(0.03)	59266.22	17.72(0.02)	59266.22	17.20(0.03)	59266.23	16.84(0.04)	59266.23	16.63(0.08)	LSC
59266.22	18.25(0.03)	59266.23	17.72(0.02)	59266.22	17.21(0.03)	59266.23	16.83(0.04)	59266.23	16.65(0.07)	LSC
59308.16	18.67(0.04)	59308.17	18.23(0.04)	59308.17	17.81(0.04)	59308.18	17.39(0.05)	59308.18	17.35(0.06)	LSC
59308.16	18.69(0.04)	59308.17	18.20(0.04)	59308.17	17.81(0.04)	59308.18	17.39(0.05)	59308.18	17.34(0.06)	LSC
59341.22	19.13(0.04)	59341.23	18.59(0.03)	59341.22	18.35(0.03)	59341.24	17.83(0.04)	59341.24	17.90(0.11)	LSC
59369.14	19.60(0.03)	59341.23	18.61(0.06)	59341.23	18.35(0.03)	59341.24	17.86(0.06)	59341.24	17.81(0.08)	LSC
59369.15	19.62(0.03)	59369.15	19.21(0.03)	59369.15	18.85(0.03)	59369.16	18.25(0.07)	59369.17	18.32(0.06)	LSC
59379.08	19.72(0.04)	59369.16	19.19(0.04)	59369.15	18.84(0.04)	59369.17	18.26(0.05)	59369.17	18.30(0.06)	LSC
59379.09	19.73(0.03)	59379.10	19.30(0.05)	59379.09	19.06(0.05)	59379.10	18.24(0.08)	59379.11	18.67(0.16)	LSC
59387.08	19.84(0.16)	59379.10	19.29(0.05)	59379.09	19.06(0.05)	59379.11	18.30(0.07)	59379.11	18.65(0.15)	LSC
59387.09	20.06(0.17)	59387.10	19.57(0.08)	59387.09	19.26(0.09)	59387.10	18.44(0.05)	59387.11	18.55(0.09)	LSC
59395.06	19.99(0.05)	59387.10	19.56(0.08)	59387.09	19.04(0.09)	59387.11	18.42(0.05)	59387.11	18.63(0.10)	LSC
59395.06	19.99(0.06)	59395.07	19.74(0.04)	59395.07	19.37(0.04)	59395.08	18.62(0.06)	59395.09	18.67(0.07)	LSC
59403.05	20.17(0.04)	59395.08	19.65(0.04)	59395.07	19.35(0.04)	59395.08	18.58(0.05)	59395.09	18.73(0.07)	LSC
59403.05	20.26(0.04)	59403.06	19.84(0.03)	59403.06	19.51(0.04)	59403.07	18.70(0.04)	59403.07	18.84(0.10)	LSC
-	-	59403.06	19.83(0.03)	59403.06	19.49(0.05)	59403.07	18.70(0.04)	59403.08	18.89(0.10)	LSC

TABLE G1: ZTF

MJD	g' (err) [mag]	r' (err) [mag]	MJD	g' (err) [mag]	r' (err) [mag]
59184.50	-	19.39(0)	59278.4	-	16.92(0.041)
59184.52	19.17(0.00)	-	59281.25	-	17.00(0.034)
59185.51	19.39(0.00)	-	59291.34	17.95(0.07)	-
59185.54	-	19.53(0)	59291.34	-	17.13(0.035)
59187.49	-	18.85(0)	59293.25	-	17.15(0.044)
59187.53	18.98(0.00)	-	59293.29	17.97(0.06)	-
59189.47	-	16.71(0)	59296.32	18.02(0.09)	-
59189.51	19.18(0.00)	-	59296.34	-	17.23(0.054)
59193.54	-	17.84(0.054)	59298.31	-	17.28(0.052)
59195.49	-	16.87(0.041)	59298.32	17.92(0.10)	-
59198.52	16.07(0.03)	-	59302.25	-	17.33(0.051)
59200.44	15.68(0.04)	-	59304.25	17.97(0.08)	-
59200.52	-	15.61(0.032)	59304.31	-	17.33(0.047)
59203.53	15.38(0.03)	-	59307.25	-	17.36(0.044)
59205.53	15.25(0.02)	-	59310.25	18.14(0.08)	-
59216.52	-	15.25(0.022)	59310.3	-	17.41(0.04)
59216.54	15.77(0.03)	-	59312.23	18.15(0.10)	-
59220.46	16.16(0.09)	-	59312.27	-	17.41(0.039)
59222.47	-	15.49(0.039)	59314.25	-	17.45(0.05)
59224.48	-	15.61(0.029)	59316.27	-	17.49(0.052)
59224.52	16.45(0.03)	-	59319.25	18.28(0.08)	-
59226.48	-	15.69(0.033)	59321.23	18.28(0.07)	-
59226.52	16.57(0.04)	-	59323.23	-	17.61(0.04)
59228.45	16.70(0.03)	-	59323.26	18.30(0.10)	-
59228.48	-	15.77(0.034)	59325.23	18.39(0.09)	-
59230.44	-	15.87(0.025)	59325.25	-	17.63(0.047)
59230.46	16.82(0.05)	-	59334.19	18.48(0.08)	-
59232.48	-	15.95(0.035)	59336.21	18.55(0.07)	-
59232.52	16.92(0.04)	-	59336.3	-	17.79(0.059)
59250.36	17.43(0.05)	-	59338.21	18.52(0.09)	-
59250.40	-	16.48(0.04)	59338.21	-	17.81(0.071)
59252.37	-	16.49(0.04)	59340.25	-	17.82(0.06)
59252.38	17.47(0.04)	-	59342.25	-	17.87(0.056)
59254.40	-	16.49(0.051)	59345.19	-	17.92(0.058)
59254.44	17.48(0.11)	-	59347.18	18.69(0.10)	-
59256.37	17.55(0.05)	-	59349.18	-	17.97(0.069)
59256.40	-	16.55(0.03)	59349.19	18.64(0.10)	-
59258.38	17.57(0.07)	-	59352.24	-	17.96(0.085)
59262.34	-	16.66(0.027)	59357.2	18.37(0.00)	-
59262.41	17.66(0.13)	-	59359.19	-	18.06(0.082)
59265.31	-	16.73(0.036)	59362.18	18.85(0.12)	-
59267.33	-	16.76(0.034)	59362.26	-	18.16(0.066)
59267.36	17.64(0.08)	-	59366.19	-	18.16(0.06)
59269.44	17.64(0.06)	-	59366.25	19.07(0.17)	-
59271.30	-	16.81(0.036)	59368.22	-	18.20(0.074)
59271.38	17.57(0.13)	-	59370.22	19.08(0.14)	-
59275.30	17.74(0.10)	-	59372.19	-	18.34(0.163)
59275.34	-	16.88(0.043)	59372.2	19.08(0.27)	-
59278.32	17.77(0.07)	-	59374.23	19.18(0.10)	-

TABLE H1: LT

MJD	g' (err) [mag]	r' (err) [mag]	i' (err) [mag]	z' (err) [mag]
59196	16.811(0.004)	16.653(0.010)	16.808(0.007)	16.910(0.005)
59197	16.416(0.011)	16.314(0.022)	16.485(0.016)	16.623(0.013)
59198	16.145(0.019)	16.068(0.017)	16.236(0.013)	16.382(0.016)
59201	15.581(0.009)	15.549(0.019)	15.705(0.014)	15.860(0.011)
59204	15.383(0.201)	15.308(0.052)	15.481(0.085)	15.672(0.065)
59205	-	-	15.430(0.316)	15.588(0.064)
59206	15.255(0.028)	15.198(0.024)	15.303(0.005)	15.430(0.010)
59212	15.414(0.009)	15.176(0.019)	15.152(0.009)	15.280(0.005)
59243	17.178(0.011)	16.420(0.006)	16.171(0.002)	15.921(0.013)
59248	17.304(0.009)	16.498(0.027)	16.284(0.010)	16.011(0.020)
59260	17.497(0.011)	16.686(0.014)	16.538(0.003)	16.146(0.002)
59265	17.522(0.004)	16.760(0.002)	16.641(0.013)	16.218(0.005)
59269	17.609(0.007)	16.813(0.009)	16.722(0.006)	16.287(0.007)
59271	17.663(0.005)	16.841(0.002)	16.741(0.001)	16.311(0.002)
59272	17.590(0.005)	16.871(0.006)	16.733(0.013)	16.320(0.003)
59276	17.664(0.018)	16.919(0.014)	16.823(0.009)	16.396(0.011)
59285	17.787(0.002)	17.045(0.001)	17.035(0.028)	16.524(0.021)
59287	17.800(0.017)	17.086(0.001)	17.052(0.015)	16.502(0.008)
59289	17.824(0.003)	17.093(0.012)	17.072(0.013)	16.572(0.009)
59291	17.865(0.008)	17.135(0.009)	17.116(0.004)	16.588(0.003)
59295	17.908(0.005)	17.207(0.013)	17.210(0.005)	16.696(0.002)
59323	18.266(0.020)	17.571(0.096)	17.631(0.009)	17.128(0.004)
59344	18.534(0.005)	17.871(0.072)	18.006(0.004)	17.555(0.004)
59351	-	-	17.989(0.005)	17.751(0.081)
59359	18.932(0.141)	18.389(0.014)	18.119(0.004)	17.892(0.101)

TABLE II: UBVRI ALFOSC AFOSC Morivan

<i>MJD</i>	<i>B</i> (err) [<i>mag</i>]	<i>V</i> (err) [<i>mag</i>]	Source
59310.964	18.715(0.045)	-	AFOSC
59203.28	15.636(0.012)	15.357(0.009)	ALFOSC
59205.225	15.508(0.012)	15.245(0.051)	ALFOSC
59206.14	15.47(0.015)	15.192(0.013)	ALFOSC
59216.29	16.016(0.042)	15.406(0.047)	ALFOSC
59230.19	17.386(0.02)	16.227(0.015)	ALFOSC
59232.155	17.504(0.016)	16.326(0.025)	ALFOSC
59235.14	17.615(0.012)	16.438(0.012)	ALFOSC
59239.2	17.719(0.012)	16.568(0.022)	ALFOSC
59363.9	19.326(0.019)	-9(0.000)	ALFOSC
59396.89	19.896(0.047)	19.279(0.023)	ALFOSC
59201.145	15.837(0.02)	15.564(0.018)	CCD
59223.115	16.811(0.032)	15.881(0.043)	CCD
59225.075	17.032(0.021)	15.977(0.012)	CCD
59227.125	17.205(0.032)	16.066(0.017)	CCD
59230.116	17.378(0.025)	16.213(0.011)	CCD
59232.052	17.491(0.034)	16.318(0.014)	CCD
59240.061	-	16.644(0.031)	CCD
59243.037	17.9(0.093)	16.653(0.029)	CCD
59244.011	17.9(0.09)	16.716(0.037)	CCD
59249.043	17.934(0.037)	16.826(0.020)	CCD
59260.963	18.134(0.064)	16.977(0.026)	CCD
59264.955	18.111(0.141)	17.087(0.081)	CCD
59269.943	18.107(0.078)	-	CCD
59270.006	-	17.125(0.047)	CCD
59274.975	18.175(0.065)	17.16(0.049)	CCD
59277.009	18.203(0.244)	17.243(0.105)	CCD
59281.912	18.247(0.059)	17.287(0.065)	CCD
59285.897	18.315(0.045)	17.339(0.032)	CCD
59289.916	18.41(0.059)	-	CCD
59290.056	-	17.421(0.043)	CCD
59290.883	18.453(0.063)	17.424(0.034)	CCD
59296.964	-	17.532(0.038)	CCD
59302.898	18.598(0.248)	17.565(0.140)	CCD
59306.929	18.566(0.086)	17.668(0.062)	CCD
59310.858	18.702(0.059)	17.686(0.044)	CCD
59313.917	18.632(0.093)	17.718(0.055)	CCD
59317.98	18.804(0.059)	17.841(0.043)	CCD
59320.843	18.705(0.084)	17.858(0.047)	CCD
59323.939	18.718(0.185)	17.982(0.069)	CCD
59337.857	19.054(0.106)	18.231(0.080)	CCD
59351.861	19.152(0.102)	18.416(0.084)	CCD
59360.852	19.317(0.001)	-9(0.000)	CCD
59360.866	-	18.511(0.145)	CCD

TABLE J1: ugvriz ALFOSC AFOSC Morivan

<i>MJD</i>	<i>u'</i> (err) [mag]	<i>g'</i> (err) [mag]	<i>r'</i> (err) [mag]	<i>i'</i> (err) [mag]	<i>z'</i> (err) [mag]	Source
59263.062	-	17.593(0.018)	16.746(0.014)	16.588(0.016)	16.257(0.014)	AFOSC
59287.05	-	-	-	-	16.578(0.018)	AFOSC
59289.-	-	17.857(0.038)	17.062(0.032)	16.963(0.032)	16.55(0.018)	AFOSC
59310.964	19.798(0.105)	-	-	-	17.049(0.023)	AFOSC
59203.29	16.011(0.012)	15.42(0.007)	15.395(0.007)	15.534(0.009)	15.743(0.016)	ALFOSC
59205.23	15.868(0.021)	15.308(0.014)	15.225(0.065)	15.338(0.068)	15.608(0.016)	ALFOSC
59206.14	15.886(0.02)	15.26(0.007)	15.206(0.008)	15.304(0.006)	15.549(0.016)	ALFOSC
59216.295	17.123(0.037)	15.661(0.045)	15.217(0.025)	15.161(0.012)	15.363(0.015)	ALFOSC
59230.195	19.019(0.03)	16.758(0.015)	15.969(0.012)	15.719(0.019)	15.753(0.016)	ALFOSC
59232.16	19.088(0.047)	16.897(0.05)	16.053(0.049)	15.791(0.062)	15.825(0.016)	ALFOSC
59235.14	19.214(0.036)	17.012(0.009)	16.16(0.014)	15.949(0.021)	15.886(0.016)	ALFOSC
59239.205	19.347(0.037)	17.158(0.015)	16.281(0.021)	16.004(0.035)	15.957(0.016)	ALFOSC
59363.905	20.75(0.059)	-	-	-	18.104(0.018)	ALFOSC
59396.89	-	19.686(0.026)	18.611(0.038)	18.652(0.020)	18.909(0.019)	ALFOSC
59201.147	16.09(0.028)	15.598(0.017)	15.602(0.02)	15.745(0.026)	-	CCD
59223.123	18.034(0.106)	16.286(0.022)	15.639(0.028)	15.476(0.030)	-	CCD
59225.083	18.372(0.087)	16.458(0.009)	15.723(0.007)	15.533(0.008)	-	CCD
59227.123	18.541(0.128)	16.61(0.015)	15.826(0.011)	15.616(0.012)	-	CCD
59230.101	18.916(0.17)	-	-	-	-	CCD
59230.13	-	16.755(0.019)	15.966(0.009)	15.706(0.016)	-	CCD
59232.034	18.653(0.19)	-	-	-	-	CCD
59232.066	-	16.889(0.014)	16.049(0.01)	15.788(0.013)	-	CCD
59240.101	-	17.188(0.028)	16.311(0.011)	16.077(0.034)	-	CCD
59243.053	-	17.24(0.039)	16.355(0.019)	16.154(0.020)	-	CCD
59244.027	-	17.297(0.04)	16.403(0.019)	16.162(0.017)	-	CCD
59249.075	-	17.369(0.029)	16.508(0.016)	16.298(0.036)	-	CCD
59260.983	-	17.532(0.018)	16.71(0.026)	16.483(0.013)	-	CCD
59264.975	-	17.592(0.097)	16.756(0.069)	16.503(0.064)	-	CCD
59270.03	-	17.635(0.053)	16.82(0.046)	16.692(0.041)	-	CCD
59274.995	-	17.782(0.047)	16.912(0.044)	16.781(0.029)	-	CCD
59277.028	-	17.802(0.07)	16.843(0.115)	16.989(0.412)	-	CCD
59281.929	-	17.791(0.036)	17.002(0.023)	16.754(0.091)	-	CCD
59285.917	-	17.829(0.029)	17.053(0.02)	16.971(0.023)	-	CCD
59290.903	-	17.918(0.032)	17.193(0.019)	17.047(0.017)	-	CCD
59295.864	-	17.989(0.048)	-	-	-	CCD
59296.977	-	17.989(0.032)	17.26(0.018)	17.2(0.039)	-	CCD
59302.918	-	18.044(0.147)	17.305(0.109)	17.386(0.110)	-	CCD
59306.946	-	18.125(0.055)	17.424(0.032)	17.427(0.044)	-	CCD
59310.879	-	18.128(0.056)	17.429(0.029)	17.437(0.032)	-	CCD
59313.937	-	18.162(0.034)	17.442(0.039)	17.415(0.034)	-	CCD
59317.997	-	18.286(0.052)	17.442(0.043)	-9(0.000)	-	CCD
59320.863	-	18.258(0.078)	17.509(0.036)	17.51(0.051)	-	CCD
59323.955	-	18.273(0.045)	17.614(0.049)	17.477(0.048)	-	CCD
59337.913	-	18.447(0.06)	17.761(0.03)	17.843(0.047)	-	CCD
59351.88	-	18.659(0.051)	17.892(0.049)	18.021(0.071)	-	CCD
59360.876	-	18.973(0.251)	18.039(0.157)	-9(0.000)	-	CCD
59361.851	-	-	18.049(0.034)	18.249(0.078)	-	CCD

TABLE K1: NIR data

<i>MJD</i>	<i>J</i> (err) [<i>mag</i>]	<i>H</i> (err) [<i>mag</i>]	<i>K</i> (err) [<i>mag</i>]	Source
59194	16.895(0.053)	16.843(0.039)	16.638(0.031)	SOFI
59217	14.487(0.023)	14.499(0.034)	14.255(0.027)	SOFI
59240	15.214(0.044)	14.984(0.031)	14.721(0.075)	NOT
59306	17.225(0.072)	16.724(0.042)	16.536(0.09)	NOT

TABLE L1: *grRiIz* photometry for GRB 190829A/SN 2019oyw. Photometry has not been corrected for host or galactic extinction as well as k-correction and GRB afterglow. Phase is given relative to initial detection and is in rest-frame.

UTC	MJD	Phase[days]	Mag(err)	Instrument
<i>g</i> -band				
2019 – 08 – 30.15	58725.15	0.29	20.88(0.05)	LT
2019 – 08 – 30.16	58725.16	0.30	20.90(0.05)	LT
2019 – 08 – 30.21	58725.21	0.35	21.34(0.06)	LT
2019 – 08 – 30.22	58725.22	0.36	21.14(0.06)	LT
2019 – 08 – 30.22	58725.22	0.37	21.26(0.05)	LT
2019 – 08 – 31.11	58726.11	1.19	22.61(0.14)	LT
2019 – 08 – 31.15	58726.15	1.23	22.84(0.31)	LT
2019 – 09 – 05.17	58731.17	5.88	23.70(0.51)	LT
2019 – 09 – 14.13	58740.13	14.18	22.21(0.80)	LT
<i>r</i> -band				
2019 – 08 – 30.15	58725.15	0.30	19.74(0.02)	LT
2019 – 08 – 30.21	58725.21	0.35	20.03(0.02)	LT
2019 – 08 – 30.23	58725.23	0.37	20.13(0.02)	LT
2019 – 08 – 31.12	58726.12	1.20	21.68(0.07)	LT
2019 – 08 – 31.15	58726.15	1.23	21.78(0.16)	LT
2019 – 09 – 02.16	58728.16	3.08	22.25(0.08)	LT
2019 – 09 – 03.13	58729.13	3.98	21.97(0.09)	LT
2019 – 09 – 04.21	58730.21	4.99	21.70(0.08)	LT
2019 – 09 – 05.14	58731.14	5.85	21.66(0.06)	LT
2019 – 09 – 05.17	58731.17	5.88	21.84(0.14)	LT
2019 – 09 – 06.17	58732.17	6.81	21.53(0.06)	LT
2019 – 09 – 10.16	58736.16	10.5	21.29(0.04)	LT
2019 – 09 – 11.20	58737.20	11.47	21.37(0.05)	LT
2019 – 09 – 14.13	58740.13	14.19	20.94(0.33)	LT
2019 – 09 – 14.17	58740.17	14.23	21.25(0.18)	LT
2019 – 10 – 04.07	58760.07	32.67	22.31(0.07)	LT
2019 – 11 – 28.98	58815.98	84.52	24.27(0.46)	LT

UTC	MJD	Phase[days]	Mag(err)	Instrument
<i>R</i> -band				
2019 – 08 – 30.06	58725.06	0.22	18.42(0.09)	Pozaneko
2019 – 08 – 30.07	58725.07	0.22	18.50(0.09)	Pozaneko
2019 – 08 – 30.36	58725.36	0.49	19.94(0.01)	VLT
2019 – 08 – 30.36	58725.36	0.49	19.95(0.01)	VLT
2019 – 08 – 30.99	58725.99	1.08	20.51(0.48)	Pozaneko
2019 – 09 – 01.30	58727.30	2.29	21.80(0.04)	VLT
2019 – 09 – 01.30	58727.30	2.29	21.84(0.04)	VLT
2019 – 09 – 02.97	58728.97	3.84	22.16(0.16)	Pozaneko
2019 – 09 – 04.95	58730.95	5.68	21.58(0.15)	Pozaneko
2019 – 09 – 05.93	58731.93	6.59	21.42(0.15)	Pozaneko
2019 – 09 – 06.04	58732.04	6.68	21.35(0.20)	Pozaneko
2019 – 09 – 10.95	58736.95	11.23	21.35(0.17)	Pozaneko
2019 – 09 – 12.92	58738.92	13.06	21.52(0.15)	Pozaneko
2019 – 09 – 16.88	58742.88	16.74	22.07(0.27)	Pozaneko
2019 – 09 – 17.91	58743.91	17.69	22.18(0.24)	Pozaneko
<i>i</i> -band				
2019 – 08 – 30.15	58725.15	0.30	18.83(0.01)	LT
2019 – 08 – 30.21	58725.21	0.35	19.09(0.02)	LT
2019 – 08 – 30.22	58725.22	0.36	19.11(0.02)	LT
2019 – 08 – 30.23	58725.23	0.37	19.14(0.01)	LT
2019 – 08 – 31.10	58726.10	1.18	20.74(0.05)	LT
2019 – 08 – 31.14	58726.14	1.21	20.72(0.04)	LT
2019 – 08 – 31.15	58726.15	1.23	20.72(0.09)	LT
2019 – 09 – 02.15	58728.15	3.08	21.76(0.07)	LT
2019 – 09 – 03.12	58729.12	3.97	21.44(0.10)	LT
2019 – 09 – 04.20	58730.20	4.98	21.34(0.06)	LT
2019 – 09 – 05.13	58731.13	5.84	21.37(0.09)	LT
2019 – 09 – 05.17	58731.17	5.88	21.22(0.14)	LT
2019 – 09 – 06.16	58732.16	6.80	21.23(0.07)	LT
2019 – 09 – 10.14	58736.14	10.49	20.99(0.04)	LT
2019 – 09 – 11.18	58737.18	11.45	20.91(0.05)	LT
2019 – 09 – 14.13	58740.13	14.19	20.90(0.07)	LT
2019 – 10 – 04.06	58760.06	32.66	21.64(0.05)	LT
2019 – 10 – 12.01	58768.01	40.04	21.83(0.21)	LT

UTC	MJD	Phase[days]	Mag(err)	Instrument
<i>i</i> -band cont.				
2019 – 10 – 18.16	58774.16	45.74	21.70(0.14)	LT
2019 – 10 – 19.17	58775.17	46.67	22.30(0.18)	LT
2019 – 10 – 19.17	58775.17	46.67	22.40(0.22)	LT
2019 – 11 – 28.98	58815.98	84.51	22.94(0.20)	LT
<i>I</i> -band				
2019 – 09 – 01.31	58727.31	2.30	20.79(0.03)	VLT
2019 – 09 – 03.35	58729.35	4.19	20.76(0.03)	VLT
2019 – 09 – 03.35	58729.35	4.19	20.86(0.04)	VLT
2019 – 09 – 03.36	58729.36	4.20	20.79(0.03)	VLT
2019 – 09 – 11.18	58737.18	11.45	20.40(0.04)	VLT
2019 – 09 – 11.18	58737.18	11.45	20.46(0.03)	VLT
2019 – 09 – 11.18	58737.18	11.45	20.46(0.04)	VLT
2019 – 09 – 11.21	58737.21	11.48	20.32(0.03)	VLT
2019 – 09 – 11.21	58737.21	11.48	20.32(0.03)	VLT
2019 – 09 – 11.21	58737.21	11.48	20.44(0.04)	VLT
2019 – 09 – 15.33	58741.33	15.30	20.34(0.03)	VLT
2019 – 09 – 15.33	58741.33	15.30	20.42(0.04)	VLT
2019 – 09 – 21.25	58747.25	20.79	20.48(0.04)	VLT
2019 – 09 – 21.25	58747.25	20.79	20.49(0.04)	VLT
2019 – 09 – 21.25	58747.25	20.79	20.53(0.04)	VLT
2019 – 09 – 21.28	58747.28	20.82	20.49(0.03)	VLT
2019 – 09 – 21.28	58747.28	20.82	20.49(0.03)	VLT
<i>z</i> -band				
2019 – 08 – 30.15	58725.15	0.30	18.19(0.02)	LT
2019 – 08 – 30.21	58725.21	0.36	18.43(0.02)	LT
2019 – 08 – 31.13	58726.13	1.21	20.03(0.04)	LT
2019 – 09 – 01.31	58727.31	2.30	20.70(0.03)	VLT
2019 – 09 – 02.16	58728.16	3.09	20.87(0.09)	LT
2019 – 09 – 03.14	58729.14	3.99	21.16(0.18)	LT
2019 – 09 – 04.22	58730.22	5.00	20.85(0.11)	LT
2019 – 09 – 14.13	58740.13	14.18	20.13(0.21)	LT
2019 – 09 – 15.08	58741.08	15.06	20.21(0.13)	LT
2019 – 09 – 16.11	58742.11	16.03	20.17(0.12)	LT
2019 – 10 – 10.06	58766.06	38.23	21.43(0.12)	LT
2019 – 10 – 11.00	58768.00	40.02	21.28(0.21)	LT
2019 – 10 – 11.03	58767.03	39.13	21.62(0.14)	LT
2019 – 10 – 12.00	58768.00	40.03	21.37(0.18)	LT
2019 – 10 – 18.10	58774.10	45.68	21.80(0.47)	LT
